From Atmospheric to Pressurized Solid Oxide Cells

Zur Erlangung des akademischen Grades eines

Doktors der Ingenieurwissenschaften (Dr.-Ing.)

von der KIT-Fakultät für Elektrotechnik und Informationstechnik des Karlsruher Instituts für Technologie (KIT)

angenommene

Dissertation

von

M.Sc., Großelindemann Cedric

geboren in Bonn

Tag der mündlichen Prüfung: 15.09.2025
Hauptreferent: PD Dr.-Ing. André Weber
1. Korreferent: Prof. Dr. Jan Froitzheim
2. Korreferent: apl. Prof. Dr.-Ing. Alexander Colsmann

Kurzfassung

Hochtemperatur-Festelektrolytzellen stellen für die Kopplung verschiedener Energiesektoren eine vielversprechende Technologie dar. Diese können im Elektrolysebetrieb mithilfe von erneuerbaren Energien Wasserstoff generieren, welcher in nachfolgenden Prozessketten zur Erzeugung wertvoller Chemikalien genutzt oder in Tanks für mobile Anwendungen gespeichert werden kann. Somit lassen sich saisonal bedingte Schwankungen der Verfügbarkeit von erneuerbaren Energien ausgleichen. Die Speicherung und häufig auch Nutzung des Wasserstoffs erfolgt dabei bei höheren Betriebsdrücken und erfordert eine Kompression auf das benötigte Druckniveau. Insbesondere die erste Stufe einer mechanischen Verdichtung stellt sich dabei als besonders energie- sowie kostenintensiv heraus. Bisher verfügbare kommerzielle Systeme werden bei nahezu atmosphärischen Druckbedingungen betrieben. Im Hinblick auf die optimale Integration in die Prozesskette soll das Druckniveau der Hochtemperatur-Elektrolyse erhöht werden, um eine Steigerung der Kosteneffizienz zu ermöglichen. Hochtemperatur-Festelektrolytzellen können umgekehrt im Brennstoffzellenbetrieb Wasserstoff nutzen. Eine Kopplung mit einer Gasturbine ermöglicht hierbei eine Steigerung der Leistungsdichte im Überdruckbetrieb.

Die Bereitstellung einer wettbewerbsfähigen Leistungsfähigkeit eines Systems mit Hochtemperatur-Festelektrolytzellen erfordert die serielle Verschaltung einer Vielzahl an Zellen. Im Rahmen dieser Arbeit wird ein kleinflächiger Ausschnitt einer solchen Zelle elektrochemisch charakterisiert und modelliert. Dabei lassen sich durch eine gezielte Variation der Betriebsbedingungen verschiedene Zustände im später eingesetzten Zellstapel abbilden. Ziel ist es dabei, die verschiedenen Verlustprozesse der Zelle mithilfe der elektrochemischen Impedanzspektroskopie sowie der Verteilung der Relaxationszeiten zu charakterisieren und modellieren. In Vorgängerarbeiten wurde hierzu eine Vielzahl an Studien unter atmosphärischem Druck durchgeführt. Die Erhöhung des Druckniveaus auf 11 bar_a in dieser Arbeit erfordert die Erweiterung und den Umbau von vorhandener Prüfstandstechnologie am Institut für Angewandte Materialien – Elektrochemische Technologien. Aus der Literatur bekannte Prüfstände für den Druckbetrieb sind mit einem Drucktank ausgestattet, wobei der brenngas- sowie luftseitig anliegende Druck ausgeglichen wird, um ein mechanisches Versagen der Zelle sowie der Abdichtung zu unterbinden. Im Rahmen dieser Arbeit wurde ein neuartiges Konzept im Labormaßstab im Hinblick auf die Abdichtung der Zelle sowie Druckregelung ohne Verwendung eines Drucktanks entwickelt sowie experimentell erstmals demonstriert. Dabei kommt ein neuartiges metallisches Zellgehäuse zum Einsatz, welches durch Glaslot und mechanische Kompression abgedichtet wird. Differenzdrücke zwischen Brenngas- und Luftseite werden durch eine der Zelle nachgeschaltenen Brennkammer minimiert.

Dies erfordert eine Reihe an Voruntersuchungen und Referenzmessungen bei atmosphärischen Druckbedingungen in bereits vorhandenen Prüfständen. Zunächst wird eine elektrolyt-gestützte Zelle mit einer Nickel/Gadolinium-dotierten Ceroxid Brenngaselektrode sowie 3 mol.% Yttrium-stabilisierten Zirkonoxid Elektrolyt und $La_wSr_xCo_yFe_zO_{3-\delta}$ Luftelektrode unter atmosphärischen Bedingungen charakterisiert. Dies wird durch eine Überlagerung von Prozessen der

Brenngas- sowie Luftelektrode erschwert, weshalb symmetrische Zellen eingesetzt werden. Hinzu kommt eine weitere aus der Literatur bekannte Überlagerung der Gasdiffusions- sowie Aktvierungspolarisation der Brenngaselektrode. Hier wird die Entfaltung der Gasdiffusion mithilfe eines Brenngasgemisches mit Stickstoff und Helium überwunden, sodass die Zelle parametriert werden kann. Somit wird ein impedanz-basiertes 0-dimensionales Kennlinienmodell für den Betrieb mit Wasserstoff/Wasserdampf sowie Kohlenstoffmonoxid/-dioxid vorgestellt und validiert. Mithilfe des Kennlinienmodells lässt sich das Strom-Spannungsverhalten unter erhöhten Betriebsdrücken vorhersagen. Für den in dieser Arbeit entwickelten Druckmessplatz ist eine stack-nahe Kontaktierung mit metallischen Interkonnektoren vorgesehen. Hieraus ergeben sich zusätzlich zu den intrinsichen Zellverlusten weitere durch Chrom-Verdampfung und – Vergiftung der Luftelektrode sowie Limitierungen in der Gasversorgung und erhöhte Kontaktwiderstände. Diese Einflüsse werden ebenfalls in Vorversuchen unter atmosphärischen Bedingungen analysiert.

Zunächst wurden drei verschiedene metallische Interkonnektoren (Crofer 22 APU/AISI 441/UNS S44330) mit und ohne Auftragung einer Cer-Cobalt-Schutzschicht untersucht. Es konnte gezeigt werden, dass unabhängig vom Stahl mithilfe der Schutzschicht eine nahezu ideale Leistungsfähigkeit der Zelle möglich ist. Die Beschichtung verringert dabei signifikant die Kontaktwiderstände. Durch mikrostrukturelle Untersuchungen der beschichteten metallischen Interkonnektoren wurde gezeigt, dass sich hierbei ähnliche Chromoxidschichten ausbilden sowie ein Cobalt-Mangan-Spinell an der Oberfläche vorliegt. Anhand einer mikrostrukturellen Untersuchung der Luftelektrode konnte gezeigt werden, dass Chromverdampfung und die daraus resultierende Vergiftung der Elektrode durch die Beschichtung minimiert werden konnte.

Abschließend konnte erstmalig der Druckbetrieb einer elektrolytgestützten Zelle ohne Drucktank in einem eigens in dieser Arbeit entwickelten Prüfstandsaufbau gezeigt werden. Hierbei wurde in einer ersten Version ein aluminiumoxidbildender Stahl für das Zellgehäuse verwendet, sodass ein Einfluss durch Chromvergiftung der Zelle durch das Gehäuse minimiert wird. Das auf Glaslot basierende Abdichtungskonzept konnte dabei Druckgradienten von 10 bar im Vergleich zur Atmosphäre selbst nach einem Thermozyklus standhalten. Darüberhinaus wurden Erwartungen auf Basis von Vorsimulationen und Literatur bestätigt wobei die Leerlaufspannung sowie Leistungsdichte signifikant mit höherem Druck steigen. Die Leistungsdichte im Brennstoffzellenbetrieb stieg dabei um 20% in Wasserstoff/Luft bei 850 °C und 11 bar_a. Weiterhin wurde das Konzept auf eine anoden-gestützte Zelle mithilfe eines zusätzlichen Dichtrahmens in einem unbeschichteten Crofer 22 H Zellgehäuse erweitert, welches sich ebenfalls mit Glaslot abdichten lässt. Das Crofer 22 H erweist sich dabei im Hinblick auf die Fertigung als vorteilhaft im Vergleich zum aluminiumoxidbildenden Stahl. Hierbei durchgeführte Tests in einem unbeschichteten Crofer 22 H Zellgehäuse zeigen jedoch negative Einflüsse durch Chromverdampfung auf die Zelle und erfordern eine weitere Optimierung.

Abstract

High-Temperature solid oxide cells represent a promising technology with regard to the coupling of different energy sectors. In electrolysis mode solid oxide cells are able to generate hydrogen or syngas, which can be used in several chemical downstream processes or stored in tanks for mobile applications. Thus, fluctuations in seasonally occuring energy supply can be balanced out. Downstream processes operate at higher pressures which requires compression of the hydrogen as commercially available high temperature electrolyzers operate at pressures close to atmospheric conditions. The first stage of the mechanical compression of hydrogen is especially energy and cost intensive. Thus, the pressurization of solid oxide electrolysis cells is a promising factor for increasing the overall process efficiency. In addition, solid oxide cells can be reversely operated in the fuel cell mode, and when coupled with a gas turbine, power density can be increased in the pressurized mode.

To achieve competitive power densities, a large number of cells need to be serially connected in a stack. The present work electrochemically characterized and modeled small scale solid oxide cells in the atmospheric and pressurized mode. With systematic variation of operating parameters such as temperature or gas composition, different positions of the cell in the stack could be mimicked. By means of electrochemical impedance spectroscopy and the subsequent distribution of relaxation times, individual performance limiting loss mechanisms of the cell were characterized and modeled. Pressurized testing of single cells up to 11 bar_a required the modification and extension of existing solid oxide cell testing technology at the Institute for Applied Materials – Electrochemical Technologies. All pressurized test sites known from literature are equipped with a heavy and voluminous pressure vessel and the need to align fuel, oxidant and vessel pressure to avoid a mechanical failure of the cell and/or stack. This usually results in a complex differential pressure control system. In the present work, a new concept based on a new glass ceramic sealed metallic cell housing was therefore developed for pressurized operation without a pressure vessel. In addition, a unique pressure regulation system based on a downstream combustor was demonstrated to minimize pressure gradients between fuel and air side.

Initially, this testing set-up required a series of pre- and reference measurements. At first, an electrolyte-supported cell with a Nickel/Gadolinia-doped ceria fuel electrode, 3 mol.% yttria-stabilized zirconia and $La_wSr_xCo_yFe_zO_{3-\delta}$ air electrode was characterized at atmospheric pressure with an existing test bench. This was performed with an ideal contacting in order to solely observe the intrinsic losses of the cell. An overlap of processes of fuel and air electrode was observed and solved with the characterization of symmetrical cells. With respect to the fuel electrode, a severe overlap of processes has been reported in the literature for gas diffusion and activation polarization losses and impedes an unambiguous process assignment of fuel electrode processes in the impedance spectra. Thus, the deconvolution of gas diffusion polarization was solved with a symmetrical cell as well as a fuel gas mixture based on nitrogen and helium. Subsequently, a zero-dimensional impedance-based direct current performance model was

developed for H_2/H_2O in comparison to CO/CO_2 operation and validated for technically relevant operation conditions.

Within the new metallic housing for pressurized testing, a stack-like contacting was applied. Thus, further loss processes may come into effect such as increased contact losses, limitations in gas supply and chromium poisoning. The stack-like contacting was therefore also characterized at atmospheric pressure with three different metallic interconnectors (Crofer 22 APU/AISI 441/UNS S44330) and a Cerium-Cobalt protective coating. Irrespective of the metal, the ideal cell performance was reached with coated metallic interconnectors as they decreased the contact resistance significantly in comparison to the uncoated state. The coated samples were investigated on a microstructural level and showed a similar chromium oxide scale with a Cobalt-Mangan spinell layer at the surface. In addition, as shown by microstructural analysis, the coating effectively blocked the chromium evaporation and subsequent chromium poisoning of the air electrode.

Finally, a similar stack-like contacting was applied for the new pressurized test bench. Here, an aluminium oxide forming steel grade was used in a first step to minimize negative impacts on the cell related to chromium poisoning. As a result of this work, an electrolyte-supported solid oxide single cell was operated up to 11 bar_a without pressure vessel within a specifically designed testing environment in this work. Here, the sealing concept could withstand pressure gradients of up to 10 bar and a full thermal cycle. The open-circuit voltage as well as power density increased as expected from literature and were confirmed by theoretical predictions. In fuel cell mode at 11 bar_a and 850 °C with hydrogen/air, an increase of power density by 20% was observed. The set-up was then also applied to testing of anode-supported cells with the help of an additional ceramic sealing frame in an uncoated Crofer 22 H cell housing. Although easier machinability and weldability of Crofer 22 H in comparison to the aluminium oxide forming steel grade was beneficial, chromium poisoning of the cell was assumed and further optimization required.

Table of Contents

Acknowledgements

This work was only made possible by the support of a number of people and cooperations who I would like to thank in the following.

At first, I would like to specially thank my supervisor André Weber. I already noticed during my master thesis at the institute how much I can learn from you. For your expertise and for everything else I am highly grateful. Of course, I remember the great times at the conferences in Boston and Lucerne. Also, it was a pleasure to attend the ICACC 2025 in Daytona Beach, USA.

During the ECS SOFC XVIII conference in Boston I met Prof. Jan Froitzheim and Dr. Mareddy Jayanth Reddy from the Chalmers University of Technology, who freely offered to perform a post-mortem analysis of the tested metallic interconnectors I had just presented. I am very grateful for this spontaneous opportunity, which resulted in a joint publication. I also greatly appreciate Prof. Jan Froitzheim taking over a part of the examination of this thesis.

I would like to thank the 3rd examiner apl. Prof. Dr.-Ing. Alexander Colsmann for the time and effort evaluating this thesis.

In addition, I would like to thank Prof. Dr.-Ing. Ulrike Krewer for the support when inviting international students.

My colleague Felix Kullmann and I started our PhD journey on the same day. First under pandemic rules but soon we were seated in the same office. We were on the same page from day one and worked well together. I really enjoyed many discussions, where we just flipped the screen in order to discuss the latest results. Our knowledge grew continuously and we managed lots of challenges by supporting each other.

Daniel Esau and I worked together on different projects and we supervised many students during their thesis at the institute. I could always rely on your expertise and support. Next to numerous project meetings in Germany, I like to remember our business trip to the Netherlands.

The supervision of students greatly developed my expertise as well as social skills. I am very happy that Daniel Ewald could join our group at the institute after writing his master thesis with us and knowledge could be shifted to the new generation. I enjoyed the office times together a lot.

I would like to highly thank all students for their effort at the institute (list in alphabetic order of the last name): Frank Manuel Bauer, Jan Daubenthaler, Martin Deichelbohrer, Marvin Dorn, Sören Drotleff, Daniel Tobias Ewald, Oliver Fritz, Andreas Geiger, Mischa Geörg, Esther Heil, Fabian Herburger, Marius Jens Kleinfeld, Felix Lubik, Felix Leonce Martinez Martinez, Marvin Necker, Sven Piduch, Sören Peter Sckuhr and Manuel Seim.

A DAAD scholarship provided me with the opportunity to twice work abroad as a research intern during my studies at KIT. As I greatly enjoyed this time, it was my pleasure to realize this for incoming students at our institute as internships funded by DAAD RISE. During the last

years Daniel Esau and I hosted Kristella Putz, Elizabeth Katzman and Daniel Kesler on research internships.

On a regular basis I organized after work social events with different get-togethers of the fuel cell group with lots of good food. In addition, I would like to thank Wolfgang Menesklou for organizing team-building events that had a clear positive impact on the atmosphere at the institute.

Without the mechanical workshop, the newly developed cell housing for pressurized testing would not have been possible. Thus, I highly appreciate the support from Stefan Ziegler, Simon Rothardt, Daniel Hintermayer, Andreas Pauly as well as Jochen Ritter. Welding of the metallic housing was critical and thankfully performed by Ralf Rössler at IAM-WK.

Our technician Annette Schucker supported with great SEM graphs. I am also grateful for microstructural analysis performed by Florian Wankmüller, Tibor Lehnert, Ardavan Makvandi and Heike Störmer at LEM.

I would like to thank Marika Schäfer, Martina Wagner and Elke-Sénégas-Rouvière in the secretarial office for their kind support. Also, I would like to thank our technician Alexander Boschmann for his effort at the institute.

Our facility manager Joachim Nagler helped many times with several problems – thank you very much.

Whenever I had a question regarding IT or with regard to the test bench software, Torsten Johannsen was always a great help to me.

The time at the institute began with my master thesis, which was thankfully supervised by Niklas Russner and Sebastian Dierickx.

In a strong cooperation with Svetlana Korneychuk and Prof. Astrid Pundt we learned a lot about the reduction process of a Ni/YSZ fuel electrode with impressive insights by *In-Situ* TEM. Thank you very much for this great cooperation which was awarded at the EFCF 2024.

This work was only possible with a strong network of project partners who delivered e.g. state-of-the-art experimental cells or materials. Thus, I highly appreciate the support from Kerafol Keramische Folien GmbH & Co. KG with Franz-Martin Fuchs for providing electrolytes and the Sunfire SE with especially Christian Geipel and Chen-Yu Tsai for producing the test cells. In addition, the CeCo-coating of the metallic interconnectors was thankfully provided by Niklas Norrby, Mikael Stenström, Shunyi Li and Jörgen Westlinder at Alleima AB. I would like to further thank Norbert Menzler for discussions at project meetings and conferences as well as for the LSCF contact paste. Furthermore, I would like to thank the SCHOTT AG for providing different glass ceramic sealings. A new metallic cell housing made of Crofer 22 H was realized by raw materials supplied by VDM Metals International GmbH.

In addition, I gratefully acknowledge funding from the Helmholtz Society Innovation Pool project "Solar hydrogen: high purity and compressed" (38.03.02) and from the Federal Ministry of Research, Technology and Space (BMFTR 03HY124C) within the flagship project H2Giga –

HTEL Stacks: „Ready for Gigawatt“. In addition, the international cooperation within the project „SOE-Mod“ provided a great chance to enlarge my network as I got to know Michiel Langerman and Frans van Berkel at TNO, who I would like to thank for their hospitality in Petten and Alkmaar as well as the supply of experimental cells.

In a podcast edition together with Gabi Zachmann at “KIT-Nachgefragt” we talked about hydrogen and my PhD topics which was a great experience for me.

The time during the PhD is shaped by numerous ups and downs. Thus, I sincerely thank my family and friends for always supporting me and especially Franziska who is always there for me.

1 Introduction[1]

This work investigates the transition from atmospheric to pressurized solid oxide cells (SOCs) and is based on the characterization of intrinsic as well as stack-like cell behavior at atmospheric conditions. This knowledge is then transferred to a newly developed test bench enabling tests under pressurized operating conditions. The motivation behind this work and its scope are described in the following chapter.

1.1 Motivation

For a carbon-neutral economy, hydrogen (H_2) is needed for multiple conversion technologies within the chemical, cement, steel and transportation industries (Figure 1) and is clearly an important link between different sectors of industry.

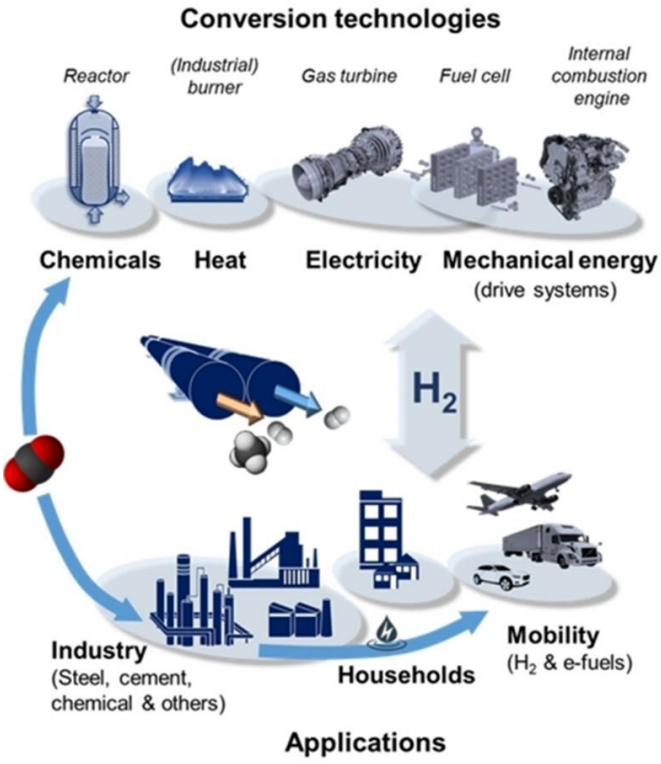

Figure 1 Principal sketch of hydrogen coupled to different conversion technologies and its usage in industry, households and mobility. Graphic taken from Ref. [1].

The “Green Deal” [3] of the European Union (EU) aims for Europe to become the first climate neutral continent. Based on this, the goals from the Paris agreement [4] in 2015 are to reduce

[1] Parts of the introduction have been published in M. Ivanova, …, C. Grosselindemann et al., *Angew. Chem.*, **62**, e202218850 (2023) [1] and C. Grosselindemann et al., *J. Power Sources*, **614**, 234963 (2024) [2].

global warming to ideally 1.5 °C in comparison to the pre-industrial era. Here, the generation and use of green hydrogen (H_2) based on renewable energies can play a key role by linking different energy sectors for the decarbonization of value chains (see Figure 1). Thus, the German government developed the National Hydrogen Strategy (NHS) [5] in 2020 in order to accelerate the market ramp up. In the context of the Russian aggression against Ukraine, this need was sharpened in 2023 as unilateral energy imports proved to be insufficient for the security of the national energy supply. Thus, a more independent and diverse energy mix is clearly needed. The compression of hydrogen is crucial to the different value chains from generation to the use of hydrogen (Figure 2). Hydrogen is used in the chemical industry at elevated pressures as shown for the ammonia synthesis, a crucial chemical for fertilizers and ship fuel, whose production runs at pressures up to 300 bar_a. When hydrogen is stored in a tank for a car, it needs to be compressed up to 700 bar_a.

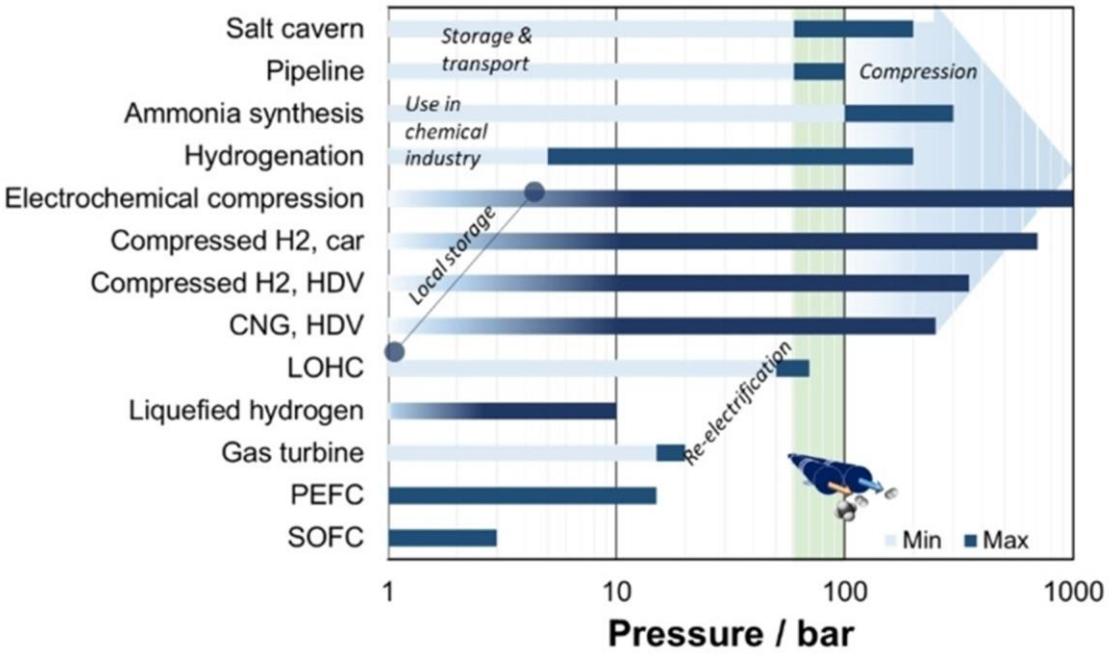

Figure 2 Pressure levels of hydrogen in the supply chain. Graphic taken from Ref. [1].

Up to now, the majority of H_2 is mainly generated by steam reforming of methane resulting in high emissions of carbon dioxide (CO_2) and is labeled as grey H_2. In contrast, a variety of technologies exists at different Technology Readiness Levels (TRL, ranging from fundamental research (1) to a mature technology (9)) in order to generate pure and compressed hydrogen from solar power. High TRL values are reached for alkaline (TRL $8-9$), polymer exchange membrane (TRL $8-9$) and solid oxide cell-based water electrolysis (TRL $6-7$). Further technologies such as photoelectrochemical or thermochemical water splitting (both TRL 5), pyrolysis of hydrocarbons (turquois H_2, low TRL), plasma conversion technology (TRL $2-4$) and electrochemical H_2 separation and compression (TRL < 5) still need significant improvement towards commercial application [1]. Considering the TRL, a focus was recently put on

water electrolysis applications and the NHS targets were raised in 2023 to at least 10 GW electrolysis capacity in Germany by 2030 [5]. Further demands need to be supplied by imports of hydrogen. In case of a gaseous supply of hydrogen in the importing country, liquified hydrogen represents the most efficient import option [6]. In addition, the availability of renewable energies and levelized costs for the production of hydrogen are highly dependent on the position around the globe. However, a large-scale production of electrolysis units is needed. Among the various types of water electrolysis, a key technology offering the highest efficiencies for H_2 production is solid oxide cell based water electrolysis [1] which is in the focus of this work. These cells also have the ability to run reversely in the fuel cell mode so that electrical energy can be generated and are not limited to hydrogen/steam (H_2/H_2O) fuel gas mixtures. Among a large fuel flexibility [7] operation with carbon monoxide/-dioxide (CO/CO_2) and reformate mixtures of H_2/H_2O/CO/CO_2 is possible for fuel cell and electrolysis mode. In case of co-electrolysis a synthesis gas consisting of H_2 and CO can be generated, which can be fed into chemical reactors creating valuable chemical products.

SOCs are mostly operated close to atmospheric pressure as the ceramic cells and available high temperature sealants are sensitive towards pressure gradients, which leads to problems regarding gas tightness and pressure regulation [8]. However, it has been known for a long time that pressurized operation of a solid oxide fuel cell (SOFC) enables a higher power density and efficiency and coupling with a gas turbine can further increase system performance [9–12]. In the case of electrolysis, the produced hydrogen has to be compressed to a level meaningful for the specific application. Mechanical hydrogen compressors are a well-developed technology [13]. However, they still have considerable limitations as they are quite bulky and require a high energy input. In particular, the first compression step from ambient pressure to several bar_a (bar_a is used for absolute pressure) is critical. Previous studies have shown a decrease of approx. $4-5\%$ energy efficiency considering a downstream compressor for H_2 to 30 bar [14,15]. Thus, through bypassing the first compression step for the downstream processes the overall process efficiency can be increased. In literature, SOC systems and testing devices for cells and stacks were realized with a pressure vessel [8,16–26], resulting in voluminous, costly and heavy systems. As cells and sealants used in stacks are considered to be limited to pressure gradients in the range of a few hundred $mbar_a$, a complex pressure control strategy is required to align vessel-, fuel- and oxidant pressures. [2] This shall be targeted in this work of which scope is described below.

1.2 Scope of this Work

The electrochemical characterization and modeling of SOCs is crucial in order to further lift the TRL towards the commercialization of this technology. SOCs need to be further optimized so that longevity and high performance is guaranteed. In this work, a SOC was characterized by electrochemical impedance spectroscopy and the subsequent distribution of relaxation times with respect to the intrinsic losses of the cell in an ideal contacting environment with 1 cm^2 single cells at atmospheric pressure. Based on this the cell was parametrized to develop an impedance-based zero-dimensional (0D) direct current (dc) performance model in H_2/H_2O and CO/CO_2 mode. In a real SOC stack, the cells are contacted with metallic interconnectors which

results in limitations in gas supply, increased contact losses as well as chromium poisoning. Thus, a stack-like contacting of the SOC with metallic flow fields was investigated with three different steel grades (Crofer 22 APU/ AISI 441/ UNS S44330) and characterized based on a method by Kornely et al. [27]. Here, the impact of a protective Cerium-Cobalt (CeCo) coating was analyzed electrochemically as well as on a microstructural level.

These investigations under atmospheric pressure provided a basis for a newly developed pressurized test bench, which is based on existing SOC testing technology [28] at the Institute for Applied Materials – Electrochemical Technologies. In this thesis, a new concept for pressurized testing of single cells without pressure vessel was designed including a glass-ceramic sealed metallic housing. In addition, a unique pressure regulation with a single downstream pressure controller was introduced. For the first time, a solid oxide cell was operated without pressure vessel up to 11 bar_a in a stack-like environment. The theoretical predictions of the open-circuit voltage and impact of pressure on the polarization resistance will be shown. The developed concept is fully transferable to stack-level.

2 Fundamentals

In this chapter the theoretical background related to this thesis is summarized. Solid oxide cells can reversely be operated in fuel cell as well as electrolysis mode, which is useful for H_2-based energy storage systems [1]. The working principle is explained in the fuel cell mode. With respect to electrolysis mode, all processes run vice versa.

2.1 Working Principle[1]

SOFCs are operated in a temperature range of 600 – 900 °C as the oxygen ion conductivity of the solid electrolyte is activated at these temperatures. In contrast, cells based on proton conducting ceramic electrolytes are operated at a comparably lower temperature between 400 – 650 °C [1]. This work focusses on cells with oxygen ion conducting electrolytes. In Figure 3, the working principle schematic of the SOFC is shown. In general, a three-layer set-up can be seen with two porous electrodes at the air and fuel side. In between a gas tight solid electrolyte is placed which separates the gas phase from fuel and air side. Hydrogen is supplied at the fuel side via gas channels and air at the air side. At the three-phase boundary, the reaction zone evolves between gas phase/electronic- and ionic conducting phase.

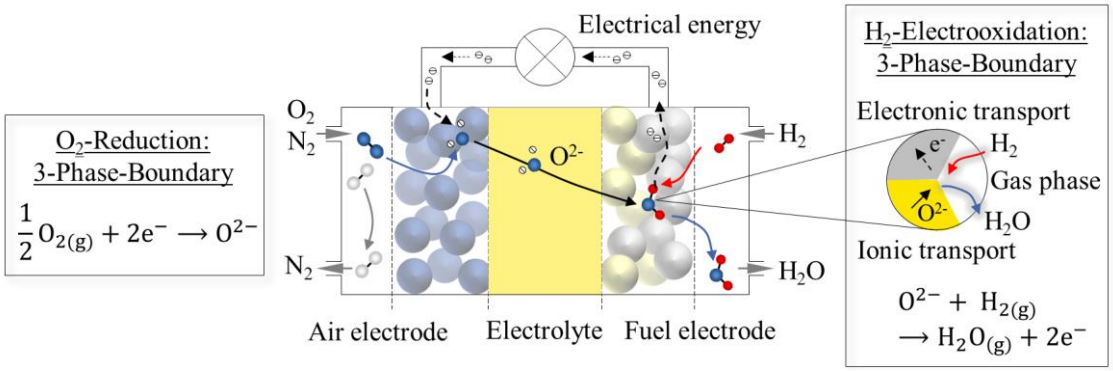

Figure 3 Working principle schematic of a solid oxide fuel cell. Adapted and modified from Ref. [29,30].

The overall reaction is described in equation (1).

$$H_{2(g)} + \frac{1}{2} O_{2(g)} \rightleftharpoons H_2O_{(g)} \qquad (1)$$

In equation (2), oxygen (O_2) is reduced by two electrons to an oxygen ion at the air electrode, which migrates through the electrolyte due to a concentration gradient of the oxygen partial

[1] Parts of this chapter have been published in M. Ivanova, …, C. Grosselindemann et al., *Angew. Chem.*, **62**, e202218850 (2023) [1].

pressure p_{O_2} between air and fuel side. The oxygen partial pressure at the fuel side $p_{O_2,FE}$ results from the equilibrium of the fuel gas mixture between hydrogen (H_2) and steam (H_2O) [31], which can also be described with equation (1).

$$\frac{1}{2}O_{2(g)} + 2e^- \rightleftharpoons O^{2-}_{Electrolyte} \tag{2}$$

Subsequently, the electrooxidation of hydrogen (H_2) as shown in equation (3) takes place. Here steam (H_2O) is generated by releasing two electrons.

$$O^{2-}_{Electrolyte} + H_{2(g)} \rightleftharpoons H_2O_{(g)} + 2e^- \tag{3}$$

In this work, ideal gases are assumed and the ideal gas law is shown in equation (4) with V denoting the volume and N_i the amount of substance regarding the species i.

$$p_i V = N_i \tilde{R} T \tag{4}$$

The partial pressure p_i of the species i is described by Dalton´s law in equation (5) with the molar fraction $\tilde{y}_i$ and the absolute pressure p.

$$p_i = \tilde{y}_i \cdot p \tag{5}$$

2.2 Open-circuit Voltage

In the open-circuit state an electrochemical equilibrium results since electrons from the electrooxidation do not migrate via the external load. An electrical field evolves in the opposite direction to the diffusion of oxygen ions in the electrolyte. This can be described based on equation (6) for the Nernst-voltage U_N with $\tilde{R}$ denoting the universal gas constant, T the temperature, z the number of transferred electrons (here $z = 2$), F the Faraday constant and $p_{O_2,el}$ the oxygen partial pressure at fuel (FE) and air electrode (AE) respectively.

$$U_N = \frac{\tilde{R}T}{zF} \cdot \ln\left(\frac{p_{O_2,AE}}{p_{O_2,FE}}\right)^{0.5} \tag{6}$$

With the law of mass action the Nernst-equation, which equals the open-circuit voltage U_{OCV}, can be expressed with the molar fractions of hydrogen $\tilde{y}_{H_2,FE}$ and steam $\tilde{y}_{H_2O,FE}$ at the fuel side as well as oxygen $\tilde{y}_{O_2,AE}$ at the air side with the absolute pressure p in equation (7). $\Delta_R G_0(T)$ denotes the free standard reaction enthalpy [32].

$$U_N = U_{OCV} = -\frac{\Delta_R G_0(T)}{zF} - \frac{\tilde{R}T}{zF} \cdot \ln\left(\frac{\tilde{y}_{H_2O,FE}}{\left(\tilde{y}_{O_2,AE} \cdot p\right)^{0.5} \cdot \tilde{y}_{H_2,FE}}\right) \tag{7}$$

The theoretical dependency of the OCV [33] as a function of the overall pressure is shown in Figure 4 based on equation (7) for exemplary conditions at $T = 800$ °C with 50% H_2 (balance H_2O) and air as the oxidant up to 15 bar_a. With increasing pressure, the OCV is increasing. This is the case for double-sided pressurization (fuel + air side). As can be seen by the Nernst-equation (7), only the air side pressure is relevant. So in case of a single-sided pressurization of the fuel, the increase of OCV can be excluded [34].

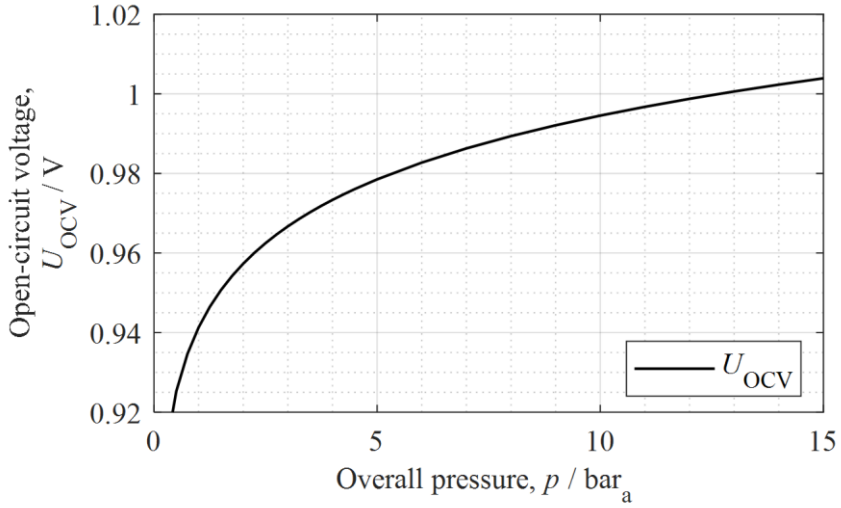

Figure 4 Simulated OCV as a function of the overall pressure p at $T = 800$ °C with 50% H_2 (balance H_2O) and air as the oxidant.

The simulation of the current voltage behavior when the cell is operated under load requires an OCV minus losses model [35], which is described in the following section.

2.3 Current-Voltage Characteristics

When the cell is operated under load, the current-voltage characteristics describe the direct current (dc) behavior of the SOFC. An example is shown in Figure 5. Starting from U_{OCV} the cell voltage U_{cell} is decreased by different physical loss mechanisms as shown in equation (8). These include ohmic losses η_{ohm}, activation losses $\eta_{\mathrm{act},EL}$ and gas diffusion losses $\eta_{\mathrm{diff},EL}$ of the electrodes (EL) at fuel and air side respectively. The theoretical open-circuit voltage U_{th} is lowered since leakage in the system or cell can occur. Furthermore, fuel utilization corresponding to the conversion of the fuel gas mixture can occur as well. However, fuel utilization is neglected in this work as small-scale cells with an active area of 1 cm^2 and high gas flow rates prevent significant gradients in temperature and gas conversion.

$$U_{\mathrm{cell}} = U_{\mathrm{OCV}} - \eta_{\mathrm{ohm}} - \eta_{\mathrm{act,FE}} - \eta_{\mathrm{act,AE}} - \eta_{\mathrm{diff,FE}} - \eta_{\mathrm{diff,AE}} \qquad (8)$$

An OCV minus losses model predicts the cell performance and provides quantitative information about different loss mechanisms which are limiting the cell performance [35].

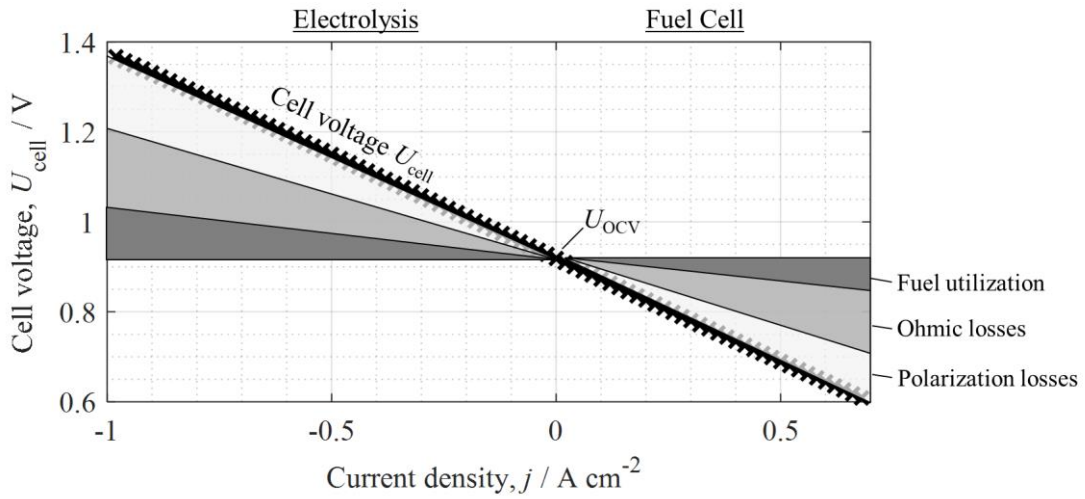

Figure 5 Current-voltage curve with schematic voltage losses in electrolysis as well as fuel cell mode.

2.4 Loss Mechanisms[2]

The individual loss mechanisms are described in the following section.

2.4.1 Ohmic Losses

In equation (9) ohmic losses are described by the ohmic law with a proportional character of the current density j and the ohmic resistance R_{ohm}.

$$\eta_{\mathrm{ohm}} = j \cdot R_{\mathrm{ohm}} \tag{9}$$

R_{ohm} can be expressed by an Arrhenius approach in equation (10) with the material specific constant B_{ohm}.

$$R_{\mathrm{ohm}}(T) = \frac{T}{B_{\mathrm{ohm}}} \cdot \exp\left(\frac{E_{\mathrm{act,ohm}}}{\tilde{R}T}\right) \tag{10}$$

2.4.2 Activation Losses

In addition, the Butler-Volmer approach is applied for the fuel and air electrode in order to describe activation losses $\eta_{\mathrm{act},EL}$ caused by the charge transfer reaction in equation (11). Here,

[2] Loss mechanisms have been described in detail by Leonide et al. [36] and are summarized here. Parts of this chapter have also been presented in a master thesis by C. Grosselindemann [30] and published in C. Grosselindemann et al., *ECS Trans.*, **103**, 1375-1393 (2021) [37] as well as C. Grosselindemann et al., *J. Electrochem. Soc.*, **168**, 124506 (2021) [38].

$j_{0,EL}$ denotes the exchange current density, which describes the catalytic activity of the electrode. Further, the charge transfer coefficient α_{EL} of the electrodes (EL) specifies the symmetry of the energy barrier of the activation in case of a positive or negative overpotential.

$$j = j_{0,EL}\left[\exp\left(\alpha_{EL}\frac{zF\eta_{\mathrm{act},EL}}{\tilde{R}T}\right) - \exp\left(-(1-\alpha_{EL})\frac{zF\eta_{\mathrm{act},EL}}{\tilde{R}T}\right)\right] \qquad (11)$$

The exchange current densities for fuel $j_{0,\mathrm{FE}}$ and air electrode $j_{0,\mathrm{AE}}$ are shown in the equations (12) and (13) respectively. At this point, the reference pressure ($p_{\mathrm{ref}} = 1.013\ \mathrm{bar_a}$) is needed as well as an exponential prefactor γ_{EL} and the activation energy $E_{\mathrm{act},EL}$ of the corresponding electrode. Here, the dimensionless exponents a and b describe the hydrogen and steam partial pressure dependency of the fuel electrode´s exchange current density, whereas m denotes the oxygen partial pressure dependency of the air electrode´s exchange current density. The impact of overall pressure p becomes obvious in equation (12) and (13).

$$j_{0,\mathrm{FE}} = \gamma_{\mathrm{FE}}\left(\frac{\tilde{y}_{\mathrm{H_2,FE}}\cdot p}{p_{\mathrm{ref}}}\right)^{a}\left(\frac{\tilde{y}_{\mathrm{H_2O,FE}}\cdot p}{p_{\mathrm{ref}}}\right)^{b}\exp\left(-\frac{E_{\mathrm{act,FE}}}{\tilde{R}T}\right) \qquad (12)$$

$$j_{0,\mathrm{AE}} = \gamma_{\mathrm{AE}}\left(\frac{\tilde{y}_{\mathrm{O_2,AE}}\cdot p}{p_{\mathrm{ref}}}\right)^{m}\exp\left(-\frac{E_{\mathrm{act,AE}}}{\tilde{R}T}\right) \qquad (13)$$

2.4.3 Gas Diffusion Losses

Gas diffusion as well as convection define the two mechanisms for mass transport. In a system for SOCs fuel and air are supplied by a convective flow based on a pressure gradient towards the cells in a stack. Within the porous electrodes of the cells, this gradient can be neglected, so that gas diffusion is the dominant mechanism based on a concentration gradient between gas channel and the active reaction sites at the electrodes. Different phenomena of gas diffusion need to be considered in terms of the porous three-dimensional structure of the electrodes. Thus, gas transport is limited by collisions of gas molecules with each other (molecular gas diffusion), but also possibly by collisions of gas molecules with the edges of the pores. Here, the Knudsen number Kn in equation (14) is a critical measure, if Knudsen gas diffusion needs to be considered as well ($Kn \gg 1$). Λ represents the mean free path and L_{C} a characteristic length.

$$Kn = \frac{\Lambda}{L_{\mathrm{C}}} \qquad (14)$$

As shown in the work by Joos et al. [39], Knudsen gas diffusion needs to be considered as pore diameters of $400 - 600$ nm were identified in electrodes of solid oxide cells.

The molar gas diffusion coefficient of a binary gas mixture with the gas species i in j ($D_{\mathrm{mol},ij}$) can be described by the Chapman-Enskog theory [40] in equation (15). Here, $\widetilde{M}_{i/j}$ defines molar mass of each species, $\sigma_{i/j}$ the Lennard-Jones-length and Ω_{D} the collision integral. Further information about the calculation of $\sigma_{i/j}$ and Ω_{D} can be found in the appendix 7.1 and 7.2. As

can be seen, the $D_{\mathrm{mol},ij}$ is correlating with $T^{1.5}$ to the temperature and is inverse proportional to the absolute pressure. The parameters needed for the calculation of the molecular gas diffusion coefficient are listed in the appendix in Table A 1 - Table A 3.

$$D_{\mathrm{mol},ij} = 1.86 \cdot 10^{-3} \cdot \frac{T^{1.5} \cdot \sqrt{\widetilde{M}_i^{-1} + \widetilde{M}_j^{-1}} \cdot \mathrm{atm} \cdot \mathrm{\AA}^2 \cdot \mathrm{cm}^2 \sqrt{\mathrm{g\,mol^{-1}}}}{p \cdot \sigma_{ij}^2 \cdot \Omega_{\mathrm{D}} \cdot \mathrm{K}^{1.5} \cdot \mathrm{s}} \tag{15}$$

In case of a ternary gas mixture, the Wilke-Ansatz [41] can be applied in equation (16).

$$D_{\mathrm{mol},i} = \frac{1 - \tilde{y}_i}{\sum_{j \neq i} \left(\frac{\tilde{y}_j}{D_{\mathrm{mol},ij}} \right)} \tag{16}$$

If Knudsen gas diffusion needs to be considered, then the gas diffusion coefficient is calculated with equation (17) and the pore diameter d_{p}. The Knudsen gas diffusion coefficient shows a temperature dependency of $T^{0.5}$ and is independent of pressure.

$$D_{\mathrm{Kn},i} = \frac{d_{\mathrm{p}}}{3} \sqrt{\frac{8\tilde{R}T}{\pi \widetilde{M}_i}} \tag{17}$$

With the help of the Bosanquet-approach [42], molecular and Knudsen gas diffusion can be seen as parallel resistors and are combined to D_i in equation (18).

$$\frac{1}{D_i} = \frac{1}{D_{\mathrm{mol},i}} + \frac{1}{D_{\mathrm{Kn},i}} \tag{18}$$

An effective gas diffusion coefficient is calculated in equation (19) by considering the micro-structure parameter Ψ_{EL}. The latter is defined as the ratio of porosity ε_{EL} to tortuosity τ_{To} of the porous electrode in equation (20).

$$D_{\mathrm{eff},i} = \Psi_{EL} \cdot D_i \tag{19}$$

$$\Psi_{EL} = \frac{\varepsilon_{EL}}{\tau_{\mathrm{To}}} \tag{20}$$

2.4.3.1 Gas Transport at the Fuel Side

Based on the Nernst-equation the overpotential at the fuel electrode of gas diffusion $\eta_{\mathrm{diff,FE}}$ is presented in equation (21). Based on this a gas diffusion resistance shall be derived as shown in Ref [43].

$$\eta_{\mathrm{diff,FE}} = \frac{\tilde{R}T}{2F} \ln \left(\frac{\left(p_{\mathrm{H_2O,FE}}\right)^{\mathrm{TPB}} \cdot p_{\mathrm{H_2,FE}}}{p_{\mathrm{H_2O,FE}} \cdot \left(p_{\mathrm{H_2,FE}}\right)^{\mathrm{TPB}}} \right) \tag{21}$$

A film model is needed in order to derive a term for the partial pressures of hydrogen $\left(p_{\mathrm{H_2,FE}}\right)^{\mathrm{TPB}}$ and steam $\left(p_{\mathrm{H_2O,FE}}\right)^{\mathrm{TPB}}$ at the three-phase boundary (TPB). This requires the following assumptions:

- Stationary mass transport
- Stagnating film volume
- Concentration gradient located in the film
- Linear character of concentration gradient
- In bulk volume no concentration gradient
- Any convective flows are neglected

The molar flow density $\dot{n}_i$ is shown in equation (22) based on Fick´s law of gas diffusion in a linear approach. $\tilde{c}_i$ denotes the molar concentration ($\tilde{c}_i = \frac{N_i}{V} = \frac{p_i}{\tilde{R}T} \cdot P_{\mathrm{corr}}$), P_{corr} a conversion factor of 10^5 Pa bar^{-1} and s the length of the gas diffusion path. In addition, the gas diffusion coefficient is assumed to be independent of the concentration.

$$\dot{n}_i = -D_{\mathrm{eff},i} \frac{\delta \tilde{c}_i}{\delta s} \tag{22}$$

The transport direction of hydrogen is opposite to the one from steam and thus an additional flux according to the Dusty-Gas-Model [42] is not required [44]. In equation (23), the absolute value of the mass transport density of hydrogen $\left|\dot{n}_{\mathrm{H_2}}\right|$ and steam $\left|\dot{n}_{\mathrm{H_2O}}\right|$ is equal and proportional to the current density j based on Faraday´s law.

$$\left|\dot{n}_{\mathrm{H_2}}\right| = \left|\dot{n}_{\mathrm{H_2O}}\right| = \frac{j}{2 \cdot F} \tag{23}$$

With the help of equation (22) and (23) as well as integrating over the gas diffusion length L_{FE} the partial pressures of hydrogen and steam are resulting at the three-phase-boundary in (24) and (25) respectively.

$$\left(p_{\mathrm{H_2,FE}}\right)^{\mathrm{TPB}} = p_{\mathrm{H_2,FE}} - \frac{\tilde{R}TL_{\mathrm{FE}}}{2FD_{\mathrm{eff,H_2}}P_{\mathrm{corr}}} \cdot j \tag{24}$$

$$\left(p_{\mathrm{H_2O,FE}}\right)^{\mathrm{TPB}} = p_{\mathrm{H_2O,FE}} + \frac{\tilde{R}TL_{\mathrm{FE}}}{2FD_{\mathrm{eff,H_2O}}P_{\mathrm{corr}}} \cdot j \tag{25}$$

Based on the equations (21) - (25) the gas diffusion losses $\eta_{\mathrm{diff,FE}}$ are shown in equation (26) [43,44].

$$\eta_{\mathrm{diff,FE}} = \frac{\tilde{R}T}{2F} \ln\left(\frac{1 + \frac{\tilde{R}TL_{\mathrm{FE}}}{2FD_{\mathrm{eff,H_2O}}p_{\mathrm{H_2O,FE}}P_{\mathrm{corr}}} \cdot j}{1 - \frac{\tilde{R}TL_{\mathrm{FE}}}{2FD_{\mathrm{eff,H_2}}p_{\mathrm{H_2,FE}}P_{\mathrm{corr}}} \cdot j}\right) \tag{26}$$

The resulting gas diffusion resistance $R_{\mathrm{diff,FE}}$ at the fuel electrode under OCV conditions is shown in equation (27).

$$R_{\text{diff,FE}} = \left(\frac{\tilde{R}T}{2F}\right)^2 \cdot L_{\text{FE}} \cdot \frac{1}{p} \cdot \left(\frac{1}{D_{\text{eff,H}_2} \cdot y_{\text{H}_2,\text{FE}}} + \frac{1}{D_{\text{eff,H}_2\text{O}} \cdot y_{\text{H}_2\text{O,FE}}}\right) \frac{1}{P_{\text{corr}}} \tag{27}$$

With regard to the impact of pressure on the gas diffusion resistance, the different gas diffusion regimes need to be considered [45]. In case of pure molecular gas diffusion, the gas diffusion coefficient is inversely proportional to the overall pressure $D_{\text{mol},ij} \sim {}^{1}/_{p}$. Thus, the influence of pressure is leveled out when inserting $D_{\text{mol},ij}$ to equation (27). Considering combined molecular and Knudsen gas diffusion according to equation (18), an impact of pressure towards the gas diffusion resistance needs to be considered for comparably low pressures as shown in Ref. [45].

2.4.3.2 Gas Transport Air Electrode

The overpotential related to gas diffusion at the air electrode $\eta_{\text{diff,AE}}$ can be described with the Nernst-equation in (28) as well. $\left(p_{\text{O}_2,\text{AE}}\right)^{\text{TPB}}$ denotes the oxygen partial pressure at the three-phase boundary.

$$\eta_{\text{diff,AE}} = \frac{\tilde{R}T}{4F} \ln\left(\frac{p_{\text{O}_2,\text{AE}}}{\left(p_{\text{O}_2,\text{AE}}\right)^{\text{TPB}}}\right) \tag{28}$$

At the air electrode, an additional flux ($\tilde{y}_{\text{O}_2} \cdot \dot{n}$) needs to be considered based on the Dusty-Gas-Model theory since oxygen is consumed without generating a gaseous product. $\tilde{y}_{\text{O}_2}$ denotes the molar fraction of oxygen. [44] The total molar flux density $\dot{n}$ corresponds to $\dot{n}_{\text{O}_2}$ in equation (29) since nitrogen is not affecting the electrochemical reaction.

$$\dot{n}_{\text{O}_2} = -D_{\text{eff,O}_2} \frac{\delta \tilde{c}_{\text{O}_2}}{\delta s} + \tilde{y}_{\text{O}_2} \cdot \dot{n} \equiv -D_{\text{eff,O}_2} \frac{\delta \tilde{c}_{\text{O}_2}}{\delta s} + \tilde{y}_{\text{O}_2} \cdot \dot{n}_{\text{O}_2} \tag{29}$$

The molar flow density of oxygen $\dot{n}_{\text{O}_2}$ is equally proportional to the current density as shown in equation (30).

$$\left|\dot{n}_{\text{O}_2}\right| = \frac{j}{4 \cdot F} \tag{30}$$

The oxygen partial pressure at the three-phase boundary in equation (31) can be derived based on the same model assumptions as for the fuel electrode.

$$\left(p_{\text{O}_2,\text{AE}}\right)^{\text{TPB}} = p_{\text{O}_2,\text{AE}} - \left(1 - \frac{p_{\text{O}_2,\text{AE}}}{p}\right) \frac{\tilde{R}TL_{\text{AE}}}{4FD_{\text{eff,O}_2}P_{\text{corr}}} \cdot j \tag{31}$$

Subsequently, $\eta_{\text{diff,AE}}$ can be described based on equation (28) and (31) which evolves in (32).

$$\eta_{\text{diff,AE}} = \frac{\tilde{R}T}{4F} \ln\left(\frac{1}{1 - \frac{\tilde{R}TL_{\text{AE}}\left(1 - p_{\text{O}_2,\text{AE}}/p\right)}{4FD_{\text{eff,O}_2}p_{\text{O}_2,\text{AE}}P_{\text{corr}}} \cdot j}\right) \tag{32}$$

The resulting gas diffusion resistance is calculated with the help of the ohmic law under OCV conditions in equation (33).

$$R_{\mathrm{Diff,AE}} = \left.\frac{\delta\eta_{\mathrm{Diff,AE}}}{\delta j}\right|_{j=0} = \left(\frac{\tilde{R}T}{4F}\right)^2 \cdot \frac{L_{\mathrm{AE}}}{D_{\mathrm{eff},O_2} \cdot p}\left(\frac{1}{\tilde{y}_{O_2}} - 1\right)\frac{1}{P_{\mathrm{corr}}} \qquad (33)$$

Regarding a cell exhibiting a Ni/YSZ fuel electrode, the abovementioned equations were suitable to simulate the current-voltage behavior. However, additional terms might become essential for a Ni/GDC fuel electrode. The required modifications of the dc performance model are discussed in chapter 5.1 [38].

2.5 Electrochemical Impedance Spectroscopy

The loss mechanisms individually described in chapter 2.4 can only be seen in summary in the current-voltage curve as shown in Figure 6. Thus, the overall resistance R can be extracted only at a characteristic operating point. To deconvolute the individual losses of the cell, electrochemical impedance spectroscopy can be applied [46,47]. Either in OCV or a stationary operating point, the cell is excited at a certain frequency f with a sinusoidal signal either in galvanostatic or potentiostatic mode. Finally, the corresponding response signal can be measured. In addition, a pseudo-potentiostatic mode can be chosen as well, where the voltage response is pre-defined and a corresponding current amplitude is set and vice versa a pseudo-galvanostatic mode.

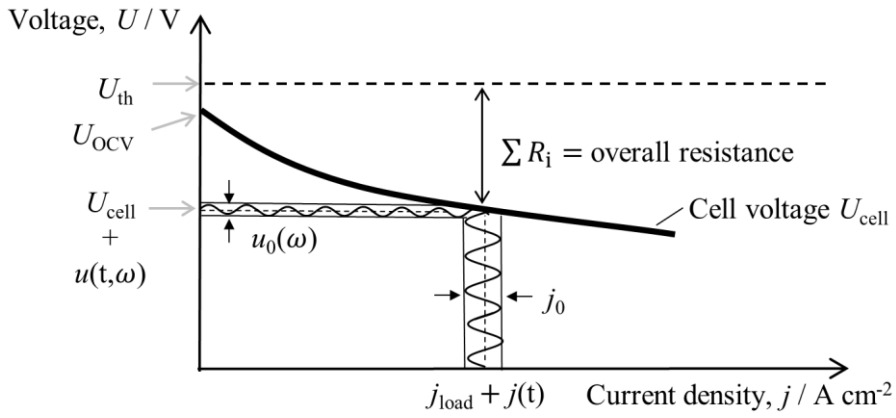

Figure 6 Current-voltage curve of an electrochemical system with excitation of a current signal and measured voltage response. Modified from Ref. [30,48].

With regard to the galvanostatic mode, the excitation can be expressed with $j(t) = j_0 \cdot \sin(\omega t)$. Here, j_0 denotes the current amplitude of the signal, and $\omega = 2\pi f$ the angular frequency. Based on the stimulus, a phase-shift is resulting $\phi(\omega)$ as well as a change in the voltage amplitude $u_0(\omega)$. Thus, the resulting voltage response can be expressed as $u(t,\omega) = u_0(\omega) \cdot \sin\big(\omega t + \phi(\omega)\big)$. Small excitations are applied to linearize the system in the operating point, which is beneficial to investigate the impedance spectra [28]. In equation (34) the complex

impedance is described as the ratio of voltage response and excitation amplitude. This can be also expressed with the real part $Z'(\omega)$ as well as imaginary part $Z''(\omega)$ of the complex impedance.

$$Z(\omega) = \frac{u(t,\omega)}{j(t)} = \frac{u_0(\omega)}{j_0} \cdot e^{i\phi(\omega)} = |Z(\omega)| \cdot e^{i\phi(\omega)} = Z'(\omega) + i \cdot Z''(\omega) \tag{34}$$

The frequency is varied between a set minimum ($\omega \longrightarrow 0$) and maximum ($\omega \longrightarrow \infty$) to obtain the entire impedance spectra with characteristic loss processes covered, as exemplified in Figure 7. Here, the negative imaginary part is plotted as a function of the real part to show the capacitive behavior of the electrochemical system. Depending on the testing environment and operating conditions, inductive loops can evolve as well [49,50]. The overall resistance is defined as the sum of ohmic and polarization resistance with $R = R_{\mathrm{ohm}} + R_{\mathrm{pol}}$. With respect to the ohmic resistance, it can be extracted at the intercept of the spectra at high frequencies ($\omega \longrightarrow \infty$) with the real part axis.

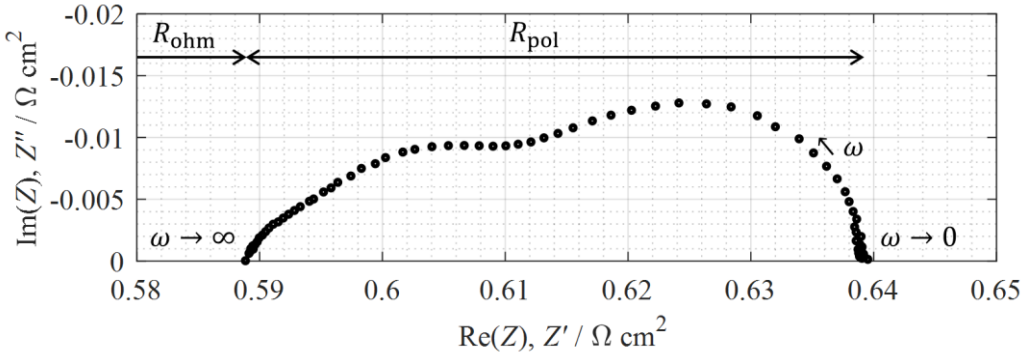

Figure 7 Exemplified Nyquist-plot with separation of ohmic R_{ohm} and polarization resistance R_{pol}. Adapted from Ref. [30,38].

An optimal signal to noise ratio (SNR) is needed for the amplitude so that noise by a rather too small amplitude as well as information loss by a comparably too large amplitude can be avoided. The validity of a measured spectra needs to be confirmed with a Kramers-Kronig test to verify a linear, causal, time-invariant and finite system [51].

The impedance spectra can be described with equivalent circuit models, of which elements are introduced in the following section.

2.5.1 Electrochemical Equivalent Circuit Elements

A comprehensive description of equivalent circuit elements is already given in Ref. [29,36]. Thus, the elements needed in this work are shown and summarized. In general, it is the goal to model each loss process of the cell with an electrochemical equivalent circuit element. All processes therefore need to be separable in the spectra and differ in their time constants. The simplest element is provided as an ohmic resistor, which can describe charge transport losses.

This basic element can be used in parallel with a capacitance (C) to model an electrochemical process by an RC-Element in Figure 8 (a). Every electrochemical system can be described with a series of RC-elements [52]. In order to account for deviations from the ideal electrode as they occur in a real system, an RQ-Element as described below is used. [46,47]

2.5.1.1 RQ-Element

With the help of the RQ-Element as shown in equation (35), inhomogeneities caused by material properties, microstructure and operating conditions can be considered. Instead of a capacitance, a constant phase element (Q) as shown in Figure 8 (b) is used. The difference between an ideal and real system can be expressed with the exponent p_{RQ}, which varies between 0 and 1. The case of $p_{\mathrm{RQ}} = 1$ represents the ideal case with an RC-Element. For a real electrode with $p_{\mathrm{RQ}} < 1$ the shape of the curve is shrinked.

$$Z_{\mathrm{RQ}}(\omega) = Z_{\mathrm{R}} \| Z_{\mathrm{Q}} = \frac{R_{\mathrm{RQ}}}{1+(i\omega\cdot\tau_{\mathrm{RQ}})^{p_{\mathrm{RQ}}}}, \text{ mit } 0 \leq p_{\mathrm{RQ}} \leq 1 \tag{35}$$

Based on the locally distributed time constants, a mean value of τ_{RQ} results in equation (36) with the characteristic frequency f_{RQ}.

$$\tau_{\mathrm{RQ}} = \frac{1}{2\pi \cdot f_{\mathrm{RQ}}} \tag{36}$$

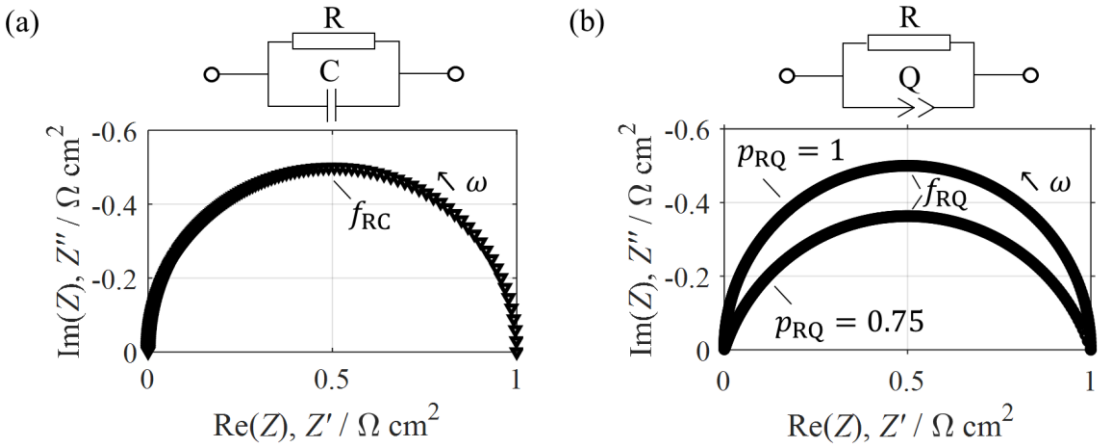

Figure 8 (a) Modeled RC-Element and (b) RQ-Element with $p_{\mathrm{RQ}} = 1$ and $p_{\mathrm{RQ}} = 0.75$. Modified from Ref. [30].

2.5.1.2 Warburg-Element

Voltage losses caused by gas diffusion in the electrodes were extensively described in chapter 2.4. The impedance of this loss process can be expressed as a generalized Finite-Length-Warburg-Element (G-FLW) in equation (37). Here, R_{WB} denotes the resistance of the G-FLW and τ_{WB} the time constant. This element represents a Transmission-Line-Model (TLM) with the capacitive pore volume of the electrode. The ideal case of 1-dimensional (1D) gas diffusion is defined with $n_{\mathrm{WB}} = 0.5$. Deviations as they occur in a real system are accounted for $0 \leq n_{\mathrm{WB}} \leq 0.5$. [46,47]

$$Z_{\mathrm{G-FLW}}(\omega) = R_{\mathrm{WB}} \cdot \frac{\tanh[(i\omega \cdot \tau_{\mathrm{WB}})^{n_{\mathrm{WB}}}]}{(i\omega \cdot \tau_{\mathrm{WB}})^{n_{\mathrm{WB}}}}, \text{ mit } 0 \leq n_{\mathrm{WB}} \leq 0.5 \tag{37}$$

For the ideal case, the characteristic time constant $\tau_{\mathrm{WB,ideal}}$ is provided in equation (38) with the characteristic gas diffusion length L_{C} and the effective gas diffusion coefficient D_{eff}.

$$\tau_{\mathrm{WB,ideal}} = \frac{L_{\mathrm{C}}^2}{D_{\mathrm{eff}}} \text{ with } n = 0.5 \tag{38}$$

The characteristic frequency is calculated with equation (39).

$$f_{\mathrm{WB}} = \frac{2.53}{2\pi \cdot \tau_{\mathrm{WB}}} \tag{39}$$

Figure 9 (a) shows two modeled G-FLW with the exponents $n = 0.35$ and $n = 0.5$ respectively.

2.5.1.3 Gerischer Element

The Gerischer element [53] represents a TLM as well with its impedance shown in equation (40) including the corresponding resistance $R_{\mathrm{Gerischer}}$ as well as $\tau_{\mathrm{Gerischer}}$. In numerous previous studies it was used to describe the surface exchange of O_2 coupled with oxygen ion transport in the bulk of the air electrode [36,54].

$$Z_{\mathrm{Gerischer}}(\omega) = \frac{R_{\mathrm{Gerischer}}}{\sqrt{1 + i\omega \cdot \tau_{\mathrm{Gerischer}}}} \tag{40}$$

In Figure 9 (b), an exemplary shape of the Gerischer element is presented.

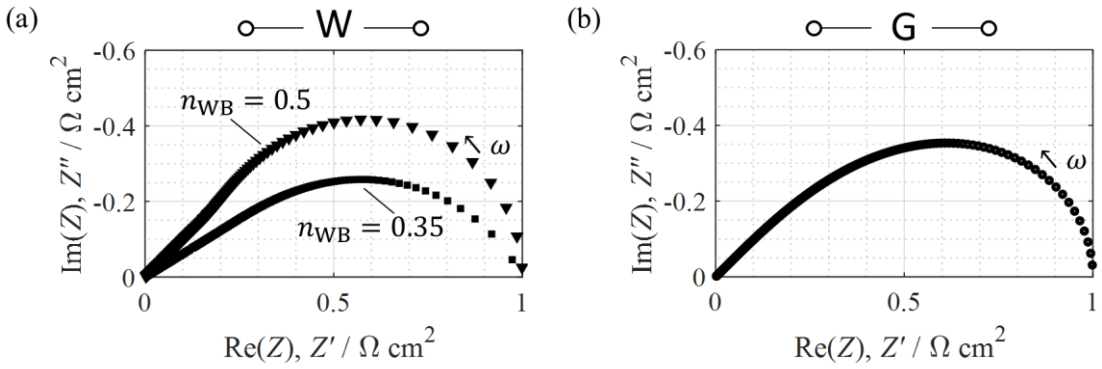

Figure 9 (a) Exemplary modeled Warburg-Element with $n_{\mathrm{WB}} = 0.35$ and $n_{\mathrm{WB}} = 0.5$ and (b) exemplary modeled Gerischer-Element. Modified from Ref. [30].

The detailed description of a SOC with a Transmission-Line-Model is out of the scope of this work and thus referred to corresponding contributions in literature [55–59].

An equivalent circuit model can describe the measured spectra. However, various circuit models are theoretically possible in order to replicate the spectra. In addition, processes in the impedance spectra can overlap, which makes an unambiguous deconvolution more difficult. The distribution of relaxation times (DRT) was therefore developed at this institute [60]. With the

help of the DRT a physically motivated equivalent circuit model of the measured electrochemical system can be determined.

2.5.2 Distribution of Relaxation Times

The DRT represents a mathematical transformation of the measured impedance spectra in order to visualize the individual loss processes. This method takes advantage of the individual time constant of each loss process. The impedance in equation (41) can be described with a continuous distribution function γ_τ with the relaxation times τ since any capacitive system can be expressed with RC-elements.

$$Z(\omega) = R_{\mathrm{ohm}} + R_{\mathrm{pol}} \cdot \int_0^\infty \frac{\gamma_\tau}{1+i\omega\tau} d\tau \text{ , mit } \int_0^\infty \gamma_\tau d\tau = 1 \qquad (41)$$

For reasons of simplicity, the integration of the polarization contribution is solved with a series of N RC-elements and described in a discrete function in equation (42) with logarithmically distributed relaxation times τ_n.

$$Z(\omega) = R_{\mathrm{ohm}} + R_{\mathrm{pol}} \cdot \sum_{n=1}^{N} \frac{\gamma_n}{1+i\omega\tau_n}, \text{ mit } \sum_{n=1}^{N} \gamma_n = 1 \qquad (42)$$

This equation needs to be solved numerically and represents a mathematic ill posed problem. A regularization by Tikhonov [61] can be applied to stabilize and smooth the solution with the help of the regularization parameter λ_{DRT}. Noise from measurements and artifacts can be minimized. An optimum of λ_{DRT} is needed, since parameters chosen too high can result in a loss of crucial information about the loss processes. This optimum needs to be identified for each system of interest individually. The numerical distribution function is denoted as $g_{(\tau)}$. In Figure 10 (a), an exemplary DRT is shown with two ideal processes described with two RC-Elements. The DRT calculation results in Dirac pulses $\delta(f - f_{\mathrm{n}})$ at the frequencies f_{n}. For an ideal RC process, one characteristic peak frequency is found and provides information of the corresponding relaxation time of the process. In case of real electrodes with inhomogeneities in e.g. microstructure, a distribution of relaxation times around a characteristic peak frequency is found. The resistance of the processes corresponds with the area enclosed underneath the peak (Figure 10 (b)). However, processes with similar relaxation times can overlap in the DRT as well, which needs to be considered in the process assignment. As shown in previous works [36,62], operating parameters such as temperature and/or gas compositions need to be systematically and independently varied in a sensitivity analysis to trigger characteristic properties of the loss processes to clearly deconvolute them.

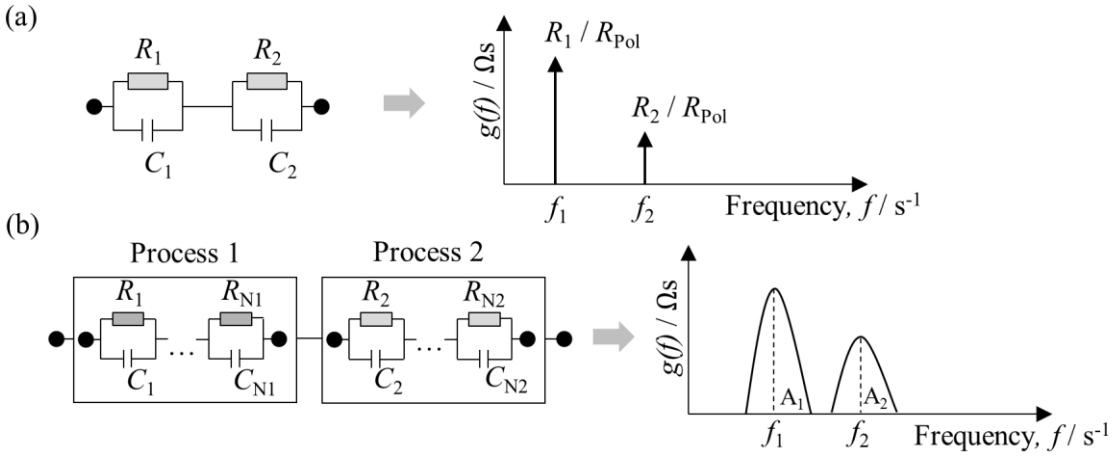

Figure 10 Schematic principle of the DRT with two ideal processes in (a) and two real processes in (b). Adapted from Ref. [29,30,32].

2.5.3 Complex Non-Linear Least Square Fit

Once a physically meaningful equivalent circuit model is found, the parameters of the individual elements which determine the shape and location of the modeled process e.g. resistance, characteristic frequency need to be approximated to the experimental data. Thus, the complex non-linear least square (CNLS) fit is introduced in this section. Based on the calculated DRT and shape of peaks, characteristic starting values can be extracted for the fitting procedure. The fit runs until a pre-defined stop criterion S reached a minimum (Min) in equation (43) and the fitting result reaches the targeted quality. As an alternative, a pre-defined number of iterations can be set as well. In equation (43), the error r_i of the DRT as well as real Z' and imaginary Z'' part can be weighted with the factor W_i [63]. The ratio of Z': Z'': DRT is at least set to 2: 1: 1. The errors are calculated in equation (44) and (45) as a function of all parameters $\vec{x}$ in the equivalent circuit model.

$$S = \sum_{m_1=1}^{M} \left[W_{Z'} \cdot r_{Z',m_1}^2 + W_{Z''} \cdot r_{Z'',m_1}^2 + W_{\mathrm{DRT}} \cdot r_{\mathrm{DRT,m_1}}^2 \right] \longrightarrow Min. \tag{43}$$

$$r_{\mathrm{Z,m}} = \frac{Z_{\mathrm{Meas}}(\omega_{\mathrm{m}}) - Z_{\mathrm{Mod}}(\omega_{\mathrm{m}}, \vec{x})}{|Z_{\mathrm{Meas}}(\omega_{\mathrm{m}})|} \tag{44}$$

$$r_{\mathrm{DRT,m}} = \frac{\gamma_{\mathrm{Meas}}(\omega_{\mathrm{m}}) - \gamma_{\mathrm{Mod}}(\omega_{\mathrm{m}}, \vec{x})}{|\gamma_{\mathrm{Meas}}(\omega_{\mathrm{m}})|} \tag{45}$$

3 Materials, Designs and Operation of Solid Oxide Cells[3]

Material selection for SOCs and stacks is based on chemical and thermomechanical compatibility with the solid electrolyte, i.e., fluorites, perovskites, etc. [1,64]. The high operating temperatures enable the use of cost-saving precious metal-free electrocatalysts as well as electrolytes free of per- and polyfluoroalkyl substances (PFAS) [65]. On the other hand, thermally activated aging is accelerated, so current research is aimed at lowering the operating temperature [66,67]. This expands the possibilities of a more cost-effective material selection for stack and peripheral components, e.g., for interconnects, heat exchangers, etc. SOCs are not limited to H_2 fuel: they can be fed with reformate gas mixtures, ammonia or even internally reform hydrocarbons [7,68,69]. In the electrolysis mode, syngas or carbon monoxide can be produced for subsequent chemical processes applying electricity and heat from solar power. [1,70,71]. SOCs can be manufactured with different mechanical support layers resulting in electrolyte-, anode- or metal-supported cells. A large variety of SOC designs and materials exist and have been investigated in literature. In Ref. [72] a comprehensive overview about materials and designs of SOCs is given. In this work, a summary of relevant materials is provided below.

3.1 Electrolyte

For the electrolyte, ceramic materials such as yttria-stabilized zirconia can be used. The oxygen ion conductivity based on the Hopping mechanism depends on the doping concentration of yttria and thus the number of oxygen vacancies. 3 mol.% yttria stabilized zirconia (3YSZ) has a comparatively lower ionic conductivity, but higher mechanical stability in comparison to 8 mol.% yttria-stabilized zirconia (8YSZ). Other electrolyte materials are investigated such as scandia stabilized zirconia [72]. Zirconia-based electrolytes fulfill the requirements for negligible electronic conductivity, which is not the case for alternative electrolytes such as Gd- or Sm-doped ceria [1,72]. In addition, proton conducting ceramic cells (PCCs) [73,74] also represent a promising alternative electrolyte material since in this case dry H_2 can be generated in electrolysis mode. Thus, steam does not need to be removed anymore in comparison to cells with an oxygen ion conducting electrolyte. In addition, the operating temperature can be significantly decreased to $400 - 650$ °C [1]. However, due to the comparatively low TRL value and lack of reproducibility and longevity of PCCs, this work focuses on state-of-the-art oxygen ion conduction electrolytes.

Electrolyte processes of the cell type investigated in this work were investigated by Kullmann et al. [75]. Temperatures as low as 350 °C were chosen to shift the dielectric polarization of the

[3] Parts of this chapter have been published in M. Ivanova, …, C. Grosselindemann et al., *Angew. Chem.*, **62**, e202218850 (2023) [1].

electrolyte into an accessible frequency range. Two main contributions resulting from grain boundary and grain resistance were identified. It was demonstrated that with electrochemical impedance spectroscopy various processes from low frequencies e.g. gas diffusion to high frequencies with grain processes can be analyzed with this method [75].

3.2 Fuel Electrode[4]

Fuel electrodes conventionally consist of a porous cermet with nickel and one of the aforementioned ceramic electrolyte materials. The main challenges are associated with achieving high electrocatalytic activity, ionic conductivity and low degradation at the same time [1]. For a cell with a Ni/YSZ fuel electrode this means an electronic conducting nickel phase as well as ion conducting YSZ phase. This material is already commercially applied in cells manufactured at e.g. Elcogen [76] and Solydera [77]. Nickel / yttria-stabilized zirconia (Ni/YSZ) fuel electrodes represent state-of-the-art electrodes in order to reach out for high performance and durability. However, the resistance towards Ni coarsening or depletion as well as the redox stability can be further improved [72]. This can be achieved by applying a nickel / gadolinium-doped ceria (Ni/GDC) cermet leading to more resilient electrodes towards carbon deposition [78], sulfur poisoning [79,80] and redox stability [81] as well as improved electro-catalytic activity [72]. The higher robustness of Ni/GDC electrodes is due to the mixed electronic/ionic conductivity of GDC [82,83] at high temperatures and reducing atmosphere [84]. In comparison to Ni/YSZ fuel electrodes, the charge transfer reactions are no longer restricted to active three phase boundaries that are necessarily in direct contact with the nickel-, the electrolyte- and the pore-matrix [84] as shown in Figure 11. Contact losses within the Ni-matrix are compensated by the electronic conductivity of the GDC phase. Nevertheless, there is a demand for nickel as a catalyst [85–87]. In addition, a pure GDC-layer results in a drastic increase of the polarization resistance by about two orders of magnitude [88]. In the work by Kullmann et al. [59] it was shown, that an infiltration of nickel particles into GDC fuel electrodes leads to a decrease of the polarization resistance by a factor of four.

Furthermore, a GDC layer between the Ni/GDC electrode and YSZ electrolyte increases performance and tolerance against poisoning effects [88,89]. Unachukwu et al. [90] stated, that the interlayer may have a significant impact on the electrochemical behavior.

[4] Parts of this chapter have been published in C. Grosselindemann et al., *ECS Trans*., **103**, 1375-1393 (2021) [37] and C. Grosselindemann et al., *J. Electrochem. Soc*., **168**, 124506 (2021) [38].

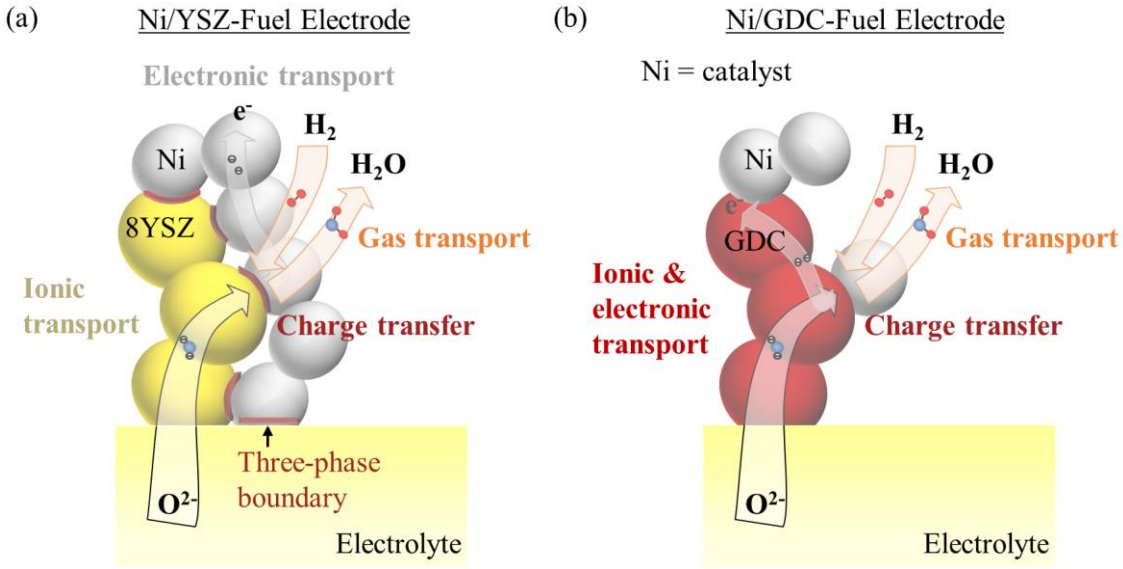

Figure 11 (a) Scheme of Ni/YSZ (adapted from Ref. [57]) and (b) Ni/GDC fuel electrode.

In contrast, the work by Nenning et al. [91], Uecker et al. [92,93] and Shaur et al. [58] state the feasibility of a single-phase GDC fuel electrode. Yet the role of three phase boundaries at Ni/GDC electrodes compared to double phase boundaries of pure GDC electrodes in electrochemical performance is not completely clarified. TLM modeling of a single phase GDC fuel electrode with a single phase Ni-contact layer was shown by Kullmann et al. where the gas diffusion could be neglected [55].

SOCs with a Ni/GDC fuel electrode are commercialized for electrolyte-supported cells (ESC) by e.g. Kerafol Keramische Folien GmbH & Co. KG [94] or Sunfire SE [95]. Due to the chemical expansion of the GDC, an ASC purely based on Ni/GDC is not feasible. Thus, research groups are working on a concept of an ASC with Ni/YSZ mechanical support layer and a Ni/GDC functional layer as shown by Lenser et al. [96]. In the work by Klitkou [97] such type of cells were manufactured with a reduced sintering temperature to avoid interdiffusion. However, both studies concluded that a significant performance increase in comparison to state-of-the-art ASCs with Ni/YSZ fuel electrodes is still needed.

3.3 Air Electrode[5]

Common air electrodes are perovskite-type lanthanum manganites, ferrites and cobaltites and commonly consist of a ABO_3 structure [1,54,72,98,99]. $La_{1-x}Sr_xMnO_{3-\delta}$/8YSZ is a well-known material for SOC air electrodes [100,101]. Here, the active reaction sites are limited to the three-phase boundaries [72]. Thus, a performance increase can be achieved with a mixed ionic and electronic conductor such as $La_wSr_xCo_yFe_zO_{3-\delta}$, a state-of-the-art material already applied in commercialized cells [36,38]. However, in case of strontium (Sr) in LSCF air elec-

[5] Parts of this chapter have been published in M. Ivanova, …, C. Grosselindemann et al., *Angew. Chem.*, **62**, e202218850 (2023) [1].

trodes, the formation of secondary phases of $SrZrO_3$ (SZO) significantly effects the performance of the air electrode [102], which is avoided by applying GDC interlayers.

3.4 Designs[6]

Due to the all-solid-nature of SOCs, various designs [103] have been developed in the last decades. In addition to (micro-) tubular designs, planar types consisting of flat multilayer structures are the most common type nowadays [72], being electrolyte-supported (ESC), fuel electrode-supported (ASC) and metal-supported cells (MSC). [104–107] To obtain technically meaningful current and voltage levels for a system, individual cells are connected in series in a stack. In a planar SOC stack design, the cells are stacked between metallic interconnectors (see chapter 3.7), that ensure bipolar contact with the electrodes of the neighboring cells. Contacting and gas supply are realized by flow field structures, while protective coatings (chapter 3.7) are required to prevent corrosion of the metallic interconnects and to reduce Cr evaporation, that is harmful for the air electrode. Glass, glass ceramics, metallic solders or compressive gaskets are applied for a gas-tight seal. [1]

Various SOC cell and stack designs have been used in commercial or pre-commercial SOFC-systems. The largest market to date is the Combined Heat and Power (CHP) systems developed by various companies [10,76,108–114]. Even though most of these companies have started developing cells, stacks and systems for solid oxide electrolysis cell (SOEC) applications, the number of commercially available high-temperature electrolyzers remains limited. An example is the Sunfire SOEC-system [95,108] with H_2 production rate of $750\ m_N^3\ h^{-1}$ at up to 850 °C, conversion efficiencies above 84% (considering the lower heating value), a consumption of $3.6\ kWh\ m_N^{-3}$ produced H_2 with purity above 99.95% after an additional purification stage. While SOFC lifetimes of $4-10$ years have been achieved with different cells, stacks and systems, the proven lifetimes of SOECs are mostly below 20 kh [115], which is mainly related to the fact that the intensive SOEC development only started in the last decade. [1] The straightforward approach of using SOFC cells and stacks for SOEC applications has proven to be critical in terms of lifetime and durability. Thus, new electrode, cell and stack concepts for electrolysis operation are being developed. In addition, another research focus is on improvements at the system level, e.g., through external heat coupling [116] or reduced water quality requirements (seawater) [1,117,118]. A recycling process for ceramics in SOCs was shown by Sarner et al. [119].

[6] Parts of this chapter have been published in M. Ivanova, …, C. Grosselindemann et al., *Angew. Chem.*, **62**, e202218850 (2023) [1].

3.5 Operation in H_2/H_2O[7]

In the case of full cells exhibiting a Ni/GDC fuel electrode and an LSCF/GDC air electrode, an unambiguous process assignment by electrochemical impedance spectroscopy (EIS) measurements and subsequent distribution of relaxation times (DRT) analysis was not achieved up to now, since different processes in fuel and air electrodes strongly overlap in the spectrum. As a first step, symmetrical cells can be used in order to separate fuel and air electrode processes. Alternatively, in the work by Hagen et al. [120], a LSM-YSZ air electrode was used to move the corresponding loss processes away from Ni/GDC loss processes in the spectra, so that the resistance of the Ni/GDC could be identified and quantified. However, the charge transfer and gas diffusion at the Ni/GDC fuel electrode also strongly overlap in the impedance spectra [56,79,89,121]. The latter is caused by the oxygen non-stoichiometry of GDC, which results in a large chemical capacity, shifting the relaxation frequency of the charge transfer process to lower relaxation frequencies [82,121]. To overcome this issue and visualize the gas diffusion process, gas mixtures containing different inert gases can be applied as shown for Ni/YSZ [122] and Ni/GDC [56,123,124] in previous studies.

Based on the modeling approach by Leonide et al. [36] this work strives for the characterization of an electrolyte-supported solid oxide cell with Ni/GDC fuel electrode, 3 mol-% yttria-stabilized zirconia (3YSZ) electrolyte and LSCF/GDC air electrode as well as the development of a zero-dimensional cell model for fuel cell and electrolysis mode [36,125]. Therefore, a comprehensive understanding and quantification of the individual loss processes occurring in a solid oxide cell is needed, which is also crucial regarding targeted cell development [57]. In order to deconvolute the individual loss mechanisms in a solid oxide cell, EIS and the subsequent DRT analysis represent powerful methods. This approach has been successfully demonstrated for electrolyte-supported cells [60,122], anode-supported cells [36] and metal supported cells [126,127]. Applying this methodology, the physicochemical loss processes occurring in the cells can be identified by their relaxation frequencies and characteristic operating parameter dependencies. The quantification is realized by means of complex non-linear least square (CNLS)-fitting. Based on the obtained results, zero-dimensional dc cell models, which are based on common electrochemical approaches as Butler-Volmer and Fick´s laws, can be developed and parameterized.

In this study, a method for the deconvolution of gas diffusion and activation polarization within the Ni/GDC fuel electrode of an ESC by EIS measurements is presented. By quantifying the associated electrochemical losses, a zero-dimensional cell model is parameterized, which is capable for predicting the cell performance over a wide technically relevant SOC operating range.

[7] Parts of this chapter have been published in C. Grosselindemann et al., *ECS Trans.*, **103**, 1375-1393 (2021) [37] and C. Grosselindemann et al., *J. Electrochem. Soc.*, **168**, 124506 (2021) [38].

3.6 Operation in CO/CO_2[8]

Among the various types of fuel cells and electrolyzers [1], only solid oxide cells show a high fuel flexibility and can, next to hydrogen, operate on carbon monoxide and reformate/syngas [7,129–132]. Physicochemical cell models that are able to simulate the cell behavior within a wide range of technically relevant operating conditions are a useful tool to optimize the cell design, evaluate optimum operating strategies and simulate the cell behavior on stack and system level [104,125,133–135]. In the work by Leonide et al. this was developed separately for hydrogen/steam (H_2/H_2O) and carbon monoxide/carbon dioxide (CO/CO_2) fuel gas mixtures [104,136]. There, the operation with CO/CO_2 fuel gas mixtures leads to a significant impact on the electrochemical behavior of the anode-supported cell with Ni/8YSZ fuel electrode resulting in a higher activation energy of the fuel electrode with $E_{\mathrm{act,FE,CO/CO_2}} = 118.64$ kJ mol^{-1} in comparison to $E_{\mathrm{act,FE,H_2/H_2O}} = 105.04$ kJ mol^{-1} [104,136]. Further, the gas diffusion losses in the 1 mm thick anode substrate are increasing due to the substrate thickness and the low effective gas diffusion coefficients [136]. In the work by Shaur et al. [58] TLM modeling was shown for a single-phase GDC electrode in CO/CO_2 mode.

However, gradients with respect to temperature and gas conversion along the gas channels are not considered and require a multiphysics modeling environment. This is provided in the work by Russner et al. [137] for a two-dimensional gas-channel model based on a finite element method for an ASC and ESC design, which shows the impact of individual loss contributions towards a distribution of temperature in a stack layer operated with reformate gas mixtures. Also, a single channel model for electrolysis of CO_2 in a SOC is proposed in Ref. [138]. In the field, so far the solid oxide electrolysis of CO_2 is applied in eCOs^{tm} developed by Topsoe [139–141] and in the Mars Oxygen *In Situ* Resource Utilization (Moxie) Experiment [142].

In this work, the focus is on comparing the electrochemistry of an electrolyte-supported cell with a Ni/GDC fuel electrode (FE) in H_2/H_2O in comparison to CO/CO_2 fuel gas mixtures. This study shall furthermore provide a basis for the investigation of Ni/GDC electrodes in reformate respectively syngas mixtures [68,129,143–145] and was performed in the work by Esau et al. in another contribution [146].

3.7 Metallic Interconnectors[9]

Metallic interconnectors (MICs) [148,149] are crucial for the contacting of planar SOCs [72] in a stack in order to reach out for large scale industrialization for the production of electricity (SOFC), hydrogen (H_2) and/ or mixtures of hydrogen and carbon monoxide (synthesis gas) [1,68,150]. MICs have an economic benefit regarding material and manufacturing costs as well as easier machinability in comparison to ceramic flow fields [148,149,151–153]. These can be made of chromia based alloys or ferritic stainless steels with the ability to form a chromium (Cr)

[8] Parts of this chapter have been published in C. Grosselindemann et al., *Fuel Cells*, **23**, 442-453 (2023) [128].

[9] Parts of this chapter have been published in C. Grosselindemann et al., *J. Electrochem Soc.*, **171**, 054508 (2024) [147].

oxide layer [154–157]. Ferritic stainless steels take advantage in machinability, costs, mechanical properties and have a moderately conductive oxide scale [155,158,159]. The formation of the solid (s) chromium oxide layer $Cr_2O_3(s)$ in oxidizing atmosphere is shown in equation (46) and schematically in Figure 12 where chromium $Cr(s)$ from the metallic interconnector reacts with oxygen [160].

$$4\mathrm{Cr(s)} + 3\mathrm{O_2(g)} \rightarrow 2\mathrm{Cr_2O_3(s)} \tag{46}$$

In addition, $\mathrm{Cr_2O_3(s)}$ also reacts with oxygen and evaporates to $\mathrm{CrO_3(g)}$ or together with oxygen and steam to chromium(oxy-)hydroxides $\mathrm{CrO_2(OH)_2(g)}$ in equation (47) and (48).

$$2\mathrm{Cr_2O_3(s)} + 3\mathrm{O_2(g)} = 4\mathrm{CrO_3(g)} \tag{47}$$

$$2\mathrm{Cr_2O_3(s)} + 3\mathrm{O_2(g)} + 4\mathrm{H_2O(g)} = 4\mathrm{CrO_2(OH)_2(g)} \tag{48}$$

Both chromium species can be precipitated at the air electrode by an electrochemical reaction which is thus poisoning the electrode in equation (49) and (50). Finally, the catalytic activity of the air electrode is reduced [160]. In addition, limitations in gas supply underneath the contact rib can occur as shown in Figure 12 [161].

$$4\mathrm{CrO_3(g)} + 12\mathrm{e^-} \rightarrow 2\mathrm{Cr_2O_3(s)} + 6\mathrm{O^{2-}} \tag{49}$$

$$2\mathrm{CrO_2(OH)_2(g)} + 6\mathrm{e^-} \rightarrow \mathrm{Cr_2O_3(s)} + 2\mathrm{H_2O(g)} + 3\mathrm{O^{2-}} \tag{50}$$

The steel grade Crofer 22 APU, tailormade for MIC, is extensively studied and used in commercialized stacks for fuel cell as well as electrolysis mode [108,159,162]. In order to minimize Cr-evaporation and corrosion from the MIC, protective coatings need to be applied especially on the air side [158,163,164]. This decreases chromium poisoning of the air electrode and the contact resistance between electrode and MIC. Different techniques are available in order to apply various types of coatings [148,165–167]. They can be applied by physical vapor deposition (PVD) [163], wet powder spraying (WPS) [168], atmospheric plasma spraying (APS) [166,169,170], screen printing [171–174], electrophoretic deposition [175] and sol-gel processing [176].

Numerous steel grades such as AISI 441, 444, 430, 409 and others were investigated in literature [177–182] with respect to a stack-like contacting of the SOC. Long-term stability for 40 kh of operation was shown in Ref. [183–185] for Crofer 22 APU fully coated with a (Co, Mn, Fe)$_3$O$_4$ spinel oxide. Different contact layers at the air side were investigated by Kusnezoff et al. [186]. A self-healing effect was observed for a manganese-cobalt-iron oxide coating applied by APS [169,187]. In addition, chromium evaporation also needs to be considered from balance-of-plant components upstream to the air electrode such as heat exchangers [188,189]. Furthermore, hydrogen embrittlement [190] occurs as a reversible process in a comparably narrow temperature window below approx. 100 °C [191,192]. In the work by Kniep et al. [193], it was stated

that hydrogen embrittlement may become into effect for SOC systems with respect to start-up phases or flexible operation regarding peak loads.

In this work, 3 different steel grades (Crofer 22 APU, AISI 441, UNS S44330) are investigated in the uncoated and coated state. A protective coating of cerium-cobalt (CeCo) is applied by a PVD-process. The CeCo protective layer is a commercialized product (Sanergy™ HT) by Alleima AB [194] (former Sandvik Materials Technology), which can be applied in a high volume large scale roll to roll coating process on any ferritic stainless steel grade. The protective layer consists of a top layer of metallic Co with approx. 600 nm and a Ce layer in the range of $10 - 20$ nm [163]. This type of coating was proven to be suitable for stable long-term operation of nearly 40 kh [195] and also holds self-healing properties [196]. In the work by Norrby et al. [197] a CeCo coated steel grade (AISI 441) was exposed at 800 °C in air in a box furnace for 87700 hours and showed no sign of breakaway corrosion.

In a previous study by Reddy et al. [177] different steel grades (AISI 441, 444, 430, 409) were investigated in the uncoated and coated (CeCo) state by time-resolved mass gains, chromium evaporation (denuder technique [198]) and measurements of the area-specific resistance (ASR). A different oxidation rate as well as Cr-evaporation was found between the uncoated steels. By applying a commercialized PVD coated CeCo layer the Cr-evaporation rate was reduced by $60 - 100\%$ [177]. For the uncoated steels in Ref. [177] a chromium manganese ($(Cr,Mn)_3O_4$) layer is formed at the surface of the MIC. In comparison, a cobalt manganese ($(Co,Mn)_3O_4$) layer at the surface results from the coated samples [177].

To analyze the performance on the single cell level [57,199] effects resulting from the MIC like chromium poisoning [101,179,200–202], corrosion [153,203] as well as increased contact and gas diffusion losses need to be omitted. This requires the application of an inert testing environment with ceramic flow fields and noble metal contact grids in order to analyze the ideal cell performance as described in chapter 4.2.1 [125,204,205].

In addition, to investigate the different impacts of a stack-like contacting on the cell performance, individual effects can be mimicked in a single cell test. This can for example be realized by an upstream chromium source [101] or a metallic flow field in combination with a noble metal contact mesh [179] that avoids further impacts related to increased contact and gas diffusion resistances or a stack-like flow field made from noble metal that just mimics limited gas diffusion and inhomogeneous contacting of the electrode [27].

This work focusses on the investigation of loss contributions related to the interconnector material, coatings and cell contacting / gas supply. Single cells were tested with a stack-like contacting applying a single metallic flow field geometry made from three different steel grades (Crofer 22 APU (1.4760), AISI 441 (1.4509), UNS S44330 (1.4622)) with and without a cerium-cobalt PVD-coating [167,177,206]. Cell performance and losses are evaluated by IV-characteristics, impedance spectroscopy and DRT-analysis. Based on a method developed by Kornely et al. [27] the contact loss between the MIC and the electrode is evaluated. The results of the electrochemical characterization are correlated to the Cr-oxide scale formed on the interconnectors and the existence of Cr-compounds in the air electrode. Microstructural analysis [177] of the different tested metallic interconnectors is performed by scanning-electron-

microscopy (SEM) and energy-dispersive X-ray spectroscopy (EDXS). The air electrodes are investigated by SEM-EDXS as well as TEM-EDXS when in contact with all un-/coated MICs of this work.

3.8 Glass Ceramic Sealings

In a commercial SOC stack, numerous cells and metallic interconnectors need to be sealed before its operation with a lifetime of up to 100 kh [207]. The operating environment with high temperatures ($600 - 900$ °C) as well as reducing and oxidizing atmospheres demands high requirements for the sealing. Different types of high-temperature sealings [208,209] are available on the market. Glass ceramic sealings are already applied in commercialized SOC stacks [210] and were investigated in literature [211–216]. A comprehensive introduction for glass ceramic sealings can be found in Ref. [216]. Here, a summary is provided with relevant information for this work. These sealings are provided as glass powders which are then mixed with a liquid binder to form a paste which can be directly applied by a dispensing process or casted to a tape and is placed outside of the active area of the cell between MIC and electrolyte. Once the stack with MICs, cells and sealing is in place, a thermal treatment is needed. A characteristic property is the glass transition temperature T_g. At this temperature, the degree of deformation is changing since a rigid glass turns into a rather soft state. Different cell types such as ASCs, ESCs or MSCs come along with different material configurations in their electrodes, electrolytes and mechanical support layers. Thus, various glass ceramic sealings need to be tailored for the specific operating range of the individual cells. This results in different material configurations to match the specific requirements. Common network formers are SiO_2 as well as Al_2O_3 which are needed to adjust the viscosity of the sealant in order to stabilize it [216]. However, Si-species are known to poison the electrodes as shown in Figure 12 [217,218] and inhibit electrochemical reactions resulting in a significant performance loss of the cell. Thus, the applied amount of glass ceramic sealing needs to be minimal and optimized. Most importantly the coefficient of thermal expansion (CTE) needs to be harmonized between glass ceramic sealing, the electrolyte as well as MIC to guarantee its integrity in the stack. Otherwise mechanical stresses can cause a severe failure of the joined set-up and cause a high leakage. Also, a high electrical resistivity is needed. However, interactions between the MIC and glass ceramic sealant also need to be considered. Depending on the steel grade, MICs form different chromium containing oxide scales as described in the previous chapter 3.7, which also has an impact on the functionality and longevity of the glass ceramic sealing since conducting phases can be formed. In addition, short circuits can be generated by the formation of alkaline or earth alkaline chromates and also increase gas permeability. Volatile species can be released and lead to pore formation and thus an increased leakage rate [216]. In addition, temperature gradients need to be considered with respect to the mechanical stability during thermal cycling as well as gradients along the stack during its operation [216].

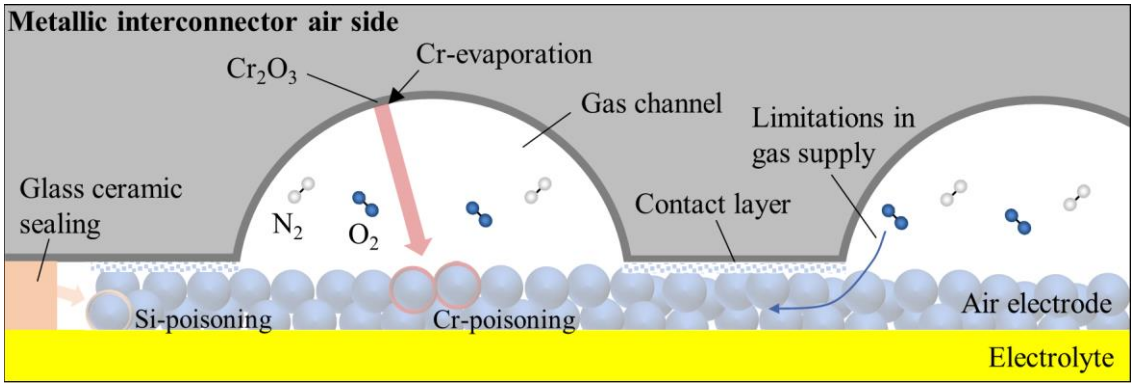

Figure 12 Schematic evaporation of Cr- and Si-species from the metallic interconnector and glass ceramic sealing respectively with subsequent poisoning of the air electrode as well as limitations in gas supply.

3.9 Pressurized Operation[10]

A comprehensive techno-economic analysis about the pressurized operation of SOECs was performed by Nami et al. [14]. Nowadays SOECs are only cost-competitive in comparison to grey hydrogen by steam reforming when a CO_2 tax is considered [14]. This can change in the future, as the authors stated, that pressurized SOEC is economically beneficial even if the system capital expenditure (CAPEX) increases by 20%. The cost of hydrogen was estimated for 2050 to 1.4 € kg^{-1} H_2 for pressurized SOEC in comparison to 1.6 € kg^{-1} H_2 for close to atmospheric SOEC by assuming free steam. A deviation of 0.2 € kg^{-1} seems comparatively small. However, with respect to the hydrogen demands of $95 - 130$ TWh (approx. $2.85 - 4.05$ Mio. t H_2) estimated for 2030 in Germany alone [5], the economic benefit is obvious. In addition, hydrogen will be carried in large quantities by ammonia. The cost of producing ammonia by using a pressurized SOEC was estimated to 495 € t^{-1} and represents the cheapest option in comparison to its operation at ambient pressure [219].

Regarding SOEC operation under atmospheric pressure, the downstream mechanical compression of hydrogen can cause an efficiency loss of approx. 5% as shown in Ref. [15]. Therefore, bypassing especially the first mechanical compression stage is crucial. Thus, the coupling of a pressurized SOEC followed by a chemical reactor in a power-to-X process has been discussed as a concept and modeling basis in literature [220–222]. However, an experimental coupling of a pressurized SOEC and methanation was so far only shown in the work by Gruber et al. [223]. The pressurized operation of a solid oxide fuel cell enables a higher power density and efficiency as shown in simulative works [45,224–226] as well as experimentally for single cells [16,17,227,228] and stacks [18,229–231].

A detailed theoretical study about the influence of the pressure towards SOC performance and loss mechanisms is provided in literature [33]. In this work, the 0D-dimensional impedance-

[10] Parts of this chapter have been published in C. Grosselindemann et al., *J. Power Sources*, **614**, 234963 (2024) [2].

based performance model is used to theoretically predict the current voltage behavior under pressurized conditions and provides a reference for the first experimental results.

Until now, experiments under elevated pressure were performed in fuel cell and electrolysis mode. On cell [16,21–23,227,228,232–237] and stack level [19,24,25,230,231,238], the operating pressures were mainly set in a range of $\sim 1 - 10$ $\mathrm{bar_a}$ with limited studies [8] performed above 10 $\mathrm{bar_a}$. Although, there is one case reported by Jensen et al. [18], which operated a stack at pressures as high as 25 $\mathrm{bar_a}$. Generally, the increase of the open-circuit voltage U_{OCV} with increasing pressure is beneficial for fuel cell mode as shown in the work by Henke et al. [239]. The authors stated with the shown improvement of power density, that pressurized operation can decrease costs, weight and volume of SOFC systems as the number of cells can be minimized. Further, Cadigan et al. [230] reported the most significant results in electrochemical performance when operating a SOFC stack with metal-supported cells up to 4 $\mathrm{bar_a}$. In the work by Shy et al. [234] and Hung et al. [240], a pressurized ammonia-fueled SOFC was demonstrated as a candidate for coupling with a micro gas turbine. In Ref. [241] a unique 3D printed SOC is presented with embedded channels into the cell and enhanced mechanical stability targeted for pressurized operation. In addition, microtubular cells also seem promising for pressurized operation [242].

For electrolysis [243], an increase in U_{OCV} at higher pressures results in a slightly higher power input. Bernadet et al. [233] and Sun et al. [16] showed with tests of fuel electrode supported cells that this can be leveled out at elevated pressures of up to 10 $\mathrm{bar_a}$ and at higher current densities. In the work by Riedel et al. [24] fuel-electrode supported cells were compared in electrolysis mode with electrolyte-supported cells (ESC) on stack level with pressures up to 8 $\mathrm{bar_a}$. It was found, that the stack with ESCs only showed a minor influence towards pressurization. In comparison, a performance gain of 3% at 8 $\mathrm{bar_a}$ could be achieved for the stack with fuel electrode-supported cells. Nevertheless, the authors emphasized that other properties of the cell such as mechanical or redox stability need to be considered for the system design [24]. The negative increase of OCV for SOEC operation can be avoided by a single-sided pressurization of the fuel side and leaving the air side atmospheric as shown in Ref. [34]. However, this results in a differential pressure between fuel and air side, which causes high mechanical stresses on the cell. The experimental feasibility of such operation still needs to be further evaluated.

To the date of publishing the new test bench developed in this work in Ref. [2], all known pressurized SOC systems and testing devices for cells and stacks were realized with a pressure vessel [8,16–26], resulting in voluminous, costly and heavy systems. As cells and sealants used in stacks are considered to be limited to pressure gradients in the range of a few hundred $\mathrm{mbar_a}$, a complex pressure control strategy is required to align vessel-, fuel- and oxidant pressures. In the meantime, a dome less testing set-up was shown in the work by Langerman et al. [244] as well.

In this work, a SOC is operated at pressures of up to 11 $\mathrm{bar_a}$ in a glass-ceramic sealed cell housing without a pressure vessel. A newly developed test bench and metallic cell housing for single cell testing of SOCs with a unique pressure regulation and without external pressure balancing is introduced.

4 Experimental

The testing of experimental cells with respect to ideal and stack-like contacting as well as testing under atmospheric and pressurized conditions is described in the following section.

4.1 Experimental Cells[1]

In this work planar electrolyte-supported cells with an active cell area of 1 cm^2 were investigated. The cells exhibited a Ni/GDC fuel electrode, a 3 mol-% YSZ (3YSZ) electrolyte substrate and an LSCF air electrode. Additional GDC layers were placed in between electrodes and electrolyte. The layer thicknesses were analyzed by scanning electron microscopy (SEM) yielding in a thickness of approx. 24 µm for the fuel electrode, approx. 85 µm for the electrolyte and approx. 30 µm for the air electrode. Furthermore, a SEM image of a focused ion beam (FIB) polished fuel electrode cross section is presented in Figure 13. The FIB-polishing and SEM-imaging was performed in a SEM/FIB Thermo Scientific™ Helios G4FX DualBeam™ (Thermo Fisher Scientific, Waltham, Massachusetts, USA) instrument. Further information about the equipment can be found in Ref. [245]. Three different cell layers become visible in this SEM image, namely the 3YSZ electrolyte 1 (cf. Figure 13), a GDC interlayer 2 and a Ni/GDC fuel electrode 3. In the latter, Ni depicts the darker grey particles and GDC the lighter grey ones with black pores in between. It can be observed that the Ni particle size and amount varies from bottom to top of the electrode. This further demands the investigation of the role of three phase boundaries at Ni/GDC electrodes compared to double phase boundaries of pure GDC electrodes regarding the electrochemical performance. In order to study the processes at cathode and anode individually, symmetrical cells with nominally identical electrodes on both sides of the electrolyte were applied. Further details about the microstructure can be found in Ref. [75]. The required dimensions for placing the cell in the test bench for atmospheric testing are shown in Figure 15 (b). With respect to experimental ESCs for pressurized testing, small adjustments related to the new test bench were necessary and are described in chapter 4.3.

In addition, planar fuel electrode-supported cells (Figure 15 (a)) were analyzed with an active area of 1 cm^2. The cell is mechanically supported by a Ni/3YSZ substrate layer (500 µm thickness) and exhibits a Ni/8YSZ active functional layer (12 µm thickness) on a 8YSZ electrolyte (4 µm thickness). A GDC layer (≈ 2 µm thickness) is placed between the electrolyte and the LSCF air electrode (48 µm thickness). [246,247] The electrochemical characterization and parametrization under atmospheric conditions was performed similar to Leonide et al. [36] without changing the methodology and is therefore summarized in the appendix 7.3.

[1] Parts of this chapter have been published in C. Grosselindemann et al., *ECS Trans.*, **103**, 1375-1393 (2021) [37] and C. Grosselindemann et al., *J. Electrochem. Soc.*, **168**, 124506 (2021) [38].

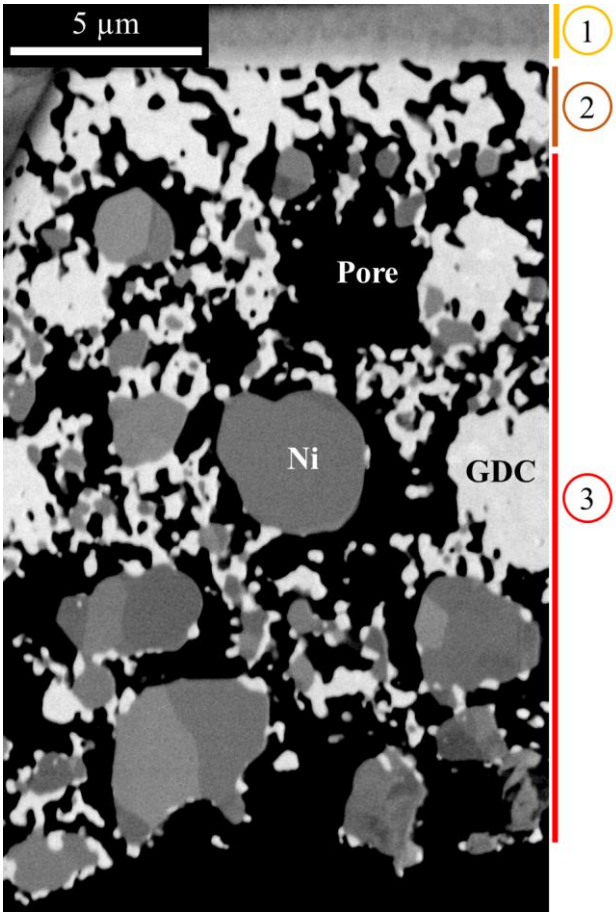

Figure 13 SEM image of a FIB-polished fuel electrode cross-section with a 3YSZ electrolyte in cell layer 1, a GDC interlayer 2 and a Ni/GDC fuel electrode 3 with Ni particles (darker grey), GDC particles (lighter grey) and black pores in between; mirror detector, electron energy: 5 keV, electron beam current: 0.4 nA. Taken from Ref. [38].

4.2 Testing under Atmospheric Pressure

Testing of SOCs under atmospheric pressure (assumed to be 1 bar_a in this work) is extensively described in Ref. [28] and summarized here. In addition, the stack-like contacting with metallic interconnectors is shown in chapter 4.2.2.

4.2.1 Ideal Contacting[2,3]

The fuel is supplied by a gas mixing unit via mass flow controllers providing gas mixtures of hydrogen (H_2), oxygen (O_2) as well as the inert gases nitrogen (N_2) and helium (He), respective-

[2] Parts of this chapter have been published in C. Grosselindemann et al., *ECS Trans*., **103**, 1375-1393 (2021) [37] and C. Grosselindemann et al., *J. Electrochem. Soc*., **168**, 124506 (2021) [38].

[3] Parts of this chapter have been published in C. Grosselindemann et al, *J. Electrochem Soc.*, **171**, 054508 (2024) [147].

ly, as shown in Figure 14 (a). A total flow rate of 250 sccm is set at each electrode side. Steam is produced in an upstream combustion chamber by mixing oxygen to the fuel (Figure 14 (d)). This enables a stable fuel humidification of up to 100 % H_2O. Alternatively, fuel gas mixtures of carbon monoxide (CO) and carbon dioxide (CO_2) can be set. In addition, reformate gas mixtures of $H_2/H_2O/CO/CO_2$ can be generated as well. However, this is not part of this study and considered in other works [68,143,146]. The test bench is shown by a CAD-model (designed in Autodesk Inventor Professional 2023) in Figure 14 (b) with a view inside the furnace. Here, a ceramic (Al_2O_3) hood is placed above the cell housing on a fully ceramic mechanical support structure and can be flushed with N_2. Below, the fuel gas mixture and oxidant are supplied with ceramic gas lines towards the cell housing. The ceramic hood is removed in Figure 14 (c) so that the ceramic cell housing placed in the middle of the furnace as well as ceramic sealing weights (approx. 750 g) become visible.

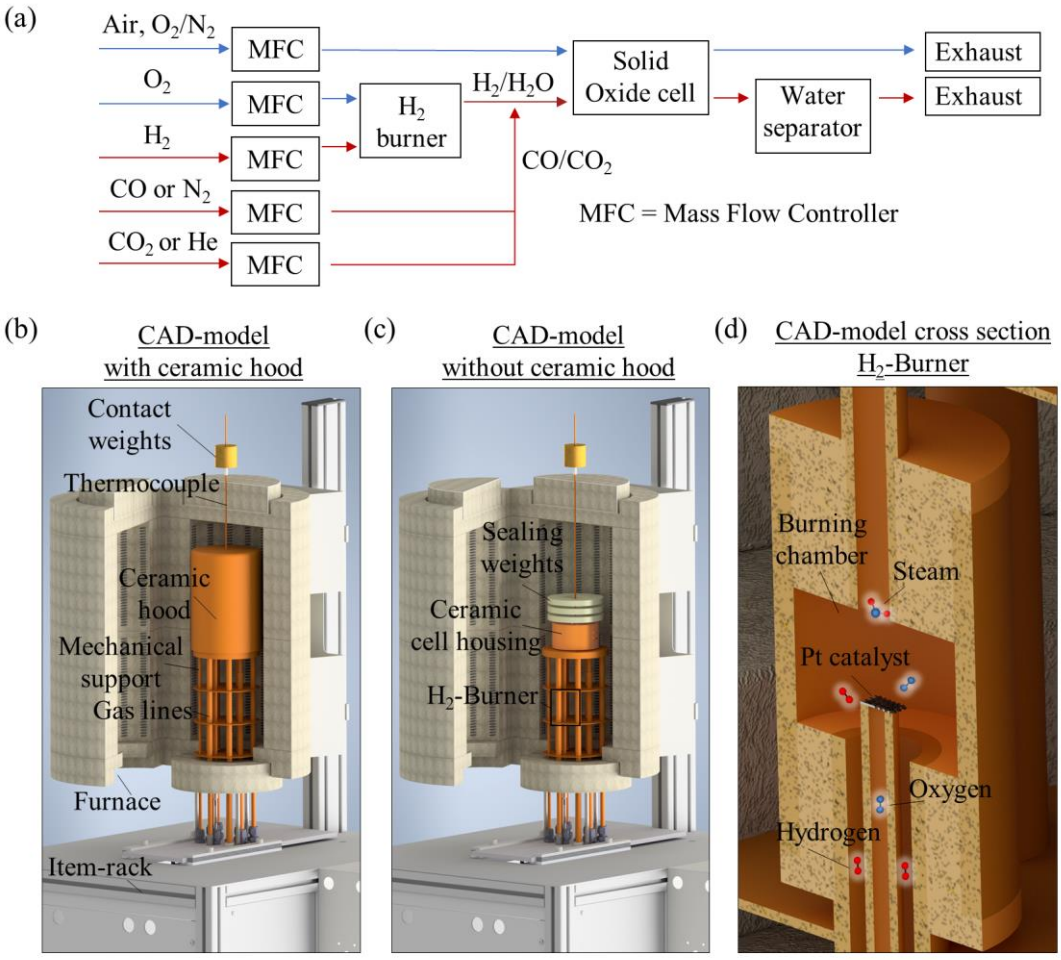

Figure 14 (a) Flowchart schematic of gas supply for the test bench under atmospheric pressure. (b) View into furnace with mounted ceramic hood for N_2-flushing. (c) View into furnace without ceramic hood. (d) Cross section of the H_2-burner with Pt catalyst mesh.

A schematic sketch of an experimental ASC with Ni/8YSZ fuel electrode and Ni/3YSZ substrate and ESC with Ni/GDC fuel electrode is shown in Figure 15 (a) and (b) respectively. Ideal

contacting is realized by an inert testing environment with respect to a ceramic (Al_2O_3) cell housing and flow fields as shown in Figure 15 (c) [28]. Regarding the small-scale active area of 1 cm^2 a gradient free system with respect to temperature and gas conversion can be assumed in comparison to cell sizes used in commercialized stacks. The cell is placed between the housing blocks for fuel and air side respectively as shown in Figure 15 (c) and (d) by a cross section of the CAD-model. Contacting of the electrode is realized by finely meshed double-layered grids with Ni at the fuel and gold at the air electrode (Figure 15 (c) and (d)). At the top of the test bench (Figure 14 (b)), contact weights (200 g) are placed on the thermocouple (type S) which is connected to the ceramic flow field at the air side and supplying the required contact force for the Au-grid onto the air electrode. The flow field is decoupled from the ceramic housing (Figure 15 (c) and (d)). Similarly, this is applied at the fuel side (bottom housing block). Contact losses resulting from this setup can be neglected [28,38,205]. The cell voltage U_{cell} results from the difference in electrical potential between the Ni grid ($\varphi_{\mathrm{mesh,FE}}$) and gold grid ($\varphi_{\mathrm{mesh,AE}}$). The contact meshes are connected with electrical feedthroughs within a ceramic capillary visible in Figure 15 (c), (d) and (e) enabling a four-point measurement set-up. In addition, smaller electrodes are placed before and after the cell to monitor the OCV. These are connected with two gold-pins at the air side (Figure 15 (d)) and Ni-meshes at the fuel side (Figure 15 (e)). Cell mounting begins with prepared meshes at the fuel side (Figure 15 (f)) and placing the cell on top afterwards (Figure 15 (g)). An Au-sealing frame is placed between the cell and housing at the air side (Figure 15 (h)). In combination with the ceramic weights, sufficient sealing of the test bench is reached.

After mounting the cell in the test rig, a predefined startup procedure was performed. Here, crucial steps like the reduction of NiO in the fuel electrode need to be conducted as the microstructure determines the cell performance significantly [248]. In the following testing phase, impedance spectra and CV-characteristics were measured at systematically varied operating conditions. The spectra were acquired by a frequency response analyzer using a pseudo-potentiostatic mode (amplitude $\leq$ 12 mV regarding the polarization resistance [28]). The frequency was varied in between 30 mHz and 10^5 Hz (Zahner Zennium E) or 1 MHz (Solartron 1260) with 12 points per decade. All experiments were conducted under open circuit conditions (OCV), except for the determination of the charge transfer coefficients α. The voltage cap was set between $0.6 - 1.4$ V.

In case of operating with CO/CO_2 [128], the thermodynamic stability of the fuel gas mixtures needs to be considered. This was checked with the open-source program Cantera [249] in order to prevent carbon deposition in the fuel electrode. In addition, the voltage cap for electrolysis mode was limited to 1.2 V. [128]

The validity of the measured spectra was verified by a Kramers Kronig Test [51]. Regarding testing under ideal contacting, ageing effects were excluded by reference measurements.

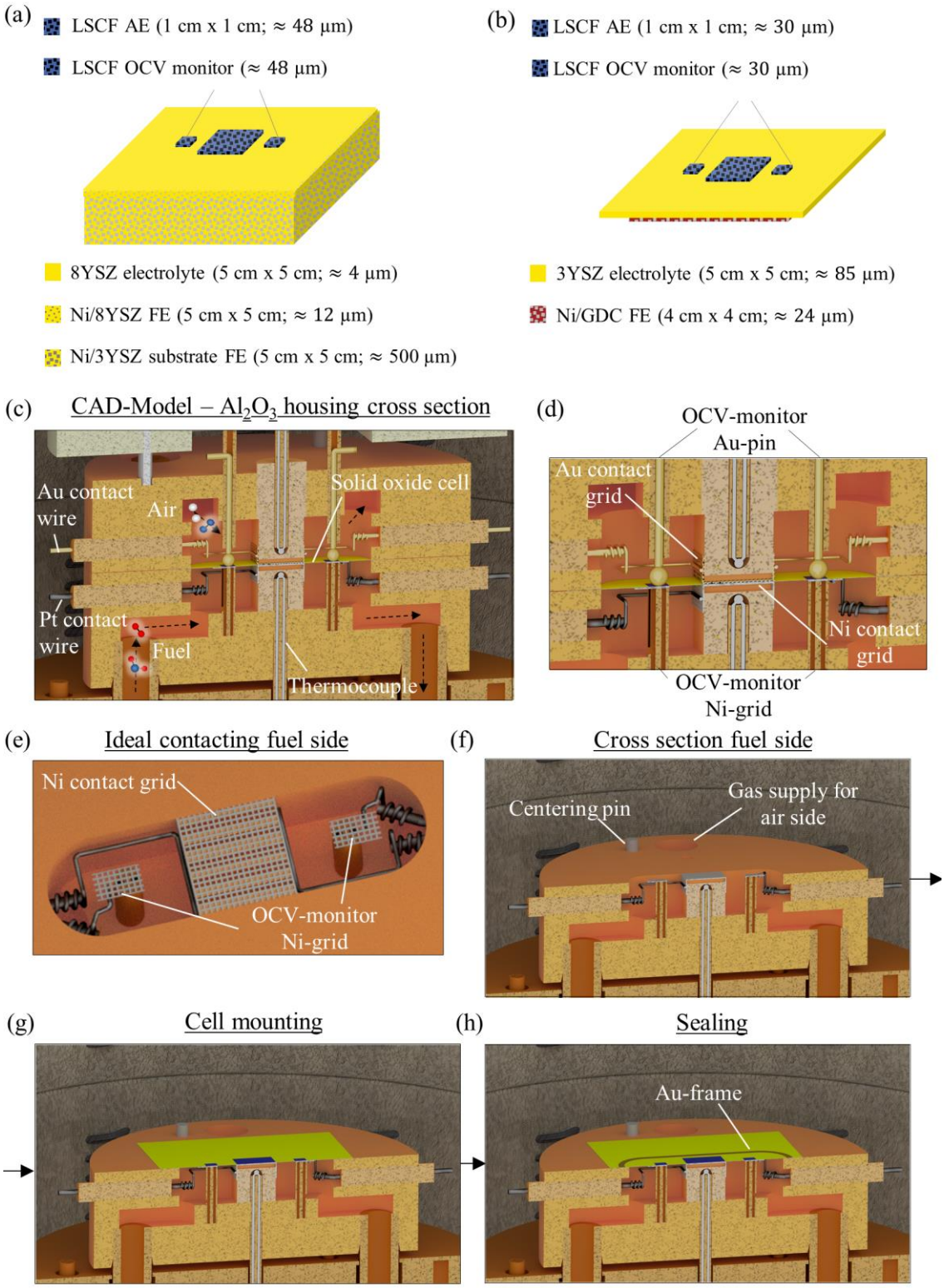

Figure 15 (a) Schematic experimental ASC with Ni/8YSZ fuel electrode and (b) ESC with Ni/GDC fuel electrode (adapted from Ref. [38]). CAD model cross sections of the Al_2O_3 housing in (c) and (d) of ideal cell contacting with OCV monitors. (e) Ideal contacting with Ni

contact grid and OCV monitors at the fuel side. (f) Housing cross section at the fuel side and subsequent cell mounting in (g). Sealing with Au-frame in (h).

4.2.2 Stack-like Contacting[4]

With respect to a stack-like contacting as shown in Figure 16 (a) metallic flow fields exhibiting a model geometry were manufactured from different steel grades Crofer 22 APU, AISI 441 and UNS S44330 by milling. To enable a uniform coating by physical vapor deposition (PVD) a flow field geometry with round channels (0.5 mm radius) was chosen. The chemical composition of the specific batches of the three steel grades is listed in the appendix in Table A 6 and Table A 7. In comparison, Crofer 22 APU has the highest content of chromium and AISI 441 has the least. To minimize Cr evaporation from uncoated parts of the samples [251], CeCo (10 nm/600 nm) was deposited on all sides and edges of the sample. The depositions were done by Alleima AB (Sanergy™ HT) using a batch PVD coater which realizes thin films in the nanometer range by evaporation of metallic Ce and Co in vacuum. Such a coating can be applied on any ferritic stainless-steel grade.

To establish a stack like contacting between electrode and metallic flow field, additional contact layers are applied. A single-layered Ni-grid is point welded onto the MIC at the fuel side. Regarding the air side, an LSCF contact paste is screen printed onto the air electrode and mounted in the liquid state. In Ref. [252] the impact of an initial dry contact paste is discussed.

For the fuel electrode side potential probes are connected to the nickel mesh as well as to the MIC at the fuel side as shown in Figure 16 (c). The potential difference between metallic interconnector $\varphi_{\mathrm{MIC,FE}}$ and contact mesh $\varphi_{\mathrm{mesh,FE}}$ results in the contact voltage loss $\eta_{\mathrm{contact,FE}}$ at the fuel electrode (FE) in equation (51).

$$\eta_{\mathrm{contact,FE}} = \varphi_{\mathrm{MIC,FE}} - \varphi_{\mathrm{mesh,FE}} \tag{51}$$

The resulting contact losses related to the contact between air electrode and MIC, i.e. mainly due to oxide scales on the steel, can be quantified with a measuring technique introduced by Kornely et al. [27]. At the air side the potential is likewise measured at the MIC. To access the potential of the LSCF contact layer, a ceramic capillary with a gold wire ending on top of the contact layer surface is plugged through a drilled hole in the MIC (Figure 16 (b) and (c)). Thus, the potential at this point can be measured and likewise the corresponding voltage loss $\eta_{\mathrm{contact,AE}}$ is defined in equation (52) by the difference between the metallic interconnector $\varphi_{\mathrm{MIC,AE}}$ and the probe $\varphi_{\mathrm{probe,AE}}$ at the air electrode (AE).

$$\eta_{\mathrm{contact,AE}} = \varphi_{\mathrm{MIC,AE}} - \varphi_{\mathrm{probe,AE}} \tag{52}$$

[4] Parts of this chapter have been published in C. Grosselindemann et al., *ECS Trans.*, **111** (6), 533-546 (2023) [250] and C. Grosselindemann et al, *J. Electrochem Soc.*, **171**, 054508 (2024) [147].

It should be noted that $\eta_{\mathrm{contact,AE}}$ includes the contact losses and the losses resulting from the in-plane conduction in the air electrode [27]. In case of an LSCF electrode and additional LSCF contact layer the latter can be neglected [161].

Furthermore, Figure 16 (d) shows a variation of the contact set-up with a metallic flow field at the fuel side and a ceramic flow field at the air side in order to allocate the impact of enhanced gas diffusion at the MIC-contacted fuel electrode.

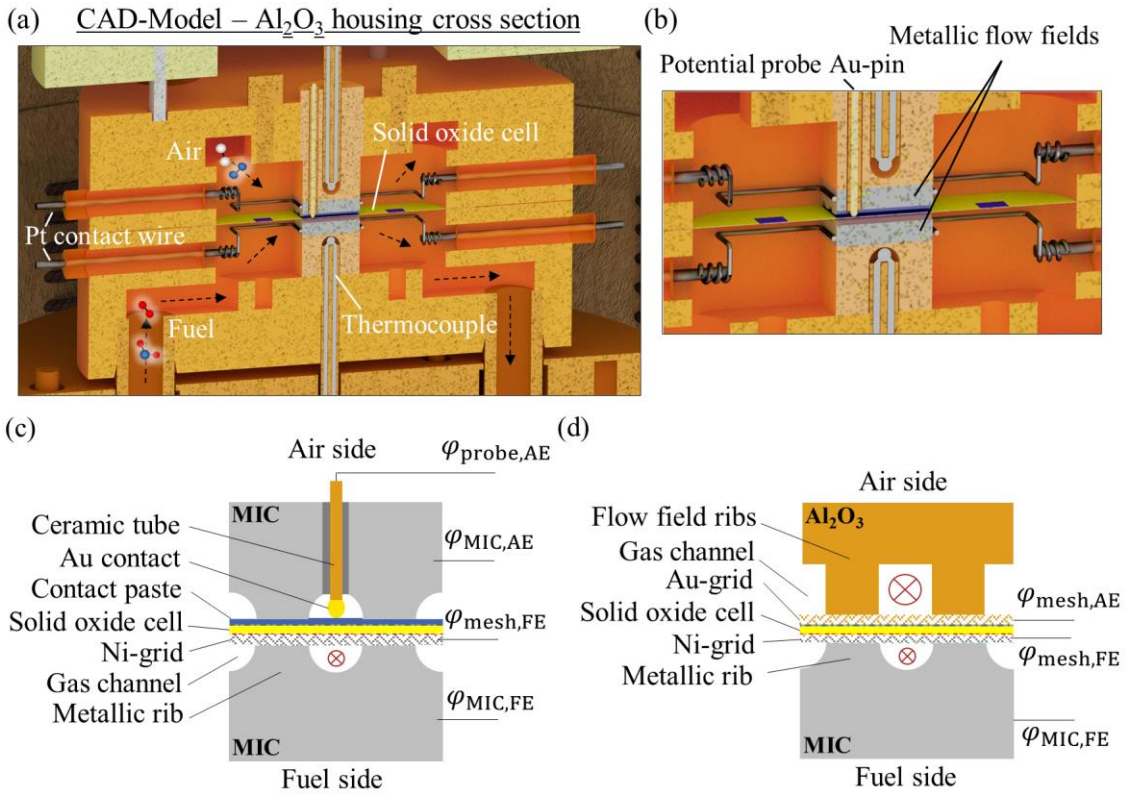

Figure 16 (a) CAD model cross section of Al_2O_3 housing and (b) with metallic flow fields and Au-pin for potential measurement at the air electrode. (c) Stack-like contacting with metallic interconnectors with welded Ni-grid (fuel side) and screen printed LSCF contact paste layer (air side) with potential probes. (d) MIC with welded Ni-grid at the fuel side and a ceramic flow field with gold mesh at the air side. Graphic (c) and (d) adapted and taken from Ref. [147].

Sufficient drying and sintering of the initially liquid LSCF contact paste was realized at 850 °C in air for 24 h. In the following testing phase, impedance spectra and IV-characteristics were measured at systematically varied operating conditions.

Degradation effects during the rather short test of approx. 200 h were evaluated from reference measurements at start and end of test. The ideal contacted cell as well as all experiments with coated MICs showed nearly no performance change ($<$ 5%), whereas a significant degradation (10 – 40%) was observed in case of uncoated MICs. For comparison spectra and IV-characteristics of tests with uncoated MICs were taken at the start of test.

4.2.2.1 Post test analysis of Metallic Interconnectors

The tested un-/coated metallic interconnectors were analyzed post-mortem by preparing cross-sections with a Leica EM TIC 3X Broad Ion Beam (BIB) milling system. The microstructure of the oxide layers was investigated by a JEOL JSM-7800F Prime SEM with an Oxford Instruments Energy-Dispersive X-ray spectrometer using 10 kV for imaging and 15 kV for EDXS.

In addition, EDXS of the electrodes was performed with a Quanta FEG 650 scanning electron microscope equipped with a Bruker Quantax 400 SSD energy-dispersive X-ray detector. Processing of data was performed using the Bruker ESPRIT software package.

Furthermore, samples were prepared for investigation in a transmission-electron microscope (TEM) by preparing lamellas with a focused-ion-beam (FIB) in a SEM. The preparation of the lamella was done with a Thermo Scientific™ Helios G4 FX Dual-Beam (Thermo Fisher Scientific). Afterwards, it was investigated in the OSIRIS ChemiStem TEM from Thermo Fisher Scientific at 200 kV.

4.3 Pressurized Single Cell Testing[5]

Test bench design, cell dimensions, pressure regulation and electrochemical characterization are described in the following sections.

4.3.1 Gas Supply and Pressure Regulation

The gas supply is realized via a gas mixing unit as described for the test bench under atmospheric pressure in chapter 4.2.1 [28]. Likewise, an upstream combustion chamber is located inside the fuel gas line as can be seen in Figure 17 (a) (H_2-burner). Here, steam is produced by mixing oxygen to the fuel. This enables up to 100% steam in the fuel gas. A total flow rate of 250 sccm per electrode is set as well. In this test bench a new pressure control concept is applied that is based on a single pressure controller, removing the need to control the differential pressure between fuel and air side as shown in the flowchart schematic in Figure 17 (a). No further pressure tank is needed in order to balance the pressure. Additionally, in comparison to Figure 14 (a) and Ref. [28] here the off-gas from the fuel and air side is united in a downstream combustor as shown in Figure 17 (a). Thus, only one gas phase is remaining after the off-gas burner. For a reliable, oscillation free operation of the downstream pressure regulator the steam needs to be removed, which is realized by a water separator [253].

4.3.2 Pressurized Test Bench

The new test bench is based on existing SOC testing technology [28] described in chapter 4.2 which was redesigned to enable pressurized operation without a pressure vessel or complex pressure control strategies. The designing and engineering process as well as mounting with

[5] Parts of this chapter have been published in C. Grosselindemann et al., *J. Power Sources*, **614**, 234963 (2024) [2].

demonstration of functionality was a key part in this thesis. The pressurized test bench developed in this thesis is shown with a CAD-model (designed in Autodesk Inventor Professional 2023) in Figure 17 (b) with a front view and (c) side view. A view inside the furnace is presented in Figure 17 (d). In comparison to Figure 14 and Ref. [28], a metallic cell housing enabling a cell integration by glass-ceramic sealants is designed. The commonly used fully ceramic set-ups with gold or ceramic sealants are critical regarding gas tightness at elevated pressures as tubes are simply plugged together. The metallic cell housing is made of APMT (Kanthal® [254]) as this material combines high stability and creep strength under oxidizing and reducing atmospheres with low Cr-evaporation due to the Al_2O_3 oxide scale. This material was chosen to maintain inert testing conditions as good as possible in comparison to the ideal contacting set-up described in chapter 4.2.1. The fuel (bottom) and the air side (top) of the housing were machined from 30 mm APMT sheets. The APMT gas lines for fuel and air supply inside the furnace are welded to the fuel and air side housing. Welding of APMT represented a major challenge in this work, since a well-defined welding protocol has to be considered [254]. It is of great importance to avoid a localized heat impact by open flames on the APMT material to avoid the formation of cracks. Thus, homogeneous heating needs to be performed accordingly in a suitable furnace regarding housing and tube dimensions. This includes a pre-heat treatment of 250 °C (+/− 50 °C) followed by welding at 250 °C (not allowed below 200 °C) and an immediate post-heat treatment at 850 °C (+/− 20 °C) for 1 h. Another pre-oxidation at 1050 °C for 8 h was carried out. Alternatively, tubes made of Alloy 600 could be soldered with silver (XPAg8CuO0,5Cu/S, Innobraze GmbH) into the APMT housing.

Fuel and air supply in the housing plates is realized via milled gas lines schematically shown in Figure 17 (e-f). The metallic housing blocks are compressed between two Al_2O_3-plates by two Al_2O_3 rods (Figure 17 (e)). It is recommended to get the Al_2O_3-plates manufactured in the final shape already and strictly avoid milling afterwards with respect to crack formation. The ceramic rods (35 mm in diameter) are fixed at the test rig outside of the furnace. From the top an inflatable boot provides the force for compression in order to withstand the driving force from the gas phase at the electrodes as shown in Figure 17 (e). Depending on open (unsealed) cell area and operating pressure level this force has to be adjusted. In this study a pressure of 7 bar_a was applied to the inflatable boot corresponding to a force of approx. 8 kN. The Al_2O_3 plates between ceramic rod and APMT housing block distribute the clamping force equally. With this, a critical point force from the ceramic rod into the metal housing block can be avoided, as the metal would be bended regarding its lower toughness. However, a decoupled contact force on the flow field towards the cell cannot be applied in this set-up as it is realized for atmospheric test benches (see chapter 4.2.1).

In this work, fuel and air side are pressurized equally. As shown in Ref. [14,34], it is the further goal to pressurize the fuel side only, so that the increase of OCV can be avoided. An operation of the test bench with differential pressure having the fuel side pressurized and the air side atmospheric is in general possible and can be investigated in a future work.

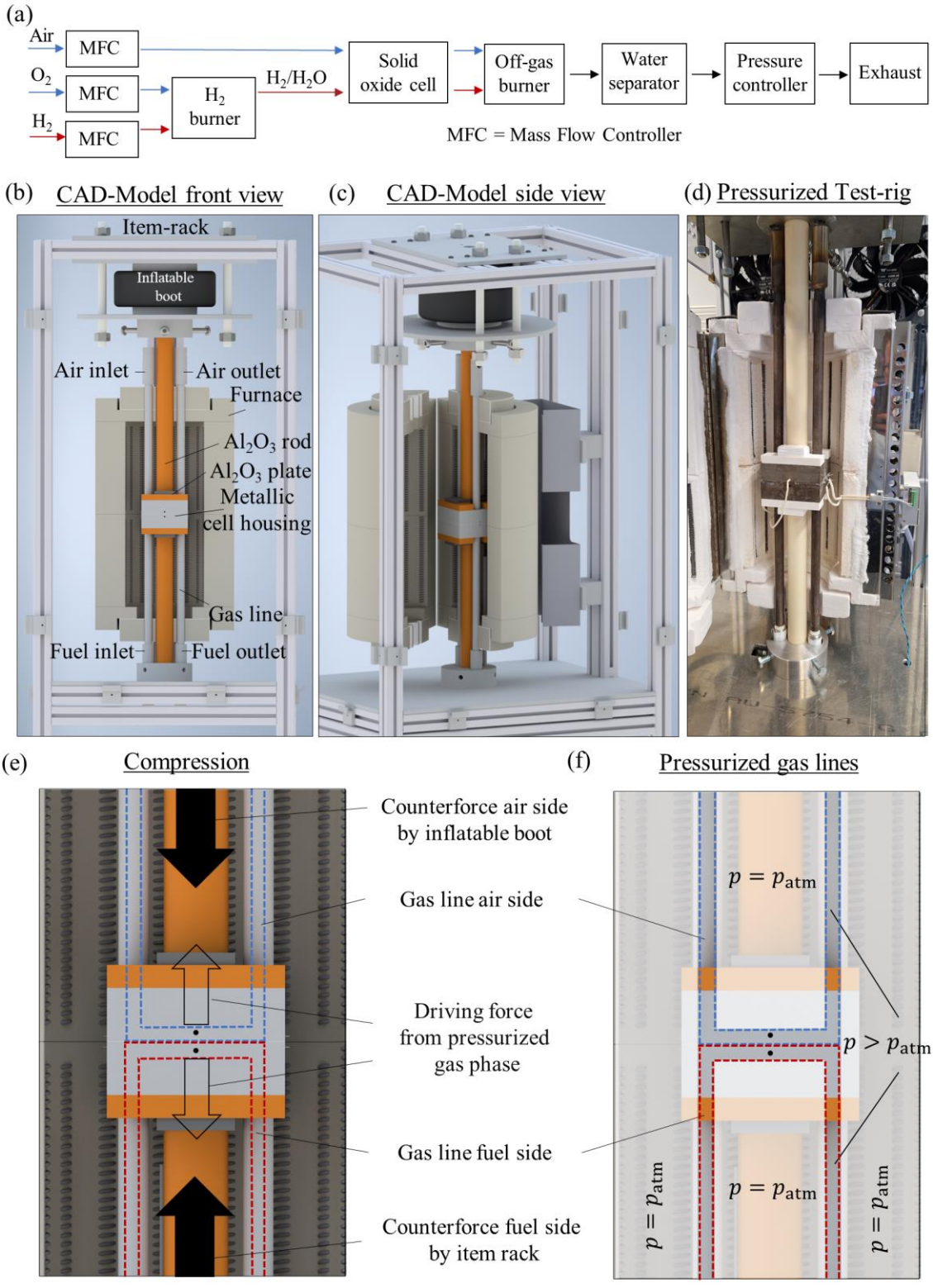

Figure 17 (a) Flowchart schematic with one pressure regulator only. (b) CAD-model front view as well as (c) side view and (d) view into furnace of pressurized test bench. (e) Schematic

compression with inflatable boot and ceramic rods. (f) Scheme of pressurized lines without a pressure vessel. Graphic taken from Ref. [2].

4.3.3 Cell Mounting Electrolyte-supported Cell

Planar electrolyte-supported cells with an active electrode area of 1 x 1 cm^2 as described in chapter 4.1 were investigated (see Figure 18 (a)). Even though the APMT is an Al_2O_3-former and thus electrically insulating at the surface, the area of the electrolyte sheet of 100 mm x 100 mm is equal to the metallic cell housing (see Figure 18 (g)). This further ensures electrical insulation between the two metallic housing parts. The contacting was adapted from the previous chapter 4.2.2 regarding a stack-like contacting with metallic flow fields shown in Figure 18 (b) and (e). Here, a CeCo protective coating is also applied at the air side.

In Figure 18 (d) a cross section of the metallic housing is shown with the CAD model. As the Al_2O_3 oxide scale on the APMT-housing is insulating, the metallic flow fields are contacted in a four-point measurement setup via Pt-wires and electrical feedthroughs to ensure a reliable electrical connection. The feedthroughs are realized by platinum wires insulated by Al_2O_3 capillaries towards the metallic housing plates (Figure 18 (c)). A gas- and pressure tight sealing is realized by silver soldering (XPAg8CuO0,5Cu/S, Innobraze GmbH) the capillary and likewise Pt wire into the metallic housing block. This worked well during first tests in terms of sealing as the silver fills up small gaps of approx. 0.1 mm. However, the Pt wires became brittle with time, so that longterm testing with several mounted cells becomes impossible. Thus, the Pt-wires were subsequently sealed with glass ceramic sealing paste as well (G018-392). The glass-ceramic sealing paste requires a comparably larger sealing gap of approx. 1 mm.

An additional ceramic tube is placed inside the APMT fuel gas line, which does not fulfill criteria in terms of sealing but serves as a thermal protective layer with respect to the upstream H_2-burner. The metallic flow fields are placed on exchangeable positioning blocks enabling a high flexibility regarding single cell contacting as shown in Figure 18 (d) and (e).

Prior to cell mounting, a LSCF contact paste is screen printed onto the air electrode as described in chapter 4.2.2 and shown in Figure 18 (b). The metallic flow field at the fuel side is in contact with a 3D flexible Ni-knit ensuring a good contacting of the fuel electrode even without the well-defined contacting pressure available in the atmospheric test bench (Figure 18 (b)). Contact layers at fuel and air side have to provide a sufficient flexibility during mounting. The gas- and pressure tight sealing of the cell is realized by a glass ceramic sealing paste based on the glass powder G018-281 (SCHOTT AG, [209]) for ESCs that is applied outside the active cell area onto the metallic housing (Figure 18 (f)) prior to cell mounting. The cell is then placed on the housing in Figure 18 (g). Afterwards another layer of glass ceramic sealing is applied onto the cell in Figure 18 (h) to ensure gas tightness between the air side and the metallic cell housing. Thus, the pressurized area in Figure 18 (i) inside the housing is minimized to an area of 4.48 cm^2. The maximum sealing width in this setup is 34 to 43 mm, which is significantly larger than a typical sealing width in stacks. A pre-defined thermal protocol for binder burnout and sealing is performed prior to cell testing.

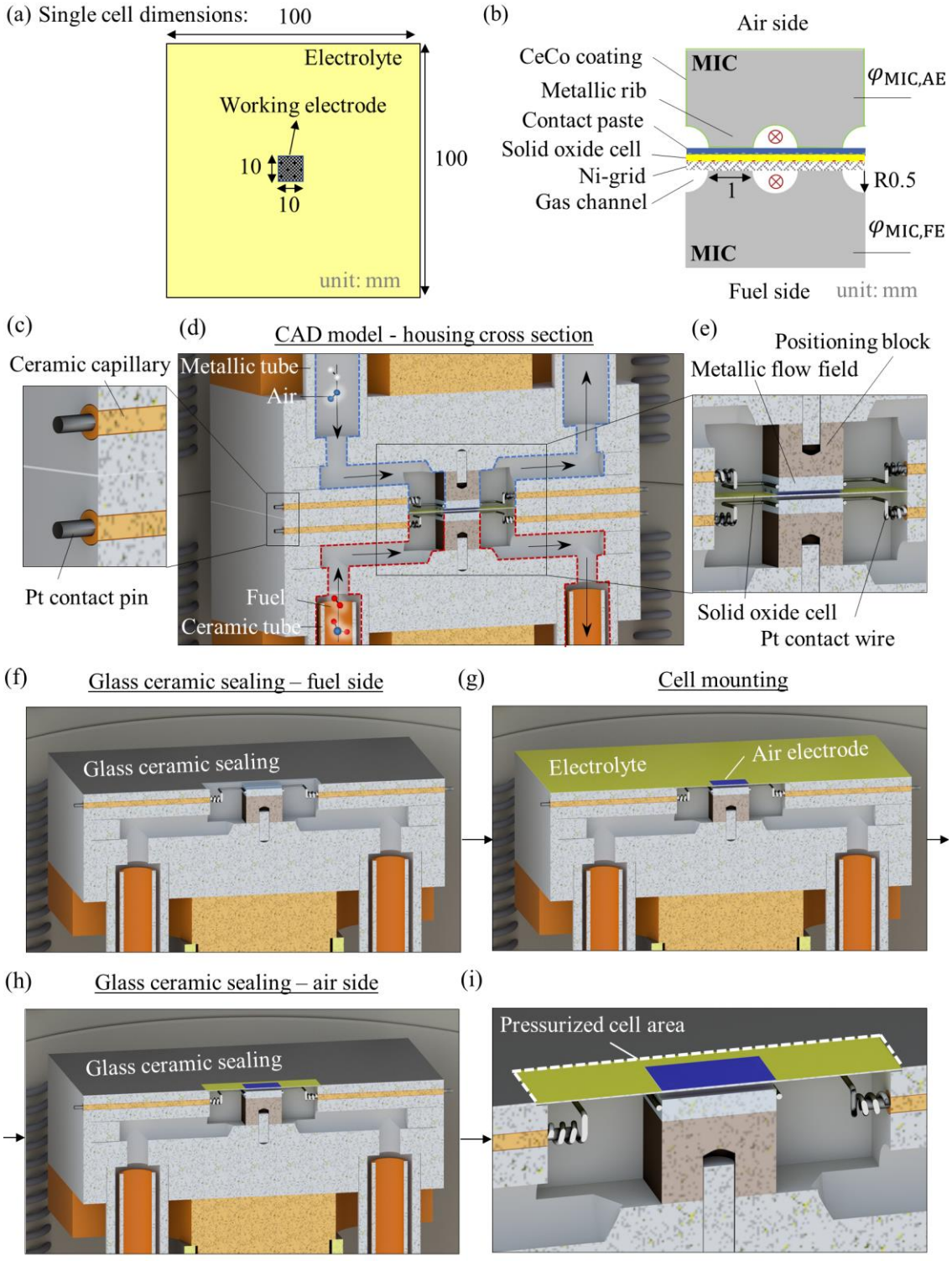

Figure 18 (a) Single cell dimensions and (b) schematic contacting with metallic flow fields. (c) CAD-model cross section with Pt contact wires in ceramic capillary and (d) CAD model cross-section of metallic cell housing. (e) Stack-like contacting with metallic flow fields, positioning blocks and Pt contact wires. (f) Glass ceramic sealing at the fuel side before mounting the cell in

(g). Glass ceramic sealing at the air side in (h) after cell mounting with pressurized cell area in (i). Graphic taken and adapted from Ref. [2].

After cell testing and cooling down to ambient temperature, the two metallic housing plates and the cell were still connected by the glass ceramic sealing, which required further efforts for demounting and cleaning of the metallic cell housing. Next to the metallic housing made of APMT, a housing made of Crofer 22 H (18 mm sheets) with welded gas tubes made of AISI Alloy 600 was manufactured and tested in this work (welded with VDM FM 625). Here, the material combination was chosen as welding is not as critical in comparison to APMT. In addition, Crofer 22 H represents "the" steel grade for SOC technology.

In comparison to the reference test benches exhibiting full ceramic housings and contacting by gold and Ni-meshes respectively [28], the metallic housing and flow fields and the application of the glass ceramic sealant might affect the cell performance by Cr- or Si-species poisoning the electrode. Effects from the stack-like contacting set-up are discussed in chapter 5.3. Poisoning effects from Si-components from the glass ceramic sealing need to be considered [255] and investigated.

4.3.4 Cell Mounting Anode-supported Cell

The newly developed test bench is designed to test any type of planar SOC, such as ASCs as well. Differences in comparison to cell mounting of an ESC in chapter 4.3.3 are described in the following section.

For the ASC the same cell dimensions are applied as in Figure 15 (a) with the 50 mm x 50 mm electrolyte area, which is smaller in comparison to Figure 18 (a) for the ESC. The comparatively thick and porous anode-support layer needs to be sealed as well, which would not be possible having a 100 mm x 100 mm area. However, the active cell area remains 1 cm^2. Here, an additional ceramic sealing frame is needed and placed onto the metallic housing block at the fuel side in Figure 19 (a), which should have the same thickness as the cell. Subsequently the experimental cell is mounted in the center (Figure 19 (b)). The gap between ceramic frame and cell is filled with glass ceramic sealing (G018-392) (Figure 19 (c)), resulting in the pressurized cell area in (d).

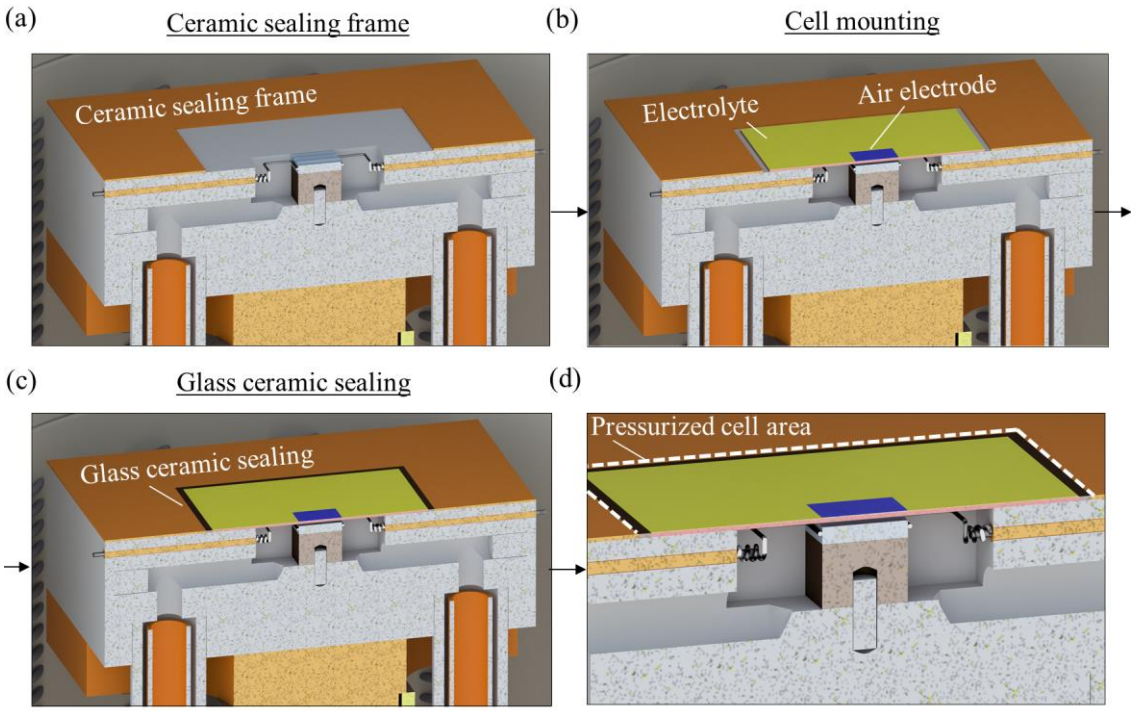

Figure 19 CAD model cross sections with placing a ceramic sealing frame in (a), mounting the cell in (b), applying the glass ceramic sealing in (c) and the indicated pressurized cell area in (d).

5 Results and Discussion

In the following section the results of ideal contacting in H_2/H_2O mode are compared with CO/CO_2 operation as well as stack-like contacting. In addition, results with the newly developed pressurized test bench are shown.

5.1 Ideal Contacting H_2/H_2O[1]

Regarding a first analysis of processes under an ideal contacting environment at the air and fuel electrode, impedance spectra of a full cell shall be compared with those of the electrodes taken from symmetrical cell measurements. Figure 20 (a) shows the spectrum of the full cell, (b) of the LSCF air electrode and (c) of the Ni/GDC fuel electrode. It should be noted that in (b) and (c) the spectrum of a single electrode is displayed, i.e. the measured spectrum of the symmetrical cell divided by two, whereas in the further figures the full spectra and the related DRTs of the symmetrical cells are displayed. The different ohmic resistances can be explained by different electrolyte thicknesses of the cells. The visible deviation between the full cell and the addition of fuel and air electrode impedance taken from symmetrical cell measurements might originate from minor leakages in the full cell measurement that can be excluded in symmetrical cell measurements as well as minor temperature differences.

A more detailed analysis of the LSCF air electrode is shown in chapter 7.4 of the appendix as similar properties and parameter dependencies as reported in [104] were observed. Recapitulatory, for low oxygen partial pressures a peak at frequencies between $0.3 - 10$ Hz becomes visible in the DRT. It strongly depends on the oxidant composition but shows approximately no operating temperature dependency, and thus is attributed to the gas diffusion process in the air electrode. It should be noted that the related resistance is negligibly small for technically meaningful operating conditions. In addition, a coupling of the charge transfer with the solid-state diffusion of oxygen ions could be identified in a process around $2 - 500$ Hz, which corresponds to the oxygen reduction in the mixed electronic-ionic conducting LSCF-cathode modelled by a Gerischer element [256].

This work focuses on results obtained from symmetrical cells with Ni/GDC electrodes in order to identify and quantify the processes in the fuel electrode. The challenge to overcome here is illustrated in the DRT of a temperature variation with a fixed gas mixture of 80% H_2 and 20% H_2O in Figure 21. The temperature covers a range of 600 °C to 900 °C. According to previous studies [82,146], the DRT can be divided into two major peaks in the low frequency $P_{\mathrm{LF1,s}}$ and middle frequency range $P_{\mathrm{LF2,s}}$ as indicated in the DRT in Figure 21. These contributions include gas diffusion, charge transfer reactions in the electrode and ionic transport in the GDC-matrix of

[1] Results of this chapter were partly generated in the master thesis by C. Grosselindemann (2020) [30] and re-worked in the beginning of the PhD with finally publishing in C. Grosselindemann et al., *ECS Trans*., **103**, 1375-1393 (2021) [37] and in C. Grosselindemann et al., *J. Electrochem. Soc*., **168**, 124506 (2021) [38].

the electrode. Obviously, all visible peaks in the DRT are thermally activated. Since a gas diffusion process should exhibit a $T^{0.5}$ temperature dependency, the direct correlation of one of those two DRT-peaks to the gas diffusion process is impossible [104]. As gas diffusion is an unavoidable process in the fuel electrode, the observed temperature dependency of the DRT-peaks suggest that the gas diffusion process is covered by the thermally activated electrochemical processes [56,79,89,121]. Furthermore, three minor peaks are visible at frequencies above 100 Hz ($P_{HF,s}$), which are not further analyzed in this study. Suggestions for their origin are given in Ref. [82].

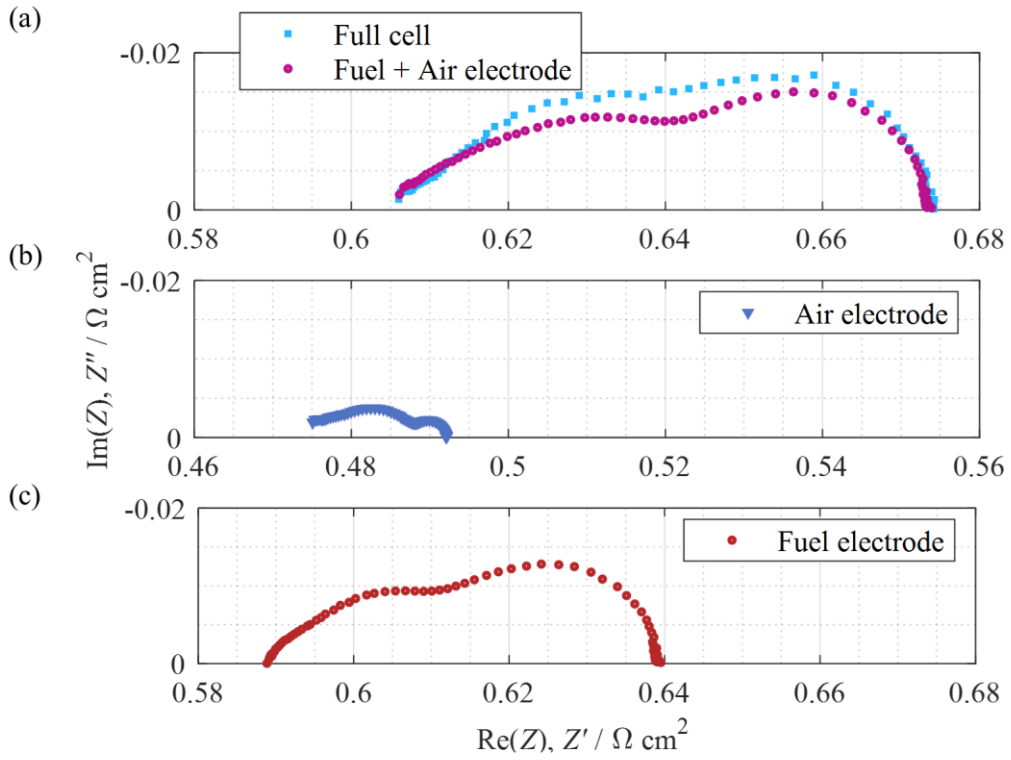

Figure 20 (a) Spectra of full cell and sum of fuel and air electrode (T = 800 °C, fuel gas mixture of 65% H_2 (balanced with H_2O) and synthetic air at the air electrode), (b) the LSCF air electrode (T = 800 °C, synthetic air as oxidant) and (c) a Ni/GDC fuel electrode (T = 806 °C, fuel gas mixture of 65% H_2 (balanced with H_2O)). Graphic formatted and taken from Ref. [38].

5.1.1 Gas Transport Conditions

The fuel gas supply of the symmetrical cell is shown in Figure 22. Gas transport processes will occur in the gas channels of the flow field (convective and diffusive), the contact mesh (predominantly diffusive) and the porous fuel electrode (diffusive). This complex 3D setup is simplified to a virtual gas diffusion layer with a thickness L, whose impact on the gas diffusion resistance is modeled with the approach described in Ref. [43]. The dimensions of the gas channel, Ni contact mesh [257] as well as the porous fuel electrode are shown in Table 1. It becomes obvious that the thickness of the fuel electrode differs by more than one order of magnitude compared to the contact mesh and even more compared to the thickness of the gas

channel. Since the gas diffusion resistance represents a function of the thickness of the gas diffusion layer L [43], which is dominated by the anode substrate in ASCs [205], the gas diffusion inside the just 24 µm thick porous fuel electrode in the investigated ESC presumably can be neglected [82], whereas gas diffusion in the Ni mesh and the gas channels has to be considered.

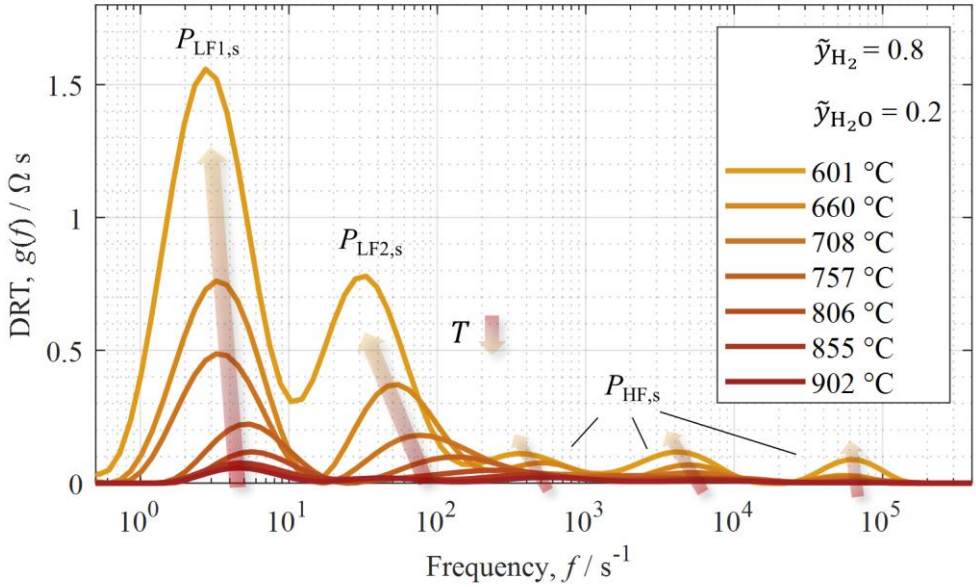

Figure 21 DRTs of spectra measured during a temperature variation between 600 °C and 900 °C with a gas mixture of 80% H_2 and 20% H_2O of a symmetrical cell with Ni/GDC fuel electrodes. Adapted from Ref. [38].

With respect to "pore" diameters > 100 µm in gas channel and contact mesh, Knudsen diffusion can be neglected and the gas diffusion coefficients D_i are based on molecular gas diffusion solely. The Knudsen number Kn has been calculated for a temperature of 800 °C with a gas mixture of 50% H_2 and 50% H_2O and is shown in Table 1.

Table 1 Dimensions and microstructural parameters of gas channel, Ni contact mesh [257] and porous fuel electrode as well as Knudsen criteria Kn. ([c]SEM, [d]estimated)

	Thickness µm	Width, pore diameter µm	Porosity ε_{por} -	Kn -
Gas channel	1000	1000	1	$4.4 \cdot 10^{-4}$
Ni contact mesh [257]	≈ 240	≈ 250	≈ 0.64	$18 \cdot 10^{-4}$
Porous fuel electrode	≈ 24[c]	< 0.6[d]	≈ 0.35[d]	0.73

Therefore, the binary gas diffusion coefficients can be calculated by Chapman-Enskog [258]. Gas diffusion coefficients for components in a gas mixture with more than two components on total are calculated by Wilke [41].

According to Primdahl et al. [43], the gas diffusion resistance $R_{\mathrm{diff,FE}}$ at the fuel electrode can be calculated by equation (27).

In our setup the microstructure parameter Ψ and the thickness L represent unknown parameters, which can be summarized in an effective gas diffusion parameter G_{eff} accounting for an averaged diffusion length L in a (macroporous) medium with effective gas diffusion properties Ψ described by equation (53).

$$G_{\mathrm{eff}} = \frac{\Psi}{L} \tag{53}$$

This parameter, which is solely depending on geometrical and microstructural features of the test setup and the cell, is not depending on temperature or gas composition and thus can be used to calculate $R_{\mathrm{diff,FE}}$ for arbitrary operating conditions.

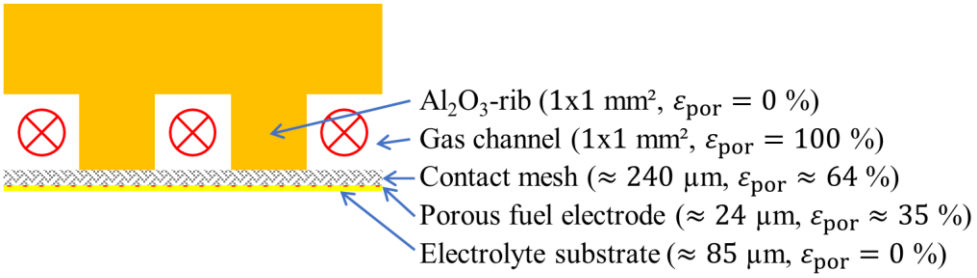

Figure 22 Sketch of the gas transport along the cell´s surface in the cell test setup. In the 1 cm² test benches a gas supply via gas channels with Al_2O_3 flow fields is employed. Details can be found in [28]. Graphic taken from Ref. [38].

5.1.2 Quantification of the Gas Diffusion Process

In the following section a procedure in order to overcome the overlap of activation and gas diffusion polarization in the spectrum with similar time constants is suggested. The subsequent experiment by the application of symmetrical cells with Ni/GDC fuel electrodes is designed to enlarge the gas diffusion resistance $R_{\mathrm{diff,FE}}$ at the fuel electrodes (FE) with the help of equation (27) [43].

To analyze the gas diffusion process and quantify G_{eff}, a high accuracy test should be performed at operating conditions enlarging the gas diffusion resistance $R_{\mathrm{diff,FE}}$. As $R_{\mathrm{diff,FE}}$ is proportional to $T^{0.5}$, a high operating temperature of 850 °C is preferable, which also leads to a decrease of all thermally activated polarization processes. Also, low partial pressures of the reactant 10% H_2 and the reaction product 5% H_2O with an appropriate balancing by inert gases, nitrogen and helium, are selected. This ensures reducing atmospheres to avoid Ni-oxidation and a sufficient content of steam to keep the charge transfer resistance at a low level. Based on the principles of the kinetic gas theory, two ternary gas mixtures with different gas diffusion properties can be applied as hydrogen and steam diffuse with different velocities in nitrogen or helium respectively. The molecular gas diffusion coefficients at 852 °C for hydrogen diffusing in the

above-mentioned steam/nitrogen- and steam/helium-mixture differ by a factor of about 2: $D_{H_2,(H_2O,N_2)} = 0.70 \cdot 10^{-3}$ m² s⁻¹ and $D_{H_2,(H_2O,He)} = 1.38 \cdot 10^{-3}$ m² s⁻¹.

The measured EIS spectra with corresponding DRT are shown in Figure 23 for a symmetrical cell with Ni/GDC fuel electrodes. The application of two different inert gases results in a difference of the polarization resistance of 37 mΩ cm² at a temperature of 852 °C. As the two inert gases are electrochemically inactive, other processes such as charge transfer and ionic charge transport are not affected and the difference in the spectra relies on gas diffusion solely, as shown by Sonn et al. [122] for the Ni/YSZ fuel electrode. This experiment proves the existence of a gas diffusion process, which is predominantly attributed to gas diffusion in the Ni mesh and the flow field. Observing the DRT of the symmetrical cell in Figure 23 (b), the gas diffusion process becomes visible in a frequency range of $0.4 - 100$ Hz and thus strongly overlaps with the charge transfer process in the fuel electrode. It should be noted that the large gas diffusion contribution observed in the spectra is related to the selected operating conditions i.e. a highly diluted fuel.

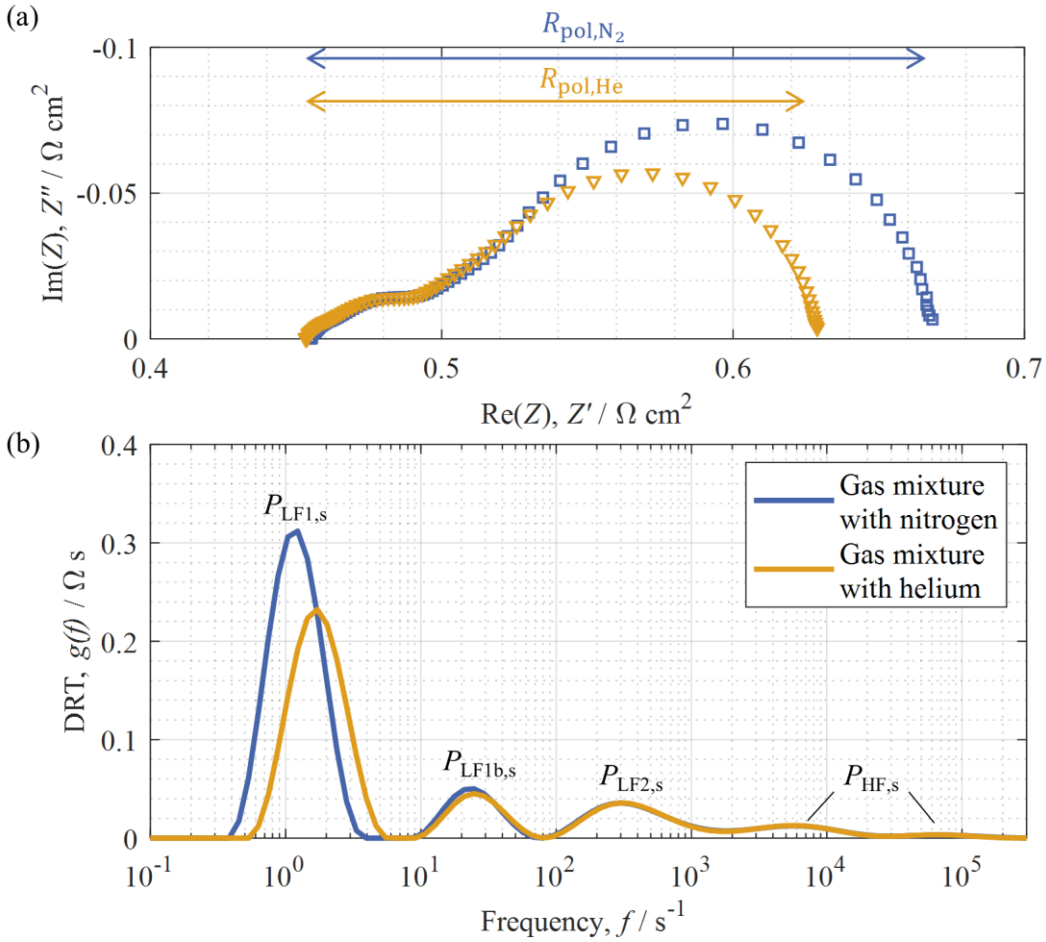

Figure 23 (a) Impedance spectra and (b) DRT of a symmetrical cell with Ni/GDC fuel electrodes with two ternary gas mixtures with the inert gases nitrogen and helium respectively (T = 852°C, gas composition: 10% H_2, 5% H_2O, 85% inert gas). Adapted from Ref. [37,38].

The effective gas diffusion geometry parameter G_{eff} shall be obtained from the difference of the polarization resistances indicated in Figure 23 (a). Based on the assumptions described above it is claimed that the difference of the polarization resistance between the gas mixture with nitrogen $R_{\mathrm{pol,N_2}}$ and helium $R_{\mathrm{pol,He}}$ equals the difference of the gas diffusion resistance in equation (54).

$$R_{\mathrm{pol,N_2}} - R_{\mathrm{pol,He}} \equiv R_{\mathrm{diff,N_2}} - R_{\mathrm{diff,He}} = \Delta R_{\mathrm{diff}} \tag{54}$$

The unknown geometry parameter G_{eff} can now be determined in equation (55).

$$G_{\mathrm{eff}} = \left(\frac{\tilde{R}T}{2F}\right)^2 \cdot \frac{1}{\Delta R_{\mathrm{diff}}} \cdot \frac{1}{P_{\mathrm{corr}}} \cdot \ldots$$
$$\left[\frac{1}{D_{\mathrm{H_2,(H_2O,N_2)}} \cdot p_{\mathrm{H_2}}} + \frac{1}{D_{\mathrm{H_2O,(H_2,N_2)}} \cdot p_{\mathrm{H_2O}}} - \frac{1}{D_{\mathrm{H_2,(H_2O,He)}} \cdot p_{\mathrm{H_2}}} - \frac{1}{D_{\mathrm{H_2O,(H_2,He)}} \cdot p_{\mathrm{H_2O}}}\right] \tag{55}$$

With the help of the effective geometry parameter G_{eff} it is now possible to predict the gas diffusion resistance for any set of operating conditions using equation (27). To evaluate reproducibility appropriate impedance measurements were conducted at different temperatures. The resulting differences in the polarization resistances $\Delta R_{\mathrm{pol,FE}}$ of the symmetrical cells as well as the subsequent determined geometry parameters are listed in Table 2. Also, the mean value and the standard deviation at each temperature are shown. The calculation of the resulting effective gas diffusion geometry parameter G_{eff} is conducted with halved resistances to account for one electrode.

Table 2 Difference of the polarization resistances $\Delta R_{\mathrm{pol,FE}}$ of the symmetrical cells with Ni/GDC fuel electrodes for sym-an1 and sym-an2 for a gas mixture of 10% H_2, 5% H_2O, balanced with N_2 and He respectively. The calculation of the resulting effective gas diffusion geometry parameter G_{eff} is conducted with halved resistances to account for one electrode.

sym-an1			sym-an2			Mean value	Standard deviation
T °C	$\Delta R_{\mathrm{pol,FE}}$ mΩ cm²	G_{eff} m^{-1}	T °C	$\Delta R_{\mathrm{pol,FE}}$ mΩ cm²	G_{eff} m^{-1}	$\bar{G}_{\mathrm{eff}}$ m^{-1}	σ m^{-1}
753	43	627.66	755	42	642.93	635.30	7.63
803	38	719.32	804	41	666.85	693.09	26.24
852	37	747.75	853	40	691.84	719.80	27.96
902	38	736.87	902	38	736.87	736.87	0

It should be noted that the observed deviations in G_{eff} are related to rather small variations of the measured polarization resistance (< 5 mΩ cm²). Furthermore, the resulting $R_{\mathrm{diff,FE}}$ is much smaller than the overall resistance of the cell and will become even smaller for realistic fuel mixtures without 85% of inert gases. As discussed above, the accuracy in determining G_{eff} is increasing with increasing operating temperatures. Thus, the values at 902 °C with

$G_{\mathrm{eff}} = 736.87$ m^{-1} are more reliable than those at much lower temperatures, where the activation polarization dominates the polarization resistance.

5.1.3 Determination of the Activation Polarization Resistance

With the objective of establishing a dc cell model, polarization contributions in the impedance spectra of the electrodes can be simplified by RQ-elements [205] and more complex approaches as transmission line models [57,199] can be avoided. To quantify the activation polarization resistance $R_{\mathrm{act,FE}}$ of the Ni/GDC fuel electrode, the low (P_{LF1} + P_{LF1b}) and middle frequency (P_{LF2}) processes including the gas diffusion are summed up to obtain $R_{\mathrm{pol,FE}}$. To account for one electrode the values from the CNLS-fit are divided by 2. Then the gas diffusion resistance $R_{\mathrm{diff,FE}}$ is calculated according to (27) and subtracted in equation (56).

$$R_{\mathrm{act,FE}} = R_{\mathrm{pol,FE}} - R_{\mathrm{diff,FE}} \tag{56}$$

It is now possible to quantify the activation resistance of the Ni/GDC fuel electrode $R_{\mathrm{act,FE}}$, which enables the further parameterization in order to develop a zero-dimensional cell model [104,125]. In comparison to a direct fitting of the spectra this approach provides a higher accuracy as G_{eff} is previously determined under ideal conditions enabling a precise calculation of $R_{\mathrm{diff,FE}}$ for technically relevant operating points.

5.1.4 Activation Energy Fuel Electrode

Figure 24 shows the resulting ASR values for activation processes of a single fuel electrode for a variation of temperature between 600 °C and 900 °C in steps of 50 °C with a gas mixture of 80% H_2 and 20% H_2O according to the spectra in Figure 21. The resistance of the fuel electrode´s activation indicates an Arrhenius behavior and therefore this approach is applied in order to determine the activation energy of the fuel electrode $E_{\mathrm{act,FE}}$. The latter can be extracted by the slope of fitting equation (57) to the measured data.

$$R_{\mathrm{act,FE}}(T) = B_{\mathrm{FE}} \cdot \exp\left(\frac{E_{\mathrm{act,FE}}}{\tilde{R}T}\right) \tag{57}$$

This results in an activation energy of the fuel electrode of $E_{\mathrm{act,FE}} = 90.54$ kJ mol^{-1} (0.94 eV) and a cell specific constant of $B_{\mathrm{FE}} = 2.9517 \cdot 10^{-6}$ Ω cm^2. Hagen et al. [120] found an activation energy of 46 kJ mol^{-1} for the Ni/GDC fuel electrode.

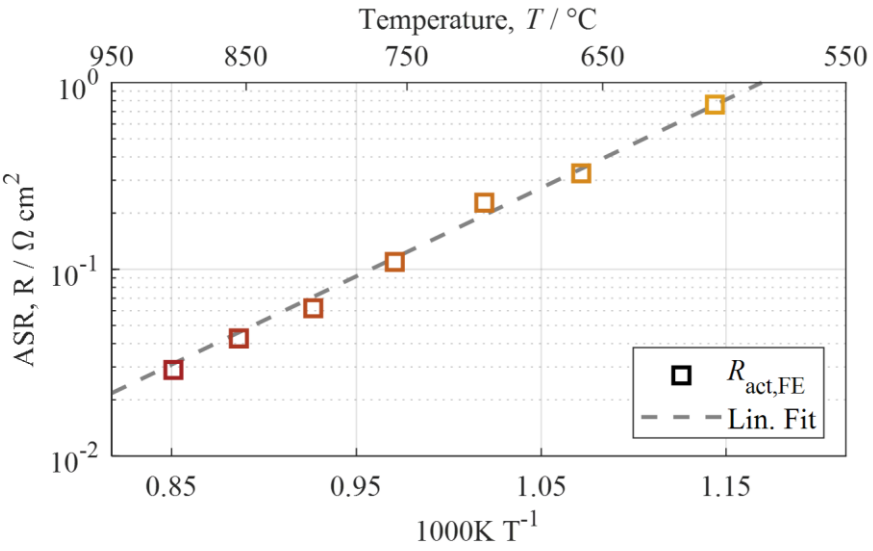

Figure 24 Arrhenius-Plot of a temperature variation between 600 °C and 900 °C in steps of 50 °C with a gas mixture of 80% H_2 and 20% H_2O, using the ASR values of a single fuel electrode. Formatted and taken from Ref. [38].

5.1.5 Exponent *a*

The determination of the exponent a in order to describe the hydrogen partial pressure dependency of the fuel electrode´s exchange current density follows the approach by Leonide et al. [104]. Thus, the exponent a is extracted by a variation of the hydrogen partial pressure with a fixed amount of steam by adding nitrogen as an inert component to the fuel gas mixture. Therefore, a variation of the hydrogen (80%, 40%, 20%, 10%) with a constant steam content of 20% and balanced with N_2, at $T = 754$ °C is shown in Figure 25 (a) for a symmetrical cell. After determining the activation resistance $R_{\mathrm{act,FE}}$ by subtracting the calculated gas diffusion resistance from the overlapping resistance it can now be plotted as a function of the hydrogen molar fraction in a double logarithmic scale in Figure 25 (c). According to Leonide et al. [104], the exponent a can now be identified by the negative value of the slope in Figure 25 (c) at 598 °C, 658 °C, 754 °C, 804 °C, 853 °C, and 902 °C.

On the contrary, in case of the Ni/YSZ fuel electrode the exponent a was not depending on temperature according to Ref. [104], whereas in case of the Ni/GDC fuel electrode a significant temperature dependency of the exponent a is observed.

The resulting exponents are listed in Table 3. The differences are ranging over an order of magnitude with the accentuation of two temperature dependent plateaus ranging from approx. 600 °C to 750 °C and from 800 °C to 900 °C respectively.

Table 3 Temperature dependency of the exponent a between 600 °C and 900 °C.

Temperature °C	a -
598	0.019
658	0.035
754	0.051
804	0.166
853	0.139
902	0.178

At comparatively low temperatures a mean value of $a(T = 600 - 750\,°C) = 0.035$ with a standard deviation of 0.013 and for higher temperatures a mean value of $a(T = 800 - 900\,°C) = 0.161$ with a standard deviation of 0.016 was determined. The temperature dependency can be explained by the assumptions related to the application of a generalized Butler-Volmer (BV) approach in [104]. The coupling of charge transfer and ionic transport in the active electrode volume is described by the overall activation resistance $R_{\mathrm{act,FE}}$, which is subsequently used to calculate the parameters of the BV-equation. This approach was suitable for the Ni/YSZ-fuel electrode as the electrochemical reaction is limited to the three phase boundaries and the ionic conductivity of the YSZ-matrix is not affected by the oxygen partial pressure. For the Ni/GDC fuel electrode the situation is different. Ionic and electronic conductivity of GDC are depending on the oxygen partial pressure at the fuel electrode, i.e. the fuel gas composition and furthermore the electrochemical activity of the GDC-surfaces will be affected by gas composition and temperature. These complex interactions presumably result in the observed temperature dependency of the exponent a. The unexpected discontinuous temperature dependency cannot be further explained on the given data basis. A more comprehensive investigation of this observed temperature dependency has to be carried out.

5.1.6 Exponent *b*

Subsequently, the determination of the exponent *b* in order to describe the steam partial pressure dependency of the fuel electrode´s exchange current density was carried out by a variation of the steam content with a fixed amount of hydrogen and balanced with nitrogen [104]. In Figure 25 (b) DRTs of the symmetrical cell are shown for a variation of steam with 30%, 20%, 12%, 8% and 4% with a constant amount of 60% H_2 and balanced with N_2 at $T = 755$ °C. The activation resistance $R_{\mathrm{act,FE}}$ is determined by equation (57). Similarly, impedance measurements under these conditions have been performed at 598 °C, 658 °C, 706 °C, 755 °C, 804 °C, 853 °C and 902 °C. The results are plotted in Figure 25 (d) and also reveal a temperature dependency of the exponent b.

In addition, the resulting exponents are shown in Figure 26 as a function of temperature and reveal a linear character.

This can be linearly fitted and described by equation (58).

$$b = \frac{0.0012}{\mathrm{K}} \cdot T - 0.9892 \tag{58}$$

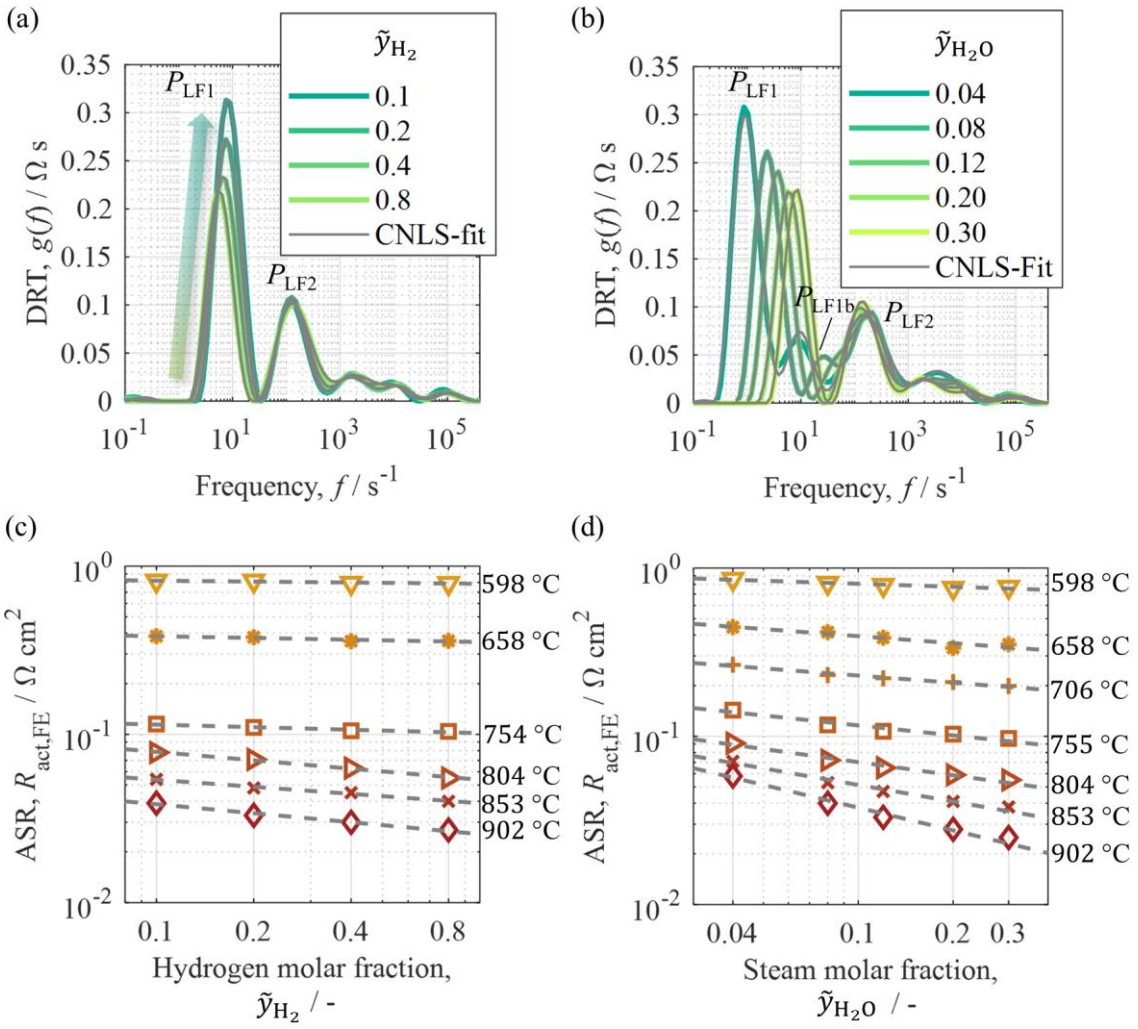

Figure 25 DRTs of a symmetrical cell with Ni/GDC fuel electrodes for a variation of (a) 80%, 40%, 20%, 10% H_2 and a constant steam content of 20% balanced with N_2, at $T = 754$ °C and (b) with a variation of 30%, 20%, 12%, 8% and 4% steam and 60% H_2 balanced with N_2, at $T = 755$ °C. (c) Determination of the exponent a, and (d) of the exponent b, at temperatures between 600 °C and 900 °C in steps of approx. 50 °C using the ASR-values of a single electrode. Adapted from Ref. [38].

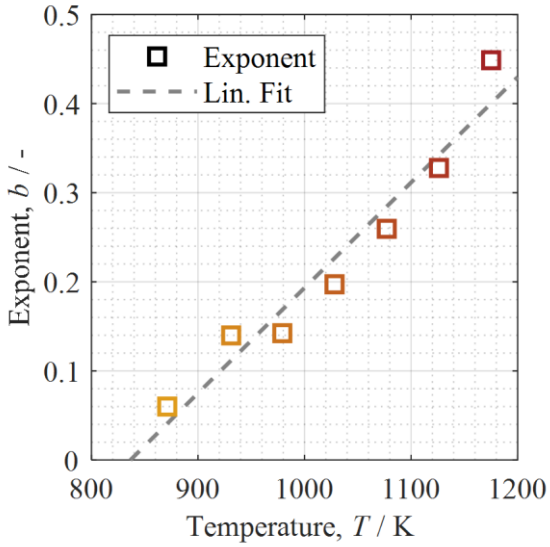

Figure 26 Temperature dependency of the exponent b with a linear fit ($R^2 = 0.9435$). Taken from Ref. [38].

5.1.7 Prefactor γ_{FE}

The prefactor γ_{FE} can be described by equation (59) including the cell specific constant B_{FE} [104].

$$\gamma_{FE} = \frac{\tilde{R}T}{2FB_{FE}} \cdot \left[\left(\frac{p_{H_2,FE}}{p_{ref}} \right)^a \left(\frac{p_{H_2O,FE}}{p_{ref}} \right)^b \right]^{-1} \tag{59}$$

The above-mentioned evaluation for the cell specific constant B_{FE} has been operated for a fuel gas mixture of 80% H_2 and 20% H_2O by varying temperature at atmospheric pressure. Therefore, these conditions are applied in order to determine the prefactor γ_{FE} [104]. In addition, a temperature dependency of the exponents a and b has been identified as shown above, which has to be included when calculating γ_{FE} in equation (60).

$$\gamma_{FE}(T) = 1.46 \cdot 10^5 (\mathrm{A\,m^{-2}K^{-1}}) \cdot \left[(0.8)^{a(T)} \cdot (0.2)^{b(T)} \right]^{-1} \cdot T \tag{60}$$

The fuel electrode is now fully parametrized except for the charge transfer coefficient.

5.1.8 Charge Transfer Coefficient

In contrast to the previously discussed parameters obtained from symmetrical cells at OCV, the charge transfer coefficient α_{EL} has to be determined from full cells in a polarized state. Considering a cell exhibiting a Ni/YSZ fuel electrode, different charge transfer coefficients have been found for SOEC and SOFC mode [104,125]. This shall also be examined for the full cell with a Ni/GDC fuel electrode.

In this study, the charge transfer coefficient of the LSCF air electrode α_{AE} could not be characterized adequately, because the polarization resistance of the air electrode is smaller compared to the fuel electrode and being overlapped by the latter in the spectrum. Therefore, the charge transfer coefficient of the air electrode is assumed to be equal to the one determined by Leonide et al. [104] as it is the same type of electrode and thus $\alpha_{\mathrm{AE}} = 0.65$ is assumed.

Regarding the SOEC mode a current density of -0.1 A cm^{-2}, -0.2 A cm^{-2}, -0.4 A cm^{-2} as well as -0.6 A cm^{-2} with a fuel gas mixture of 38% H_2 (balance H_2O) with synthetic air at the air electrode at $T = 745$ °C was set, which is shown in the DRT in Figure 27 (a). Further, for SOFC mode a fuel gas mixture of 80% H_2 (balance H_2O) with pure oxygen at the air electrode at $T = 750$ °C by varying the load starting from 0.05 A cm^{-2} up to 0.25 A cm^{-2} in steps of 0.05 A cm^{-2} was applied. Pure oxygen is used in order to minimize processes at the air electrode. The corresponding results are appearing in Figure 27 (b). Also, measurement artifacts have been omitted at frequencies larger than 10^4 Hz.

Here, the two main contributions in the lower and middle frequency range are summarized to R_{load} which is plotted for the two modes in Figure 28 (a) and (b) respectively. It can be described by a second-degree polynomial fit as a function of the current density j in equation (61).

$$R_{\mathrm{load}}(j) = \frac{\partial \eta_{\mathrm{load}}}{\partial j} = q_1 \cdot j^2 + q_2 \cdot j \cdot + q_3 \tag{61}$$

The corresponding coefficients q_1, q_2 and q_3 are listed in Table 4.

Table 4 Coefficients of the second-degree polynomial describing R_{load} as a function of the current density j.

Operating-mode	q_1	q_2	q_3
SOEC	0.0294	0.0344	0.1212
SOFC	-0.1057	0.0015	0.1138

The integration of equation (61) leads to an overpotential in equation (62). In order to obtain the activation overpotential at the fuel electrode, the overpotential for gas diffusion at the fuel electrode and activation at the air electrode is calculated and subtracted at the corresponding current density. In this case, the gas diffusion at the air electrode is neglected. Under OCV-conditions ($j = 0$) results $\eta_{\mathrm{act,FE}}(j = 0) = 0$ and therefore, q_4 levels zero.

$$\eta_{\mathrm{act,FE}}(j) = \frac{1}{3} \cdot q_1 \cdot j^3 + \frac{1}{2} \cdot q_2 \cdot j^2 + q_3 \cdot j + q_4 - \eta_{\mathrm{diff,FE}}(j) - \eta_{\mathrm{act,AE}}(j) \tag{62}$$

With the help of equation (62) the activation overpotential can now be calculated as a function of the current density j and is plotted in Figure 28 (c) and (d) for SOEC and SOFC mode respectively. These curves can be described with the Butler-Volmer equation and with the help of the Matlab^{tm}-solver fsolve the charge transfer coefficients can be extracted.

Regarding the SOEC mode a charge transfer coefficient of $\alpha_{\mathrm{FE,SOEC}} = 0.59$ and for SOFC mode $\alpha_{\mathrm{FE,SOFC}} = 0.76$ resulted.

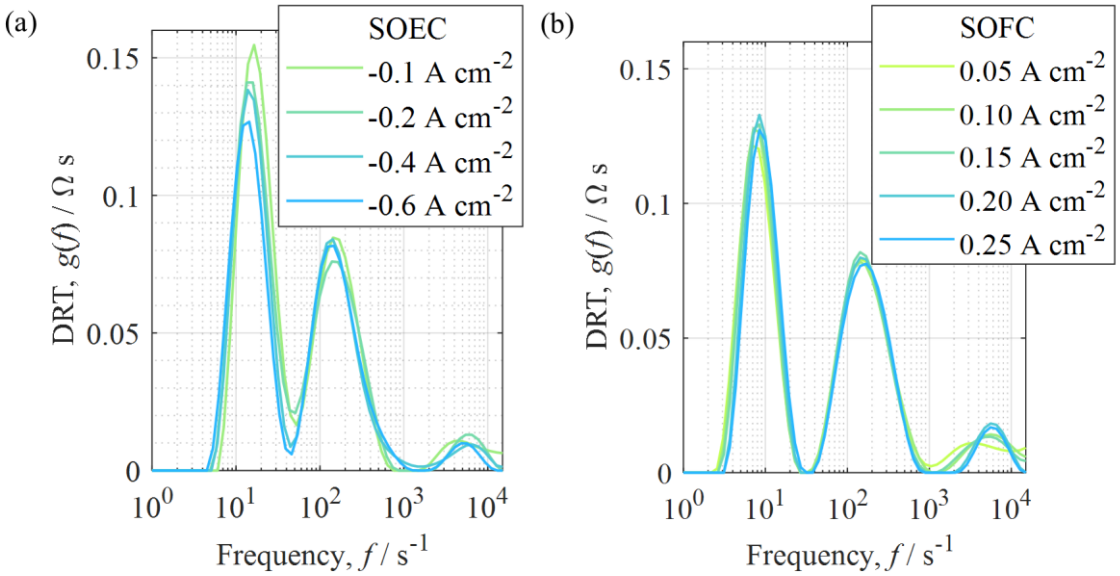

Figure 27 (a) DRT of the variation of the electrical load in SOEC mode with a fuel gas mixture of 38% H_2 (balance H_2O) with synthetic air at the air electrode at $T = 745$ °C and (b) DRT of a variation of the electrical load in SOFC mode with a fuel gas mixture of 80% H_2 (balance H_2O) with pure oxygen at the air electrode at $T = 750$ °C. Formatted and taken from Ref. [38].

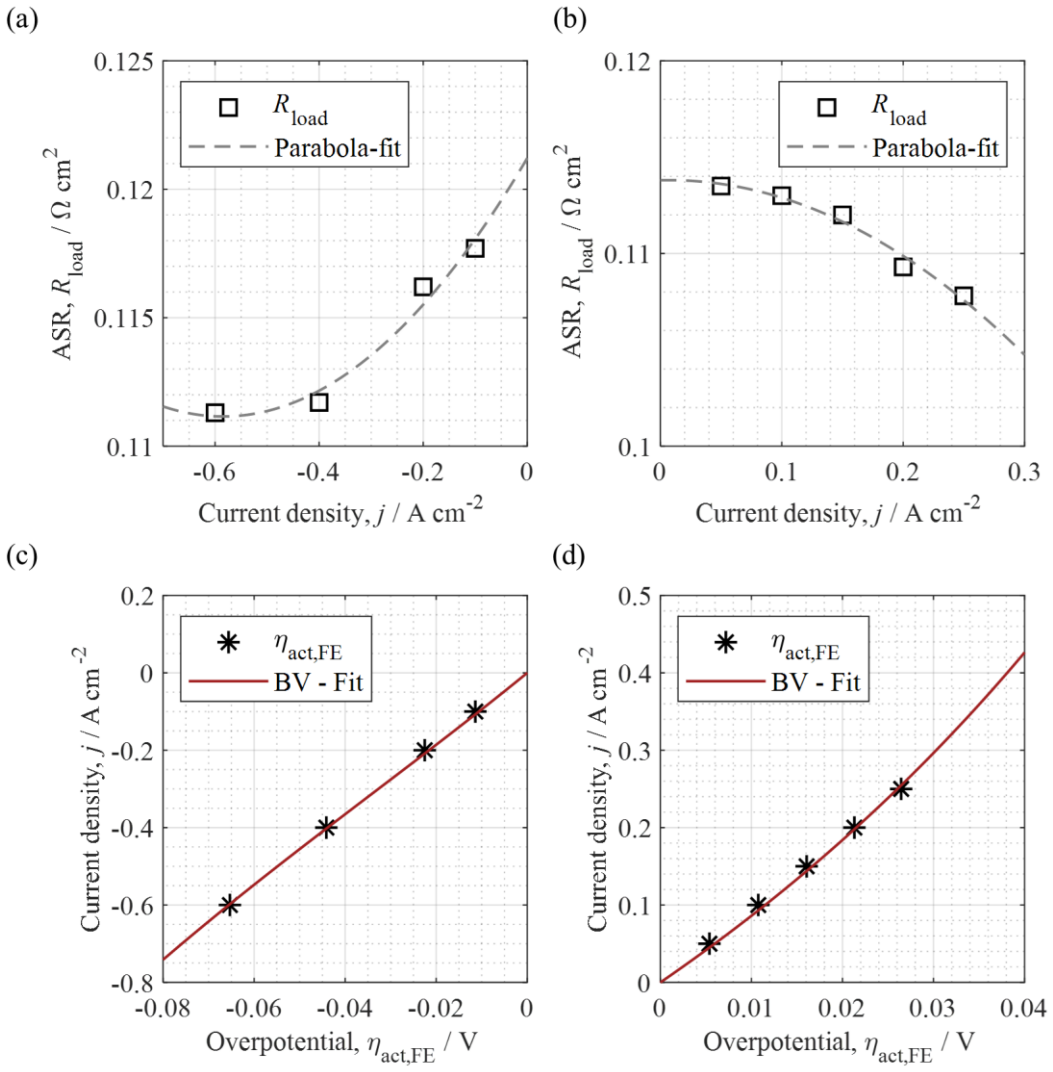

Figure 28 (a) Resistance $R_{load}(j)$ as a function of the current density in SOEC mode with a fuel gas mixture of 38% H_2 (balance H_2O) with synthetic air at the air electrode at $T = 745$ °C. (c) Determination of the charge transfer coefficient in SOEC mode. (b) Resistance $R_{load}(j)$ as a function of the current density in SOFC mode with a fuel gas mixture of 80% H_2 (balance H_2O) with pure oxygen at the air electrode at $T = 750$ °C. (d) Determination of the charge transfer coefficient in SOFC mode. Taken from Ref. [38].

5.1.9 Ohmic Losses

In order to quantify the ohmic losses the thermal behavior of the area specific ohmic resistance $R_{ohm}(T)$ is investigated for a full cell. For this purpose, a fuel gas mixture of 80% H_2 (balance H_2O) as well as synthetic air at the air electrode was set at temperatures of 600 °C, 651 °C, 700 °C, 750 °C, 800 °C, 850 °C, and 897 °C. The validation of the zero-dimensional model has also been examined with this full cell. Thus, the logarithm of temperature divided by the area specific ohmic resistance is plotted in Figure 29 corresponding to the

logarithm of the ionic conductivity times temperature as a function of temperature. By assuming a temperature independent activation energy of the ohmic losses it can be determined by the slope of the linear fit with the help of the Arrhenius equation for the area specific ohmic resistance (10). As can be seen in Figure 29, this cannot be sufficiently applied, because a slight deviation can be seen at temperatures higher than 800 °C and subsequently two sections of temperature are observed in order to describe the Arrhenius behavior. A non-linear description is therefore necessary in order to quantify the ohmic losses.

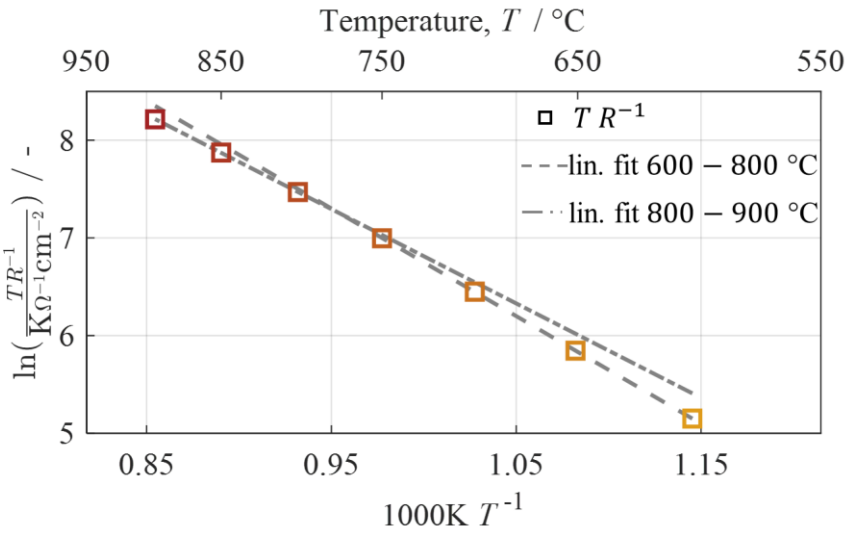

Figure 29 Plot of the temperature divided by the area specific ohmic resistance R_{ohm} of a full cell as a function of temperature with separate linear fits in two sections of temperature with (i) 600 − 800 °C and (ii) 800 − 900 °C with a fuel gas mixture of 80% H_2 (balance H_2O) as well as synthetic air at the air electrode. Formatted and taken from Ref. [38].

Thus, considering that the ohmic losses are dominating in an electrolyte-supported compared to a fuel electrode-supported cell and combined with less doping of the 3YSZ compared to 8YSZ, the temperature dependency of the ohmic activation energy cannot be neglected. Therefore, the ohmic resistance shall be described by a parabola-fit. At first, equation (10) is transferred dimensionless in equation (63) by Ω cm² in order to take the logarithm of it. Subsequently, it shall be equaled with $y = k_1x^2 + k_2x + k_3$ in equation (64), where the variable x denotes $x = \frac{1000\mathrm{K}}{T}$ with K denoting the unit Kelvin.

$$y = \ln\left(\frac{R_{\mathrm{ohm}}(T)}{\Omega\,\mathrm{cm}^2}\right) = \ln\left(\frac{T}{B_{\mathrm{ohm}}}\cdot\frac{1}{\Omega\,\mathrm{cm}^2}\right) + \frac{E_{\mathrm{act,ohm}}}{\tilde{R}T} \tag{63}$$

$$\ln\left(\frac{1000\mathrm{K}}{B_{\mathrm{ohm}}}\cdot\frac{1}{\Omega\,\mathrm{cm}^2}\cdot\frac{1}{\mathrm{x}}\right) + \frac{E_{\mathrm{act,ohm}}}{1000\mathrm{K}\cdot\tilde{R}}\cdot x = k_1x^2 + k_2x + k_3 \tag{64}$$

It is assumed that the original approach by extracting the ohmic activation energy $E_{\mathrm{act,ohm}}$ from the linear slope can be transferred to the parabola likewise in order to extract the ohmic activa-

tion energy from the slope of the parabola. Therefore, equation (64) is derived by x and solved for $E_{\mathrm{act,ohm}}$ in equation (65). The latter can now be described as a function of temperature.

$$E_{\mathrm{act,ohm}} = 1000\mathrm{K} \cdot \tilde{R} \left(2k_1 x + k_2 + \frac{1}{x} \right) \tag{65}$$

Subsequently, the cell specific parameter B_{ohm} can be obtained by solving equation (64) to equation (66).

$$B_{\mathrm{ohm}} = \frac{1000\mathrm{K}}{x} \frac{1}{\Omega\,\mathrm{cm}^2} \cdot \exp\left(-\left(k_1 x^2 + k_2 x + k_3 - \frac{E_{\mathrm{act,ohm}}}{1000\mathrm{K} \cdot \tilde{R}} \cdot x \right) \right) \tag{66}$$

Finally, the parabola fit is shown in Figure 30 with a sufficient agreement to the ohmic resistance.

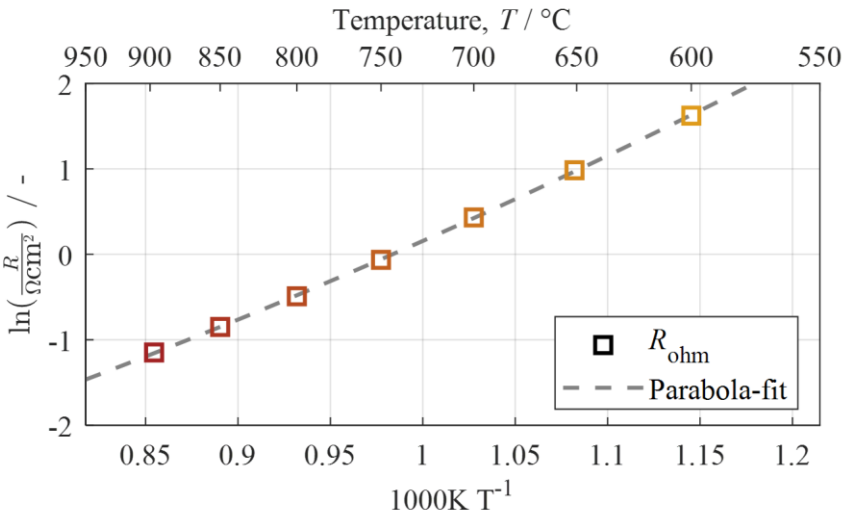

Figure 30 Arrhenius-plot of the area specific ohmic resistance R_{ohm} for a temperature variation of 600 °C, 651 °C, 700 °C, 750 °C, 800 °C, 850 °C, and 897 °C with a second-degree polynomial fit for a fuel gas mixture of 80% H_2 (balance H_2O) and synthetic air at the air electrode. Formatted and taken from Ref. [38].

By applying the introduced method, the polynomial coefficients can be obtained and are listed in Table 5.

Table 5 Polynomial coefficients for an active area of 1 cm² in order to describe the ohmic resistance in the Arrhenius plot in Figure 30.

Experimental full cell	k_1	k_2	k_3
	3.8374	1.9162	−5.5970

5.1.10 Model Parameters

The relevant parameters in order to model the current-voltage behavior in a zero-dimensional approach are listed in Table 6. Apart from the adaptions described above, no further changes in the model and its parameterization [104] were necessary. Furthermore, the parameters have been varied independently in order to investigate their sensitivity towards the model. The experimentally obtained voltage at a current density of 0.5 A cm^{-2} with a gas mixture of 65% H_2 (balanced with H_2O) at a temperature of 850 °C was chosen as a reference. Therefore, the last column in Table 6 indicates the deviation from the simulated voltage in relation to the measured voltage, when the parameter is varied by $\pm$ 20 % in its value and thus showing the sensitivity towards the model.

Table 6 Model parameters of the zero-dimensional cell model [104] adapted to a solid oxide cell with Ni/GDC fuel electrode, 3YSZ electrolyte and LSCF air electrode. ($T_1 = 600 - 750$ °C; $T_2 = 800 - 900$ °C)

Parameter	Unit	Value	Sensitivity $+20\,\%, -20\,\%$
$E_{\mathrm{act,ohm}}$	J mol^{-1}	$1000\mathrm{K} \cdot \tilde{R}\left(2k_1 x + k_2 + \frac{1}{x}\right)$ with $x = \frac{1000\mathrm{K}}{T}$	-
B_{ohm}	K $(\Omega\ m^2)^{-1}$	$\frac{1000\mathrm{K}}{x}\frac{10^4}{\Omega\ \mathrm{m}^2} \cdot \exp\left(-\left(k_1 x^2 + k_2 x + k_3 - \frac{E_{\mathrm{act,ohm}}}{1000\mathrm{K} \cdot \tilde{R}} \cdot x\right)\right)$	$+4.4\,\%, -8\,\%$
k_1	-	3.8374	-
k_2	-	1.9162	-
k_3	-	−5.5970	-
$E_{\mathrm{act,FE}}$	kJ mol^{-1}	90.54	$-9.3\,\%, +1.6\,\%$
B_{FE}	$\Omega\ m^2$	$2.95 \cdot 10^{-10}$	$-1\,\%, 0\,\%$
$a(T_1)$	-	0.035	-
$a(T_2)$	-	0.161	$-0.6\,\%, -0.6\,\%$
$b(T)$	-	$\frac{0.0012}{\mathrm{K}} \cdot T - 0.9892$	$-0.5\,\%, -0.7\,\%$
$\gamma_{\mathrm{FE}}(T)$	A m^{-2}	$1.46 \cdot 10^5 (\mathrm{A\ m^{-2} K^{-1}}) \cdot \left[0.8^{a(T)} \cdot 0.2^{b(T)}\right]^{-1} \cdot T$	-
$\alpha_{\mathrm{FE,SOEC}}$	-	0.59	-
$\alpha_{\mathrm{FE,SOFC}}$	-	0.76	$-0.4\,\%, -0.7\,\%$
G_{eff}	m^{-1}	736.87	$-0.5\,\%, -0.6\,\%$
$E_{\mathrm{act,AE}}$	kJ mol^{-1}	144.54	$-1.7\,\%, -0.5\,\%$
B_{AE}	$\Omega\ m^2$	$1.5185 \cdot 10^{-14}$	$-0.6\,\%, -0.6\,\%$
m	-	0.42	$-0.6\,\%, -0.6\,\%$
$\gamma_{\mathrm{AE}}(T)$	A m^{-2}	$5.47 \cdot 10^9 (\mathrm{A\ m^{-2} K^{-1}}) \cdot T$	-
α_{AE}	-	0.65 [104]	$-0.6\,\%, -0.6\,\%$
Ψ_{AE}	-	0.048	$-0.6\,\%, -0.6\,\%$

It becomes obvious, that the model is mostly sensitive towards the cell specific constant regarding the ohmic losses B_{ohm}. The ohmic losses in this particular case with the empirical determination presented above are independent of the ohmic activation energy. Another parameter with high impact represents the activation energy of the fuel electrode $E_{\mathrm{act,FE}}$. All other parameters only show a rather small influence when varied by $\pm$ 20 %.

5.1.11 Model Validation

The cell voltage can now be modeled with equation (8) as all of the unknown parameters are determined. The model covers operating temperatures from 600 °C to 900 °C with arbitrary fuel mixtures of hydrogen and steam in a cell voltage range from 600 to 1400 mV. To obtain an excellent agreement with measured CV-characteristics the temperature increase due to self-heating of the cell has to be considered in the model. This was realized by using the cell temperature measured by a thermocouple approx. 2 mm above the cell surface. Furthermore, the measured open-circuit voltage is used in order to correct minor leakages below 2% in the test bench. Exemplary, a validation is shown for a fuel gas mixture of 65% H_2 in Figure 31 (a) and 35% H_2 in (b) (balanced with H_2O) and synthetic air at the air electrode.

The developed zero-dimensional cell model represents the measured current-voltage behavior in excellent agreement with a deviation ≤ 3 % for both SOFC and SOEC mode. The remaining deviation between calculated and measured current-voltage curves is most probably caused by the difference between the internal cell temperature (electrolyte temperature) and the measured temperature [259].

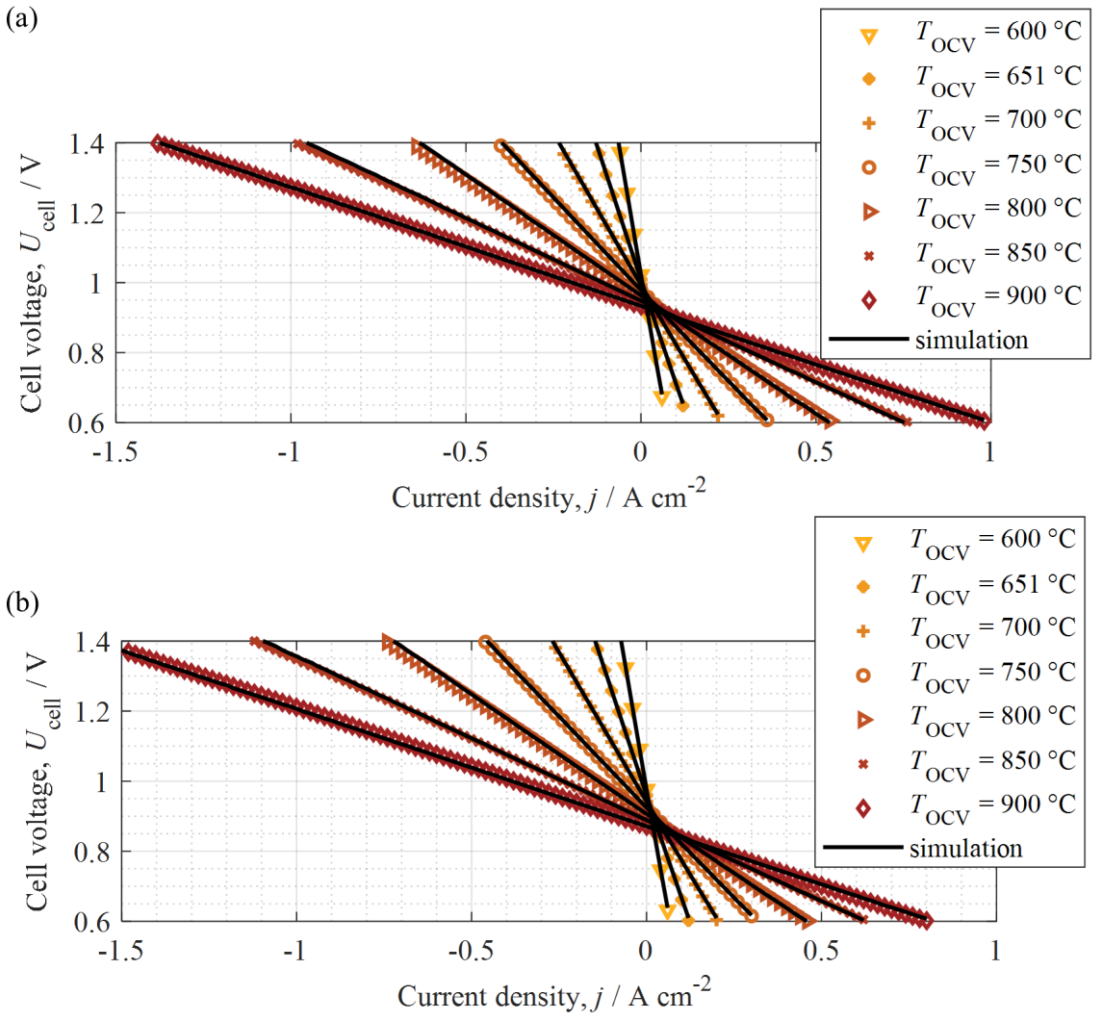

Figure 31 Variation of temperature between 600 °C and 900 °C with measured as well as simulated (continuous line) current-voltage characteristics for SOEC and SOFC mode with a fuel gas mixture of 65% H_2 (a) and of 35% H_2 (b) balanced with H_2O and synthetic air as the oxidant. Formatted and taken from Ref. [38].

It is now possible to quantify the individual loss contributions (Figure 32). Regarding the investigated ESC the ohmic losses are dominating the cell performance as expected. An about one order of magnitude smaller overvoltage has to be attributed to the activation losses at the fuel electrode. The fuel and air electrodes gas diffusion losses as well as the air electrode activation losses (testing with synthetic air) are in the range of a few mV only and thus can almost be neglected. Gas diffusion losses in the air electrode can only be analyzed at very low oxygen partial pressures in the applied setup. It should be noted that this can change drastically if the cell is contacted by a thin contact layer in a stack [260].

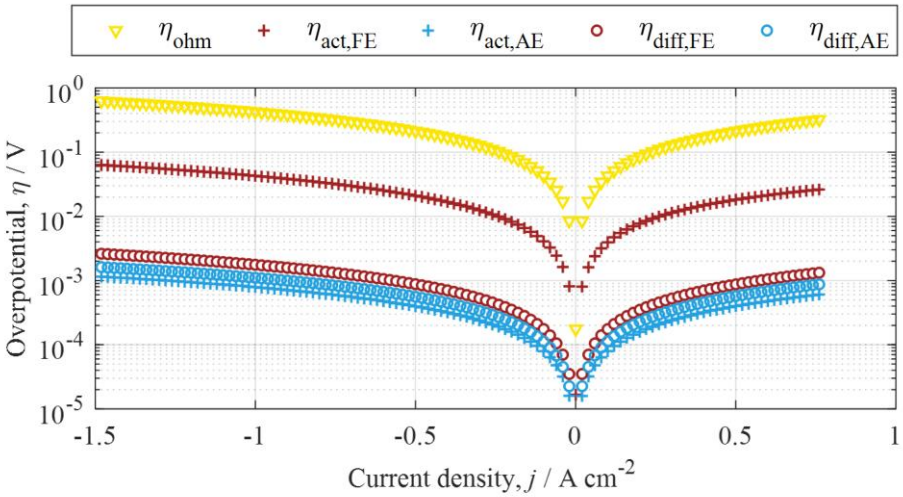

Figure 32 Absolute values of the ohmic η_{ohm}, activation $\eta_{act,FE/AE}$ as well as gas diffusion losses $\eta_{diff,FE/AE}$ as a function of the current density j in SOEC and SOFC mode with a fuel gas mixture of 65% H_2 (balanced with H_2O) and synthetic air at the air electrode with $T_{OCV} = 850$ °C. Taken from Ref. [38].

5.2 Ideal Contacting H_2/H_2O vs. CO/CO_2[2]

This chapter focusses on fuel gas mixtures of CO/CO_2 and the related processes at the Ni/GDC fuel electrode. Fuel electrodes exhibiting a Ni/GDC fuel electrode reportedly show an overlap of electrochemical processes and gas diffusion in the spectra [56,79,82,89,121]. In a previous study the operation with CO/CO_2 fuel gas mixtures resulted in a shift of the gas diffusion towards lower frequencies in the spectra [261]. Figure 33 shows a DRT with a temperature variation between $T = 750$ °C and $T = 900$ °C of a symmetrical cell with Ni/GDC fuel electrodes with 50% CO (balance CO_2). All peaks in the DRT indicate a thermally activated behavior. Thus, none of the peaks can solely be related to gas diffusion, which shows a comparatively low dependence on temperature ($T^{0.5}$). In the spectra, the expected contribution of the CO/CO_2 gas diffusion process is not clearly visible, which suggests that the thermally activated electrochemical process at the fuel electrode overlaps with the gas diffusion process. This overlap of several processes needs to be deconvoluted with the method described in chapter 5.1.2 and 5.1.3 so that the activation and gas diffusion polarization processes can be quantified.

In the impedance spectra, quantifying polarization contributions with rather complex transmission line models [56,57,199] shall be avoided and thus, they are simply quantified by RQ-Elements [38,205]. The values of the CNLS-fit are divided by two accounting for one electrode. Thus, by subtracting the simulated gas diffusion resistance [43] from the measured overall

[2] Parts of this chapter have been published in C. Grosselindemann et al., *Fuel Cells*, **23**, 442-453 (2023) [128].

polarization resistance, the activation polarization can be quantified [38]. The subsequent investigation of parameter dependencies is shown in the following.

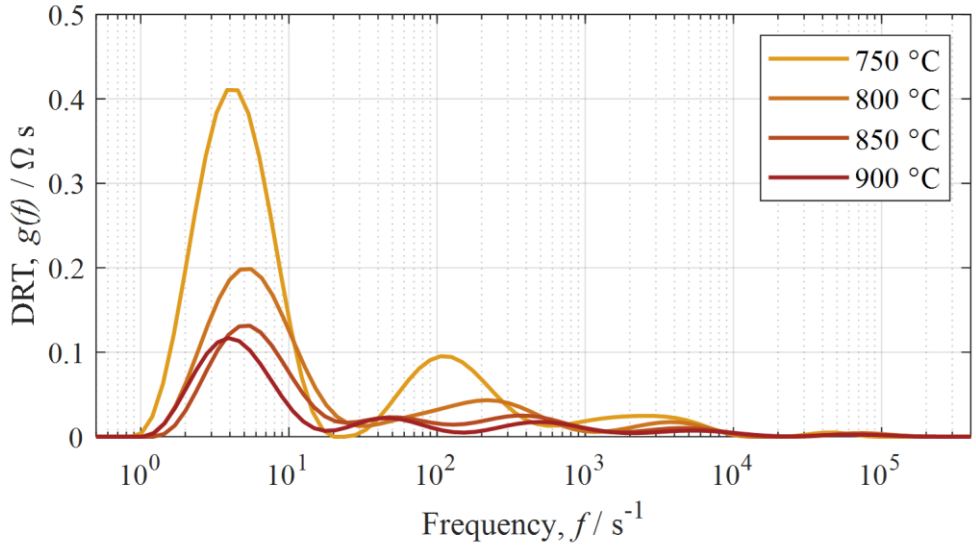

Figure 33 DRT with a variation of temperature of a symmetrical cell with Ni/GDC fuel electrodes with 50% CO (balance CO_2) between $T = 750$ °C and $T = 900$ °C. Graphic formatted and taken from Ref. [128].

5.2.1 Activation Energy Fuel Electrode

The area specific resistance (ASR) values of the activation $R_{\mathrm{act,FE}}$ are plotted as a function of temperature in Figure 34. A temperature range between 650 °C and 900 °C in steps of 50 °C for a gas composition with 40% CO (balance CO_2, triangle symbol) is shown. An Arrhenius behavior of the fuel electrode´s activation resistance can be observed. Therefore, the activation energy can be determined by the slope of the linear fit. An activation energy of $E_{\mathrm{act,FE,CO/CO_2}} = 111.51$ kJ mol^{-1} (1.16 eV) was found with a cell specific constant $B_{\mathrm{FE,CO/CO_2}} = 3.0295 \cdot 10^{-7}$ Ω cm^2. For comparison the values from the operation in H_2/H_2O mode between 600 °C and 900 °C in steps of 50 °C are also presented in Figure 34 with 80% H_2 (balance H_2O, square symbol). For the operation in H_2/H_2O an activation energy of $E_{\mathrm{act,FE,H_2/H_2O}} = 90.54$ kJ mol^{-1} (0.94 eV) and a cell specific constant of $B_{\mathrm{FE,H_2/H_2O}} = 2.9517 \cdot 10^{-6}$ Ω cm^2 was extracted [38]. In the work by Unachukwu et al. [262] an activation energy of 99 ± 2 kJ mol^{-1} was found and correlated with the ad-/desorption processes as well as charge transfer on the fuel electrode in overlap with the surface exchange on the oxygen electrode.

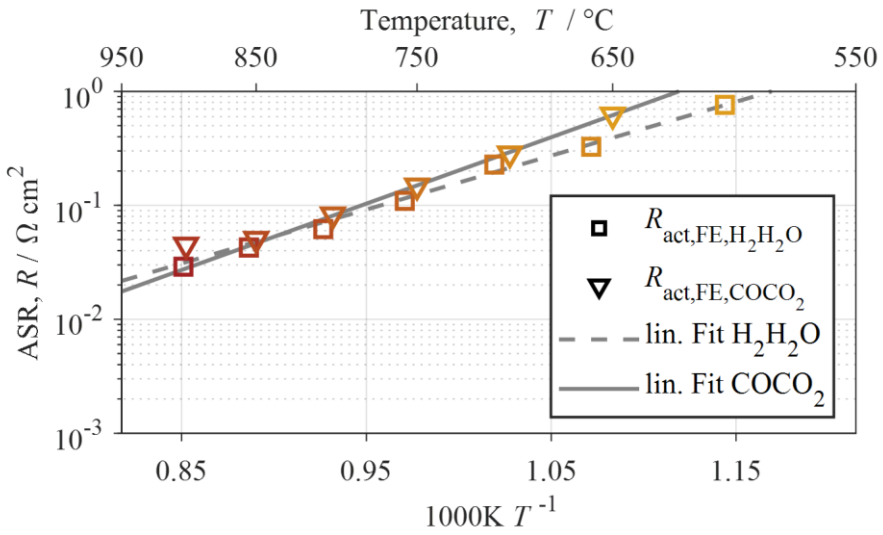

Figure 34 Arrhenius-plot of a temperature variation between 650 °C and 900 °C in steps of 50 °C for a gas composition with 40% CO (balance CO_2, triangle symbol) and between 600 °C and 900 °C for 80% H_2 (balance H_2O, square symbol) [38], using the ASR values of a single electrode. Graphic formatted and taken from Ref. [128].

5.2.2 Exponents *c* and *d*

The partial pressure dependency of the fuel electrode´s exchange current density towards CO and CO_2 can be described with the exponents c and d. These are determined similarly to Leonide et al. [104,125,136,205] by varying one of the fuel components individually by keeping the other species on a constant level and balancing with the inert component N_2. Figure 35 shows the DRTs of a symmetrical cell with a Ni/GDC fuel electrode for a variation of (a) the carbon monoxide molar fraction of 10%, 20%, 30%, 40%, and 50% CO, with a constant carbon dioxide content of 20% CO_2 and balanced with N_2, at $T = 850$ °C and (b) a variation of the carbon dioxide content of 20%, 30%, 40%, 50% and 60% CO_2 with a constant CO of 40% and balanced with N_2, at $T = 850$ °C.

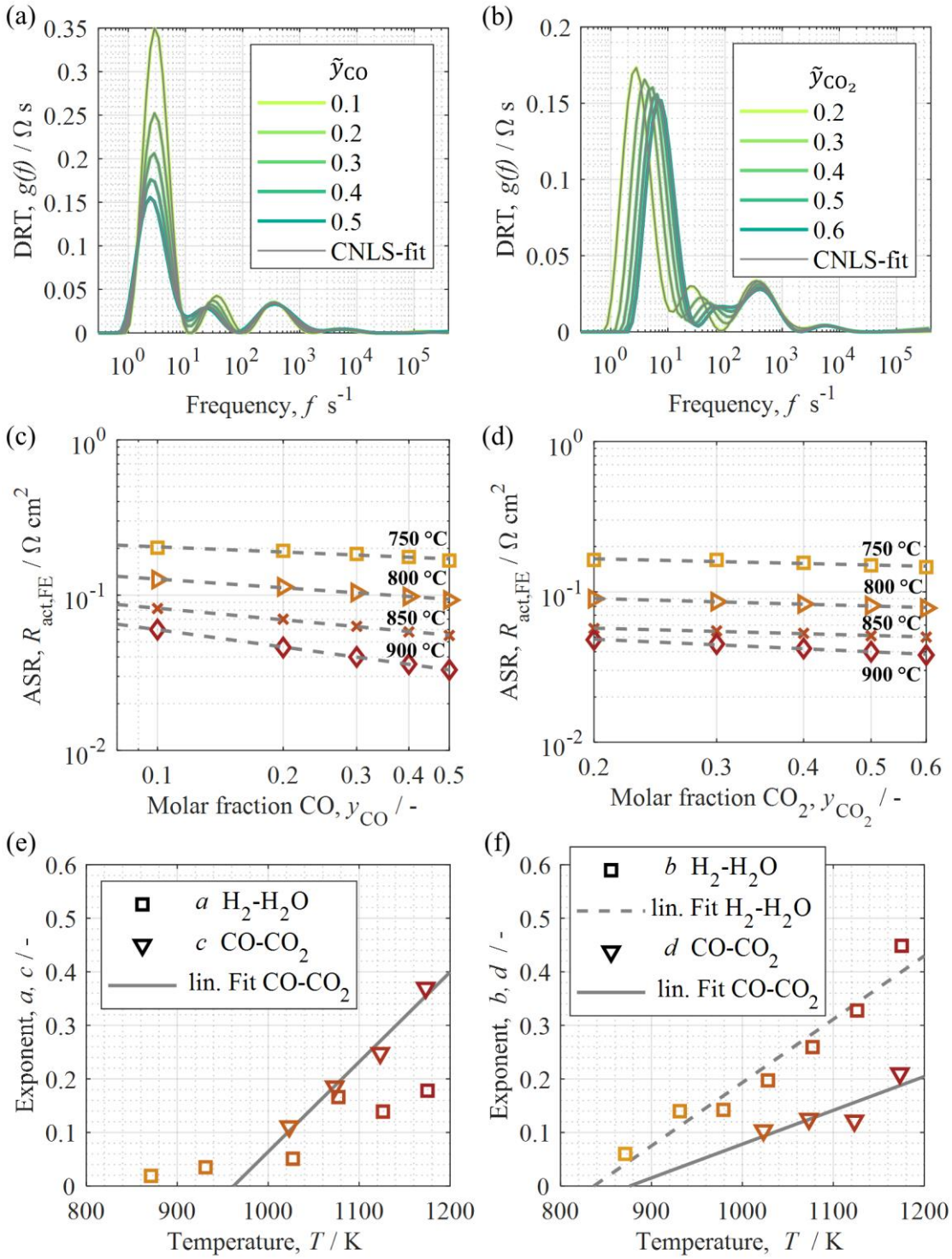

Figure 35 DRTs of a symmetrical cell with Ni/GDC fuel electrodes for a variation of (a) carbon monoxide content of 10%, 20%, 30%, 40%, and 50%, with a constant amount of carbon dioxide of 20% and balanced with N_2, at $T = 850$ °C and (b) a variation of the carbon dioxide partial content of 20%, 30%, 40%, 50% and 60% with a constant amount of CO of 40% and balanced with N_2, at $T = 850$ °C. (c) Determination of the exponent c, and (d) of the exponent

d, at temperatures between 750 °C and 900 °C using the ASR-values of a single electrode. (e) Temperature dependency of the exponent c and (f) d for operation with CO/CO_2 and H_2/H_2O. Graphic formatted and taken from Ref. [128].

Processes at relaxation frequencies exceeding 100 Hz are hardly affected by the fuel gas composition. The corresponding ASR values from a single electrode resulting from the CNLS-fit are plotted as a function of the (c) CO partial pressure and (d) CO_2 partial pressure for temperatures between 750 °C and 900 °C in Figure 35. The exponents c and d respectively, can then be obtained by extracting the negative value of the slope of the linear fit. In agreement with H_2/H_2O atmospheres [38] a temperature dependency of the exponents can be observed in Figure 35 (e) and (f) for CO/CO_2 mode as well. By a linear approximation the equations (67) and (68) describe the temperature dependency of $c(T)$ and $d(T)$, respectively with K as the unit Kelvin.

$$c(T) = \frac{0.0017}{\mathrm{K}} \cdot T - 1.6136 \tag{67}$$

$$d(T) = \frac{0.00063}{\mathrm{K}} \cdot T - 0.5527 \tag{68}$$

5.2.3 Ohmic Losses

The area specific ohmic resistance $R_{\mathrm{ohm}}(T)$ needs to be analyzed for a full cell by the thermal behavior. Similar to chapter 5.1.9, the ohmic activation energy and cell specific constant was examined. The equations with polynomial coefficients are displayed in Table A 5 in the Appendix. Compared to chapter 5.1.9, different polynomial coefficients were found. The cells tested for H_2/H_2O and CO/CO_2 originate from the same type and were tested in the same test bench. Nevertheless, small deviations in the electrolyte thickness as well as operating temperature might result in a rather small discrepancy of the ohmic losses.

5.2.4 Model Parameters

Table 7 represents selective model parameters related to the fuel electrode of the ESC with Ni/GDC fuel electrode investigated here and an ASC with Ni/YSZ fuel electrode in H_2/H_2O and CO/CO_2 mode respectively [36,38,62,136].

Furthermore, the full parameter set required for modeling the current-voltage behavior in a zero-dimensional dc performance model for CO/CO_2 fuel gas mixtures is listed in the Appendix in Table A 5. No changes to the model were necessary compared to the methods applied for the parametrization in H_2/H_2O operation [38]. With respect to parameters not shown here (e.g. charge transfer coefficients: $\alpha_{\mathrm{FE,SOEC}} = 0.67$ and $\alpha_{\mathrm{FE,SOFC}} = 0.42$), no significant changes were found in comparison to chapter 5.1.8 [38]. Parameters for the ASC in H_2/H_2O and CO/CO_2 mode were determined in Ref. [36,62,104,125,136].

Table 7. Selective model parameters of the zero-dimensional cell model for the fuel electrode of the ESC with Ni/GDC fuel electrode and the ASC with Ni/YSZ fuel electrode in H_2/H_2O and CO/CO_2.

Parameter	Unit	ESC with Ni/GDC	ASC with Ni/YSZ
$E_{\mathrm{act,FE,H_2/H_2O}}$	kJ mol^{-1}	90.54 [38]	105.04 [104]
$E_{\mathrm{act,FE,CO/CO_2}}$	kJ mol^{-1}	111.51	118.64 [136]
$a(T = 600 - 750\ °C)$	-	0.035 [38]	−0.10 [104]
$a(T = 800 - 900\ °C)$	-	0.161 [38]	−0.10 [104]
$b(T)$	-	$\frac{0.0012}{\mathrm{K}} \cdot T - 0.9892$ [38]	0.33 [104]
$c(T)$	-	$\frac{0.0017}{\mathrm{K}} \cdot T - 1.6136$	−0.058 [136]
$d(T)$	-	$\frac{0.00063}{\mathrm{K}} \cdot T - 0.5527$	0.25 [136]

5.2.5 Model Validation

In Figure 36 measured and simulated (continuous line) IV-curves are shown in a temperature range between $T = 700$ °C and $T = 900$ °C with different gas compositions of 30% CO (a) and 50% CO (b) (balance CO_2) with synthetic air at the air electrode. A voltage range of 600 to 1200 mV is covered. The model represents an excellent agreement with the experimentally measured IV-curves (deviation of less than 4%). Considering that the actual model is isothermal and does not consider self heating effects and the relevant parameters are obtained at OCV, the slightly higher / lower predicted voltages in the SOEC- and SOFC-mode respectively are to be expected [263].

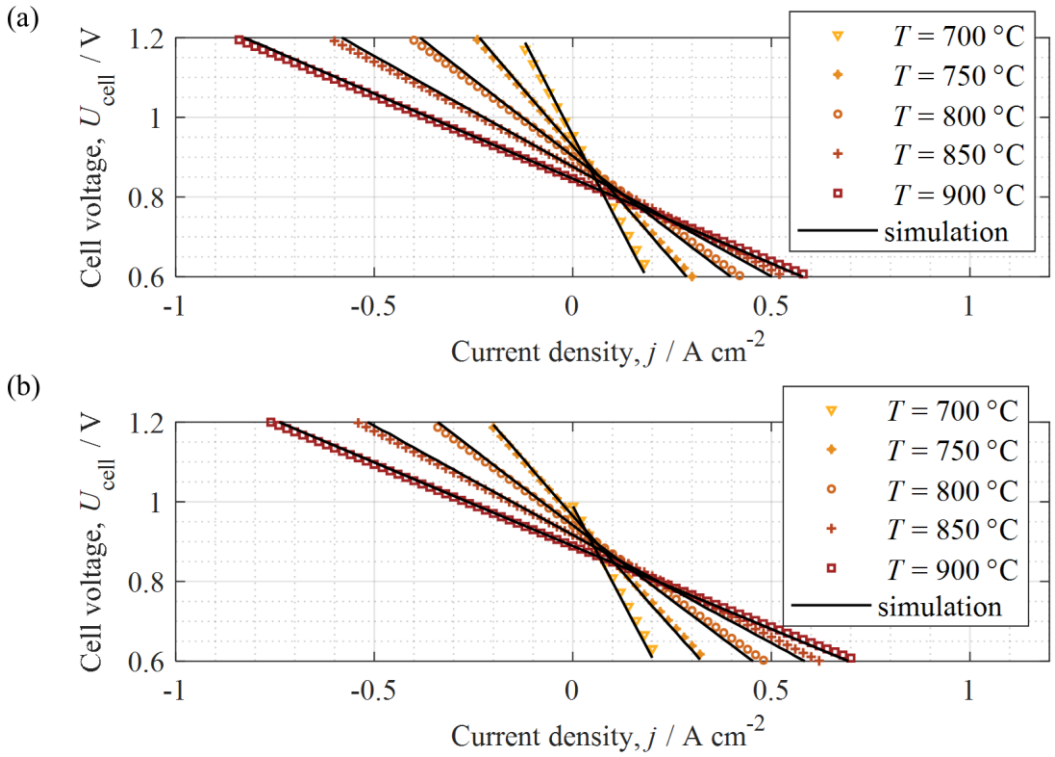

Figure 36 Variation of temperature between $T = 700$ °C and $T = 900$ °C with experimental and simulated (continuous line) IV-curves in SOEC as well as SOFC mode with a fuel gas mixture of (a) 30% CO and (b) 50% CO (balance CO_2) with synthetic air at the air electrode. Graphic formatted and taken from Ref. [128].

5.2.6 Simulation Studies

This approach enables a differentiated investigation of the individual loss mechanisms [122,125,136]. The simulated absolute values of the ohmic losses η_{ohm}, activation $\eta_{\mathrm{act,FE}}$ as well as gas diffusion losses $\eta_{\mathrm{diff,FE}}$ are shown in Figure 37 as a function of the current density for the operation with a fuel mixture of 50% CO (balance CO_2) and synthetic air at the air electrode at $T = 850$ °C. The ohmic losses remain dominant as expected for an electrolyte-supported cell. The largest relative difference between CO/CO_2 and H_2/H_2O mode can be observed for the gas diffusion losses, since CO and CO_2 molecules exhibit a comparably lower gas diffusion coefficient. In any case, as the electrode thickness of the investigated ESCs is rather low, the overall gas diffusion losses are below ohmic and activation losses, which might be different for fuel electrode supported cells. Visible differences in the ohmic losses were already discussed above.

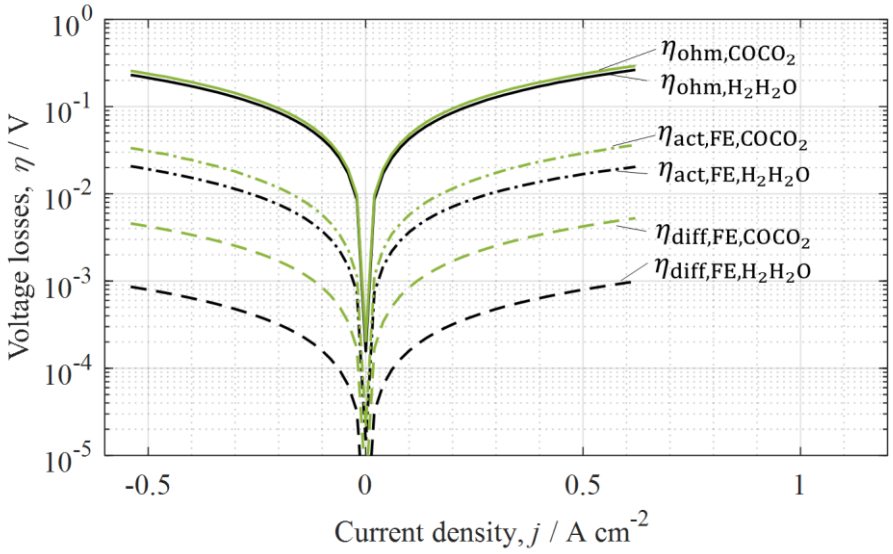

Figure 37 Simulated absolute values of the ohmic η_{ohm}, gas diffusion $\eta_{\mathrm{diff,FE}}$ and activation overpotentials $\eta_{\mathrm{act,FE}}$ in electrolyzer and fuel cell mode for the operation with 50% CO (balance CO_2) as well as 50% H_2 (balance H_2O) with synthetic air at the air electrode at $T = 850$ °C. Graphic formatted and taken from Ref. [128].

The deviations between the two atmospheres become more obvious by subtracting the losses for activation and gas diffusion losses for H_2/H_2O from the corresponding losses for CO/CO_2 operation in Figure 38.

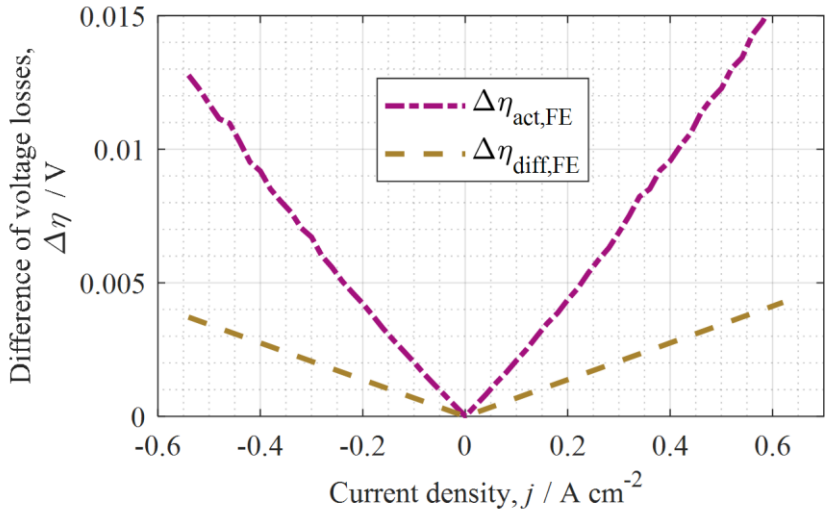

Figure 38 Difference of the simulated absolute values of gas diffusion $\Delta\eta_{\mathrm{diff,FE}}$ and activation overpotentials $\Delta\eta_{\mathrm{act,FE}}$ in electrolyzer and fuel cell mode for the operation with 50% CO (balance CO_2) as well as 50% H_2 (balance H_2O) with synthetic air at the air electrode at $T = 850$ °C. Graphic formatted and taken from Ref. [128].

In Figure 39 simulated IV-curves of an ASC with Ni/YSZ fuel electrode [136] and the ESC with Ni/GDC fuel electrode investigated in this study are compared for 40% H_2 (balance H_2O, dashed line) and 40% CO (balance CO_2) at $T = 800$ °C. However, there is only a minor difference between H_2/H_2O and CO/CO_2 fuel for the ESC with Ni/GDC fuel electrode, a larger impact can be observed for the ASC with Ni/YSZ fuel electrode. Especially for higher current densities a significantly higher performance loss is seen for the CO/CO_2 fuel. This is related to higher gas diffusion losses as a result of the 1 mm thick porous fuel electrode substrate of the fuel electrode supported cell [136]. In case of CO_2-electrolysis the gas diffusion results in a gradient in CO-ratio towards the anode functional layer. At -1.5 A cm^{-2} and 1.38 V the CO-ratio increases from 40% in the gas channel to 92% in the electrochemically active functional layer. The higher CO-ratio leads to the formation of approx. 2.8 mol.% carbon based on a thermodynamic calculation in Cantera [249]. The ESC shows a less pronounced influence when operating on CO/CO_2 fuel mixtures.

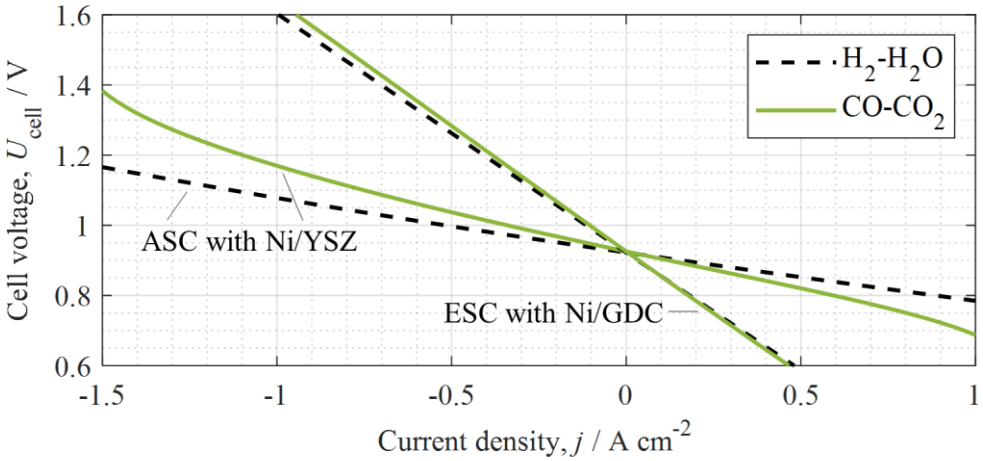

Figure 39 Simulated IV-curves of an ASC with Ni/YSZ fuel electrode and ESC with Ni/GDC fuel electrode with 40% H_2 (balance H_2O, dashed line) and 40% CO (balance CO_2) and air at the air electrode at $T = 800$ °C. Graphic formatted taken from Ref. [128].

5.2.7 Current Voltage Characteristics of H_2/H_2O and CO/CO_2

The comparison of the performance between H_2/H_2O and CO/CO_2 mode shall further be illustrated in Figure 40 for an electrolyte-supported cell with Ni/GDC fuel electrode by measured IV-curves with 50% H_2 (balance H_2O) as well as 50% CO (balance CO_2) and air at the air electrode at $T = 850$ °C. The electrochemical conversion of CO/CO_2 seems to perform on a similar level as for H_2/H_2O. Further, the abovementioned discussed differences of activation and gas diffusion polarization still do not have a major impact compared to the ohmic losses regarding this cell design.

The comparison of the behavior of the fuel gas mixtures H_2/H_2O to CO/CO_2 separately delivers a basis for further investigations of reformate gas mixtures [68,143], where the water-gas-shift reaction needs to be considered as well as reforming reactions. In addition, further analysis as shown for an ASC with Ni/YSZ fuel electrode by Kromp et al. [68] was performed by Esau et

al. [150] in order to judge if CO/CO_2 behaves electrochemically active in the presence of H_2/H_2O.

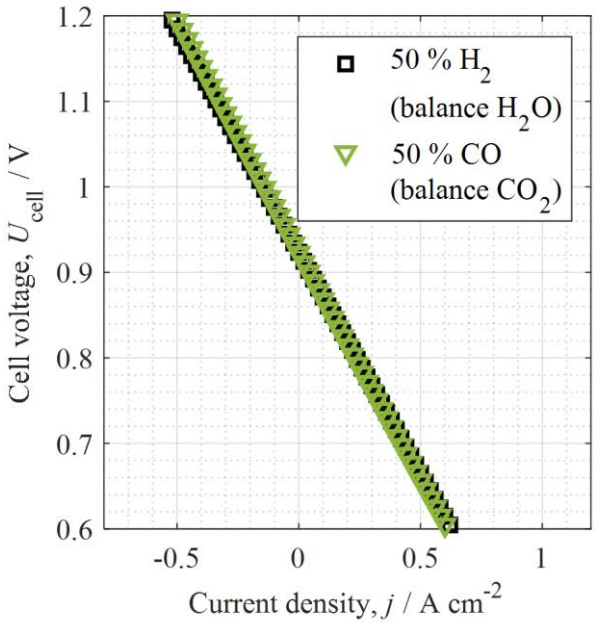

Figure 40 Measured current voltage characteristics in electrolyzer and fuel cell mode for the operation with 50% H_2 (balance H_2O) as well as 50% CO (balance CO_2) and air at the air electrode at $T = 850$ °C. Graphic formatted and taken from Ref. [128].

The characterization with ideal contacting is crucial regarding insights towards the intrinsic losses and the subsequent optimization of the cell. However, in a SOC-stack when the cells are contacted with metallic interconnectors, effects like chromium poisoning, increased contact resistances and limitations in gas supply need to be considered [161,260].

5.3 Stack-like Contacting[3]

In the following section, the impact of the protective coating for the stack-like contacting is shown by measured IV-characteristics and compared to the defined ideal case.

5.3.1 IV-Characteristics

Figure 41 shows that the ideal contacting with ceramic flow fields reaches the highest performance. The lowest benchmark was defined for stack-like contacting with uncoated Crofer 22 APU flow fields without LSCF contact paste at the air side (denoted Crofer 22 APU*). Subsequently, it indicates the lowest performance as seen in Figure 41. As expected, all other configurations of contacting perform between the higher and lower benchmark. The uncoated steel

[3] Parts of this chapter have been published in C. Grosselindemann et al., *ECS Trans.*, **111** (6), 533-546 (2023) [250] and C. Grosselindemann et al., *J. Electrochem Soc.*, **171**, 054508 (2024) [147].

grades show a substantial deviation from ideal behavior. Uncoated AISI 441 indicates a somewhat higher performance as compared with uncoated Crofer 22 APU and UNS S44330. The application of the CeCo protective coating on the MICs generates a significant performance increase. All coated MICs reach a maximum current density that is similar to the ideal behavior and thus cannot be clearly separated from each other. The performance variations are in the range of nominally identical ideally contacted cells ($+/-$ 0.02 A cm^{-2} at 1.4 V) and thus should not be related to the applied steel grade.

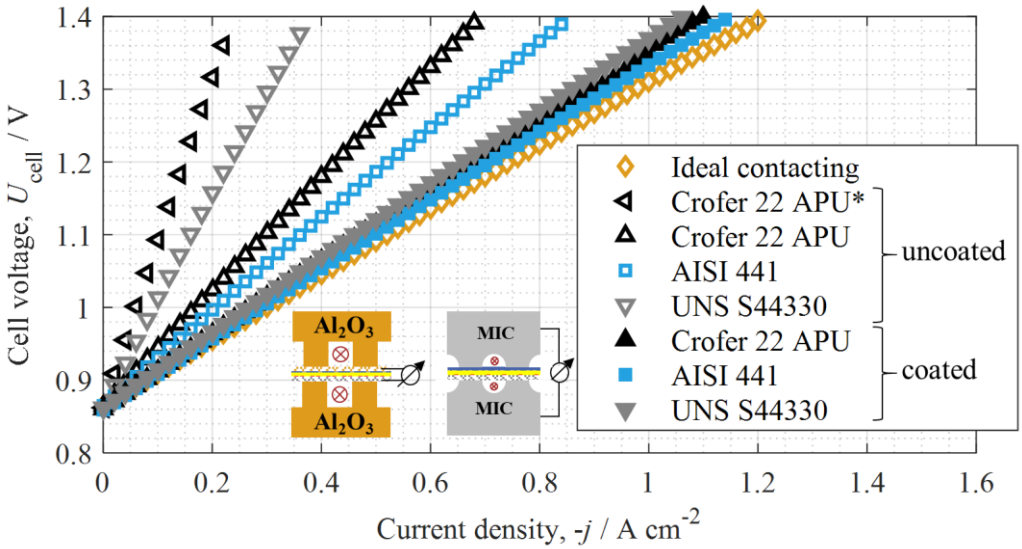

Figure 41 IV-characteristics of ideal contacting, Crofer 22 APU* (uncoated and without contact paste), un-/coated Crofer 22 APU, AISI 441 and UNS S44330 in electrolysis mode at $T = 850$ °C with 20% H_2 (balance H_2O) and air at the air electrode. Graphic taken from Ref. [147].

In order to analyze the impact of the MIC-contacting on the fuel side, an ideal contacting of the air side was combined with the stack like contacting at the fuel side (Figure 42). When measuring the voltage between gold mesh (AE) and MIC (FE), a similar performance results when measured between gold mesh (AE) and nickel grid (FE). The stack-like contacting at the air side is mainly responsible for the performance decrease, which might be related to Cr-poisoning and an enhanced contact resistance related to oxide scales on the MIC.

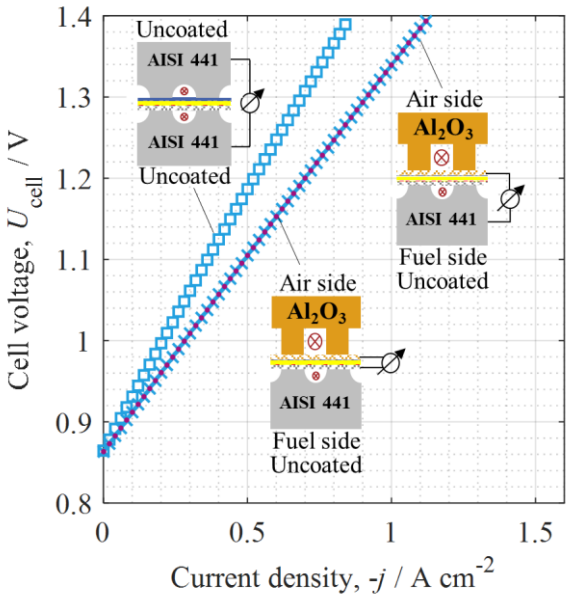

Figure 42 IV-characteristics of AISI 441 (MIC both sides uncoated and MIC uncoated fuel side only) in electrolysis mode at $T = 850$ °C with 20% H_2 (balance H_2O) and air at the air electrode. Graphic taken from Ref. [147].

5.3.2 Contact Loss Air Side

Further investigations with targeted measurements of potential probes at fuel and air side were conducted in order to determine the individual contact losses. In case of an ideal contacting the resistance between gold mesh / LSM-electrode and Ni mesh / Ni-YSZ electrode at 850 °C is $<$ 3 mΩ·cm² and $<$ 2 mΩ·cm² respectively[204]. In comparison to LSM air electrodes, the contact loss becomes even smaller for LSCF electrodes due to the higher conductivity [161].

With respect to the fuel side, the point-welded nickel mesh on the metallic flow field is in contact with the nickel rich contact layer of the fuel electrode. Contact losses measured between $2 - 5$ mΩ cm² are not shown here. Thus, the point welded finely meshed Ni-grid provides sufficient contacting of the fuel electrode´s surface.

Figure 43 presents voltage losses in electrolysis mode due to contacting at the air side at $T = 850$ °C with 20% H_2 (balance H_2O) and air at the air electrode and compares un-/coated Crofer 22 APU as well as AISI 441. Coating of the MICs with CeCo shows a significant decrease of the measured contact loss with a comparably larger decrease for Crofer 22 APU. Here, $\eta_{\mathrm{contact,AE}}$ includes the contact losses and the losses resulting from the in-plane conduction in the air electrode [27]. The latter can be neglected for an LSCF electrode and additional LSCF contact layer [161]. The corresponding contact resistances extracted from the slope ($R_{\mathrm{contact,AE}} = \frac{\partial \eta_{\mathrm{contact,AE}}}{\partial j}$) are summarized in Table 8. Additionally, the difference of the contact resistance $\Delta R_{\mathrm{contact,AE}}$ between un-/ coated MICs is given. Similar results were observed in fuel cell mode as well and are not shown here.

IV-characteristics of ideal contacting are again shown in Figure 44 in comparison to the resulting voltage of the potential difference between $\varphi_{\mathrm{MIC,FE}}$ and $\varphi_{\mathrm{MIC,AE}}$ as well as $\varphi_{\mathrm{mesh,FE}}$ and $\varphi_{\mathrm{probe,AE}}$ of uncoated Crofer 22 APU. When regarding the difference between the mesh at the fuel side $\varphi_{\mathrm{mesh,FE}}$ and the probe at the air side onto the air electrode $\varphi_{\mathrm{probe,AE}}$ the contact losses of the MICs are excluded. Thus, a performance like the ideal case can be observed. The decrease of performance is thus mainly dominated by the contact loss $\eta_{\mathrm{contact,AE}}$ at the air side of uncoated Crofer 22 APU. Similar results were observed for AISI 441 and UNS S44330.

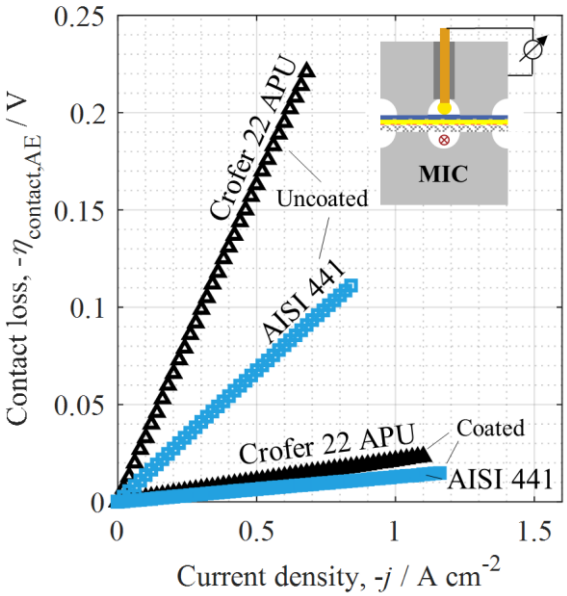

Figure 43 Contact loss of un-/coated Crofer 22 APU and AISI 441 in electrolysis mode at $T = 850$ °C with 20% H_2 (balance H_2O) and air at the air electrode. Graphic taken from Ref. [147].

To further evaluate the loss contributions, coated MICs are compared with uncoated MICs as well as ideal contacting by electrochemical impedance spectroscopy and the subsequent analysis of the distribution of relaxation times.

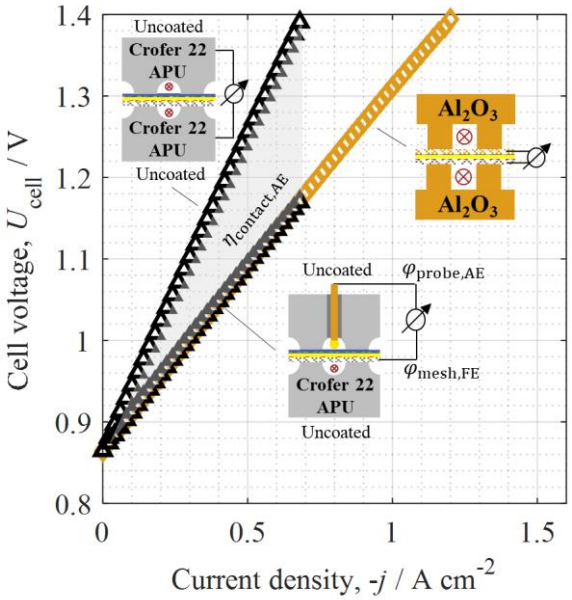

Figure 44 IV-characteristics of ideal contacting and uncoated Crofer 22 APU with measured potential difference between $\varphi_{\mathrm{MIC,FE}}$ and $\varphi_{\mathrm{MIC,AE}}$ as well as $\varphi_{\mathrm{mesh,FE}}$ and $\varphi_{\mathrm{probe,AE}}$ in electrolysis mode at $T = 850$ °C with 20% H_2 (balance H_2O) and air at the air electrode and corresponding contact loss $\eta_{\mathrm{contact,AE}}$ indicated in grey area. Graphic reformatted and taken from Ref. [147].

5.3.3 Impedance Analysis

Figure 45 shows the impedance spectra in (a) for Crofer 22 APU and (b) for AISI 441 at $T = 850$ °C with 95% H_2 (balance H_2O) and air at the air electrode. The ohmic resistance is significantly decreased by the applied CeCo coating for both MICs (Crofer 22 APU 36%, AISI 441 22%).

5.3.3.1 Ohmic Resistance: Impedance vs. Potential Probes

The difference of the ohmic resistance $\Delta R_{0,\mathrm{EIS}}$ extracted from the impedance measurements between un-/coated MICs is given in Table 8 and should be related to the difference of contact resistance between un- and coated MICs. For Crofer 22 APU, the determination of the difference of the contact resistance at the air side $\Delta R_{\mathrm{contact,AE}}$ by potential probes results in a deviation of 67 mΩ cm^2 in comparison to $\Delta R_{0,\mathrm{EIS}}$. However, for AISI 441 both methods deliver similar values.

5.3.3.2 Polarization Resistance

The corresponding distribution of relaxation times (DRT) are shown in Figure 45 (c, d). With respect to cells exhibiting a Ni/GDC fuel electrode an overlap of processes in the spectra needs to be considered [55,56,79,82,89,120,121,128]. Several processes are overlapping underneath the lowest frequency peak such as gas diffusion and activation polarization at the fuel side. Gas diffusion losses at the air side might also be coming into effect [161,260]. In the mid frequency

range from 10 Hz to approx. 10^3 Hz the stack-like contacting with CeCo coating shows a decrease in the polarization resistance by approx. 30%. Typically, the surface exchange process at the air electrode can be found in this frequency range [38,104]. The lower polarization resistance might be referred to less Cr-evaporation of the MIC at the air side due to the protective coating and thus a lower negative impact. However, in terms of process assignment of the peaks, those cannot be fully dedicated to the air electrode as processes of the fuel side overlap as well [38]. The overall polarization R_{pol} resistance is summarized in Table 8.

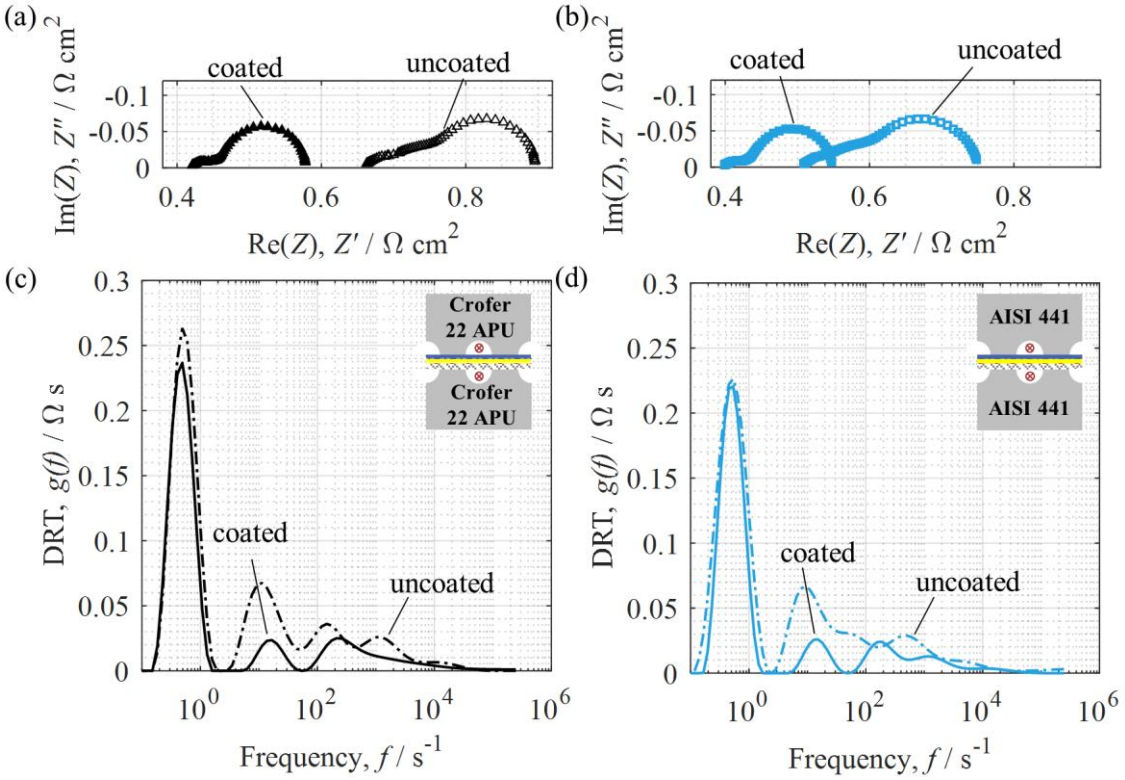

Figure 45 (a) Impedance spectra and (c) DRT of Crofer 22 APU (un-/coated) and (b) and (d) of AISI 441 (un-/coated) at $T = 850$ °C with 95% H_2 (balance H_2O) and air at the air electrode. Graphic taken from Ref. [147].

Table 8. Extracted contact resistance $R_{\mathrm{contact,AE}}$ related to Figure 43 for un-/coated Crofer 22 APU and AISI 441 with calculated difference between un-/coated MICs $\Delta R_{\mathrm{contact,AE}}$ at 850 °C. Difference of the ohmic resistance $\Delta R_{\mathrm{0,EIS}}$ related to Figure 45 by impedance spectroscopy at 850 °C.

	Uncoated	Coated		
	$R_{\mathrm{contact,AE}}$		$\Delta R_{\mathrm{contact,AE}}$	$\Delta R_{\mathrm{0,EIS}}$
Material	[Ω cm²]		[Ω cm²]	[Ω cm²]
Crofer 22 APU	0.325	0.021	0.304	0.237
AISI 441	0.132	0.013	0.119	0.112

In the following section, the electrochemical results will be correlated to the oxide scales formed on the different MICs and chromium in the air electrode.

5.3.4 Microstructure Analysis – Metallic Interconnectors

With the help of the microstructural analysis of the metallic interconnectors, further insights on the basis of the electrochemical characterization can be obtained. Figure 46 shows SEM cross sections of the uncoated and coated MICs of the three different steel grades with un-/coated in (a, d) Crofer 22 APU, (b, e) AISI 441, and (c, f) UNS S44330. Uncoated samples show significant variation in thickness and microstructure of the oxide scales. In comparison, the coated samples show quite similar thickness and microstructures of the oxide scales. Here, the comparatively very thin Ce oxide-layer ($10 - 20$ nm) of the PVD-coating [163] appears as indicated in Figure 46. This behavior is similar to earlier findings by Reddy et al.[177].

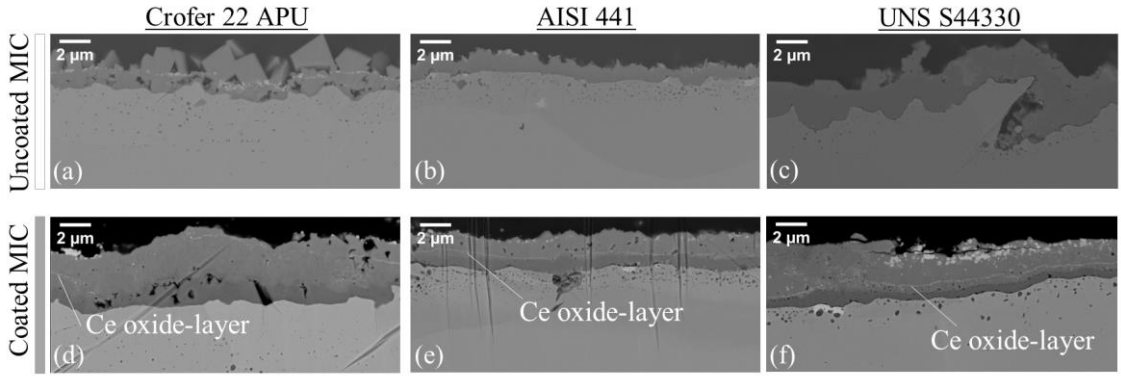

Figure 46 SEM backscattered electron micrographs of the air side of un-/coated (a, d) Crofer 22 APU, (b, e) AISI 441, (c, f) UNS S44330 tested for approx. 200 h. Graphic taken from Ref. [147].

The EDXS-results are presented in Figure 47 with (a-c) un- and (d-f) CeCo coated Crofer 22 APU, AISI 441 and UNS S44330. Starting from the iron (Fe)-rich bulk of the MIC appearing in green, different oxide (O) layers become visible at the surface. In case of all uncoated MICs in Figure 47 (a-c), a chromium-rich oxide layer is found that is significantly thicker for uncoated UNS S44330 in comparison to uncoated Crofer 22 APU and AISI 441. In addition, a manganese (Mn) rich layer is visible at the surface due to formation of a Cr-Mn-spinel at the surface of the different MICs as observed by Reddy et al. [177].

As shown in Figure 47 uncoated AISI 441 exhibits the thinnest Cr-oxide layer which can be correlated to the lower contact resistance (Table 8) in comparison to Crofer 22 APU.

With respect to the CeCo coated metallic interconnectors, similar thickness of Cr_2O_3 oxide scale can be observed in Figure 47 (d-f). This supports the electrochemical measurement since coated MICs show a performance and contact loss close to the ideal, chromium free contact set-up with ceramic flow fields. Moreover, the thinner chromia scale and lower Cr outward diffusion into the cathode in the presence of CeCo coating resulted in improved contact resistance compared to the uncoated MICs. In contrast to the uncoated samples, a cobalt (Co) layer is visible for all CeCo coated samples indicating the formation of a Co-Mn spinel layer at the surface, as also observed by Reddy et al. [177]. This Co-Mn layer has a higher conductivity [264] in comparison to a Cr-Mn spinel for the uncoated samples. The thin ($10 - 20$ nm) cerium oxide layer is

not visible in the EDXS. Further, strontium (Sr) and lanthanum (La) can be observed above the Co-Mn rich oxide layer for Crofer 22 APU and UNS S44330, which is presumably related to the application of the LSCF contact layer and the sintering process during the start- and heat-up phase prior to cell testing.

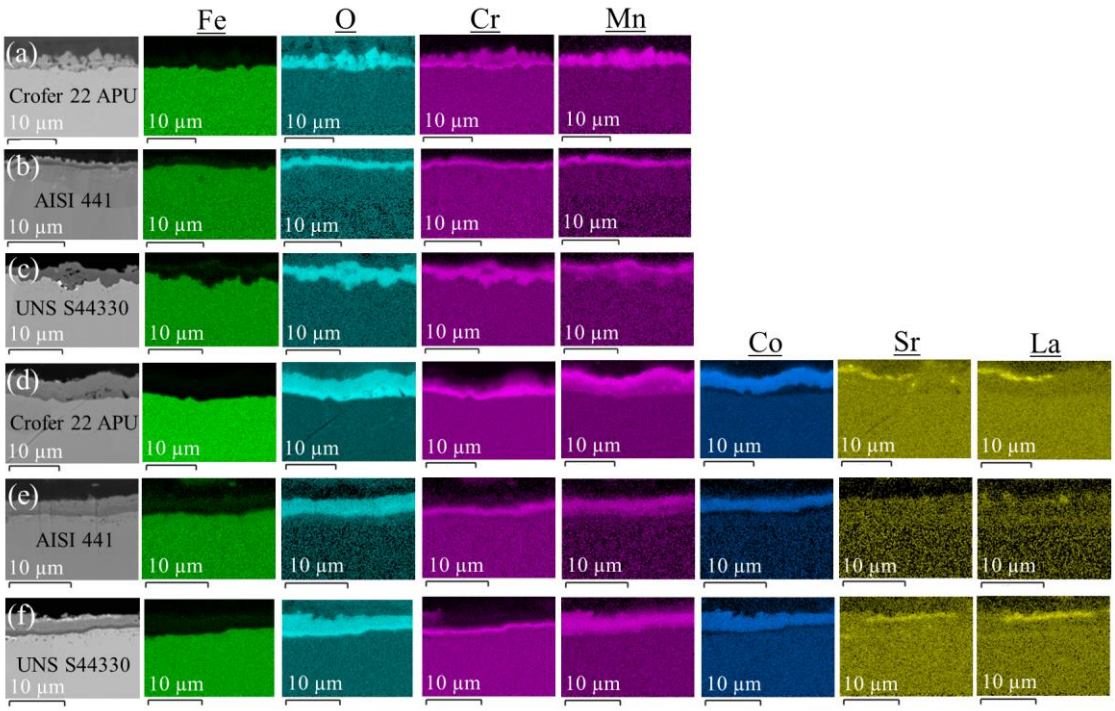

Figure 47 EDXS-Analysis of the air side oxide scale of un-/coated (a, d) Crofer 22 APU, (b, e) AISI 441, (c, f) UNS S44330. Graphic taken from Ref. [147].

5.3.5 Cr-poisoning Air Electrode

The air electrode was investigated in more detail by a TEM-analysis with respect to Cr-poisoning when in contact with an uncoated MIC made of Crofer 22 APU.

5.3.5.1 TEM-EDXS Analysis

Figure 48 shows a TEM image of the LSCF current-collector layer in (a). Here, the rather thick boundary between LSCF and LSCF/GDC area results from a stabilization of the TEM-sample. In addition, EDXS is presented in Figure 48 (b) – (j). The presence of Cr is clearly visible in the LSCF layer with a formation of $SrCrO_4$ as expected from Ref. [265,266].

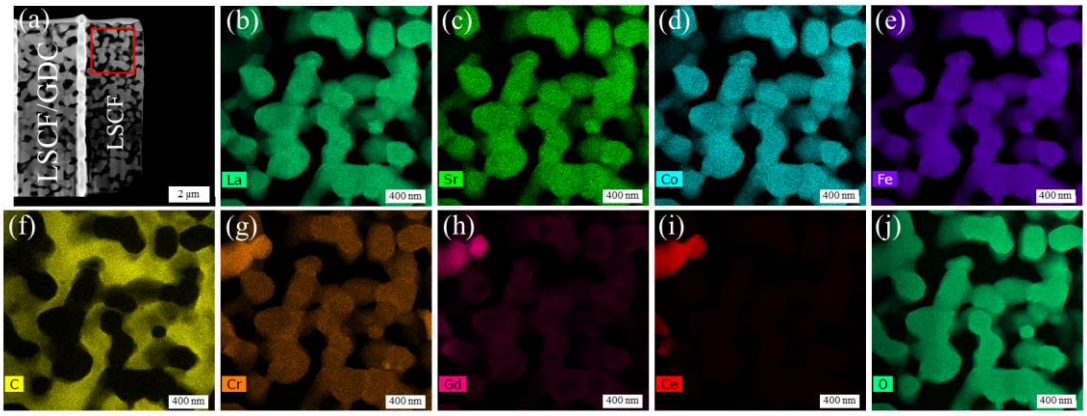

Figure 48 EDXS-TEM of the LSCF current-collector layer.

In Figure 49 the interface between LSCF and GDC is investigated. It can be observed, that Cr predominantly is present in the LSCF as well as GDC phase.

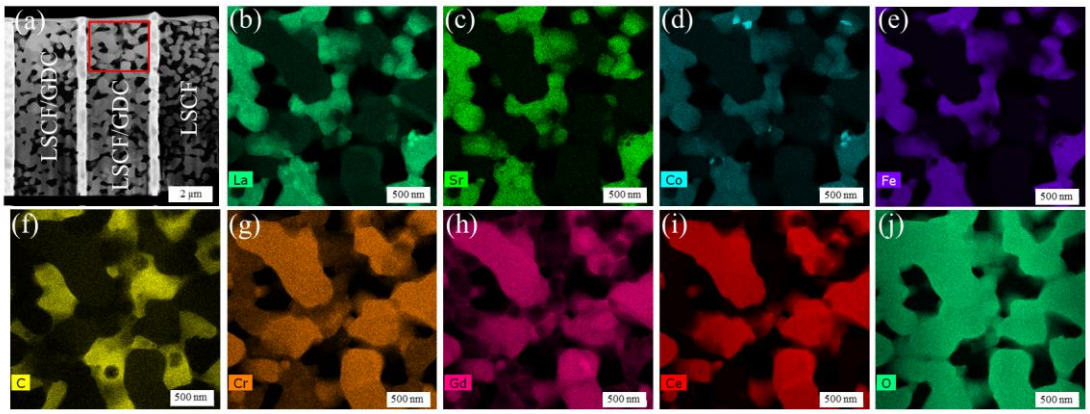

Figure 49 EDXS-TEM of the LSCF/GDC layer.

No Cr-species were found in the GDC barrier layer between electrode and electrolyte, which may need further investigation and might be related to the rather short testing time of approx. 200 h.

With the help of the TEM, only small areas can be investigated. Regarding a quantification of Cr-poisoning, a SEM-EDXS analysis is shown in the following section.

5.3.5.2 SEM-EDXS Analysis

With respect to the SEM-EDXS measurements, different locations of the LSCF layer were investigated with overall areas between approx. $3000 - 5000$ µm^2 for each cell. Thus, an extraction of the energy-dispersive X-ray spectra is shown as a mean value between the different locations in Figure 50 for un-/coated (a) Crofer 22 APU, (b) AISI 441 and (c) UNS S44330. For comparability, all spectra are normalized to the peak of lanthanum (La), as it is assumed that all samples have the same amount of La in the dedicated LSCF layer. Un-/coated Crofer 22 APU (Figure 50 (a)) has the smallest difference in the spectra in comparison to the other two

MICs. For the peak of Cr, a clear difference can be observed in Figure 50 (b) and (c) between un-/coated AISI 441 and UNS S44330.

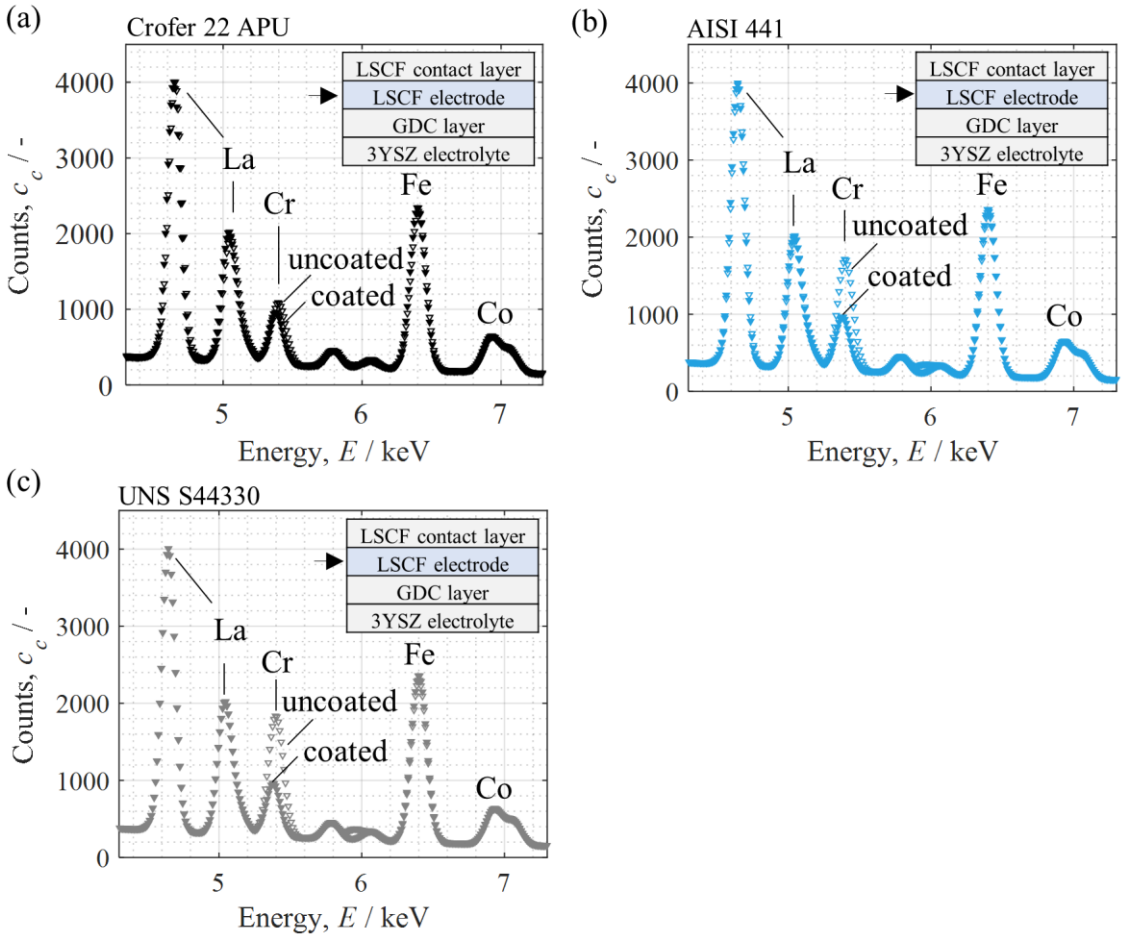

Figure 50 Extraction of energy-dispersive X-ray spectra of the LSCF air electrode contacted with un-/coated (a) Crofer 22 APU, (b) AISI 441 and (c) UNS S44330. Graphic modified and taken from Ref. [147].

Table 9 shows the quantitative analysis of the EDXS measurements with the mean value of the Cr content $\bar{x}_{Cr}$ in the LSCF layer. Of note, the measurement technique was performed within certain limits as shown by the standard deviations σ_{Cr} in Table 9.

Table 9. Overall polarization resistance R_{pol} of the cell at 850 °C with 95% H_2 (balance H_2O) in contact with un-/coated Crofer 22 APU, AISI 441 and UNS S44330. Mean values of the Cr content $\bar{x}_{Cr}$ as well as standard deviation σ_{Cr} in the LSCF layer by EDXS analysis.

	Crofer 22 APU			AISI 441			UNS S44330		
	R_{pol} [Ω cm²]	$\bar{x}_{Cr}$ [at.%]	σ_{Cr} [at.%]	R_{pol} [Ω cm²]	$\bar{x}_{Cr}$ [at.%]	σ_{Cr} [at.%]	R_{pol} [Ω cm²]	$\bar{x}_{Cr}$ [at. %]	σ_{Cr} [at.%]
uncoated	0.242	3.12	(+/-) 2.91	0.242	9.35	(+/-) 4.57	0.425	11.08	(+/-) 0.98
coated	0.160	0.62	(+/-) 0.48	0.153	0.66	(+/-) 0.32	0.163	0.56	(+/-) 0.48

Nevertheless, similar polarization resistances with almost no chromium in the LSCF layer are found in case of coated MICs. The CeCo coating blocks the Cr-evaporation effectively. Also, neglectable amounts of chromium were found in the fuel electrode and are not shown here.

The findings from this work with respect to an ideal as well as stack-like contacting under atmospheric pressure deliver a basis for the new pressurized test bench since a similar stack-like contacting with CeCo-coated MICs is applied there.

5.4 Pressurized Testing of Solid Oxide Cells

Pressurized testing on single cell level is shown for an electrolyte- as well as an anode-supported cell in the following.

5.4.1 Pressurized Testing of an Electrolyte-supported Cell[4]

First measurements with the modified test bench set-up for pressurized testing are shown in the following for the metallic housing made of APMT and the electrolyte-supported cell with Ni/GDC fuel electrode.

5.4.1.1 N_2 Pressure Test

Gas tightness of the glass ceramic sealing of the new pressurized test bench was confirmed with a nitrogen (N_2) pressure test. Here, at 850 °C with 250 sccm N_2 per electrode the pressure was increased stepwise up to 11 bar_a absolute pressure as shown in Figure 51. After a holding time of 30 min., the gas flow was switched off resulting in a pressure drop of approx. 6 $bar_a\ h^{-1}$, which corresponds to an average leakage rate of 3 sccm. Once the gas flow is switched back on again, the 11 bar_a are reached again after approx. 6 min. This shows sufficient compression and sealing of the cell which was achieved via the inflatable boot and the glass ceramic sealing. Thermal cycling experiments revealed that even after a full thermal cycle the pressure of 11 bar_a could be achieved again. Within the testing phase, the pressure should be changed with a rate of 3 – 5 $mbar_a\ s^{-1}$ to avoid pressure gradients between anode and cathode resulting from different gas volumes and flow rates to both compartments.

[4] Parts of this chapter have been published in C. Grosselindemann et al., *J. Power Sources*, **614**, 234963 (2024) [2].

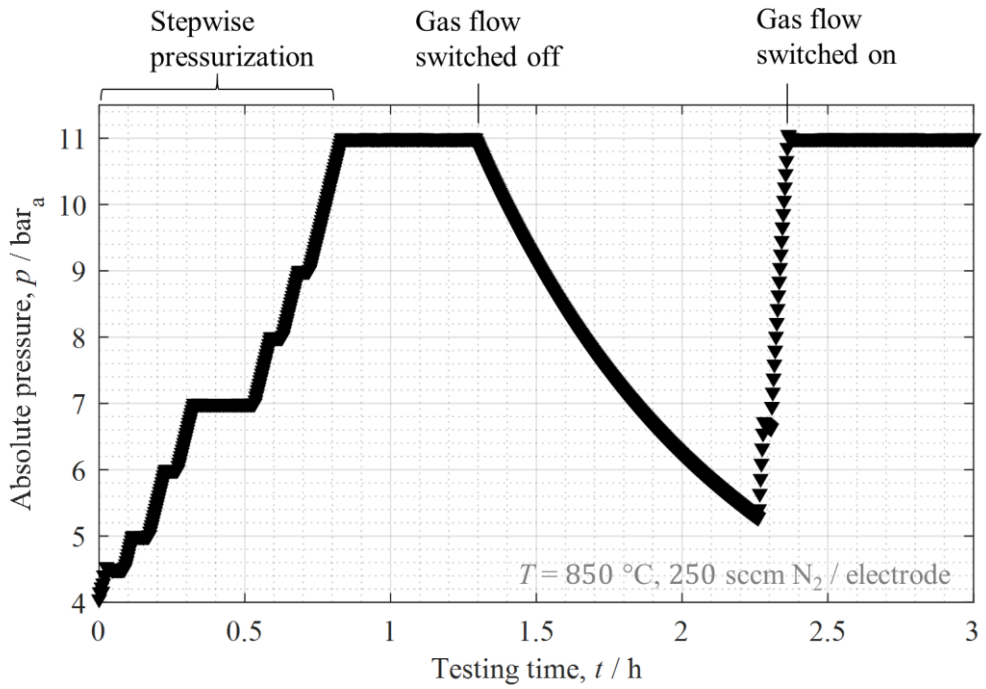

Figure 51 Pressure test at 850 °C with 100% N_2 and increase of absolute pressure up to 11 bar_a with glass ceramic sealing G018-281. Graphic reformatted and taken from Ref. [2].

5.4.1.2 Open-circuit Voltage

Figure 52 (a) shows the dependency of the open-circuit voltage as a function of the absolute pressure p at 850 °C with 100% H_2 at the fuel side and synthetic air at the air side. An open-circuit voltage of 1.352 V was reached at atmospheric pressure which corresponds to a leakage $< 0.015\%$ H_2O in H_2 for measurement #1. The pressure was then increased up to 9 bar_a absolute pressure resulting in an $U_{OCV} = 1.42$ V. By calculation of the Nernst-equation, the measured increase of U_{OCV} can be described in good agreement with a steam content of 0.0125% H_2O and a relative error of $< 1\%$. Considering these comparably low steam contents, the Nernst-equation behaves sensitive to small changes. For measurement #2, the pressure was raised to 11 bar_a with a slightly higher but still tolerable leakage resulting in 0.135% H_2O in the fuel. Here, at pressures above 5 bar_a the deviation from the Nernst-equation increases with a relative error of $< 2\%$. Likewise, this is shown in Figure 52 (b) for a set fuel gas mixture of 50% H_2 (balance H_2O) and synthetic air at the air side with up to 4 bar_a absolute pressure. The measured voltages correspond to a steam content of 52.5%. This deviation in the steam content most probably originates from an off-set of the flow controllers. The observed impact of pressure on the open-circuit voltage is in good agreement with the Nernst equation and findings in previous studies [16,33].

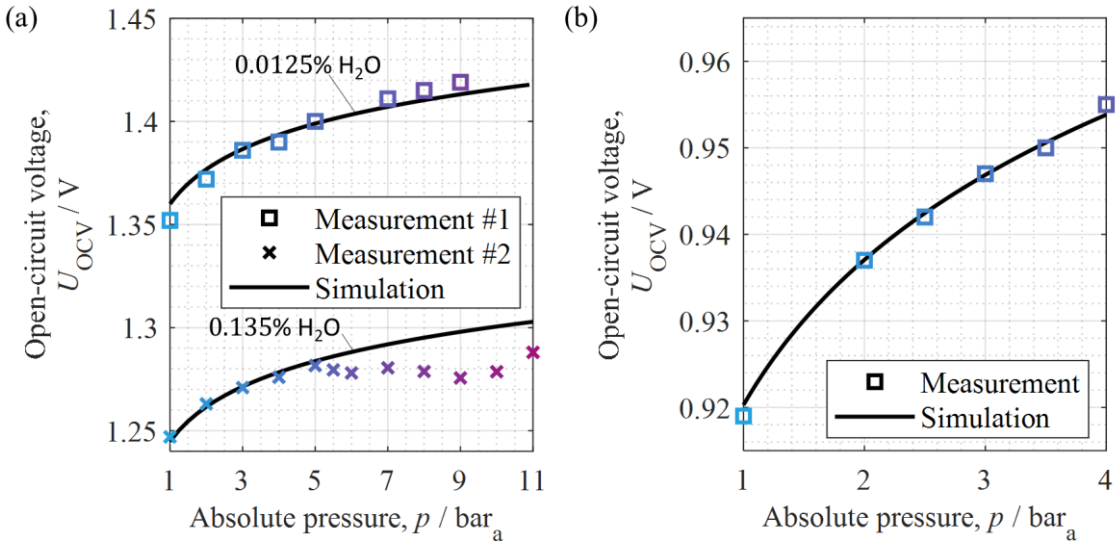

Figure 52 (a) Measured and simulated OCV as a function of the absolute pressure p with 100% H_2 at the fuel side (simulation with 0.0125% H_2O leakage for measurement #1 and 0.135% H_2O leakage for measurement #2) and synthetic air at the air side at 850 °C. (b) OCV as a function of the absolute pressure with 50% H_2 (balance H_2O, simulation with 52.5% H_2O) and synthetic air at the air side. Graphic taken from Ref. [2].

5.4.1.3 IV-Characteristics

First results of IV-characteristics and power density P_{cell} in SOFC mode at 850 °C with 100% H_2 at the fuel side and synthetic air at the air side are shown in Figure 53 (a). As expected from previous works [16,18], the increase in open-circuit voltage with pressurization is beneficial for SOFC mode as a higher performance is observed with increasing pressure.

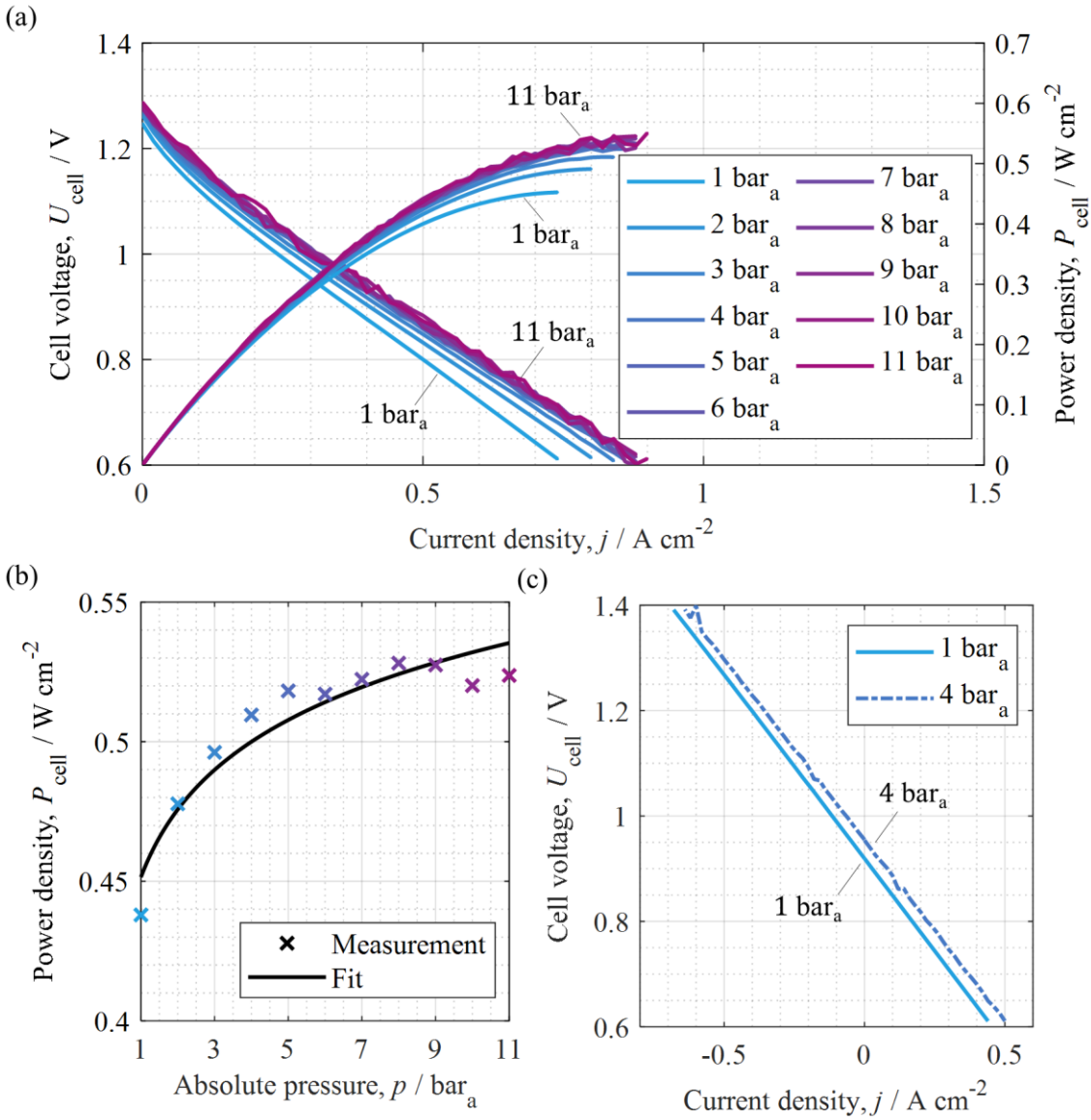

Figure 53 (a) IV-characteristics and power density P_{cell} in SOFC-mode at 850 °C with 100% H_2 and synthetic air at the air side between $1-11$ bar$_a$. (b) Power density P_{cell} as a function of the absolute pressure p at 850 °C with 100% H_2/synthetic air at 0.7 V with logarithmic fit. (c) IV-characteristics at 850 °C with 50% H_2 (balance H_2O) and synthetic air at the air side between $1-4$ bar$_a$. Graphic taken from Ref. [2].

The power density P_{cell} at 0.7 V (850 °C with 100% H_2 and synthetic air) is shown in Figure 53 (b) as a function of the absolute pressure p between $1-11$ bar$_a$. In comparison to atmospheric pressure an increase of approx. 20% can be achieved at 11 bar$_a$ regarding a cell voltage of 0.7 V, which can be confirmed by calculations with the performance model developed in chapter 5.1. The major increase of power density was observed between atmospheric conditions and 5 bar$_a$. The positive impact of pressure on the power density was proved in a number of previous experimental works [229,239]. In the work by Henke et al. [239] it was also shown, that with an increase of pressure the highest influence can be seen at low pressures. In Figure 53

(b) the power density with increasing pressure was interpolated according to equation (69) similar to Ref. [239] with the variables *A* and *B*. The authors stated a logarithmic behavior of power density with increasing pressure, which was confirmed in this work in Figure 53 (b) (goodness of fit: $R^2 = 0.902$).

$$y(x) = A \ln(x) + B \tag{69}$$

Figure 53 (c) shows the IV-characteristics at 850 °C with 50% H_2 (balance H_2O) and synthetic air at the air side between $1 - 4$ bar_a. As expected from the theoretical study [33], the increase of U_{OCV} appears positive for the fuel cell and disadvantageous for electrolysis mode. A higher performance at 4 bar_a can be observed in comparison to atmospheric pressure in fuel cell mode, which is also consistent with previous studies [233,239]. With respect to an electrolyte-supported cell design, the effect of pressure in electrolysis mode is comparably small and similar to findings by Riedel et al. [24].

5.4.1.4 Impedance Analysis

To evaluate the impact of the stack like contacting, reference measurements at atmospheric pressure were conducted with identical cells and air electrode contacting. Figure 54 displays impedance spectra and corresponding DRTs for 21% O_2 (balance N_2) and 5% O_2 (balance N_2) at the air side and 50% H_2 (balance H_2O) at the fuel side at 850 °C in (a) and (c).

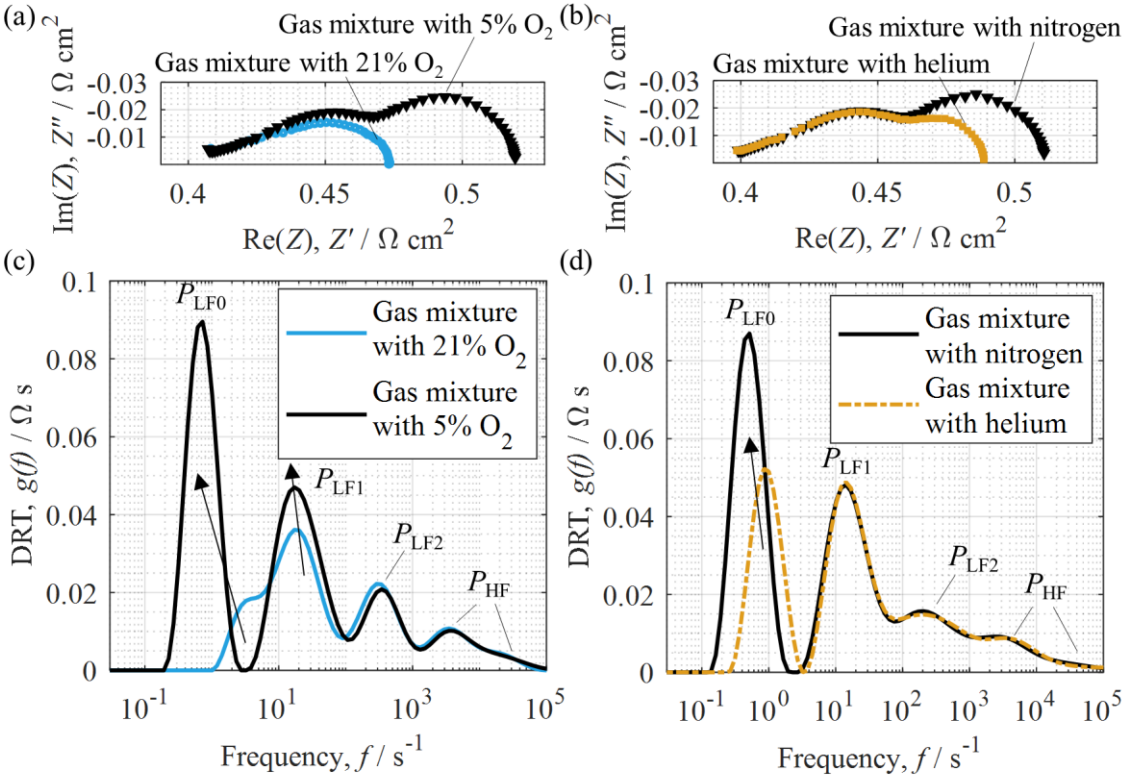

Figure 54 Impedance spectra of a stack like contacted cell at atmospheric pressure in (a) for 21% O_2 (balance N_2) and 5% O_2 (balance N_2) at the air side and with 50% H_2 (balance H_2O) at the fuel side at 850 °C with corresponding DRT in (c). Impedance spectra at atmospheric pres-

sure in (b) with 5% O_2 (balance N_2 or He) at the air side and with 50% H_2 (balance H_2O) at the fuel side at 850 °C with corresponding DRT in (d). Graphic taken from Ref. [2].

In previous studies [38,75,146] analyzing ideally contacted cells, the different peaks in the DRT were attributed to physicochemical processes. In summary, it was found that P_{LF1} contains overlapping contributions of fuel and air electrode. This includes the surface reaction coupled with ionic transport in superposition with the gas diffusion process at the fuel electrode as well as surface exchange and ionic transport in the air electrode [147,205]. P_{LF2} and P_{HF} were identified as processes related to charge transport in the GDC-phase and at the GDC / YSZ interfaces.

In case of the stack like air electrode contacting at the given conditions, an additional peak P_{LF0} becomes visible (Figure 54 (a,c)). P_{LF0} and the air electrode contribution to P_{LF1} are both affected by the oxygen partial pressure. An inert gas variation [38,122,146] of the oxidant (Figure 54 (b,d)) reveals that only P_{LF0} is affected. Thus, P_{LF0} can be attributed to gas diffusion polarization at the air side. In the work by Geisler et al. [161] it was found that in-plane gas diffusion in the contact and cathode layers underneath the ribs of the flow field has a significant impact on cell performance. In order to quantify the impact of gas diffusion in this study, a method from chapter 5.1.2 is adapted. The difference of the polarization resistance ΔR_{pol} (see equation (54)) between the gas mixture with nitrogen $R_{\mathrm{pol,N_2}}$ and helium $R_{\mathrm{pol,He}}$ is assumed to be equal to the difference of the gas diffusion resistance ΔR_{diff} between the two gas mixtures as shown in chapter 5.1.2.

Here, the concept of an effective gas diffusion parameter G_{eff} is adapted to the air electrode (equation (70)). Ψ_{AE} denotes the microstructure parameter and L_{AE} an averaged gas diffusion length.

$$G_{\mathrm{eff,AE}} = \frac{\Psi_{\mathrm{AE}}}{L_{\mathrm{AE}}} \tag{70}$$

The gas diffusion resistance at the air side $R_{\mathrm{diff,AE}}$ can be calculated according to equation (71) with $\tilde{R}$ denoting the universal gas constant, T the temperature, F the faraday constant, $D_{\mathrm{O_2}}$ the binary gas diffusion coefficient, $\tilde{y}_{\mathrm{O_2,AE}}$ the molar fraction of oxygen and P_{corr} an conversion factor 10^5 Pa $\mathrm{bar_a^{-1}}$. Based on Ref. [39], molecular combined with Knudsen gas diffusion is considered. Thus, $D_{\mathrm{O_2}}$ is based on the Bosanquet-approach (equation (18)) and the molecular gas diffusion coefficient $D_{\mathrm{mol,O_2}}$ is calculated by Chapman-Enskog (equation (15)) [258].

$$R_{\mathrm{diff,AE}} = \left(\frac{\tilde{R}T}{4F}\right)^2 \cdot \frac{1}{G_{\mathrm{eff,AE}}} \cdot \frac{1}{D_{\mathrm{O_2}} \cdot p}\left(\frac{1}{\tilde{y}_{\mathrm{O_2,AE}}} - 1\right) \cdot \frac{1}{P_{\mathrm{corr}}} \tag{71}$$

On the basis of equation (54) and (71) the effective gas diffusion parameter can be determined with equation (72) resulting in $G_{\mathrm{eff,AE}} = 188.74$ $\mathrm{m^{-1}}$ with a $\Delta R_{\mathrm{pol}} = 21.8$ mΩ $\mathrm{cm^2}$ in Figure 54 (b).

$$G_{\mathrm{eff,AE}} = \left(\frac{\tilde{R}T}{4F}\right)^2 \cdot \frac{1}{\Delta R_{\mathrm{diff}}} \cdot \frac{1}{p}\left(\frac{1}{\tilde{y}_{\mathrm{O_2,AE}}} - 1\right)\left(\frac{1}{D_{\mathrm{O_2,N_2}}} - \frac{1}{D_{\mathrm{O_2,He}}}\right) \cdot \frac{1}{P_{\mathrm{corr}}} \qquad (72)$$

The first impedance measurements of pressurized testing with the new test bench are presented in Figure 55 (a) with the distribution of relaxation times in Figure 55 (b). The spectra were measured at 850 °C with 50% H_2 (balance H_2O) and synthetic air at the air side at pressures of 1 and 4 bar_a.

The increase in pressure results in a decrease of the ohmic resistance by about 5 mΩ cm². Here, a number of effects discussed in literature might have contributed to this behavior. In the work by Momma et al. [228], a decrease of the ohmic resistance with increasing pressure was reported and attributed to the conductivity of the air electrode material [267] and a lower contact resistance between air electrode and current collector. Previous investigations (chapter 5.3.2) [147] of the stack like contacting revealed a contact resistance of 13 mΩ cm², which might decrease at higher pressures. Further, the conductivity in the GDC bulk in the fuel electrode and within the GDC interlayer at the air side may be influenced. The conductivity of GDC is depending on the oxygen partial pressure. Based on Wang et al. [31] the impact at the air side is assumed to be neglectable since at comparably higher oxygen partial pressures no significant change in conductivity can be observed. Regarding the fuel electrode, the oxygen partial pressure calculated with Cantera [249] at 850 °C and 50% H_2 (balanced with H_2O) is independent of pressure and thus no impact from here is expected. Additionally, the conductivity of the oxide scale of the metallic flow field exhibiting a Co-Mn spinel layer [147,177] may play a comparably larger role here. This needs to be investigated in more detail in future work.

The polarization resistance is decreasing by approx. 8 mΩ cm², which can be related to reduced activation and/or gas diffusion polarization resistances [16]. At first, the impact of pressure on the gas diffusion process at the air side P_{LF0} is discussed. The gas diffusion resistances at atmospheric pressure ($R_{\mathrm{diff,AE,atm}} = 9.4$ mΩ cm²) and 4 bar_a ($R_{\mathrm{diff,AE,4bar}_a} = 6.9$ mΩ cm²) are calculated with the help of equation (71), revealing a difference of 2.5 mΩ cm² that is contributing to the decrease in the overall polarization resistance.

The peak P_{LF1} in Figure 55 (b) at approx. 10 Hz is mostly affected by the change in pressure. In Ref. [33,45] it was shown that the gas diffusion regime determines the impact of pressure regarding the electrochemical behavior. In comparison to the air side, here a finely meshed Ni-grid is applied for contacting. Thus, based on a chapter 5.1.2 gas diffusion in the porous fuel electrode structure with molecular and Knudsen gas diffusion was neglected due to the small electrode thickness. Instead a gas diffusion layer above the electrode with pure molecular gas diffusion inside the contact mesh and gas channel can be assumed at the fuel side. The resulting gas diffusion resistance $R_{\mathrm{diff,FE}}$ at the fuel side is independent of pressure for molecular gas diffusion as shown in chapter 2.4.3.

Subsequently, the impact of pressure on P_{LF1} should solely result from a decrease of the activation polarization at the fuel and/or air electrode. The activation resistance $R_{\mathrm{act},el}$ for the electrodes (*el*) is provided in equation (73). Here, $j_{0,el}$ denotes the exchange current density of the

electrodes. It´s dependency on the pressures is shown in equation (12) and (13) for fuel and air electrode respectively.

$$R_{\mathrm{act},el} = \frac{1}{j_{0,el}} \cdot \frac{\tilde{R}T}{2F} \tag{73}$$

The dependency of the exchange current density becomes obvious and can be calculated with the parameters from Table 6.

Based on this, the activation resistance at the fuel side is calculated for atmospheric pressure ($R_{\mathrm{act,FE,atm}} = 37.5$ mΩ cm^2) as well as at 4 bar$_a$ ($R_{\mathrm{act,FE,4\ bar_a}} = 18.2$ mΩ cm^2). This results in a difference of 19.2 mΩ cm^2. As shown in the appendix in Figure 67, the activation resistance at the air side is neglectable under atmospheric pressure at 850 °C and air at the air side. The calculated impact of pressure towards the activation resistance is larger than the measured value of 8 mΩ cm^2 minus the gas diffusion at the air electrode of 2.5 mΩ cm^2. However, the model parameters were determined at atmospheric pressure and might not be valid for higher pressures. Processes underneath P_{LF2} seem to be affected with pressure as well, which may result from the coupling of P_{LF1} and P_{LF2} in a transmission line model. Processes above 10^3 Hz (P_{HF}) do not seem to be impacted by increasing pressure as they are related to bulk processes.

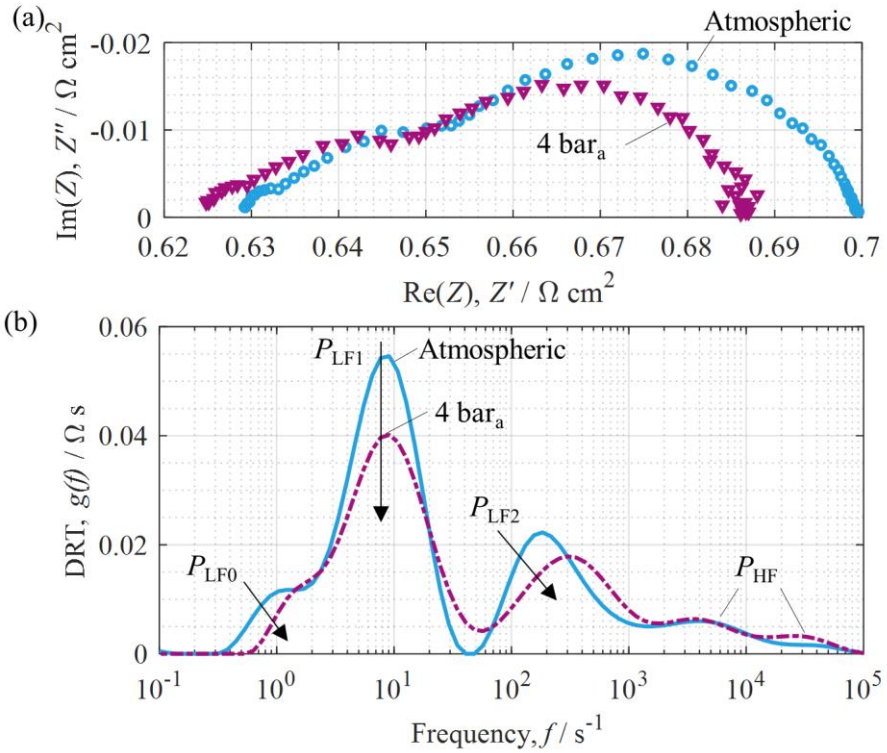

Figure 55 (a) Impedance spectra and (b) DRT at 850 °C with 50% H_2 (balance H_2O) and synthetic air at the air side between 1 bar$_a$ and 4 bar$_a$. Graphic reformatted and taken from Ref. [2].

Based on this analysis the physicochemical backgrounds of the DRT-peaks and their pressure dependencies are summarized in Table 10.

Table 10. List of physical processes at fuel and air electrode with corresponding frequency range and indication of pressure dependency.

Peak	Frequency range	Physical process		Pressure dependency
-	[Hz]	Fuel electrode	Air electrode	-
P_{LF0}	$0.5 - 3$	-	Gas diffusion	Yes
P_{LF1}	$3 - 30$	Surface reaction coupled with ionic transport in the GDC phase, overlap with gas diffusion [146]	Oxygen surface exchange coupled with O^{2-} diffusion in the bulk of the air electrode [205]	Yes
P_{LF2}	$30 - 2000$	Ionic transport in the GDC phase coupled with surface reactions + interfacial processes [146]	Dominated by O^{2-} diffusion in the bulk of the air electrode coupled with oxygen surface exchange [205]	Yes
P_{HF}	> 2000	Interfacial and bulk processes [146]	Non-surface related processes, possibly resistive interfacial processes [38]	No

5.4.2 Pressurized Testing of an Anode-supported Cell

An anode-supported cell with Ni/YSZ fuel electrode was tested with the metallic cell housing made of Crofer 22 H under pressurized operating conditions and results are shown in the following section.

5.4.2.1 Atmospheric vs. Pressurized Test Bench

Figure 56 shows a comparison of (a) impedance spectra and (b) DRT of an ASC with Ni/YSZ fuel electrode between the test bench for atmospheric and pressurized conditions at $T = 800$ °C with 50% H_2 (balance H_2O) and synthetic air at the air side. The measurements were performed at atmospheric conditions and prior to pressurization at the pressurized test rig. In Figure 56 (a) and (b) the spectra deviate in the low frequency region at approx. 1 Hz. This might be related to a comparably larger gas diffusion process at the air side [161] with respect to a stack-like contacting in the pressurized test bench in comparison to ideal contacting in the atmospheric test bench (see chapter 5.3.3). Processes in the DRT above 10 Hz remain in a similar frequency region.

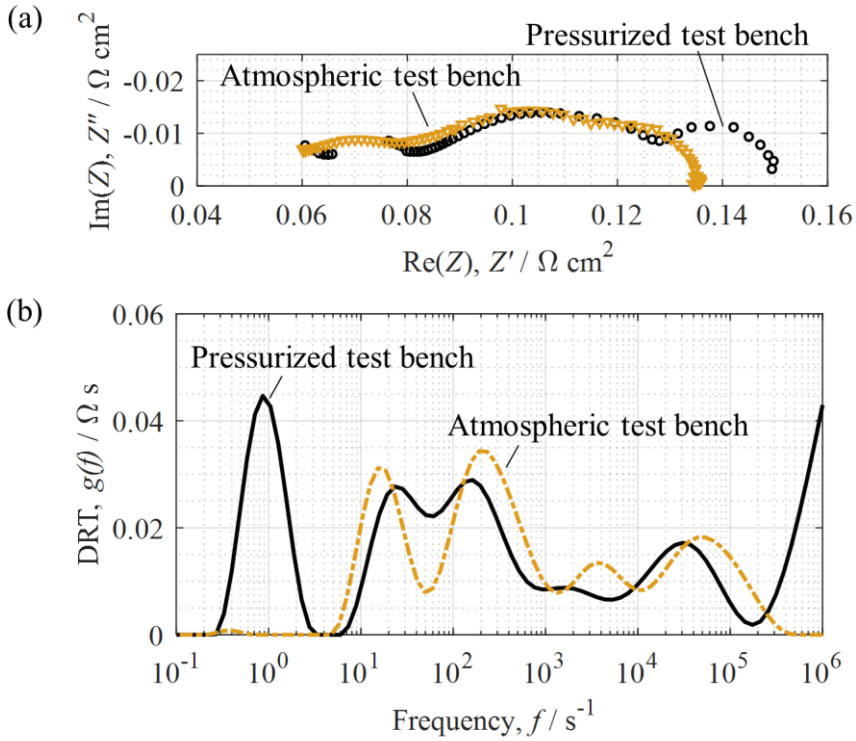

Figure 56 (a) Impedance spectra and (b) DRT of an ASC with Ni/YSZ fuel electrode between the test bench for atmospheric and pressurized conditions at $T = 800$ °C with 50% H_2 (balance H_2O) and synthetic air at the air side at atmospheric conditions.

5.4.2.2 Open-Circuit Voltage

The open-circuit voltage is shown as a function of the absolute pressure which is increased up to 6 bar_a in Figure 57 for 90% H_2 (balance H_2O) and synthetic air at the air side at 700 °C, 750 °C and 800 °C. With a simulated leackage of 1.3% H_2O the increase of OCV with increasing pressure can be described with a relative error of $< 1\%$.

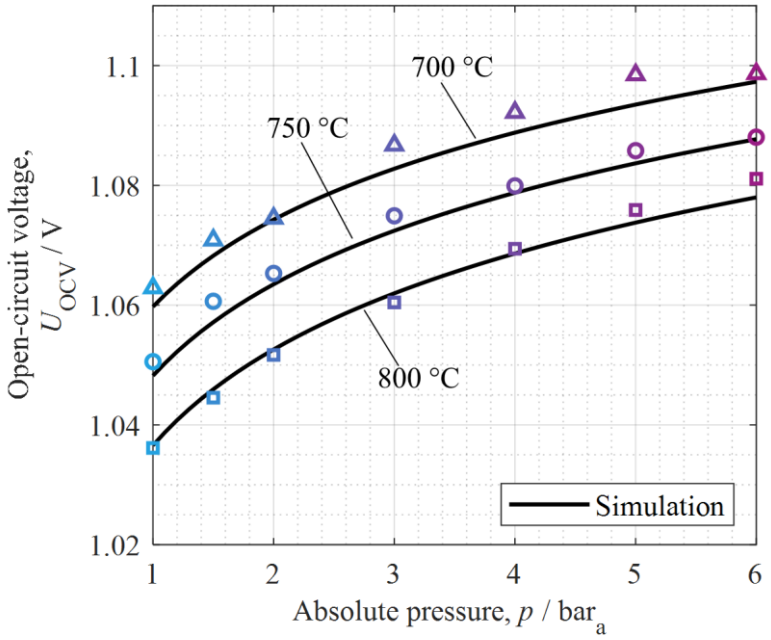

Figure 57 OCV as a function of the absolute pressure at 90% H_2 (balance H_2O) and synthetic air at the air side at 700 °C, 750 °C and 800 °C (simulation with 1.3% leackage H_2O).

5.4.2.3 Impedance Analysis

Reference measurements of the test were taken at atmospheric conditions and $T = 800$ °C with 50% H_2 (balance H_2O) and synthetic air at the air side and are presented in Figure 58 with impedance spectra in (a) and DRT in (b) with the extracted ohmic R_0 and polarization resistance R_{pol} in (c). These measurements were conducted at the beginning (denoted: 1), after approx. 23 h (denoted: 2), 40 h (denoted: 3) and at the end of the test (denoted: 4). As shown in Figure 58 (a) and (c) the ohmic resistance is increasing by a factor of ≈ 14 within 100 h of testing time. The polarization resistance increases within the first 40 h of testing and then decreased to 0.4 Ω cm² again without reaching the initial value of 0.098 Ω cm². In between the first and second reference measurement an unstable pressure setting caused voltage cycling between 0.68 V and 0.97 V which might be partly responsible for a pronounced degradation of the cell. However, the ohmic resistance and polarization resistance continue to increase afterwards as a variation of pressure at $T = 800$ °C between $1 - 6$ bar_a was conducted. For a fuel gas mixture of 90% H_2 (balance H_2O) and synthetic air at the air side this is shown in Figure 59 (a) for the DRT. At approx. 10^2 Hz the peak seems to increase with increasing pressure which is contradictory to the expected impact of pressure towards the cell behavior. The peak at 10^2 Hz is usually assigned to the oxygen surface exchange coupled with O^{2-} diffusion in the bulk of the air electrode [205] and should decrease with pressure [33]. This is the case for $T = 750$ °C in (b) and (c) at $T = 700$ °C. With respect to the reference measurements, the cell behavior cannot be related to the change in pressure independently. Regarding the uncoated Crofer 22 H cell housing sealed with a glass ceramic sealing, an impact of Cr- and/or Si-poisoning of the air electrode cannot be excluded.

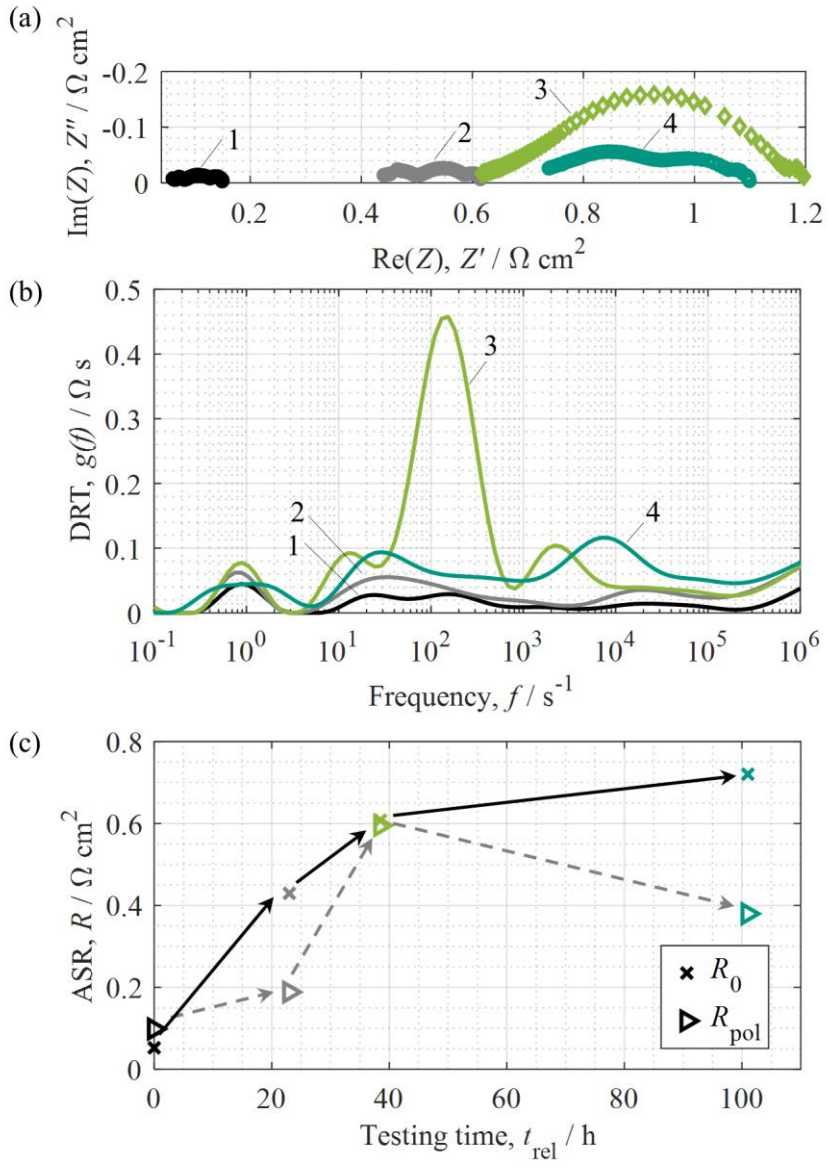

Figure 58 (a) Impedance spectra and (b) DRT of an ASC with Ni/YSZ fuel electrode at $T = 800$ °C with 50% H_2 (balance H_2O) and synthetic air at the air side at atmospheric conditions.

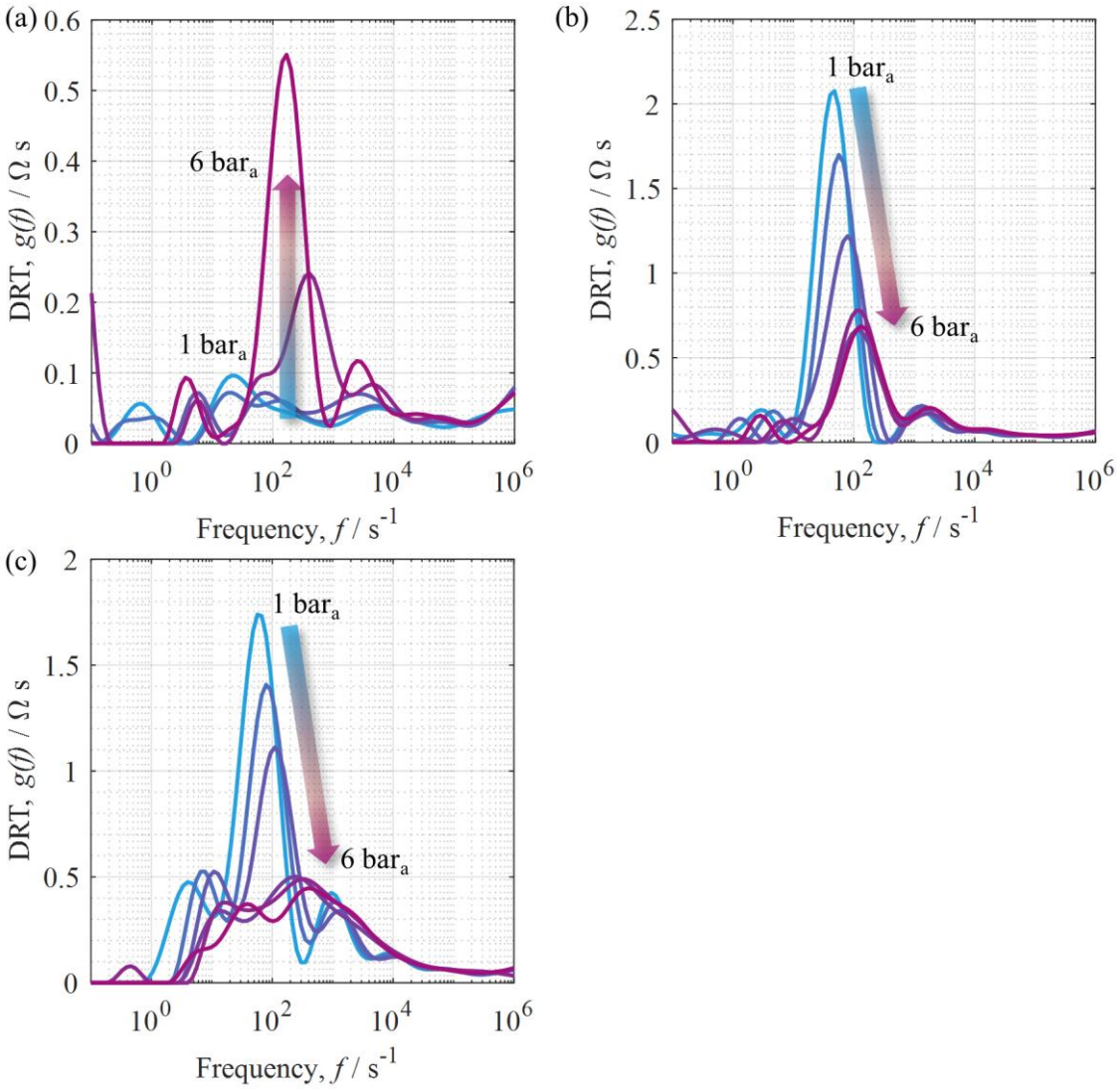

Figure 59 DRT of a pressure variation between 1 – 6 bar_a in steps of 1 bar_a with 90% H_2 (balance H_2O) and synthetic air at the air side in (a) at $T = 800$ °C, (b) at $T = 750$ °C and (c) at $T = 700$ °C.

5.4.3 Optimization Remarks

In this work, a new test bench for pressurized testing without pressure vessel was designed and demonstrated for the first time. It is based on existing testing technology [28], which was developed and optimized for several decades. Thus, the optimization process for pressurized testing is not finished with this work and will be continued in the future. In the following, the experience with the first tests is summarized with remarks on optimization.

5.4.3.1 Flow Field Contact Force

The test bench for atmospheric conditions (see chapter 4.2) is equipped with a decoupled mechanism to apply a defined contact force onto the flow field towards the cell. In terms of sealing at higher pressures, this was not yet solved for pressurized operation yet. In addition, the clamping

of the metal cell housing with Al_2O_3-plates and rods inhibits a similar solution compared to chapter 4.2. In this work, a liquid contact paste was applied during cell mounting, which supports a sufficient contacting between flow field and electrode. However, with respect to an initial dry contact layer during cell mounting a defined contact force on the flow field is needed as shown in Ref. [252].

5.4.3.2 Sealing

In a first step, sealing was realized with a glass ceramic sealing paste. As shown by the measurements of the open-circuit voltage in Figure 52 and Figure 57, this works well for the planar cells. However, the required efforts for cleaning the metallic housing after testing remain a disadvantage for quick re-mounting of the next cell for testing. Other sealing concepts and materials such as compression gaskets are also of interest [268,269]. However, a higher leakage rate is expected for these sealants and needs to be tolerated. This will be investigated in future works with this test bench.

5.4.3.3 Testing with Crofer 22 H Housing

The application of the Crofer 22 H cell housing requires a modification in order to minimize an impact of the cell housing towards the cell behavior. Thus, the metallic surface of the gas tubes needs to be minimized to avoid Cr-evaporation and subsequent poisoning of the air electrode. The inside of the metallic housing is replaced by a ceramic inlay as shown in Figure 60 (a) and (b) with an ideal contacting to create more inert conditions for cell testing, which will be tested in future work.

Alternatively, the metallic surface of the Crofer 22 H needs to be covered with a protective coating. However, due to the complex shape with inner gas channels a homogeneous application of such coating remains critical.

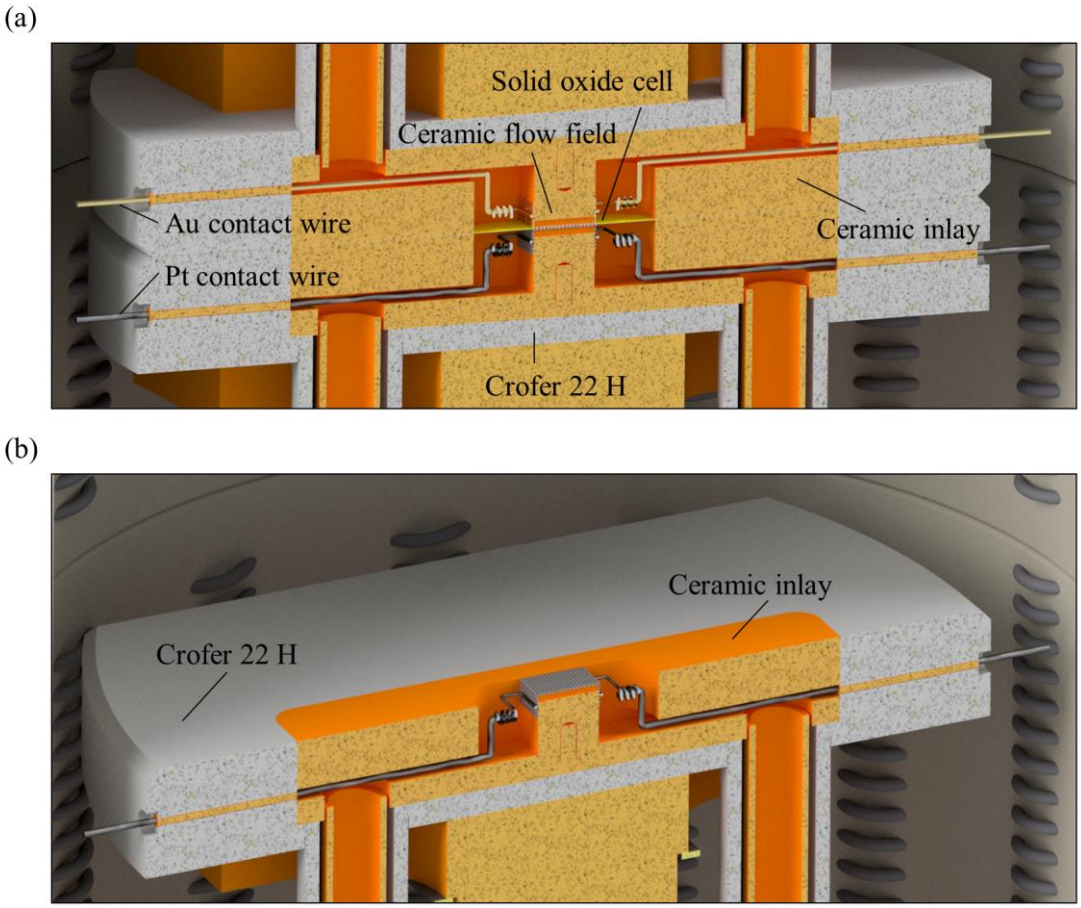

Figure 60 Modification of cell housing made of Crofer 22 H with ceramic inlay.

6 Conclusion and Outlook

In this thesis, solid oxide cells were electrochemically characterized and modeled on the way towards pressurized stacks. This included development of appropriate testing methodologies and test benches and the analysis of intrinsic losses of the cell as well as the impact of stack-like and pressurized conditions.

First, the intrinsic losses of an electrolyte-supported cell with Ni/GDC fuel electrode were described under atmospheric conditions based on a zero-dimensional dc performance model. The model precisely predicts the current-voltage characteristics over a wide temperature and gas composition range with its parametrization based on electrochemical impedance spectroscopy. In order to deconvolute the gas diffusion polarization of the Ni/GDC fuel electrode with a subsequent quantification, symmetrical cells were applied. Further, it required a method to isolate the gas diffusion process by changing a ternary inert gas mixture with nitrogen and helium respectively. An effective gas diffusion geometry parameter was defined and quantified by the difference in polarization resistance between the two inert gas mixtures. This allowed the calculation of the gas diffusion resistance for various operating conditions. For the first time, the loss contributions of gas diffusion and activation within a Ni/GDC fuel electrode were successfully separated and quantified in this work. This aproach was later on applied in the analysis of various Ni/GDC electrodes. The model demonstrated an excellent capability for accurate cell performance prediction, which was validated with experimental IV-curves over a wide range of operating conditions in both SOFC and SOEC mode. In addition, it was extended from H_2/H_2O to CO/CO_2 fuel gas mixtures for fuel cell and electrolyzer mode. Here, an excellent concordance of simulated IV-curves compared to measurements was achieved over a wide temperature range and varying gas compositions. Gas diffusion and activation losses were only slightly larger for CO/CO_2 operation compared to H_2/H_2O mode. Finally, the ohmic losses of the electrolyte-supported cell remained dominant, so that a comparable similar performance between H_2/H_2O and equivalent mixtures of CO/CO_2 was observed.

In a SOC stack the cells are in contact with metallic interconnectors resulting in additional loss mechanisms besides the intrinsic losses of the cell. Thus, different steel grades (Crofer 22 APU, AISI 441, UNS S44330) were investigated with a stack-like contacting of single cells. Here, metallic interconnectors were investigated with respect to their electrochemical behavior in the un- as well as CeCo coated state. Uncoated metallic interconnectors showed severe performance and contact losses, and based on a post-mortem analysis differences in performance could be correlated to different Cr-oxide scale layers of the MICs at the air side. A performance similar to the ideal contacting with ceramic flow fields could not be reached as an effective cap layer to avoid Cr poisoning of the LSCF electrode was missing. In comparison, metallic interconnectors coated with a CeCo PVD coating performed closely to the ideal contact set-up irrespective of the steel grade as similar Cr-oxide scales as well as Co-Mn-Oxide layers are formed at the air side. The contact resistance was decreased significantly by the coating of the metallic interconnector. In addition, due to less Cr-evaporation and subsequent poisoning of the air electrode, the polarization resistance was decreased by coating the interconnector. Finally, the correlation of

electrochemical measurements and microstructural analysis of the metallic interconnectors and the air electrode by SEM-EDX-analysis revealed that a protective coating is mandatory for high-performing solid oxide cell stacks.

The knowledge gained regarding the intrinsic losses as well as stack-like contacting is crucial for pressurized testing as the same cell type and similar stack-like contacting were utilized. In this work, a new pressurized single cell test site without pressure vessel was developed based on existing SOC testing technology. The cells were sealed in a newly developed metal housing made of an aluminium oxide forming steel grade by a glass ceramic sealant that enabled pressurization of fuel and air compartments up to 11 bar_a. In addition, a new and unique pressure regulation concept was designed and applied to minimize the differential pressures between the fuel and air sides. In comparison to complex differential pressure control strategies, a single pressure controller is applied behind a downstream off-gas burning unit which unites fuel and oxidant flow. The glass-ceramic sealed metal housing could withstand thermal cycling without mechanical failure as well as pressure variations between 1 to 11 bar_a. Predictions based on literature and the Nernst-equation regarding the pressure dependency were confirmed and excellent sealing with OCV values of up to 1.42 V were reached. An increase of power density of up to 20% was observed in SOFC-mode which was in good agreement with simulation results of the zero-dimensional performance model. As expected, the increase in OCV resulted in a slightly higher electrical power demand for SOEC. Pressurization resulted in an expected decrease of the different polarization processes, as shown by impedance spectroscopy and the subsequent distribution of relaxation times. The sealing concept was also adapted to enable testing of anode-supported cells with the help of a ceramic frame, which was sealed with a glass ceramic sealing. Here, an uncoated Crofer 22 H housing was applied. However, due to Cr-evaporation and subsequent poisoning of the air electrode, a protective coating or shielding by ceramic parts needs to be applied in a future version of the Crofer 22 H housing.

All in all, the sealing concept developed for single cells in this work could be transferred to pressurized solid oxide cell stacks in a future work.

7 Appendix

In the following appendix the parameters needed for calculating the gas diffusion coefficients are summarized from Ref. [258].

7.1 Lennard-Jones-Energy

In relation to the Boltzmann constant k_B the Lennard-Jones-energies ζ_i are listed in Table A 1 for the species i including hydrogen (H_2), steam (H_2O), oxygen (O_2), nitrogen (N_2), helium (He), carbon monoxide (CO) and carbon dioxide (CO_2) [258].

Table A 1. Lennard-Jones-Energies for hydrogen (H_2), steam (H_2O), oxygen (O_2), nitrogen (N_2), helium (He), carbon monoxide (CO) and carbon dioxide (CO_2) [258].

Parameter	Unit	H_2	H_2O	O_2	N_2	He	CO	CO_2
$\frac{\zeta_i}{k_B}$	K	59.7	809.1	106.7	71.4	10.2	91.7	195.2

According to equation (74), the Lennard-Jones-Energy can be calculated for a binary mixture ζ_{ij} with the components i and j.

$$\zeta_{ij} = \sqrt{\zeta_i \cdot \zeta_j} \tag{74}$$

The defined collision integral Ω_D in equation (75) is needed for calculating the diffusion coefficient by Chapman-Enskog with the coefficients A, B, C, D, E, F_2 *and* G as well as the reduced temperature T^*. The latter is shown in equation (76) depending on the Boltzmann constant k_B, Lennard-Jones-Energy ζ_{ij} and Temperature *T*.

$$\Omega_D = \frac{A}{(T^*)^B} + \frac{C}{exp(D \cdot T^*)} + \frac{E}{exp(F_2 \cdot T^*)} + \frac{G}{exp(H \cdot T^*)} \tag{75}$$

$$T^* = \frac{k_B \cdot T}{\zeta_{ij}} \tag{76}$$

The coefficients of the collision integral are listed in Table A 2.

Table A 2. Coefficients for the collision integral.

A	B	C	D	E	F_2	G	H
1.06036	0.15610	0.19300	0.47635	1.03587	1.52996	1.76474	3.89411

7.2 Lennard-Jones-length

The Lennard-Jones-Length σ_i is also required for calculating the gas diffusion coefficient. The values for hydrogen (H_2), steam (H_2O), oxygen (O_2), nitrogen (N_2), helium (He), carbon monoxide (CO) and carbon dioxide (CO_2) are listed in Table A 3.

Table A 3. Lennard-Jones-lengths for hydrogen (H_2), steam (H_2O), oxygen (O_2), nitrogen (N_2), helium (He), carbon monoxide (CO) and carbon dioxide (CO_2) [258].

Parameter	Unit	H_2	H_2O	O_2	N_2	He	CO	CO_2
σ_i	$\dot{A}$	2.827	2.641	3.467	3.798	2.55	3.69	3.941

Considering the Lennard-Jones-Length of a binary mixture, equation (77) is applied.

$$\sigma_{ij} = \frac{\sigma_i + \sigma_j}{2} \tag{77}$$

7.3 Parametrization and Modeling of an ASC with Ni/YSZ Fuel Electrode

The ASC with Ni/YSZ fuel electrode was characterized at atmospheric conditions on the basis of Ref. [36], where an impedance-based zero-dimensional dc performance model was developed. This was adapted to the cell used in this work with the same equivalent circuit model and is thus only summarized here.

Figure 61 demonstrates the need for an updated parametrization of the cell used in this work since a performance increase in comparison to the former cell can be observed in electrolysis mode at 750 °C with 50% H_2 (balance H_2O) and air at the air side.

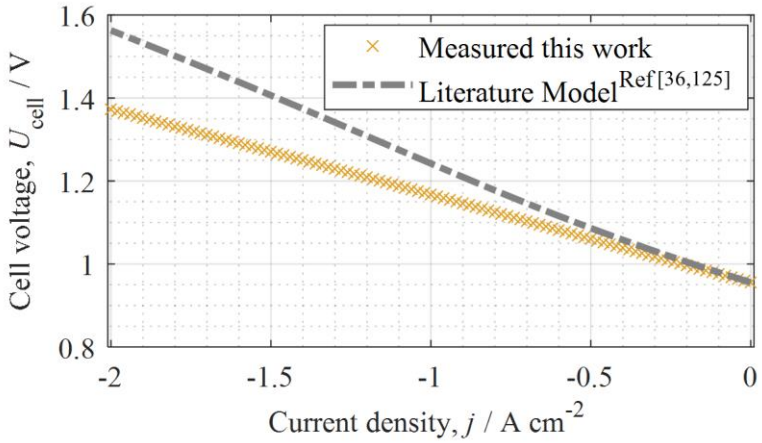

Figure 61 IV-characteristics in electrolysis mode for an ASC with Ni/YSZ fuel electrode measured in this work in comparison to a simulation from a former work [36,125] at $T = 750$ °C with 50% H_2 (balance H_2O) and synthetic air at the air side.

The model parameters found in this work are compared with Ref. [36,62] in Table A 4.

Table A 4. Model paramters for an ASC with Ni/YSZ fuel electrode, 8YSZ electrolyte and LSCF air electrode from this work in comparison to a former work**.**

Parameter	Unit	Former work	This work
$E_{\mathrm{act,ohm}}$	kJ mol^{-1}	90.31 [36]	79.06
B_{ohm}	S·K·m^{-2}	$4.19 \cdot 10^{12}$ [36]	$1.4 \cdot 10^{12}$
$E_{\mathrm{act,FE}}$	kJ·mol^{-1}	105.04 [36]	86.3
$B_{\mathrm{act,FE}}$	Ω·m^2	$3.83 \cdot 10^{-11}$ [36]	$1.61 \cdot 10^{-10}$
a	-	-0.1 [36]	-0.1
b	-	0.33 [36]	0.04
α_{FE}	-	0.727 [62]	0.72
ψ_{FE}	-	0.13 [36]	0.072
L_{FE}	µm	1000 [36]	500
$E_{\mathrm{act,AE}}$	kJ·mol^{-1}	139.86 [36]	141.6
$B_{\mathrm{act,AE}}$	Ω·m^2	$4.03 \cdot 10^{-13}$ [36]	$3.53 \cdot 10^{-13}$
m	-	0.22 [36]	0.11
α_{AE}	-	0.726 [62]	0.53
ψ_{AE}	-	0.022 [36]	0.025

The partial pressure of H_2 is varied for measured (symbols) and simulated (line) current-voltage characteristics in Figure 62 at $T = 750$ °C with 20%, 40%, 50%, and 60% H_2 (balance H_2O) and synthetic air at the air side.

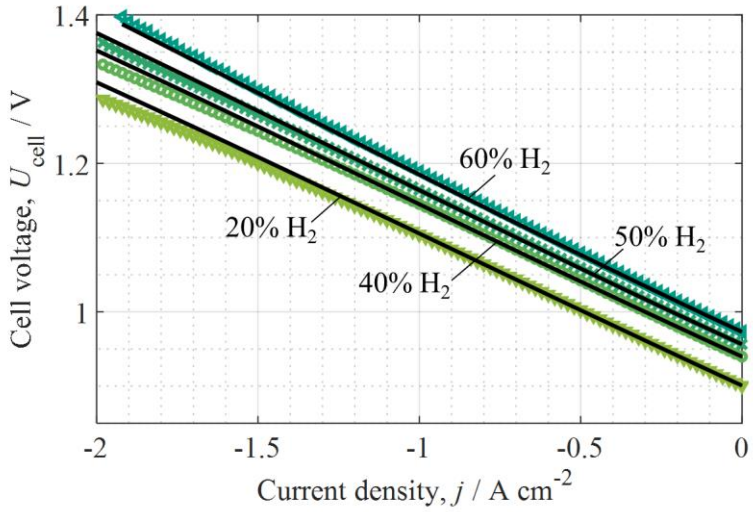

Figure 62 IV-characteristics in electrolysis mode measured (symbols) and simulated (line) for an ASC with Ni/YSZ fuel electrode at $T = 750$ °C with 20%, 40%, 50%, and 60% H_2 (balance H_2O) and synthetic air at the air side.

A variation of temperature between $T = 700$ °C, 750 °C and 800 °C with 50% H_2 (balance H_2O) and air at the air side is shown in Figure 63. The simulated current-voltage curve is experimentally validated with an error of less than 2%.

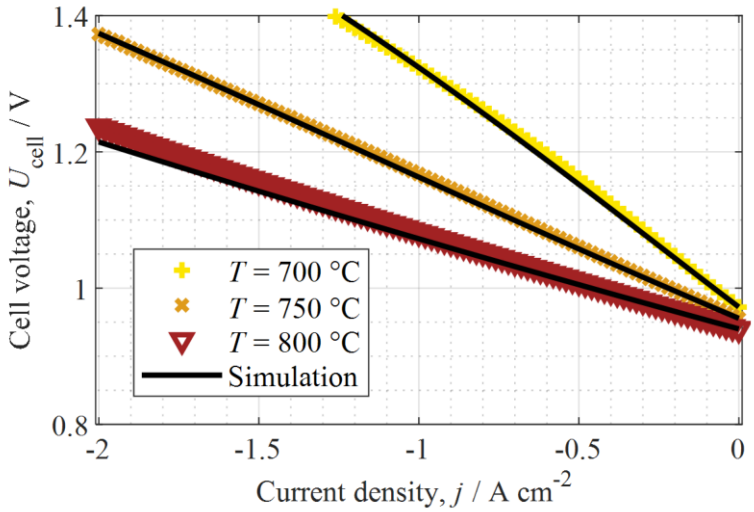

Figure 63 IV-characteristics of the ASC with Ni/YSZ fuel electrode measured and simulated (black line) at $T = 700$ °C, 750 °C and 800 °C with 50% H_2 (balance H_2O) and synthetic air at the air side.

The resulting voltage losses are shown in Figure 64 at $T = 750$ °C with 50% H_2 (balance H_2O). For this cell, ohmic losses have the largest impact on performance. In addition, activation losses at fuel and air side have a larger influence in comparison to gas diffusion losses.

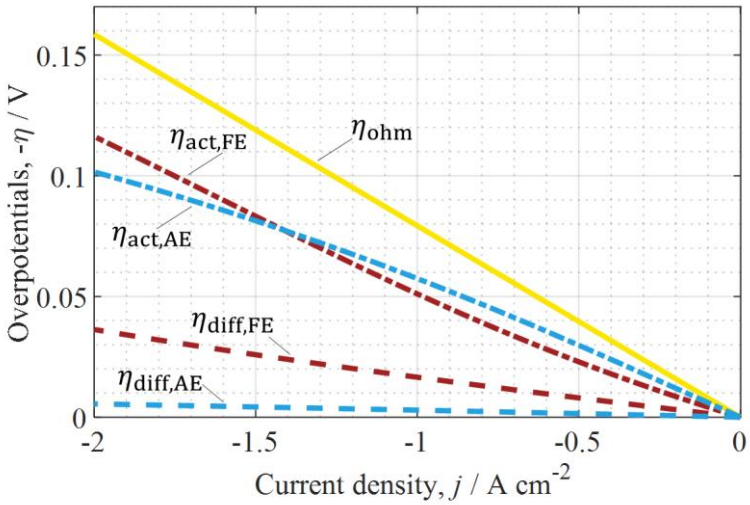

Figure 64 Individual voltage losses of the ASC with Ni/YSZ fuel electrode in electrolysis mode at $T = 750$ °C with 50% H_2 (balance H_2O) and synthetic air at the air side.

7.4 Characterization of a symmetrical Cell with LSCF Electrodes[1]

The characterization of the air electrode follows the approach by Leonide et al. [104] with no further extension regarding the extraction of the model parameters. In addition, no further significant results were observed during this work. For this reason, this part is shown in the appendix with the determination of the microstructure parameter Ψ_{AE}, the activation energy $E_{act,AE}$, the exponent m and the prefactor γ_{AE} of the air electrode.

7.4.1 Equivalent Circuit Model Air Electrode

Processes occurring at the LSCF air electrode are described with the equivalent circuit model developed by Leonide et al. [104], which has been used in previous studies [68,256]. Though, gas diffusion is described by an RQ-element. Furthermore, the coupling of charge transfer and solid-state diffusion of oxygen ions is specified by a Gerischer-element [53]. As mentioned above, processes at higher frequencies are accounted for the ohmic resistance.

7.4.2 Microstructure Parameter Air Electrode

In this work an LSCF air electrode similar to Leonide et al. [104] is applied. The loss mechanisms at the air electrode become isolated by observing symmetrical cells. Figure 65 (a) shows the DRT of a variation of the oxygen partial pressure of a symmetrical cell with LSCF elec-

[1] Results of this chapter were partly generated in the master thesis by C. Grosselindemann (2020) [30] and re-worked in the beginning of the PhD with finally publishing in C. Grosselindemann et al., *ECS Trans*., **103**, 1375-1393 (2021) [37] and in C. Grosselindemann et al., *J. Electrochem. Soc*., **168**, 124506 (2021) [38].

trodes with a gas mixture of 5%, 2% and 1% oxygen (balanced with N_2) at a temperature of 800 °C. The gas diffusion process is apparent in a frequency range of $0.5 - 10$ Hz [104] and it´s contribution to the polarization resistance is extracted with a CNLS-fit. The resulting gas diffusion resistance using the ASR values of a single electrode are shown in a double logarithmic plot in Figure 65 (b).

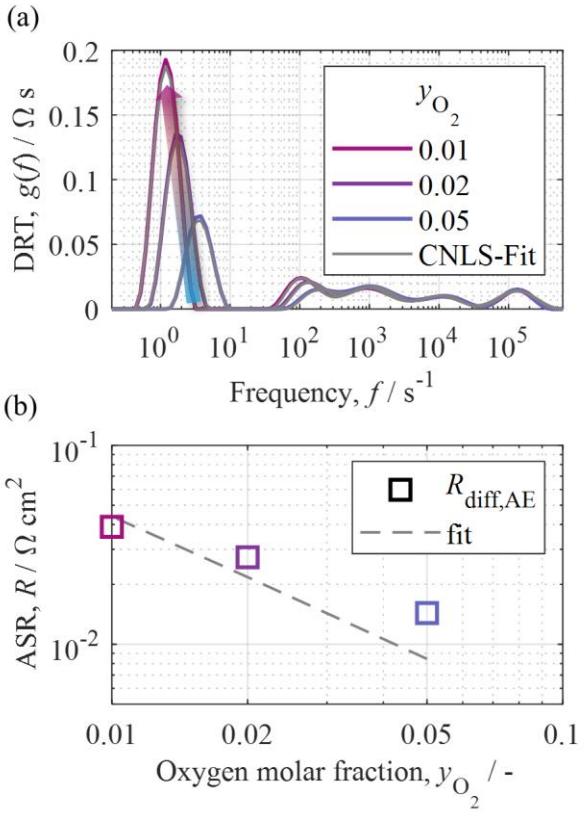

Figure 65 (a) DRT of a variation of the oxygen partial pressure of a symmetrical cell with LSCF electrodes with a gas mixture of 5%, 2% and 1% oxygen (balanced with N_2) at a temperature of 800 °C and (b) gas diffusion resistance from CNLS-fit using ASR values of a single electrode. Taken from Ref. [38].

The trend of the gas diffusion resistance as a function of the oxygen partial pressure can now be approximated with the help of equation (33) using a solver with a least-squares method in order to determine the unknown microstructure parameter Ψ_{AE} of the air electrode.

The gas diffusion length in this case remains unknown. Although, the gas diffusion within the gold-mesh is contributing to it as well [257], for the purpose of comparison to the work of Leonide [104], the gas diffusion length is set to the thickness of the single air electrode of 47 µm from the symmetrical cell. In addition, Knudsen-Diffusion needs to be considered in this case [104]. Therefore, the gas diffusion coefficient for oxygen is calculated by the Bosanquet-approach with the help of the molecular gas diffusion coefficient ($D_{O_2,mol} = 1.7879 \cdot 10^{-4}$ m^2 s^{-1}, $T = 800$ °C) as well as Knudsen-Diffusion coefficient D_{Kn,O_2}. An estimated pore radius of

600 nm was set for the determination of $D_{\mathrm{Kn,O_2}}$ resulting to $D_{\mathrm{Kn,O_2}} = 3.3705 \cdot 10^{-4}$ m² s⁻¹ at a temperature of 800 °C.

Finally, a microstructure parameter of $\Psi_{\mathrm{AE}} = 0.048$ is determined. In this case, the trend of the measured gas diffusion resistance cannot be described precisely enough with equation (33). The latter can presumably be explained by the application of a revised generation of LSCF electrodes with a likely higher porosity. Imprecision also might be explained by an estimated pore diameter. The application of a pore size distribution was beyond of the scope of this work.

7.4.3 Activation Energy Air Electrode

In order to determine the activation energy of the air electrode $E_{\mathrm{act,AE}}$ a variation of temperature between 600 °C and 900 °C in steps of 50 °C with a gas mixture of 21% O_2 (balanced with N_2) of a symmetrical air electrode is shown in Figure 66. At comparably low frequencies between $10 - 20$ Hz the gas diffusion process is apparent, as it only shows a slight correlation with temperature. In a frequency range between $100 - 400$ Hz the activation process of the air electrode indicates a clear activation by temperature. In the equivalent circuit model, this process is described by a Gerischer element [256]. By extracting the activation resistance with a CNLS-fit, it can be plotted in an Arrhenius-plot in Figure 67 using the ASR values of a single air electrode. Here, a grey area is marked with resistances of less than 10 mΩcm², indicating the possibility of measurement imprecisions as the boundaries of the frequency response analyzer are reached. However, this does not seem to have an influence yet.

The linear trend leads to Arrhenius behavior resulting in an activation energy of the air electrode of $E_{\mathrm{act,AE}} = 144.54$ kJ mol⁻¹ from the value of the slope. In addition, the cell specific constant yields to $B_{\mathrm{AE}} = 1.5185 \cdot 10^{-10}$ Ωcm². In comparison, the LSCF electrode characterized by Leonide [104] holds values of $E_{\mathrm{act,AE}} = 139.86$ kJ mol⁻¹ and $B_{\mathrm{AE}} = 4.032 \cdot 10^{-9}$ Ωcm². The deviation between the activation energies is less than 3% and with regard to a state-of-the-art electrode comparably small. Further, the cell specific constant in this case is smaller, which presumably can be explained by the application of synthetic air with 21% O_2 and 79% N_2. Thereby, contaminants present in air from the environment can be neglected.

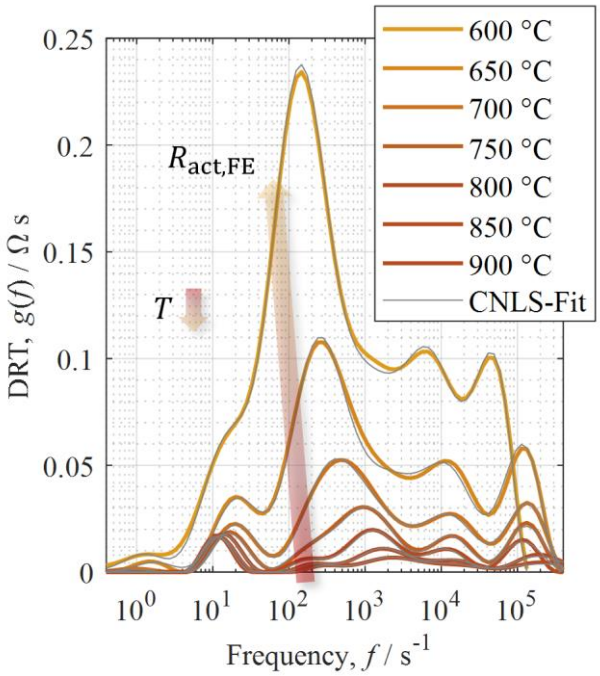

Figure 66 DRT of a temperature variation between 600 °C and 900 °C in steps of 50 °C with a gas mixture of 21% O_2 (balanced with N_2) of a symmetrical air electrode. Taken from Ref. [38].

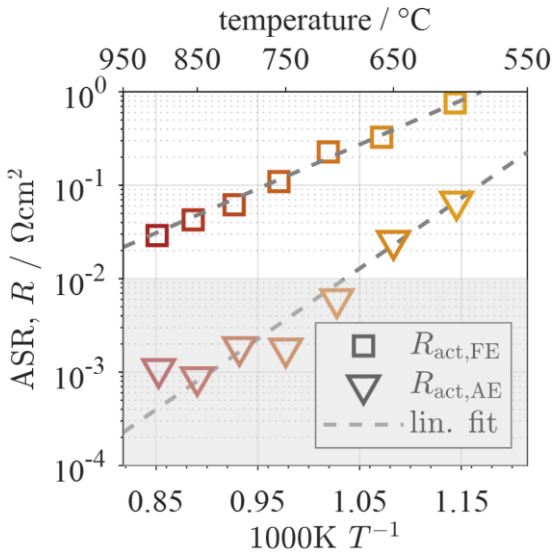

Figure 67 Arrhenius plot for a temperature variation from 600 °C to 900 °C in steps of 50 °C using the ASR values of a single fuel electrode with a gas mixture of 80% H_2 (balance H_2O) and a single air electrode with 21% O_2 (balance N_2). Taken from Ref. [38].

In addition, the activation resistances of the fuel electrode (using the ASR values of a single electrode) are also displayed and differ by an order of magnitude to the air electrode. Therefore, the activation process of the latter can presumably be neglected when simulating the dc mode as shown above.

7.4.4 Exponent m

The extraction of the exponent m describing the oxygen partial pressure dependency of the air electrode´s exchange current density follows the approach by Leonide et al. [104] as well. In Figure 68 (a) the DRT of a symmetrical cell with LSCF air electrodes is shown at a temperature of $T = 800$ °C. The data is based on a variation of the oxygen partial pressure with 21%, 12%, 5%, 2%, 1% (balanced with N_2). Subsequently, in Figure 68 (b) the resulting activation resistance using the ASR values of a single air electrode is plotted in a double logarithmic scale as a function of the oxygen partial pressure and fitted with a power law approach. The exponent m is then extracted by the negative value of the slope of the fit resulting in a value of $m = 0.42$. In comparison to Leonide et al., the exponent m in this case is larger by about a factor of two.

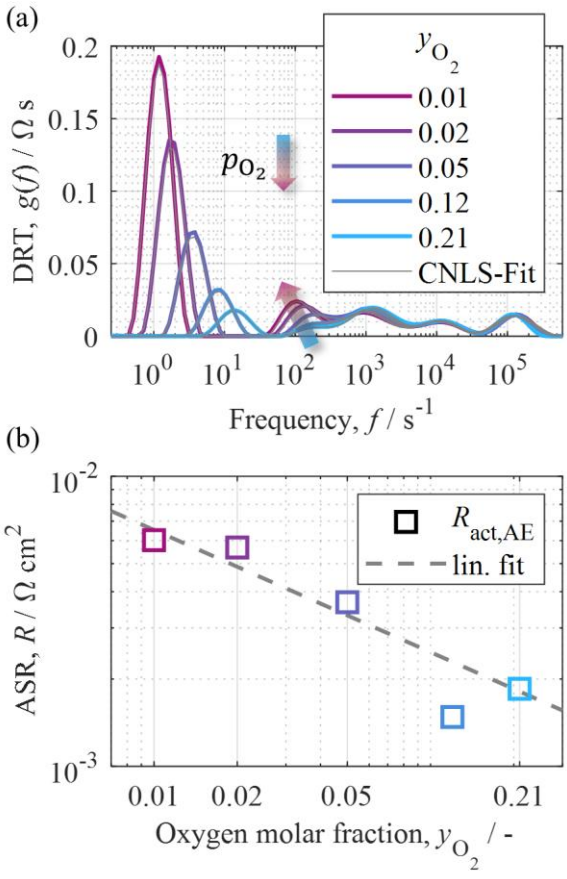

Figure 68 (a) DRT of a variation of the oxygen partial pressure at a temperature of $T = 800$ °C with 21%, 12%, 5%, 2%, 1% (balanced with N_2) and (b) determination of the exponent m using the ASR values of a single electrode. Taken from Ref. [38].

7.4.5 Prefactor γ_{AE}

The exponential prefactor γ_{AE} can be determined with the help of equation (78) [104]. The above-mentioned evaluation of the variation of temperature was performed with 21% O_2 at

atmospheric pressure. Thus, these conditions were set in order to determine the prefactor γ_{AE}. With the above-mentioned exponent m and the cell specific constant B_{AE} a value of $\gamma_{\mathrm{AE}}(T) = 5.47 \cdot 10^{9}\ (\mathrm{A\ m^{-2}\ K^{-1}}) \cdot T$ was determined compared to $\gamma_{\mathrm{AE}}(T) = 1.52 \cdot 10^{8}(\mathrm{A\ m^{-2}K^{-1}}) \cdot T$ from Leonide et al. [104].

$$\gamma_{\mathrm{AE}} = \frac{\tilde{R}T}{2FB_{\mathrm{AE}}} \cdot \left[\left(\frac{p_{\mathrm{O_2}}}{p_{\mathrm{ref}}}\right)^{m}\right]^{-1} \tag{78}$$

7.5 0D Model Parameters CO/CO_2[2]

Table A 5. Model parameters of the zero-dimensional cell model adapted to a solid oxide cell with Ni/GDC fuel electrode, 3YSZ electrolyte and LSCF air electrode for operation in CO/CO_2.

Parameter	Unit	Value
$E_{\mathrm{act,ohm}}$	J mol^{-1}	$1000\ \mathrm{K} \cdot \tilde{R}\ \left(2\ k_1\ x + k_2 + \frac{1}{x}\right)$ with $x = \frac{1000\ \mathrm{K}}{T}$ [38]
B_{ohm}	K Ω^{-1} m^{-2}	$\frac{1000\ \mathrm{K}}{x}\frac{10^4}{\Omega\ \mathrm{m^2}} \cdot \exp\left(-\left(k_1\ x^2 + k_2\ x + k_3 - \frac{E_{\mathrm{act,ohm}}}{1000\ \mathrm{K}\cdot\tilde{R}} \cdot\ x\right)\right)$ [38]
k_1	-	13.2739
k_2	-	-16.643
k_3	-	3.5519
$E_{\mathrm{act,FE}}$	kJ mol^{-1}	111.51
B_{FE}	Ω m^2	$3.0295 \cdot 10^{-11}$
$c(T)$	-	$\frac{0.0017}{\mathrm{K}} \cdot T - 1.6136$
$d(T)$	-	$\frac{0.00063}{\mathrm{K}} \cdot T - 0.5527$
$\gamma_{\mathrm{FE}}(T)$	A m^{-2}	$1.42 \cdot 10^{6}\ (\mathrm{A\ m^{-2}\ K^{-1}}) \cdot \left[0.4^{c(T)} \cdot 0.6^{d(T)}\right]^{-1} \cdot T$
$\alpha_{\mathrm{FE,SOEC}}$	-	0.67
$\alpha_{\mathrm{FE,SOFC}}$	-	0.42
G_{eff}	m^{-1}	736.87 [38]
$E_{\mathrm{act,AE}}$	kJ mol^{-1}	144.54 [38]
B_{AE}	Ω m^2	$1.5185 \cdot 10^{-14}$ [38]

[2] Parts of this chapter have been published in C. Grosselindemann et al., *Fuel Cells*, **23**, 442-453 (2023) [128].

m	-	0.42 [38]
$\gamma_{\mathrm{AE}}(T)$	A m^{-2}	$5.47 \cdot 10^{9}$ (A m^{-2} K^{-1}) $\cdot\, T$ [38]
α_{AE}	-	0.65 [104]
Ψ_{AE}	-	0.048 [38]

7.6 Chemical Composition MICs[3]

The chemical composition of the three steel grades is listed in the appendix in Table A 6 and Table A 7 [147].

Table A 6. Chemical composition of the uncoated steel grades [147].

Material	C	Si	Mn	P	S	Cr	Ni	Ti
-	%	%	%	%	%	%	%	%
Crofer 22 APU	0.004	0.02	0.44	0.003	<0.002	22.6	0.02	0.06
AISI 441 (1.4509)	0.017	0.41	0.39	0.025	0.001	17.6	0.14	0.13
UNS S44330 (1.4622)	0.015	0.47	0.39	0.029	<0.001	21	0.2	0.14

Table A 7. Part II Chemical composition of the uncoated steel grades [147].

Material	Nb	N	Cu	Mo	Al	Mg	La	Fe
-	%	%	%	%	%			%
Crofer 22 APU	<0.01	0.002	0.01	<0.01	0.013	<0.01	0.1	Bal.
AISI 441 (1.4509)	0.384	-	-	-	-	-	-	Bal.
UNS S44330 (1.4622)	0.36	0.015	0.33	-	-	-	-	Bal.

7.7 Pathways to generate Hydrogen

Green hydrogen: generated by electrolysis of water with electricity from renewable energies. CO_2 free. [270]

Grey hydrogen: Generated by fossil fuels. Approx. 10 t CO_2 per 1 t H_2. CO_2 emissions in atmosphere. [270]

[3] Parts of this chapter have been published in C. Grosselindemann et al., *J. Electrochem Soc.*, **171**, 054508 (2024) [147].

Blue hydrogen: Likewise, to grey hydrogen, but CO_2 is separated and stored, Almost CO_2-neutral overall. [270]

Turqoise hydrogen: generated by thermal splitting of methane (methane pyrolysis). Solid carbon is generated instead of CO_2. [270]

8 Publications

8.1 Journal Paper

C. Grosselindemann, N. Russner, S. Dierickx, F. Wankmüller, and A. Weber, "Deconvolution of Gas Diffusion Polarization in Ni/Gadolinium-Doped Ceria Fuel Electrodes", *J. Electrochem. Soc.*, **168**, 124506 (2021). DOI: 10.1149/1945-7111/ac3d02

M. Ivanova, R. Peters, M. Müller, S. Haas, M. F. Seidler, G. Mutschke, K. Eckert, P. Röse, S. Calnan, R. Bagacki, R. Schlatmann, **C. Grosselindemann**, L.-A. Schäfer, N. H. Menzler, A. Weber, R. van de Krol, F. Liang, F. F. Abdi, S. Brendelberger, N. Neumann, J. Grobbel, M. Roeb, C. Sattler, I. Duran, B. Dietrich, C. Hofberger, L. Stoppel, N. Uhlenbruck, T. Wetzel, D. Rauner, A. Hecimovic, U. Fantz, N. Kulyk, J. Harting, and O. Guillon, "Technological Pathways to Produce Compressed and Highly Pure Hydrogen from Solar Power", *Angew. Chem. Int. Ed.*, e202218850, 2023. doi.org/10.1002/anie.202218850

F. Kullmann, **C. Grosselindemann**, L. Salamon, F.-M. Fuchs, and A. Weber, "Impedance Analysis of electrolyte processes in solid oxide cells", *Fuel Cells*, **23**, 420-429 (2023). doi.org/10.1002/fuce.202300035

C. Grosselindemann, F. Kullmann, T. Lehnert, O. Fritz, F.-M. Fuchs, and A. Weber, "Comparison of a solid oxide cell with nickel/gadolinium-doped ceria fuel electrode during operation with hydrogen/steam and carbonmonoxide/carbon dioxide", *Fuel Cells*, **23**, 442-453 (2023). doi.org/10.1002/fuce.202300060

D. Ewald, **C. Grosselindemann**, D. Esau, F.-M. Fuchs, and A. Weber, "Stack-like Contacting in Solid Oxide Cells: Electrochemical Characterization and Modeling", *J. Electrochem. Soc.*, **171**, 044506 (2024). DOI: 10.1149/1945-7111/ad3a16

C. Grosselindemann, M. J. Reddy, H. Störmer, D. Esau, M. Dorn, F. M. Bauer, D. Ewald, L. Wissmeier, J. Froitzheim, and A. Weber, "Impact of CeCo-Coated Metallic Interconnectors on SOCs Towards Performance, Cr-Oxide-Scale, and Cr-Evaporation", *J. Electrochem. Soc.*, **171**, 054508 (2024). DOI: 10.1149/1945-7111/ad44da

D. Esau, **C. Grosselindemann**, S. Sckuhr, F. Kullmann, A. Lindner, Z. Liang, F.-M- Fuchs and A. Weber, "Electrochemical Characterization of Nickel / Gadolinia Doped Ceria Fuel Electrodes under $H_2/H_2O/CO/CO_2$-Atmospheres", *J. Electrochem. Soc.*, **171**, 054522 (2024). DOI: 10.1149/1945-7111/ad4c10

C. Grosselindemann, M. Dorn, F. M. Bauer, M. Seim, D. Ewald, D. Esau, M. Geörg, R. Rössler, A. Pundt, and A. Weber, "Pressurized Single Cell Testing of Solid Oxide Cells", *J. Power Sources*, **614**, 234963 (2024). doi.org/10.1016/j.jpowsour.2024.234963

S. Korneychuk, **C. Grosselindemann**, N.H. Menzler, A. Weber, and A. Pundt, "In-situ TEM reduction of a solid oxide cell with NiO/YSZ fuel electrode", *J. Power Sources*, **625**, 235626 (2025). doi.org/10.1016/j.jpowsour.2024.235626

8.2 Conference Paper

C. Grosselindemann, N. Russner, S. Dierickx, and A. Weber, "Deconvolution of Gas Diffusion Polarization in Ni/Gadolinium-Doped Ceria Fuel Electrodes", *ECS Trans.*, **103** (1), 1375-1393 (2021). DOI 10.1149/10301.1375ecst

C. Grosselindemann, F. Kullmann, T. Lehnert, H. Pöpke, and A. Weber, "Comparison of an SOC with Ni/CGO Fuel Electrode during Operation with H_2/H_2O and CO/CO_2", *Proceedings of the 15th European SOFC & SOE Forum (EFCF)*, July 5th-8th, 2022.

F. Kullmann, **C. Grosselindemann**, L. Salamon, F.-M. Fuchs, and A. Weber, "Investigation of interface and electrolyte processes of a state-of-the-art SOFC", *Proceedings of the 15th European SOFC & SOE Forum (EFCF)*, July 5th-8th, 2022.

C. Grosselindemann, D. Esau, M. Dorn, F. M. Bauer, L. Wissmeier, and A. Weber, "From Ideal to Stack-like Contacting of an SOC", *ECS Trans.*, **111** (6), 533 (2023). DOI: 10.1149/11106.0533ecst

D. Esau, **C. Grosselindemann**, S. P. Sckuhr, F. Kullmann, L. Wissmeier, and A. Weber, "Characterization of a Nickel/Gadolinia Doped Ceria Fuel Electrode for Co-Electrolysis", *ECS Trans.*, **111** (6), 871 (2023). DOI: 10.1149/11106.0871ecst

S. Korneychuk, **C. Grosselindemann**, L.-A. Schäfer, M. Ivanova, A. Weber, N.H. Menzler, O. Guillon, and A. Pundt, "In-Situ TEM reduction of a solid oxide cell with NiO/YSZ and NiO/BZCY materials for fuel electrode", *Proceedings of the 16th European SOFC & SOE Forum (EFCF)*, Lucerne, July 2nd-5th, 2024.

C. Grosselindemann, M. Dorn, F. M. Bauer, M. Seim, D. Ewald, D. Esau, M. Geörg, R. Rössler, A. Pundt and A. Weber, "Testing of Pressurized Solid Oxide Cells", *Proceedings of the 16th European SOFC & SOE Forum (EFCF)*, Lucerne, July 2nd-5th, 2024.

D. Ewald, **C. Grosselindemann**, D. Esau, F.-M. Fuchs, and A. Weber, "Electrochemical Characterization and Modeling of stack-like Contacting for Solid Oxide Cells", *Proceedings of the 16th European SOFC & SOE Forum (EFCF)*, Lucerne, July 2nd-5th, 2024.

8.3 Conference Contributions (Talks & Poster)

C. Grosselindemann, N. Russner, S. Dierickx, and A. Weber, oral presentation by C. Grosselindemann: "Deconvolution of Gas Diffusion Polarization in Ni/Gadolinium-Doped

Ceria Fuel Electrodes", 17th International Symposium on Solid Oxide Fuel Cells (SOFC XVII - online), July 18th-23rd, 2021.

C. Grosselindemann, F. Kullmann, D. Esau, and A. Weber, poster presentation by C. Grosselindemann: "Experimental Characterization of metallic interconnectors with potential Probes", Workshop on Corrosion and Protection of Interconnects in Connection with the EFCF, Lucerne, Switzerland July 5th, 2022.

C. Grosselindemann, F. Kullmann, T. Lehnert, H. Pöpke, and A. Weber, poster presentation by C. Grosselindemann: "Comparison of an SOC with Ni/CGO Fuel Electrode during Operation with H_2/H_2O and CO/CO_2", 15th European SOFC & SOE Forum (EFCF), Lucerne, Switzerland, July 5th-8th, 2022.

F. Kullmann, **C. Grosselindemann**, L. Salamon, F.-M. Fuchs, and A. Weber, poster presentation by F. Kullmann: "Investigation of interface and electrolyte processes of a state-of-the-art SOFC", 15th European SOFC & SOE Forum (EFCF), Lucerne, Switzerland, July 5th-8th, 2022.

T. Lehnert, F. Wankmüller, **C. Grosselindemann**, C.-Y. Tsai, D. Gerthsen, A. Weber, H. Störmer, poster presentation by T. Lehnert: "Electron Microscopic Characterization of Solid Oxide Electrolyzer Cells (SOEC) after Long-Term Operation", 23rd International Conference on Solid State Ionics (SSI-23), Boston, USA, July 17th-22nd, 2022.

D. Esau, **C. Grosselindemann**, F. Kullmann, T. Lehnert, and A. Weber, poster presentation by D. Esau: "Electrochemical Characterization of a SOC with Ni/CGO Fuel Electrode in H_2O-, CO_2- and Co-Electrolysis", 1. H2Giga Statuskonferenz, Frankfurt, Germany, September 7th-8th, 2022.

C. Grosselindemann, F. Lubik, M. Dorn, and A. Weber, poster presentation by C. Grosselindemann: "0-dimensional Performance Modeling of Solid Oxide Cells under pressurized Conditions", 19th Symposium on Fuel Cell and Battery Modeling and Experimental Validation (ModVal23), Duisburg, Germany, March 21st-23rd, 2023.

A. Koksharov, **C. Grosselindemann**, M. Riegraf, F. Kullmann, D. Esau, N. Russner, R. Costa, A. Weber, A. Latz, and T. Jahnke, poster presentation by A. Koksharov: "2D transient electrochemical model of steam electrolysis with Ni/Gd-Doped ceria (CGO) fuel electrode", 19th Symposium on Fuel Cell and Battery Modeling and Experimental Validation (ModVal23), Duisburg, Germany, March 21st-23rd, 2023.

C. Grosselindemann, D. Esau, M. Dorn, F. M. Bauer, L. Wissmeier, and A. Weber, oral presentation by C. Grosselindemann: "From Ideal to Stack-like Contacting of an SOC", 18th International Symposium on Solid Oxide Fuel Cells (SOFC XVIII), Boston, USA, May 28th- June 2nd 2023.

D. Esau, **C. Grosselindemann**, S. P. Sckuhr, F. Kullmann, L. Wissmeier, and A. Weber, oral presentation by D. Esau: "Characterization of a Nickel/Gadolinia Doped Ceria Fuel Electrode for Co-Electrolysis", 18th International Symposium on Solid Oxide Fuel Cells (SOFC XVIII), Boston, USA, May 28th- June 2nd 2023.

S. Korneychuk, **C. Grosselindemann**, N. H. Menzler, A. Weber and, A. Pundt, oral presentation by S. Korneychuk: "In-situ TEM reduction of a solid oxide cell with NiO/YSZ fuel electrode", The 20th International Microscopy Congress (IMC20), Busan, Korea, September 10th - 15th 2023.

S. Korneychuk, **C. Grosselindemann**, N. H. Menzler, A. Weber and, A. Pundt, oral presentation by S. Korneychuk: "In-situ TEM reduction of a solid oxide cell with NiO/YSZ fuel electrode", FEMS EUROMAT23, Frankfurt, Germany, September 3rd - 07th, 2023.

D. Esau, **C. Grosselindemann** and, A. Weber, poster presentation by C. Grosselindemann: "Hochtemperatur-Festelektrolytzellen: Elektrochemische Charakterisierung", 2. H2Giga-Statuskonferenz, Berlin, Germany, September 20th - 21st, 2023.

S. Korneychuk, **C. Grosselindemann**, L.-A. Schäfer, M. Ivanova, A. Weber, N.H. Menzler, O. Guillon, and A. Pundt, oral presentation by S. Korneychuk: "In-Situ TEM reduction of a solid oxide cell with NiO/YSZ and NiO/BZCY materials for fuel electrode", 18th International Symposium on Metal-Hydrogen Systems, Saint-Malo, France, 26th-31st May 2024.

S. Korneychuk, **C. Grosselindemann**, L.-A. Schäfer, M. Ivanova, A. Weber, N.H. Menzler, O. Guillon, and A. Pundt, oral presentation by S. Korneychuk: "In-Situ TEM reduction of a solid oxide cell with NiO/YSZ and NiO/BZCY materials for fuel electrode", 16th European SOFC & SOE Forum (EFCF), Lucerne, Switzerland, July 2nd-5th, 2024. (Christian Friedrich Schönbein Silver Medal)

C. Grosselindemann, M. Dorn, F. M. Bauer, M. Seim, D. Ewald, D. Esau, M. Geörg, R. Rössler, A. Pundt and A. Weber, poster presentation by C. Grosselindemann: "Testing of Pressurized Solid Oxide Cells", 16th European SOFC & SOE Forum (EFCF), Lucerne, Switzerland, July 2nd-5th, 2024.

C. Grosselindemann, M. Dorn, F. M. Bauer, M. Seim, D. Ewald, D. Esau, M. Geörg, R. Rössler, A. Pundt and A. Weber, oral presentation by C. Grosselindemann: "Testing of Pressurized Solid Oxide Cells", 16th European SOFC & SOE Forum (EFCF), Lucerne, Switzerland, July 2nd-5th, 2024.

D. Ewald, **C. Grosselindemann**, D. Esau, F.-M. Fuchs, and A. Weber, poster presentation by D. Ewald: "Electrochemical Characterization and Modeling of stack-like Contacting for Solid Oxide Cells", 16th European SOFC & SOE Forum (EFCF), Lucerne, Switzerland, July 2nd-5th, 2024.

C. Grosselindemann, D. Esau and, A. Weber, poster presentation by C. Grosselindemann and D. Esau: "Charakterisierung, Alterung und Modellierung von Hochtemperatur-Festelektrolytzellen", 3. H2Giga-Statuskonferenz, Berlin, Germany, September 17th-18th, 2024.

C. Grosselindemann, D. Ewald, M. Deichelbohrer, E. Katzman, D. Esau, M. Langerman, and A. Weber, oral presentation by C. Grosselindemann: “Pressurized testing of solid oxide single cells”, 49th International Conference and Exposition on Advanced Ceramics and Composites, Daytona Beach, Florida, USA, January 26th-31st, 2025.

C. Grosselindemann, D. Ewald, M. Deichelbohrer, E. Katzman, D. Esau, M. Langerman, and A. Weber, poster presentation by C. Grosselindemann: "Pressurized Testing and Modeling of Solid Oxide Single Cells", Symposium on Modeling and Experimental Validation of Electrochemical Energy Technologies (ModVal 2025), Karlsruhe, Germany, March 11th-12th, 2025.

D. Ewald, **C. Grosselindemann**, T. Kasselmann, F. Martinez, M. Noponen, and A. Weber, oral presentation by D. Ewald: "Utilization of a validated 0D approach for 1D SOFC performance modeling", Symposium on Modeling and Experimental Validation of Electrochemical Energy Technologies (ModVal 2025), Karlsruhe, Germany, March 11th-12th, 2025.

D. Esau, F. Kreißig, **C. Grosselindemann**, T. Baumann, J. Daubenthaler, and A. Weber, poster presentation by D. Esau: "2D FEM model for simulation of high temperature steam and co-electrolysis with a nickel/MIEC cermet electrode", Symposium on Modeling and Experimental Validation of Electrochemical Energy Technologies (ModVal 2025), Karlsruhe, Germany, March 11th-12th, 2025.

M. Deichelbohrer, **C. Grosselindemann**, D. Ewald, and A. Weber, poster presentation by M. Deichelbohrer: "Evaluation of Cell Housing Designs for Pressurized Testing of Solid Oxide Single Cells", Symposium on Modeling and Experimental Validation of Electrochemical Energy Technologies (ModVal 2025), Karlsruhe, Germany, March 11th-12th, 2025.

C. Grosselindemann, D. Esau, and A. Weber, poster presentation by C. Grosselindemann and D. Esau: "Zusammenfassung und Ausblick zur elektrochemischen Charakterisierung, Alterung und Modellierung von Hochtemperatur-Festelektrolytzellen", H2Giga Abschlusskonferenz, Frankfurt, Germany, July 2nd, 2025.

C. Grosselindemann, D. Ewald, M. Deichelbohrer, and A. Weber, ***accepted and planned*** oral presentation by C. Grosselindemann: "Testing of Pressurized Solid Oxide Single Cells", 19th International Symposium on Solid Oxide Fuel Cells (SOFC XIX), Stockholm, Sweden, July 13th – 18th, 2025.

D. Ewald, **C. Grosselindemann**, A. Lindner, T. Kasselmann, F. Martinez, M. Noponen, and A. Weber, ***accepted and planned*** oral presentation by D. Ewald: "1D Gas Channel Modeling for SOFC Performance Analysis in Aviation", 19th International Symposium on Solid Oxide Fuel Cells (SOFC XIX), Stockholm, Sweden, July 13th – 18th, 2025.

A. Makvandi, **C. Grosselindemann**, H. Störmer, A. Weber, and Y. M. Eggeler, ***accepted and planned*** poster presentation by A. Makvandi: "Understanding the effect of CeCo-coated metallic interconnectors on the structure and chemistry of LSCF-GDC composite air electrodes using transmission electron microscopy", 19th International Symposium on Solid Oxide Fuel Cells (SOFC XIX), Stockholm, Sweden, July 13th – 18th, 2025.

8.4 Student Theses

„CO_2-Electrolysis of a Solid Oxide Cell with Ni/GDC Fuel Electrode"
Person in charge: Oliver Fritz, September 2021, Bachelor thesis.
Supervisor: Cedric Großelindemann M.Sc., Felix Kullmann M.Sc.

“Sulfur Poisoning SOFC”
September 2021, Seminar thesis.
Supervisor: Cedric Großelindemann M.Sc., Felix Kullmann M.Sc.

„Materials and Properties of Proton Conducting Cells“
Person in charge: Marius Jens Kleinfeld, November 2021, Seminar thesis.
Supervisor: Cedric Großelindemann M.Sc.

„Safe Operating Window of SOCs regarding Carbon Deposition“
Person in charge: Sören C. Drotleff, January 2022, Seminar thesis.
Supervisor: Cedric Großelindemann M.Sc.

“Safe Operating Conditions for Co-Electrolysis of an SOFC with Ni/GDC Fuel Electrode”
Person in charge: Felix Lubik, April 2022, Bachelor thesis.
Supervisor: Cedric Großelindemann M.Sc.

„Impact of Sulfur Components towards Co-Electrolysis“
Person in charge: Sören Peter Sckuhr, August 2022, Bachelor thesis.
Supervisor: Daniel Esau M.Sc., Cedric Großelindemann, M.Sc.

„Investigation of metallic Interconnectors for Solid Oxide Cells under extended Operating Conditions“
Person in charge: Frank Manuel Bauer, Dezember 2022, Master thesis.
Supervisor: Cedric Großelindemann M.Sc.

„Implementing the pressurized Test Bench Components for High-Temperature Electrolysis“
Person in charge: Sven Piduch, June 2023, Technician thesis.
Supervisor: Cedric Großelindemann M.Sc.

„Investigation and Modeling of Gas Conversion of a SOC with Ni/GDC Fuel Electrode“
Person in charge: Jan Daubenthaler, May 2023, Master Thesis.
Supervisor: Daniel Esau M.Sc., Cedric Großelindemann M.Sc.

„Investigation of coated metallic Interconnectors for Solid Oxide Cells“
Person in charge: Marvin Dorn, June 2023, Master thesis.
Supervisor: Cedric Großelindemann M.Sc., Daniel Esau M.Sc.

„Investigation of a new Contact Design for Solid Oxide Electrolysis Cells“
Person in charge: Daniel Tobias Ewald, Oktober 2023, Master thesis
Supervisor: Cedric Großelindemann M.Sc., Daniel Esau M.Sc.

„Investigation of Pressurized Solid Oxide Cells“
Person in charge: Manuel Seim, March 2024, Bachelor Thesis.
Supervisor: Cedric Großelindemann M.Sc.

„Electrochemical Characterization and Parametrization of a High-Performance SOFC for Aviation Applications“
Person in charge: Felix Leonce Martinez Martinez, 2024, Bachelor thesis.
Supervisor: Daniel Ewald M.Sc., Cedric Großelindemann M.Sc.

“Techno-economic Analysis to produce Hydrogen”
Person in charge: Fabian Herburger, 2025, Seminar thesis.
Supervisor: Cedric Großelindemann M.Sc.

DAAD RISE Internships

„Electrochemical Characterization and Modeling of Solid Oxide Cells“
Person in charge: Kristella Putz, summer 2022.
Supervisor: Cedric Großelindemann M.Sc.

“Characterization of an SOEC with Ni/YSZ Fuel Electrode”
Person in charge: Elizabeth Katzman, summer 2023.
Supervisor: Cedric Großelindemann M.Sc., Daniel Esau M.Sc.

“Electrochemical Analysis of Degradation Mechanisms in Solid Oxide Cells”
Person in charge: Daniel Kesler, summer 2024.
Supervisor: Daniel Esau M.Sc., Cedric Großelindemann, M.Sc.

9 List of Figures

10 List of Tables

11 Nomenclature

Latin letters

a Exponent describing hydrogen partial pressure dependency of the fuel electrode´s exchange current density (-)

b Exponent describing steam partial pressure dependency of the fuel electrode´s exchange current density (-)

B_{ohm} Cell specific constant for ohmic resistance (K Ω^{-1} m^{-2})

B_{El} Cell specific constant for electrodes (Ω m^2)

$\tilde{c}_i$ Molar concentration (mol m^{-3})

$D_{\mathrm{mol},i}$ Molecular gas diffusion coefficient of the component i (m^2 s^{-1})

D_i Gas diffusion coefficient of the component i (m^2 s^{-1})

D_{ijk} Ternary gas diffusion coefficient with the components i, j and k (m^2 s^{-1})

$D_{\mathrm{Kn},i}$ Knudsen-Diffusion coefficient (m^2 s^{-1})

d_{P} Pore diameter (m)

E_{act} Activation energy (J mol^{-1})

F Faraday constant (As mol^{-1})

G_{eff} Effective gas diffusion parameter (m^{-1})

$\Delta_{\mathrm{R}}G_0(T)$ Free standard reaction enthalpy (J mol^{-1})

j Current density (A m^{-2})

$j_{0,el}$ Exchange current density (A m^{-2})

k_1, k_2, k_3 Polynomial coefficients

L_{FE} Gas diffusion length fuel electrode (m)

m Exponent describing oxygen partial pressure dependency of the air electrode´s exchange current density (-)

$\widetilde{M}$ Molar mass (g mol^{-1})

N Amount of substance (mol)

$\dot{n}$	Molar flux density (mol m^{-2} s^{-1})
p	Overall pressure (bar_a)
p_{ref}	Reference pressure = 1.013 bar_a
p_i	Partial pressure of the component i
P_{corr}	Conversion factor 10^5 (Pa bar_a^{-1})
P_{LF1}	Low frequency process (-)
$P_{\mathrm{LF1,b}}$	Second low frequency process (-)
P_{LF2}	Middle frequency process (-)
P_{HF}	Higher frequency processes (-)
q_1, q_2, q_3	Polynomial coefficients
$\tilde{R}$	Universal gas constant 8.314 (J mol^{-1} K^{-1})
R_{diff}	Gas diffusion resistance (Ω m^2)
R_{pol}	Polarization resistance (Ω m^2)
R_{act}	Activation resistance (Ω m^2)
ΔR_{diff}	Difference of the gas diffusion resistance (Ω m^2)
ΔR_{pol}	Difference of the polarization resistance (Ω m^2)
R_{ohm}	Ohmic resistance (Ω m^2)
s	Variable length (m)
T	Temperature (K)
U_{OCV}	Open circuit voltage (V)
U_{cell}	Cell voltage (V)
U_{th}	Theoretical voltage (V)
V	Volume
x	Variable
y	Variable
$\tilde{y}$	Molar fraction gas phase

z	Number of exchanged electrons (-)
$Z'(\omega)$	Real part of impedance (Ω m^2)
$Z''(\omega)$	Imaginary part of impedance (Ω m^2)

Greek letters

α	Charge transfer coefficient (-)
γ	Exponential prefactor (A m^{-2})
δ	Concentration of oxygen lattice vacancy (-)
ε	Porosity (-)
η	Overpotential (V)
γ_τ	Continuous distribution function
λ_{DRT}	Regularization parameter
τ_{To}	Tortuosity (-)
τ	Relaxation time (s)
σ	Standard deviation
$\sigma_{i/j}$	Lennard-Jones length (m)
Ω_{D}	Collision integral
Ψ	Microstructure parameter (-)
ω	Angular frequency (s^{-1})

Subscripts

act	Activation
AE	Air electrode
cell	Cell
corr	Correction
diff	Gas diffusion
eff	Effective

EL	Electrode
FE	Fuel electrode
H_2	Hydrogen
H_2O	Steam
He	Helium
Kn	Knudsen
load	Electrical load
mol	Molecular
N_2	Nitrogen
OCV	Open-circuit voltage
ohm	Ohmic
pol	Polarization
por	Pore
s	symmetrical cell
WB	Warburg

Abbreviations

Al_2O_3	Aluminum oxide
APS	Atmospheric plasma spraying
ASC	Anode-supported cell
ASR	Area specific resistance
AE	Air electrode
BV	Butler-Volmer
CAPEX	Capital expenditure
CHP	Combined Heat and Power
CTE	Coefficient of thermal expansion
GDC	Gadolinium-Doped Ceria

CNLS	Complex non-linear least square
CV	Current-voltage
dc	Direct current
DRT	Distribution of relaxation times
EDXS	Energy-dispersive X-ray spectroscopy
EIS	Electrochemical impedance spectroscopy
EL	Electrode
ESC	Electrolyte-supported cell
FE	Fuel electrode
FIB	Focused ion beam
G-FLW	Generalized Finite-Length-Warburg-Element
He	Helium
H_2	Hydrogen
H_2O	Steam
lin	Linear
LSCF	$La_wSr_xCo_yFe_zO_{3-\delta}$
Meas	Measured
Mod	Modeled
MIC	Metallic interconnector
Min	Minimum
MSC	Metal-supported cell
N_2	Nitrogen
O_2	Oxygen
OCV	Open-circuit-voltage
PCC	Proton conducting ceramic cell
PFAS	Per- and polyfluoroalkyl substances
PVD	Physical vapor deposition

RQ	Parallel connection of ohmic resistance and constant-phase element
SEM	Scanning electron microscopy
SOC	Solid oxide cell
SOEC	Solid oxide electrolyzer cell
SOFC	Solid oxide fuel cell
SZO	$SrZrO_3$
sym-an1	Symmetrical cell with Ni/GDC fuel electrodes 1
sym-an2	Symmetrical cell with Ni/GDC fuel electrodes 2
TEM	Transmission electron microscopy
TLM	Transmission-Line-Model
TPB	Three-phase boundary
TRL	Technology Readiness Level
WPS	Wet powder spraying
3D	Three-dimensional
3YSZ	3 mol.% yttria-stabilized zirconia
8YSZ	8 mol.% yttria-stabilized zirconia

12 References

[1] M. Ivanova, R. Peters, M. Müller, S. Haas, M.F. Seidler, G. Mutschke, K. Eckert, P. Röse, S. Calnan, R. Bagacki, R. Schlatmann, C. Grosselindemann, L.-A. Schäfer, N.H. Menzler, A. Weber, R. van de Krol, F. Liang, F.F. Abdi, S. Brendelberger, N. Neumann, J. Grobbel, M. Roeb, C. Sattler, I. Duran, B. Dietrich, C. Hofberger, L. Stoppel, N. Uhlenbruck, T. Wetzel, D. Rauner, A. Hecimovic, U. Fantz, N. Kulyk, J. Harting, O. Guillon, Technological Pathways to Produce Compressed and Highly Pure Hydrogen from Solar Power, Angew. Chem. Int. Ed. (2023). https://doi.org/10.1002/anie.202218850.

[2] C. Grosselindemann, M. Dorn, F.M. Bauer, M. Seim, D. Ewald, D. Esau, M. Geörg, R. Rössler, A. Pundt, A. Weber, Pressurized single cell testing of solid oxide cells, J. Power Sources 614 (2024) 234963. https://doi.org/10.1016/j.jpowsour.2024.234963.

[3] The European Green Deal - European Commission, (2021). https://commission.europa.eu/strategy-and-policy/priorities-2019-2024/european-green-deal_en (accessed July 26, 2024).

[4] U. Nations, The Paris Agreement, United Nations (2015). https://www.un.org/en/climatechange/paris-agreement (accessed July 26, 2024).

[5] B.-F.M. for E.A. and C. Action, National Hydrogen Strategy Update, (2023). https://www.bmwk.de/Redaktion/EN/Publikationen/Energie/national-hydrogen-strategy-update.html (accessed June 17, 2024).

[6] C. Staudt, C. Hofsäß, B. von Lewinski, F. Mörs, P. Prabhakaran, S. Bajohr, F. Graf, T. Kolb, Process Engineering Analysis of Transport Options for Green Hydrogen and Green Hydrogen Derivatives, Energy Technol. 13 (2024) 2301526. https://doi.org/10.1002/ente.202301526.

[7] A. Weber, Fuel flexibility of solid oxide fuel cells, Fuel Cells 21 (2021) 440–452. https://doi.org/10.1002/fuce.202100037.

[8] J. Brabandt, O. Posdziech, System Approach of a Pressurized High-Temperature Electrolysis, ECS Trans. 78 (2017) 2987. https://doi.org/10.1149/07801.2987ecst.

[9] R.A. George, Status of tubular SOFC field unit demonstrations, J. Power Sources 86 (2000) 134–139. https://doi.org/10.1016/S0378-7753(99)00413-9.

[10] Y. Kobayashi, Y. Ando, H. Kishizawa, K. Tomida, N. Matake, Recent Progress of SOFC-GT Combined System with Tubular Type Cell Stack at MHI, ECS Trans. 51 (2013) 79. https://doi.org/10.1149/05101.0079ecst.

[11] S.E. Veyo, S.D. Vora, K.P. Litzinger, W.L. Lundberg, Status of Pressurized SOFC/Gas Turbine Power System Development at Siemens Westinghouse, in: American Society of Mechanical Engineers Digital Collection, 2009: pp. 823–829. https://doi.org/10.1115/GT2002-30670.

[12] K. Tanaka, C. Wen, K. Yamada, Design and evaluation of combined cycle system with solid oxide fuel cell and gas turbine, Fuel 79 (2000) 1493–1507. https://doi.org/10.1016/S0016-2361(99)00293-8.

[13] G. Sdanghi, G. Maranzana, A. Celzard, V. Fierro, Review of the current technologies and performances of hydrogen compression for stationary and automotive applications, Renew. Sust. Energy Rev. 102 (2019) 150–170. https://doi.org/10.1016/j.rser.2018.11.028.

[14] H. Nami, O.B. Rizvandi, C. Chatzichristodoulou, P.V. Hendriksen, H.L. Frandsen, Techno-economic analysis of current and emerging electrolysis technologies for green

hydrogen production, Energy Convers. Manag. 269 (2022) 116162. https://doi.org/10.1016/j.enconman.2022.116162.
[15] A.A. AlZahrani, I. Dincer, Modeling and performance optimization of a solid oxide electrolysis system for hydrogen production, Appl. Energy 225 (2018) 471–485. https://doi.org/10.1016/j.apenergy.2018.04.124.
[16] X. Sun, A.D. Bonaccorso, C. Graves, S.D. Ebbesen, S.H. Jensen, A. Hagen, P. Holtappels, P.V. Hendriksen, M.B. Mogensen, Performance Characterization of Solid Oxide Cells Under High Pressure, Fuel Cells 15 (2015) 697–702. https://doi.org/10.1002/fuce.201500020.
[17] Y.D. Hsieh, Y.H. Chan, S.S. Shy, Effects of pressurization and temperature on power generating characteristics and impedances of anode-supported and electrolyte-supported planar solid oxide fuel cells, J. Power Sources 299 (2015) 1–10. https://doi.org/10.1016/j.jpowsour.2015.08.080.
[18] S.H. Jensen, X. Sun, S.D. Ebbesen, M. Chen, Pressurized Operation of a Planar Solid Oxide Cell Stack, Fuel Cells 16 (2016) 205–218. https://doi.org/10.1002/fuce.201500180.
[19] M. Tomberg, M.P. Heddrich, M. Metten, S.A. Ansar, K.A. Friedrich, Operation of a Solid Oxide Fuel Cell Reactor with Multiple Stacks in a Pressured System with Fuel Gas Recirculation, Energy Technol. 10 (2022) 2101075. https://doi.org/10.1002/ente.202101075.
[20] L. Bernadet, J. Laurencin, G. Roux, D. Montinaro, F. Mauvy, M. Reytier, Effects of Pressure on High Temperature Steam and Carbon Dioxide Co-electrolysis, Electrochim. Acta 253 (2017) 114–127. https://doi.org/10.1016/j.electacta.2017.09.037.
[21] G. Hughes, J. Railsback, D. Butts, S.A. Barnett, Electrochemical Performance of Solid Oxide Cell Oxygen Electrodes Under Pressurization, ECS Trans. 68 (2015) 687. https://doi.org/10.1149/06801.0687ecst.
[22] Q. Cacciuttolo, J. Vulliet, V. Lair, M. Cassir, A. Ringuedé, Influence of pressure on the electrical and electrochemical behaviour of high-temperature steam electrolyser La0.6Sr0.4Co0.2Fe0.8O3 anode, J. Solid State Electrochem. 22 (2018) 3663–3671. https://doi.org/10.1007/s10008-018-4048-2.
[23] C. Herradon, L. Le, C. Meisel, J. Huang, C. Chmura, Y.D. Kim, C. Cadigan, R. O'Hayre, N.P. Sullivan, Proton-conducting ceramics for water electrolysis and hydrogen production at elevated pressure, Frontiers in Energy Research 10 (2022). https://www.frontiersin.org/articles/10.3389/fenrg.2022.1020960 (accessed December 18, 2023).
[24] M. Riedel, M.P. Heddrich, A. Ansar, Q. Fang, L. Blum, K.A. Friedrich, Pressurized operation of solid oxide electrolysis stacks: An experimental comparison of the performance of 10-layer stacks with fuel electrode and electrolyte supported cell concepts, J. Power Sources 475 (2020) 228682. https://doi.org/10.1016/j.jpowsour.2020.228682.
[25] J.E. O'Brien, X. Zhang, G.K. Housley, K. DeWall, L. Moore-McAteer, High Temperature Electrolysis Pressurized Experiment Design, Operation, and Results, Idaho National Lab. (INL), Idaho Falls, ID (United States), 2012. https://doi.org/10.2172/1056004.
[26] Q. Cacciuttolo, J. Vulliet, V. Lair, M. Cassir, A. Ringuedé, Effect of pressure on high temperature steam electrolysis: Model and experimental tests, Int. J. Hydrog. Energy 40 (2015) 11378–11384. https://doi.org/10.1016/j.ijhydene.2015.04.034.
[27] M. Kornely, A. Leonide, A. Weber, E. Ivers-Tiffée, Performance limiting factors in anode-supported cells originating from metallic interconnector design, J. Power Sources 196 (2011) 7209–7216. https://doi.org/10.1016/j.jpowsour.2010.10.048.

[28] D. Klotz, A. Weber, E. Ivers-Tiffée, Practical Guidelines for Reliable Electrochemical Characterization of Solid Oxide Fuel Cells, Electrochim. Acta 227 (2017) 110–126. https://doi.org/10.1016/j.electacta.2016.12.148.
[29] S. Dierickx, Charakterisierung, Modellentwicklung und Simulation von mehrschichtigen Brenngaselektroden in Festoxid-Brennstoffzellen, (2019). https://doi.org/10.5445/KSP/1000097490.
[30] C. Großelindemann, Elektrochemische Charakterisierung und Modellentwicklung einer SOFC mit Ni/CGO-Brenngaselektrode, (2020). https://publikationen.bibliothek.kit.edu/1000139847 (accessed May 12, 2025).
[31] S. Wang, T. Kobayashi, M. Dokiya, T. Hashimoto, Electrical and Ionic Conductivity of Gd-Doped Ceria, Journal of The Electrochemical Society (2000). https://doi.org/10.1149/1.1393946.
[32] E. Ivers-Tiffée, Batterien und Brennstoffzellen - lecture script, 2016.
[33] M. Henke, C. Willich, J. Kallo, K.A. Friedrich, Theoretical study on pressurized operation of solid oxide electrolysis cells, Int. J. Hydrog. Energy 39 (2014) 12434–12439. https://doi.org/10.1016/j.ijhydene.2014.05.185.
[34] O.B. Rizvandi, H.L. Frandsen, Modeling of single- and double-sided high-pressure operation of solid oxide electrolysis stacks, Int. J. Hydrog. Energy 48 (2023) 30102–30119. https://doi.org/10.1016/j.ijhydene.2023.04.169.
[35] S.B. Beale, M. Andersson, C. Boigues-Muñoz, H.L. Frandsen, Z. Lin, S.J. McPhail, M. Ni, B. Sundén, A. Weber, A.Z. Weber, Continuum scale modelling and complementary experimentation of solid oxide cells, Prog. Energy Combust. Sci. 85 (2021) 100902. https://doi.org/10.1016/j.pecs.2020.100902.
[36] A. Leonide, SOFC modelling and parameter identification by means of impedance spectroscopy, (2010). https://doi.org/10.5445/KSP/1000019173.
[37] C. Grosselindemann, N. Russner, S. Dierickx, A. Weber, Deconvolution of Gas Diffusion Polarization in Ni/Gadolinium-Doped Ceria Fuel Electrodes, ECS Trans. 103 (2021) 1375. https://doi.org/10.1149/10301.1375ecst.
[38] C. Grosselindemann, N. Russner, S. Dierickx, F. Wankmüller, A. Weber, Deconvolution of Gas Diffusion Polarization in Ni/Gadolinium-Doped Ceria Fuel Electrodes, J. Electrochem. Soc. 168 (2021) 124506. https://doi.org/10.1149/1945-7111/ac3d02.
[39] J. Joos, Microstructural Characterisation, Modelling and Simulation of Solid Oxide Fuel Cell Cathodes, (2017). https://doi.org/10.5445/KSP/1000064791.
[40] E.L. Cussler, Diffusion: Mass Transfer in Fluid Systems, Higher Education from Cambridge University Press (2009). https://doi.org/10.1017/CBO9780511805134.
[41] D.F. Fairbanks, C.R. Wilke, Diffusion Coefficients in Multicomponent Gas Mixtures, Ind. Eng. Chem. 42 (1950) 471–475. https://doi.org/10.1021/ie50483a022.
[42] J.W. Veldsink, R.M.J. van Damme, G.F. Versteeg, W.P.M. van Swaaij, The use of the dusty-gas model for the description of mass transport with chemical reaction in porous media, The Chemical Engineering Journal and the Biochemical Engineering Journal 57 (1995) 115–125. https://doi.org/10.1016/0923-0467(94)02929-6.
[43] S. Primdahl, M. Mogensen, Gas Diffusion Impedance in Characterization of Solid Oxide Fuel Cell Anodes, J. Electrochem. Soc. 146 (1999) 2827. https://doi.org/10.1149/1.1392015.
[44] J.-W. Kim, A.V. Virkar, K.-Z. Fung, K. Mehta, S.C. Singhal, Polarization Effects in Intermediate Temperature, Anode-Supported Solid Oxide Fuel Cells, J. Electrochem. Soc. 146 (1999) 69. https://doi.org/10.1149/1.1391566.
[45] M. Henke, J. Kallo, K.A. Friedrich, W.G. Bessler, Influence of Pressurisation on SOFC Performance and Durability: A Theoretical Study, Fuel Cells 11 (2011) 581–591. https://doi.org/10.1002/fuce.201000098.

[46] J.R. Macdonald, W.B. Johnson, Fundamentals of Impedance Spectroscopy, in: Impedance Spectroscopy, John Wiley & Sons, Ltd, 2005: pp. 1–26. https://doi.org/10.1002/0471716243.ch1.
[47] A. Lasia, Impedance of Porous Electrodes, in: A. Lasia (Ed.), Electrochemical Impedance Spectroscopy and Its Applications, Springer, New York, NY, 2014: pp. 203–250. https://doi.org/10.1007/978-1-4614-8933-7_9.
[48] H. Schichlein, Experimentelle Modellbildung für die Hochtemperatur-Brennstoffzelle SOFC, (2003). https://publikationen.bibliothek.kit.edu/3952003 (accessed July 15, 2024).
[49] Y. Liu, Y. Hu, M. Juckel, N.H. Menzler, A. Weber, Method—Multi-Cell Testing with Active Driven Gas Layer Concept: Advantages and Limitations, J. Electrochem. Soc. 171 (2024) 104509. https://doi.org/10.1149/1945-7111/ad83fb.
[50] D. Brinker, N. Hensle, J. Horstmann de la Viña, I. Franzetti, L.V. Bühre, U.A. Andaluri, C. Menke, T. Smolinka, A. Weber, Inductive loops in impedance spectra of PEM water electrolyzers, J. Power Sources 622 (2024) 235375. https://doi.org/10.1016/j.jpowsour.2024.235375.
[51] M. Schönleber, D. Klotz, E. Ivers-Tiffée, A Method for Improving the Robustness of linear Kramers-Kronig Validity Tests, Electrochim. Acta 131 (2014) 20–27. https://doi.org/10.1016/j.electacta.2014.01.034.
[52] M. Schönleber, E. Ivers-Tiffée, Approximability of impedance spectra by RC elements and implications for impedance analysis, Electrochem. Commun. 58 (2015) 15–19. https://doi.org/10.1016/j.elecom.2015.05.018.
[53] S.B. Adler, J.A. Lane, B.C.H. Steele, Electrode Kinetics of Porous Mixed-Conducting Oxygen Electrodes, J. Electrochem. Soc. 143 (1996) 3554. https://doi.org/10.1149/1.1837252.
[54] C. Endler-Schuck, J. Joos, C. Niedrig, A. Weber, E. Ivers-Tiffée, The chemical oxygen surface exchange and bulk diffusion coefficient determined by impedance spectroscopy of porous La0.58Sr0.4Co0.2Fe0.8O3−δ (LSCF) cathodes, Solid State Ionics 269 (2015) 67–79. https://doi.org/10.1016/j.ssi.2014.11.018.
[55] F. Kullmann, M. Mueller, A. Lindner, S. Dierickx, E. Mueller, A. Weber, DRT analysis and transmission line modeling of ceria based electrodes for solid oxide cells, J. Power Sources 587 (2023) 233706. https://doi.org/10.1016/j.jpowsour.2023.233706.
[56] A. Nenning, C. Bischof, J. Fleig, M. Bram, A.K. Opitz, The Relation of Microstructure, Materials Properties and Impedance of SOFC Electrodes: A Case Study of Ni/GDC Anodes, Energies 13 (2020) 987. https://doi.org/10.3390/en13040987.
[57] S. Dierickx, T. Mundloch, A. Weber, E. Ivers-Tiffée, Advanced impedance model for double-layered solid oxide fuel cell cermet anodes, J. Power Sources 415 (2019) 69–82. https://doi.org/10.1016/j.jpowsour.2019.01.043.
[58] A. Shaur, M. Drazkowski, S. Zhu, B. Boukamp, H.J. M. Bouwmeester, A single-phase gadolinium-doped ceria cathode for highly efficient CO 2 electrolysis, J. Mater. Chem. A. 11 (2023) 25020–25030. https://doi.org/10.1039/D3TA03977C.
[59] F. Kullmann, D. Esau, K. Limbeck, S. Dierickx, A. Lindner, H. Störmer, A. Weber, Impact of nickel on the surface reaction in ceria-based electrodes for solid oxide cells, J. Power Sources 625 (2025) 235621. https://doi.org/10.1016/j.jpowsour.2024.235621.
[60] H. Schichlein, A.C. Müller, M. Voigts, A. Krügel, E. Ivers-Tiffée, Deconvolution of electrochemical impedance spectra for the identification of electrode reaction mechanisms in solid oxide fuel cells, J. Appl. Electrochem. 32 (2002) 875–882. https://doi.org/10.1023/A:1020599525160.
[61] A.N. Tikhonov, A.V. Goncharsky, V.V. Stepanov, A.G. Yagola, Numerical methods for the approximate solution of ill-posed problems on compact sets, in: A.N. Tikhonov, A.V. Goncharsky, V.V. Stepanov, A.G. Yagola (Eds.), Numerical Methods for the Solution of

Ill-Posed Problems, Springer Netherlands, Dordrecht, 1995: pp. 65–79. https://doi.org/10.1007/978-94-015-8480-7_3.
[62] J.-C. Njodzefon, Electrode Kinetics and Gas Conversion in Solid Oxide Cells, Department of Energy Conversion and Storage, Technical University of Denmark, Roskilde, Denmark, 2015.
[63] D. Klotz, Characterization and Modeling of Electrochemical Energy Conversion Systems by Impedance Techniques, (2012). https://doi.org/10.5445/KSP/1000029318.
[64] C. Lenser, D. Udomsilp, N.H. Menzler, P. Holtappels, T. Fujisaki, L. Kwati, H. Matsumoto, A.G. Sabato, F. Smeacetto, A. Chrysanthou, S. Molin, 9 - Solid oxide fuel and electrolysis cells, in: O. Guillon (Ed.), Advanced Ceramics for Energy Conversion and Storage, Elsevier, 2020: pp. 387–547. https://doi.org/10.1016/B978-0-08-102726-4.00009-0.
[65] Per- and polyfluoroalkyl substances (PFAS) - ECHA, (-). https://echa.europa.eu/hot-topics/perfluoroalkyl-chemicals-pfas (accessed October 9, 2024).
[66] M. Fallah Vostakola, B. Amini Horri, Progress in Material Development for Low-Temperature Solid Oxide Fuel Cells: A Review, Energies 14 (2021) 1280. https://doi.org/10.3390/en14051280.
[67] Y. Liu, M. Juckel, N.H. Menzler, A. Weber, Ni/GDC Fuel Electrode for Low-Temperature SOFC and its Aging Behavior Under Accelerated Stress, J. Electrochem. Soc. 171 (2024) 054514. https://doi.org/10.1149/1945-7111/ad4917.
[68] A. Kromp, A. Leonide, A. Weber, E. Ivers-Tiffée, Electrochemical Analysis of Reformate-Fuelled Anode Supported SOFC, J. Electrochem. Soc. 158 (2011) B980. https://doi.org/10.1149/1.3597177.
[69] H. Timmermann, W. Sawady, D. Campbell, A. Weber, R. Reimert, E. Ivers-Tiffée, Coke Formation and Degradation in SOFC Operation with a Model Reformate from Liquid Hydrocarbons, J. Electrochem. Soc. 155 (2008) B356. https://doi.org/10.1149/1.2838909.
[70] S.D. Ebbesen, C. Graves, M. Mogensen, Production of Synthetic Fuels by Co-Electrolysis of Steam and Carbon Dioxide, Int. J. Green Energy 6 (2009) 646–660. https://doi.org/10.1080/15435070903372577.
[71] L. Bernadet, C. Moncasi, M. Torrell, A. Tarancón, High-performing electrolyte-supported symmetrical solid oxide electrolysis cells operating under steam electrolysis and co-electrolysis modes, Int. J. Hydrog. Energy 45 (2020) 14208–14217. https://doi.org/10.1016/j.ijhydene.2020.03.144.
[72] D. Udomsilp, C. Lenser, O. Guillon, N.H. Menzler, Performance Benchmark of Planar Solid Oxide Cells Based on Material Development and Designs, Energy Technol. 9 (2021) 2001062. https://doi.org/10.1002/ente.202001062.
[73] K. Leonard, M.E. Ivanova, A. Weber, W. Deibert, W.A. Meulenberg, T. Ishihara, H. Matsumoto, Anode supported planar 5 × 5 cm2 SrZr0.5Ce0.4Y0.1O2.95 based solid oxide protonic fuel cells via sequential tape-casting, Solid State Ionics 379 (2022) 115918. https://doi.org/10.1016/j.ssi.2022.115918.
[74] D. Jennings, J.N. Ebert, H. Du, Q. Ma, L.-A. Schäfer, D. Sebold, J. Mayer, W. Rheinheimer, The Formation of Stacking Faults in Barium Zirconate-Type Perovskites, Chem. Mater. 35 (2023) 8382–8396. https://doi.org/10.1021/acs.chemmater.3c00787.
[75] F. Kullmann, C. Grosselindemann, L. Salamon, F.-M. Fuchs, A. Weber, Impedance analysis of electrolyte processes in a solid oxide cell, Fuel Cells 23 (2023). https://doi.org/10.1002/fuce.202300035.
[76] Elcogen, Affordable Green Hydrogen (-). https://elcogen.com/products/solid-oxide-fuel-cells/ (accessed June 28, 2024).

[77] M. Pagliari, D. Montinaro, E. Martelli, S. Campanari, A. Donazzi, Durability and kinetic effects of CO2-rich oxidizing streams on LSCF-based solid oxide fuel cells, J. Power Sources 613 (2024) 234895. https://doi.org/10.1016/j.jpowsour.2024.234895.
[78] J. Mermelstein, M. Millan, N. Brandon, The impact of steam and current density on carbon formation from biomass gasification tar on Ni/YSZ, and Ni/CGO solid oxide fuel cell anodes, J. Power Sources 195 (2010) 1657–1666. https://doi.org/10.1016/j.jpowsour.2009.09.046.
[79] V.A. Rojek-Wöckner, A.K. Opitz, M. Brandner, J. Mathé, M. Bram, A novel Ni/ceria-based anode for metal-supported solid oxide fuel cells, J. Power Sources 328 (2016) 65–74. https://doi.org/10.1016/j.jpowsour.2016.07.075.
[80] M. Riegraf, M.P. Hoerlein, R. Costa, G. Schiller, K.A. Friedrich, Sulfur Poisoning of Electrochemical Reformate Conversion on Nickel/Gadolinium-Doped Ceria Electrodes, ACS Catal. 7 (2017) 7760–7771. https://doi.org/10.1021/acscatal.7b02177.
[81] F. Thaler, D. Udomsilp, W. Schafbauer, C. Bischof, Y. Fukuyama, Y. Miura, M. Kawabuchi, S. Taniguchi, S. Takemiya, A. Nenning, A.K. Opitz, M. Bram, Redox stability of metal-supported fuel cells with nickel/gadolinium-doped ceria anode, J. Power Sources 434 (2019) 226751. https://doi.org/10.1016/j.jpowsour.2019.226751.
[82] M. Riegraf, R. Costa, G. Schiller, K.A. Friedrich, S. Dierickx, A. Weber, Electrochemical Impedance Analysis of Symmetrical Ni/Gadolinium-Doped Ceria (CGO10) Electrodes in Electrolyte-Supported Solid Oxide Cells, J. Electrochem. Soc. 166 (2019) F865. https://doi.org/10.1149/2.0051913jes.
[83] T. Nakamura, T. Kobayashi, K. Yashiro, A. Kaimai, T. Otake, K. Sato, J. Mizusaki, T. Kawada, Electrochemical Behaviors of Mixed Conducting Oxide Anodes for Solid Oxide Fuel Cell, J. Electrochem. Soc. 155 (2008) B563. https://doi.org/10.1149/1.2901047.
[84] K. Eguchi, T. Setoguchi, T. Inoue, H. Arai, Electrical properties of ceria-based oxides and their application to solid oxide fuel cells, Solid State Ionics 52 (1992) 165–172. https://doi.org/10.1016/0167-2738(92)90102-U.
[85] J.W. Fergus, Oxide anode materials for solid oxide fuel cells, Solid State Ionics 177 (2006) 1529–1541. https://doi.org/10.1016/j.ssi.2006.07.012.
[86] S. Primdahl, M. Mogensen, Mixed conductor anodes: Ni as electrocatalyst for hydrogen conversion, Solid State Ionics 152–153 (2002) 597–608. https://doi.org/10.1016/S0167-2738(02)00393-4.
[87] M. Mogensen, Sø. Primdahl, M.J. JØrgensen, C. Bagger, Composite Electrodes in Solid Oxide Fuel Cells and Similar Solid State Devices, J. Electroceram. 5 (2000) 141–152. https://doi.org/10.1023/A:1009910202330.
[88] A. Weber, T. Dickel, E. Ivers-Tiffee, Sulfur-Tolerance of Ceria-based Anodes, EFCF Proceedings (2016) 48.
[89] A. Weber, S. Dierickx, N. Russner, E. Ivers-Tiffée, (Invited) Sulfur Poisoning of Ni-Based SOFC-Anodes – Short and Long Term Behavior, ECS Trans. 77 (2017) 141. https://doi.org/10.1149/07710.0141ecst.
[90] I.D. Unachukwu, V. Vibhu, I.C. Vinke, R.-A. Eichel, L.G.J. (Bert) de Haart, Electrochemical and degradation behaviour of single cells comprising Ni-GDC fuel electrode under high temperature steam- and co-electrolysis conditions, J. Power Sources 556 (2023) 232436. https://doi.org/10.1016/j.jpowsour.2022.232436.
[91] A. Nenning, M. Holzmann, J. Fleig, A. K. Opitz, Excellent kinetics of single-phase Gd-doped ceria fuel electrodes in solid oxide cells, Mater. Adv. 2 (2021) 5422–5431. https://doi.org/10.1039/D1MA00202C.
[92] J. Uecker, I.D. Unachukwu, V. Vibhu, I.C. Vinke, L.G.J. (Bert) de Haart, R.-A. Eichel, Gadolinium Doped Ceria as Nickel–Free Fuel Electrode in High Temperature CO2-

Electrolysis, ChemElectroChem 11 (2024) e202300617. https://doi.org/10.1002/celc.202300617.
[93] J. Uecker, I.D. Unachukwu, V. Vibhu, I.C. Vinke, R.-A. Eichel, L.G.J. (Bert) de Haart, Performance, electrochemical process analysis and degradation of gadolinium doped ceria as fuel electrode material for solid oxide electrolysis cells, Electrochim. Acta 452 (2023) 142320. https://doi.org/10.1016/j.electacta.2023.142320.
[94] Technische Keramik, Kerafol (-). https://www.kerafol.com/technische-keramik/ (accessed July 19, 2024).
[95] Sunfire - Wasserstoff (HyLink), Sunfire (-). https://www.sunfire.de/de/wasserstoff (accessed March 15, 2022).
[96] C. Lenser, J. Zhang, N. Russner, A. Weber, O. Guillon, N.H. Menzler, Electro-chemo-mechanical analysis of a solid oxide cell based on doped ceria, J. Power Sources 541 (2022) 231505. https://doi.org/10.1016/j.jpowsour.2022.231505.
[97] M.P. Klitkou, Development of Novel Durable Solid Oxide Electrolysis Cells: Integration of Ni-GDC Fuel Electrodes into Fuel Electrode Supported Cells, Technical University of Denmark, Kgs. Lyngby, 2024.
[98] A. Mai, V.A.C. Haanappel, S. Uhlenbruck, F. Tietz, D. Stöver, Ferrite-based perovskites as cathode materials for anode-supported solid oxide fuel cells: Part I. Variation of composition, Solid State Ionics 176 (2005) 1341–1350. https://doi.org/10.1016/j.ssi.2005.03.009.
[99] A. Mai, V.A.C. Haanappel, F. Tietz, D. Stöver, Ferrite-based perovskites as cathode materials for anode-supported solid oxide fuel cells: Part II. Influence of the CGO interlayer, Solid State Ionics 177 (2006) 2103–2107. https://doi.org/10.1016/j.ssi.2005.12.010.
[100] L. Blum, L.G.J. (Bert) de Haart, J. Malzbender, N.H. Menzler, J. Remmel, R. Steinberger-Wilckens, Recent results in Jülich solid oxide fuel cell technology development, J. Power Sources 241 (2013) 477–485. https://doi.org/10.1016/j.jpowsour.2013.04.110.
[101] M. Kornely, N.H. Menzler, A. Weber, E. Ivers-Tiffée, Degradation of a High Performance SOFC Cathode by Cr-Poisoning at OCV-Conditions, Fuel Cells 13 (2013) 506–510. https://doi.org/10.1002/fuce.201200182.
[102] J. Szász, F. Wankmüller, V. Wilde, H. Störmer, D. Gerthsen, N.H. Menzler, E. Ivers-Tiffée, Nature and Functionality of La0.58Sr0.4Co0.2Fe0.8O3-δ / Gd0.2Ce0.8O2-δ / Y0.16Zr0.84O2-δ Interfaces in SOFCs, J. Electrochem. Soc. 165 (2018) F898. https://doi.org/10.1149/2.0031811jes.
[103] Fuel Cell Handbook (Seventh Edition), Virginia : National Energy Technology Laboratory, 2016 (-).
[104] A. Leonide, Y. Apel, E. Ivers-Tiffee, SOFC Modeling and Parameter Identification by Means of Impedance Spectroscopy, ECS Trans. 19 (2009) 81. https://doi.org/10.1149/1.3247567.
[105] N.H. Menzler, F. Tietz, S. Uhlenbruck, H.P. Buchkremer, D. Stöver, Materials and manufacturing technologies for solid oxide fuel cells, J. Mater. Sci. 45 (2010) 3109–3135. https://doi.org/10.1007/s10853-010-4279-9.
[106] V. Rojek, D. Roehrens, M. Brandner, N.H. Menzler, O. Guillon, A.K. Opitz, M. Bram, Development of High Performance Anodes for Metal-Supported Fuel Cells, ECS Trans. 68 (2015) 1297. https://doi.org/10.1149/06801.1297ecst.
[107] J. Joos, M. Ender, I. Rotscholl, N.H. Menzler, E. Ivers-Tiffée, Quantification of double-layer Ni/YSZ fuel cell anodes from focused ion beam tomography data, J. Power Sources 246 (2014) 819–830. https://doi.org/10.1016/j.jpowsour.2013.08.021.

[108] C. Geipel, K. Hauptmeier, K. Herbrig, F. Mittmann, M. Münch, M. Pötschke, L. Reichel, T. Strohbach, T. Seidel, A. Surrey, C. Walter, Stack Development and Industrial Scale-Up, ECS Trans. 91 (2019) 123. https://doi.org/10.1149/09101.0123ecst.
[109] R.T. Leah, A. Bone, A. Selcuk, M. Rahman, A. Clare, M. Lankin, F. Felix, S. Mukerjee, M. Selby, Latest Results and Commercialization of the Ceres Power SteelCell® Technology Platform, ECS Trans. 91 (2019) 51. https://doi.org/10.1149/09101.0051ecst.
[110] H. Langnickel, M. Rautanen, M. Gandiglio, M. Santarelli, T. Hakala, M. Acri, J. Kiviaho, Efficiency analysis of 50 kWe SOFC systems fueled with biogas from waste water, J. Power Sources Adv. 2 (2020) 100009. https://doi.org/10.1016/j.powera.2020.100009.
[111] M.C. Williams, S.D. Vora, G. Jesionowski, Worldwide Status of Solid Oxide Fuel Cell Technology, ECS Trans. 96 (2020) 1. https://doi.org/10.1149/09601.0001ecst.
[112] Clean, Reliable and Affordable: The Bloom Energy Server, Bloom Energy (-). https://www.bloomenergy.com/technology/ (accessed March 15, 2022).
[113] G.D. Agnew, R.D. Collins, M.B. Jörger, S.H. Pyke, R. Travis, The Components of a Rolls-Royce 1 MW SOFC System, ECS Trans. 7 (2007) 105. https://doi.org/10.1149/1.2729079.
[114] SOFC (Solid Oxide Fuel Cell) Stack - Energy Conversion Devices - KYOCERA, KYOCERA GROUP GLOBAL SITE (-). https://global.kyocera.com/prdct/ecd/sofc/ (accessed March 15, 2022).
[115] C.E. Frey, Q. Fang, D. Sebold, L. Blum, N.H. Menzler, A Detailed Post Mortem Analysis of Solid Oxide Electrolyzer Cells after Long-Term Stack Operation, J. Electrochem. Soc. 165 (2018) F357. https://doi.org/10.1149/2.0961805jes.
[116] Y. Zhao, H. Xue, X. Jin, B. Xiong, R. Liu, Y. Peng, L. Jiang, G. Tian, System level heat integration and efficiency analysis of hydrogen production process based on solid oxide electrolysis cells, Int. J. Hydrog. Energy 46 (2021) 38163–38174. https://doi.org/10.1016/j.ijhydene.2021.09.105.
[117] Z. Liu, B. Han, Z. Lu, W. Guan, Y. Li, C. Song, L. Chen, S.C. Singhal, Efficiency and stability of hydrogen production from seawater using solid oxide electrolysis cells, Appl. Energy 300 (2021) 117439. https://doi.org/10.1016/j.apenergy.2021.117439.
[118] J. Uecker, B.I. Dembele, L. Nohl, N. Eyckeler, V. Vibhu, I.C. Vinke, R.-A. Eichel, Direct Use of European Seawater in Solid Oxide Electrolysis Cells, Proceedings of the 16th European SOFC & SOE Forum (2024).
[119] S. Sarner, N. H. Menzler, J. Malzbender, M. Hilger, D. Sebold, A. Weber, O. Guillon, Towards a scalable recycling process for ceramics in fuel-electrode-supported solid oxide cells, Green Chemistry 27 (2025) 2252–2262. https://doi.org/10.1039/D4GC05883F.
[120] A. Hagen, A.K. Padinjarethil, J. Heijne, Experimental deconvolution of resistance contributions in commercial solid oxide cells with Ni-CGO electrode, Electrochim. Acta 461 (2023) 142672. https://doi.org/10.1016/j.electacta.2023.142672.
[121] M. Riegraf, V. Yurkiv, R. Costa, G. Schiller, K.A. Friedrich, Evaluation of the Effect of Sulfur on the Performance of Nickel/Gadolinium-Doped Ceria Based Solid Oxide Fuel Cell Anodes, ChemSusChem 10 (2017) 587–599. https://doi.org/10.1002/cssc.201601320.
[122] V. Sonn, A. Leonide, E. Ivers-Tiffée, Combined Deconvolution and CNLS Fitting Approach Applied on the Impedance Response of Technical Ni/8YSZ Cermet Electrodes, J. Electrochem. Soc. 155 (2008) B675. https://doi.org/10.1149/1.2908860.
[123] P.V. Aravind, J.P. Ouweltjes, J. Schoonman, Diffusion Impedance on Nickel/Gadolinia-Doped Ceria Anodes for Solid Oxide Fuel Cells, J. Electrochem. Soc. 156 (2009) B1417. https://doi.org/10.1149/1.3231490.

[124] A. Mohammed Hussain, J.V.T. Høgh, T. Jacobsen, N. Bonanos, Nickel-ceria infiltrated Nb-doped SrTiO3 for low temperature SOFC anodes and analysis on gas diffusion impedance, Int. J. Hydrog. Energy 37 (2012) 4309–4318. https://doi.org/10.1016/j.ijhydene.2011.11.087.
[125] J.-C. Njodzefon, D. Klotz, A. Kromp, A. Weber, E. Ivers-Tiffée, Electrochemical Modeling of the Current-Voltage Characteristics of an SOFC in Fuel Cell and Electrolyzer Operation Modes, J. Electrochem. Soc. 160 (2013) F313. https://doi.org/10.1149/2.018304jes.
[126] A. Kromp, J. Nielsen, P. Blennow, T. Klemensø, A. Weber, Break-down of Losses in High Performing Metal-Supported Solid Oxide Fuel Cells, Fuel Cells 13 (2013) 598–604. https://doi.org/10.1002/fuce.201200165.
[127] Th. Franco, R. Mücke, A. Weber, M. Haydn, M. Rüttinger, N.H. Menzler, A. Venskutonis, L.S. Sigl, H.P. Buchkremer, Development and Industrialization of Metal-Supported Solid Oxide Fuel Cells, EFCF Proceedings (2012) A0906.
[128] C. Grosselindemann, F. Kullmann, T. Lehnert, O. Fritz, F.-M. Fuchs, A. Weber, Comparison of a solid oxide cell with nickel/gadolinium-doped ceria fuel electrode during operation with hydrogen/steam and carbon monoxide/carbon dioxide, Fuel Cells 23 (2023). https://doi.org/10.1002/fuce.202300060.
[129] A. Kromp, H. Geisler, A. Weber, E. Ivers-Tiffée, Electrochemical impedance modeling of gas transport and reforming kinetics in reformate fueled solid oxide fuel cell anodes, Electrochim. Acta 106 (2013) 418–424. https://doi.org/10.1016/j.electacta.2013.05.136.
[130] M. Kishimoto, H. Muroyama, S. Suzuki, M. Saito, T. Koide, Y. Takahashi, T. Horiuchi, H. Yamasaki, S. Matsumoto, H. Kubo, N. Takahashi, A. Okabe, S. Ueguchi, M. Jun, A. Tateno, T. Matsuo, T. Matsui, H. Iwai, H. Yoshida, K. Eguchi, Development of 1 kW-class Ammonia-fueled Solid Oxide Fuel Cell Stack, Fuel Cells 20 (2020) 80–88. https://doi.org/10.1002/fuce.201900131.
[131] D.M. Bierschenk, M.R. Pillai, Y. Lin, S.A. Barnett, Effect of Ethane and Propane in Simulated Natural Gas on the Operation of Ni–YSZ Anode Supported Solid Oxide Fuel Cells, Fuel Cells 10 (2010) 1129–1134. https://doi.org/10.1002/fuce.201000005.
[132] T. Okanishi, K. Okura, A. Srifa, H. Muroyama, T. Matsui, M. Kishimoto, M. Saito, H. Iwai, H. Yoshida, M. Saito, T. Koide, H. Iwai, S. Suzuki, Y. Takahashi, T. Horiuchi, H. Yamasaki, S. Matsumoto, S. Yumoto, H. Kubo, J. Kawahara, A. Okabe, Y. Kikkawa, T. Isomura, K. Eguchi, Comparative Study of Ammonia-fueled Solid Oxide Fuel Cell Systems, Fuel Cells 17 (2017) 383–390. https://doi.org/10.1002/fuce.201600165.
[133] L. Wehrle, Y. Wang, P. Boldrin, N.P. Brandon, O. Deutschmann, A. Banerjee, Optimizing Solid Oxide Fuel Cell Performance to Re-evaluate Its Role in the Mobility Sector, ACS Environ. Au 2 (2022) 42–64. https://doi.org/10.1021/acsenvironau.1c00014.
[134] R.T. Leah, N.P. Brandon, P. Aguiar, Modelling of cells, stacks and systems based around metal-supported planar IT-SOFC cells with CGO electrolytes operating at 500–600°C, J. Power Sources 145 (2005) 336–352. https://doi.org/10.1016/j.jpowsour.2004.12.067.
[135] O.B. Rizvandi, S.H. Jensen, H.L. Frandsen, A modeling study of lifetime and performance improvements of solid oxide fuel cell by reversed pulse operation, J. Power Sources 523 (2022) 231048. https://doi.org/10.1016/j.jpowsour.2022.231048.
[136] A. Leonide, S. Hansmann, A. Weber, E. Ivers-Tiffée, Performance simulation of current/voltage-characteristics for SOFC single cell by means of detailed impedance analysis, J. Power Sources 196 (2011) 7343–7346. https://doi.org/10.1016/j.jpowsour.2010.10.052.
[137] N. Russner, S. Dierickx, A. Weber, R. Reimert, E. Ivers-Tiffée, Multiphysical modelling of planar solid oxide fuel cell stack layers, J. Power Sources 451 (2020) 227552. https://doi.org/10.1016/j.jpowsour.2019.227552.

[138] G. Narasimhaiah, V.M. Janardhanan, Modeling CO2 electrolysis in solid oxide electrolysis cell, J. Solid State Electrochem. 17 (2013) 2361–2370. https://doi.org/10.1007/s10008-013-2081-8.
[139] R. Küngas, P. Blennow, T. Heiredal-Clausen, T. Holt, J. Rass-Hansen, S. Primdahl, J.B. Hansen, eCOs - A Commercial CO2 Electrolysis System Developed by Haldor Topsoe, ECS Trans. 78 (2017) 2879. https://doi.org/10.1149/07801.2879ecst.
[140] R. Kungas, P. Blennow, T. Heiredal-Clausen, T.H. Nørby, D. Rasmussen, J. Rass-Hansen, P.G. Moses, J. Hansen, Commercialization of CO2 Electrolysis By Haldor Topsoe, Meet. Abstr. MA2021-03 (2021) 191. https://doi.org/10.1149/MA2021-031191mtgabs.
[141] eCOs™ - CO from CO_2 | Equipment | Products | Topsoe, (-). https://www.topsoe.com/our-resources/knowledge/our-products/equipment/ecos-co-from-co2 (accessed October 2, 2023).
[142] J.A. Hoffman, M.H. Hecht, D. Rapp, J.J. Hartvigsen, J.G. SooHoo, A.M. Aboobaker, J.B. McClean, A.M. Liu, E.D. Hinterman, M. Nasr, S. Hariharan, K.J. Horn, F.E. Meyen, H. Okkels, P. Steen, S. Elangovan, C.R. Graves, P. Khopkar, M.B. Madsen, G.E. Voecks, P.H. Smith, T.L. Skafte, K.R. Araghi, D.J. Eisenman, Mars Oxygen ISRU Experiment (MOXIE)—Preparing for human Mars exploration, Sci. Adv. 8 (2022) eabp8636. https://doi.org/10.1126/sciadv.abp8636.
[143] H. Timmermann, D. Fouquet, A. Weber, E. Ivers-Tiffée, U. Hennings, R. Reimert, Internal Reforming of Methane at Ni/YSZ and Ni/CGO SOFC Cermet Anodes, Fuel Cells 6 (2006) 307–313. https://doi.org/10.1002/fuce.200600002.
[144] E. Ivers-Tiffée, H. Timmermann, A. Leonide, N.H. Menzler, J. Malzbender, Methane reforming kinetics, carbon deposition, and redox durability of Ni/8 yttria-stabilized zirconia (YSZ) anodes, in: Handbook of Fuel Cells, John Wiley & Sons, Ltd, 2010. https://doi.org/10.1002/9780470974001.f500063.
[145] M. Chen, J.V.T. Høgh, J.U. Nielsen, J.J. Bentzen, S.D. Ebbesen, P.V. Hendriksen, High Temperature Co-Electrolysis of Steam and CO2 in an SOC Stack: Performance and Durability, Fuel Cells 13 (2013) 638–645. https://doi.org/10.1002/fuce.201200169.
[146] D. Esau, C. Grosselindemann, S. Sckuhr, F. Kullmann, A. Lindner, Z. Liang, F.-M. Fuchs, A. Weber, Electrochemical Characterization of Nickel / Gadolinia Doped Ceria Fuel Electrodes under H2/H2O/CO/CO2-Atmospheres, J. Electrochem. Soc. (2024). https://doi.org/10.1149/1945-7111/ad4c10.
[147] C. Grosselindemann, M.J. Reddy, H. Stormer, D. Esau, M. Dorn, F.M. Bauer, D. Ewald, L. Wissmeier, J. Froitzheim, A. Weber, Impact of CeCo-Coated Metallic Interconnectors on SOCs Towards Performance, Cr-Oxide-Scale, and Cr-Evaporation, J. Electrochem. Soc. (2024). https://doi.org/10.1149/1945-7111/ad44da.
[148] J.C.W. Mah, A. Muchtar, M.R. Somalu, M.J. Ghazali, Metallic interconnects for solid oxide fuel cell: A review on protective coating and deposition techniques, Int. J. Hydrog. Energy 42 (2017) 9219–9229. https://doi.org/10.1016/j.ijhydene.2016.03.195.
[149] J.W. Fergus, Metallic interconnects for solid oxide fuel cells, Mater. Sci. Eng. A 397 (2005) 271–283. https://doi.org/10.1016/j.msea.2005.02.047.
[150] D. Esau, C. Grosselindemann, S.P. Sckuhr, F. Kullmann, L. Wissmeier, A. Weber, Characterization of a Nickel / Gadolinia Doped Ceria Fuel Electrode for Co-Electrolysis, ECS Trans. 111 (2023) 871. https://doi.org/10.1149/11106.0871ecst.
[151] I. Antepara, I. Villarreal, L.M. Rodríguez-Martínez, N. Lecanda, U. Castro, A. Laresgoiti, Evaluation of ferritic steels for use as interconnects and porous metal supports in IT-SOFCs, J. Power Sources 151 (2005) 103–107. https://doi.org/10.1016/j.jpowsour.2005.02.084.

[152] W.J. Quadakkers, J. Piron-Abellan, V. Shemet, L. Singheiser, Metallic interconnectors for solid oxide fuel cells- A review, Mater. at High Temp. 20 (2003) 115–127. https://doi.org/10.3184/096034003782749071.
[153] P. Kofstad, R. Bredesen, High temperature corrosion in SOFC environments, Solid State Ionics 52 (1992) 69–75. https://doi.org/10.1016/0167-2738(92)90092-4.
[154] N. Shaigan, W. Qu, D.G. Ivey, W. Chen, A review of recent progress in coatings, surface modifications and alloy developments for solid oxide fuel cell ferritic stainless steel interconnects, J. Power Sources 195 (2010) 1529–1542. https://doi.org/10.1016/j.jpowsour.2009.09.069.
[155] M.J. Reddy, A. Visibile, J.-E. Svensson, J. Froitzheim, Investigation of coated FeCr steels for application as solid oxide fuel cell interconnects under dual-atmosphere conditions, Int. J. Hydrog. Energy 48 (2023) 14406–14417. https://doi.org/10.1016/j.ijhydene.2022.11.278.
[156] S. Megel, C. Dosch, S. Rothe, M. Kusnezoff, N. Trofimenko, V. Sauchuk, A. Michaelis, C. Bienert, M. Brandner, A. Venskutonis, W. Kraussler, L.S. Sigl, CFY-Stacks for Use in Stationary SOFC and SOEC Applications, ECS Trans. 57 (2013) 89. https://doi.org/10.1149/05701.0089ecst.
[157] M. Preininger, J. Wurm, V. Subotić, R. Schauperl, C. Hochenauer, Performance characterization of a solid oxide cell stack with chromium-based interconnects (CFY), Int. J. Hydrog. Energy 42 (2017) 28653–28664. https://doi.org/10.1016/j.ijhydene.2017.10.007.
[158] M.J. Reddy, B. Kamecki, B. Talic, E. Zanchi, F. Smeacetto, J.S. Hardy, J.P. Choi, Ł. Mazur, R. Vaßen, S.N. Basu, T. Brylewski, J.-E. Svensson, J. Froitzheim, Experimental review of the performances of protective coatings for interconnects in solid oxide fuel cells, J. Power Sources 568 (2023) 232831. https://doi.org/10.1016/j.jpowsour.2023.232831.
[159] B. Talic, S. Molin, P.V. Hendriksen, H.L. Lein, Effect of pre-oxidation on the oxidation resistance of Crofer 22 APU, Corros. Sci. 138 (2018) 189–199. https://doi.org/10.1016/j.corsci.2018.04.016.
[160] T. Kiefer, Entwicklung neuer Schutz- und Kontaktierungsschichten für Hochtemperatur-Brennstoffzellen, Forschungszentrum Jülich GmbH Zentralbibliothek, Verlag, Jülich, 2008.
[161] H. Geisler, A. Kromp, A. Weber, E. Ivers-Tiffée, Stationary FEM Model for Performance Evaluation of Planar Solid Oxide Fuel Cells Connected by Metal Interconnectors: I. Model Framework and Validation, J. Electrochem. Soc. 161 (2014) F778. https://doi.org/10.1149/2.079406jes.
[162] B. Talic, K. Norrman, T. Sand, J. Froitzheim, P.V. Hendriksen, Correlating Oxygen Electrode Degradation to Cr Vaporization from Metallic Interconnects in Solid Oxide Cell Stacks, J. Electrochem. Soc. 170 (2023) 124517. https://doi.org/10.1149/1945-7111/ad1168.
[163] C. Bernuy-Lopez, U. Bexell, M. Stenstrom, N. Norrby, J. Westlinder, The Time for Industrialization Has Come: A Pre-Coated Solution for the GW Scale, ECS Trans. 103 (2021) 1803. https://doi.org/10.1149/10301.1803ecst.
[164] J.H. Zhu, D.A. Chesson, Y.T. Yu, Review—(Mn,Co)3O4-Based Spinels for SOFC Interconnect Coating Application, J. Electrochem. Soc. 168 (2021) 114519. https://doi.org/10.1149/1945-7111/ac3a29.
[165] P. Gannon, M. Deibert, P. White, R. Smith, H. Chen, W. Priyantha, J. Lucas, V. Gorokhovsky, Advanced PVD protective coatings for SOFC interconnects, Int. J. Hydrog. Energy 33 (2008) 3991–4000. https://doi.org/10.1016/j.ijhydene.2007.12.009.
[166] N.S. Waluyo, S.-S. Park, R.-H. Song, S.-B. Lee, T.-H. Lim, J.-E. Hong, K.H. Ryu, W. Bin Im, J.-W. Lee, Protective coating based on manganese–copper oxide for solid oxide

fuel cell interconnects: Plasma spray coating and performance evaluation, Ceram. Int. 44 (2018) 11576–11581. https://doi.org/10.1016/j.ceramint.2018.03.220.
[167] M. Tomas, A. Visibile, J.-E. Svensson, J. Froitzheim, Novel coatings for protecting solid oxide fuel cell interconnects against the dual-atmosphere effect, Int. J. Hydrog. Energy 48 (2023) 18405–18419. https://doi.org/10.1016/j.ijhydene.2023.01.313.
[168] J.-E. Hong, M. Bianco, J.V. Herle, R. Steinberger-Wilckens, Properties of Spinel Protective Coatings Prepared Using Wet Powder Spraying for SOFC Interconnects, ECS Trans. 68 (2015) 1581. https://doi.org/10.1149/06801.1581ecst.
[169] N. Grünwald, D. Sebold, Y.J. Sohn, N.H. Menzler, R. Vaßen, Self-healing atmospheric plasma sprayed Mn1.0Co1.9Fe0.1O4 protective interconnector coatings for solid oxide fuel cells, J. Power Sources 363 (2017) 185–192. https://doi.org/10.1016/j.jpowsour.2017.07.072.
[170] J. Puranen, M. Pihlatie, J. Lagerbom, G. Bolelli, J. Laakso, L. Hyvärinen, M. Kylmälahti, O. Himanen, J. Kiviaho, L. Lusvarghi, P. Vuoristo, Post-mortem evaluation of oxidized atmospheric plasma sprayed Mn–Co–Fe oxide spinel coatings on SOFC interconnectors, Int. J. Hydrog. Energy 39 (2014) 17284–17294. https://doi.org/10.1016/j.ijhydene.2014.08.105.
[171] T. Brylewski, J. Dabek, K. Przybylski, J. Morgiel, M. Rekas, Screen-printed (La,Sr)CrO3 coatings on ferritic stainless steel interconnects for solid oxide fuel cells using nanopowders prepared by means of ultrasonic spray pyrolysis, J. Power Sources 208 (2012) 86–95. https://doi.org/10.1016/j.jpowsour.2012.02.015.
[172] M.-J. Tsai, C.-L. Chu, S. Lee, La0.6Sr0.4Co0.2Fe0.8O3 protective coatings for solid oxide fuel cell interconnect deposited by screen printing, J. Alloys Compd. 489 (2010) 576–581. https://doi.org/10.1016/j.jallcom.2009.09.114.
[173] S.-I. Lee, J. Hong, H. Kim, J.-W. Son, J.-H. Lee, B.-K. Kim, H.-W. Lee, K.J. Yoon, Highly Dense Mn-Co Spinel Coating for Protection of Metallic Interconnect of Solid Oxide Fuel Cells, J. Electrochem. Soc. 161 (2014) F1389. https://doi.org/10.1149/2.0541414jes.
[174] Y. Liu, D.Y. Chen, Protective coatings for Cr2O3-forming interconnects of solid oxide fuel cells, Int. J. Hydrog. Energy 34 (2009) 9220–9226. https://doi.org/10.1016/j.ijhydene.2009.09.022.
[175] A.G. Sabato, E. Zanchi, S. Molin, G. Cempura, H. Javed, K. Herbrig, C. Walter, A.R. Boccaccini, F. Smeacetto, Mn-Co spinel coatings on Crofer 22 APU by electrophoretic deposition: Up scaling, performance in SOFC stack at 850 °C and compositional modifications, J. Eur. Ceram. Soc. 41 (2021) 4496–4504. https://doi.org/10.1016/j.jeurceramsoc.2021.03.030.
[176] J.H. Zhu, Y. Zhang, A. Basu, Z.G. Lu, M. Paranthaman, D.F. Lee, E.A. Payzant, LaCrO3-based coatings on ferritic stainless steel for solid oxide fuel cell interconnect applications, Surf. Coat. Technol. 177–178 (2004) 65–72. https://doi.org/10.1016/j.surfcoat.2003.05.003.
[177] M.J. Reddy, T.E. Chausson, J.E. Svensson, J. Froitzheim, 11–23% Cr steels for solid oxide fuel cell interconnect applications at 800 °C – How the coating determines oxidation kinetics, Int. J. Hydrog. Energy (2023). https://doi.org/10.1016/j.ijhydene.2022.11.326.
[178] A. Topcu, B. Öztürk, Ö.N. Cora, Performance evaluation of machined and powder metallurgically fabricated Crofer®22 APU interconnects for SOFC applications, Int. J. Hydrog. Energy 47 (2022) 3437–3448. https://doi.org/10.1016/j.ijhydene.2021.06.036.
[179] M. Kornely, A. Neumann, N.H. Menzler, A. Leonide, A. Weber, E. Ivers-Tiffée, Degradation of anode supported cell (ASC) performance by Cr-poisoning, J. Power Sources 196 (2011) 7203–7208. https://doi.org/10.1016/j.jpowsour.2010.10.033.

[180] R. Sachitanand, M. Sattari, J.-E. Svensson, J. Froitzheim, Evaluation of the oxidation and Cr evaporation properties of selected FeCr alloys used as SOFC interconnects, Int. J. Hydrog. Energy 38 (2013) 15328–15334. https://doi.org/10.1016/j.ijhydene.2013.09.044.
[181] F. Mohsenifar, A. Irannejad, H. Ebrahimifar, Development of Mn-Co and Mn-Co-CeO2 Coatings on Crofer 22 APU Steel for Solid Oxide Fuel Cell Interconnects, J. Electrochem. Soc. 170 (2023) 124502. https://doi.org/10.1149/1945-7111/ad0ff9.
[182] B. Talic, V. Venkatachalam, P.V. Hendriksen, R. Kiebach, Comparison of MnCo2O4 coated Crofer 22 H, 441, 430 as interconnects for intermediate-temperature solid oxide fuel cell stacks, J. Alloys Compd. 821 (2020) 153229. https://doi.org/10.1016/j.jallcom.2019.153229.
[183] P. Piccardo, R. Spotorno, C. Geipel, Investigation of a Metallic Interconnect Extracted from an SOFC Stack after 40,000 h of Operation, Energies 15 (2022) 3548. https://doi.org/10.3390/en15103548.
[184] G. Ghiara, P. Piccardo, V. Bongiorno, L. Repetto, C. Geipel, R. Spotorno, Characterization of metallic interconnects extracted from Solid Oxide Fuel Cell stacks operated up to 20,000 h in real life conditions: The fuel side, Int. J. Hydrog. Energy 46 (2021) 23815–23827. https://doi.org/10.1016/j.ijhydene.2021.04.156.
[185] G. Ghiara, P. Piccardo, V. Bongiorno, C. Geipel, R. Spotorno, Characterization of Metallic Interconnects Extracted from Solid Oxide Fuel Cell Stacks Operated up to 20,000 h in Real Life Conditions: The Air Side, Energies 13 (2020) 6487. https://doi.org/10.3390/en13246487.
[186] M. Kusnezoff, N. Trofimenko, M. Müller, A. Michaelis, Influence of Electrode Design and Contacting Layers on Performance of Electrolyte Supported SOFC/SOEC Single Cells, Materials 9 (2016) 906. https://doi.org/10.3390/ma9110906.
[187] M. N, K. Santhy, B. Rajasekaran, The effect of strain induced phase transformation on the thermal expansion compatibility of plasma sprayed spinel coating on SOFC metallic interconnect – A study using in-situ high temperature X-ray diffraction, Int. J. Hydrog. Energy (2023). https://doi.org/10.1016/j.ijhydene.2023.04.322.
[188] O. Thomann, M. Pihlatie, J.A. Schuler, O. Himanen, J. Kiviaho, Method for Measuring Chromium Evaporation from SOFC Balance-of-Plant Components, Electrochem. Solid-State Lett. 15 (2012) B35. https://doi.org/10.1149/2.022203esl.
[189] M.J. Reddy, J.-E. Svensson, J. Froitzheim, Evaluating candidate materials for balance of plant components in SOFC: Oxidation and Cr evaporation properties, Corros. Sci. 190 (2021) 109671. https://doi.org/10.1016/j.corsci.2021.109671.
[190] I.M. Robertson, P. Sofronis, A. Nagao, M.L. Martin, S. Wang, D.W. Gross, K.E. Nygren, Hydrogen Embrittlement Understood, Metall Mater. Trans. A 46 (2015) 2323–2341. https://doi.org/10.1007/s11661-015-2836-1.
[191] Toh, Baldwin, JR., Stress Corrosion Cracking and Embrittlement, John Wiley & Sons, Ltd, New York, NY, 1956.
[192] I.M. Bernstein, The role of hydrogen in the embrittlement of iron and steel, Mater. Sci. Eng. 6 (1970) 1–19. https://doi.org/10.1016/0025-5416(70)90073-X.
[193] D. Kniep, S. Schewe, M. Rudolphi, M.C. Galetz, Hydrogen permeation and embrittlement behavior of ferritic SOEC/SOFC interconnect candidates, Int. J. Hydrog. Energy (2024). https://doi.org/10.1016/j.ijhydene.2024.03.337.
[194] SanergyTM HT, (-). https://www.alleima.com/en/products/coated-strip-steel/sanergy-ht/ (accessed November 10, 2023).
[195] C. Goebel, R. Berger, C. Bernuy-Lopez, J. Westlinder, J.-E. Svensson, J. Froitzheim, Long-term (4 year) degradation behavior of coated stainless steel 441 used for solid oxide fuel cell interconnect applications, J. Power Sources 449 (2020) 227480. https://doi.org/10.1016/j.jpowsour.2019.227480.

[196] C. Goebel, V. Asokan, S. Khieu, J.-E. Svensson, J. Froitzheim, Self-healing properties of Ce/Co-coated stainless steel under simulated intermediate temperature solid oxide fuel cell conditions, Surf. Coat. Technol. 428 (2021) 127894. https://doi.org/10.1016/j.surfcoat.2021.127894.
[197] N. Norrby, S. Li, M. Stenström, J. Westlinder, The Coating Effect on Interconnect Materials After >10 Years of Furnace Exposures, ECS Trans. 111 (2023) 2223. https://doi.org/10.1149/11106.2223ecst.
[198] J. Froitzheim, H. Ravash, E. Larsson, L.G. Johansson, J.E. Svensson, Investigation of Chromium Volatilization from FeCr Interconnects by a Denuder Technique, J. Electrochem. Soc. 157 (2010) B1295. https://doi.org/10.1149/1.3462987.
[199] A. Weber, Impedance analysis of porous electrode structures in batteries and fuel cells, Tm - Technisches Messen 88 (2021) 1–16. https://doi.org/10.1515/teme-2020-0084.
[200] J. Froitzheim, S. Canovic, M. Nikumaa, R. Sachitanand, L.G. Johansson, J.E. Svensson, Long term study of Cr evaporation and high temperature corrosion behaviour of Co coated ferritic steel for solid oxide fuel cell interconnects, J. Power Sources 220 (2012) 217–227. https://doi.org/10.1016/j.jpowsour.2012.06.092.
[201] A. Beez, X. Yin, N.H. Menzler, R. Spatschek, M. Bram, Insight into the Reaction Mechanism of (La0.58Sr0.40)(Co0.20Fe0.80)O3-δ Cathode with Volatile Chromium Species at High Current Density in a Solid Oxide Fuel Cell Stack, J. Electrochem. Soc. 164 (2017) F3028. https://doi.org/10.1149/2.0051710jes.
[202] N.H. Menzler, D. Sebold, Q. Fang, Chromium-Related Degradation of Thin-Film Electrolyte Solid Oxide Fuel Cell Stacks, J. Electrochem. Soc. 162 (2015) F1275. https://doi.org/10.1149/2.0101512jes.
[203] S. Fontana, R. Amendola, S. Chevalier, P. Piccardo, G. Caboche, M. Viviani, R. Molins, M. Sennour, Metallic interconnects for SOFC: Characterisation of corrosion resistance and conductivity evaluation at operating temperature of differently coated alloys, J. Power Sources 171 (2007) 652–662. https://doi.org/10.1016/j.jpowsour.2007.06.255.
[204] A. Weber, Testing of solid oxide cells at high current densities, Tm - Technisches Messen 89 (2022) 97–106. https://doi.org/10.1515/teme-2021-0102.
[205] A. Leonide, V. Sonn, A. Weber, E. Ivers-Tiffée, Evaluation and Modeling of the Cell Resistance in Anode-Supported Solid Oxide Fuel Cells, J. Electrochem. Soc. 155 (2007) B36. https://doi.org/10.1149/1.2801372.
[206] M.W. Lundberg, R. Berger, J. Westlinder, H. Holmberg, Multilayered Precoated AISI 441 for Solid Oxide Fuel Cell Interconnects, ECS Trans. 68 (2015) 1681. https://doi.org/10.1149/06801.1681ecst.
[207] Q. Fang, L. Blum, D. Stolten, Electrochemical Performance and Degradation Analysis of an SOFC Short Stack Following Operation of More than 100,000 Hours, J. Electrochem. Soc. 166 (2019) F1320. https://doi.org/10.1149/2.0751916jes.
[208] Flexitallic Deutschland, Flexitallic Deutschland (-). https://www.flexitallic.de/ (accessed July 18, 2024).
[209] SCHOTT Festoxid-Elektrolyseurzellen (SOEC), (-). https://www.schott.com/de-de/expertise/anwendungen/festoxid-elektrolyseurzellen (accessed December 15, 2023).
[210] C. Bienert, M. Brandner, S. Skrabs, A. Venskutonis, L.S. Sigl, S. Megel, W. Becker, N. Trofimenko, M. Kusnezoff, A. Michaelis, CFY-Stack Technology: The Next Design, ECS Trans. 68 (2015) 2159. https://doi.org/10.1149/06801.2159ecst.
[211] D. Gödeke, U. Dahlmann, Study on the crystallization behaviour and thermal stability of glass-ceramics used as solid oxide fuel cell-sealing materials, J. Power Sources 196 (2011) 9046–9050. https://doi.org/10.1016/j.jpowsour.2010.12.054.
[212] H. Javed, A.G. Sabato, I. Dlouhy, M. Halasova, E. Bernardo, M. Salvo, K. Herbrig, C. Walter, F. Smeacetto, Shear Performance at Room and High Temperatures of Glass–

Ceramic Sealants for Solid Oxide Electrolysis Cell Technology, Materials 12 (2019) 298. https://doi.org/10.3390/ma12020298.
[213] H. Javed, A.G. Sabato, K. Herbrig, D. Ferrero, C. Walter, M. Salvo, F. Smeacetto, Design and characterization of novel glass-ceramic sealants for solid oxide electrolysis cell (SOEC) applications, Int. J. Appl. Ceram. Technol. 15 (2018) 999–1010. https://doi.org/10.1111/ijac.12889.
[214] J. Suffner, C. Dobler, Long Term Behavior of Viscous High-Temperature Sealing Glasses, ECS Trans. 57 (2013) 2375. https://doi.org/10.1149/05701.2375ecst.
[215] J. Schilm, A. Rost, M. Kusnezoff, S. Megel, A. Michaelis, Glass ceramics sealants for SOFC interconnects based on a high chromium sinter alloy, Int. J. Appl. Ceram. Technol. 15 (2018) 239–254. https://doi.org/10.1111/ijac.12811.
[216] J. Schilm, M. Kusnezoff, A. Rost, Glass Ceramic Sealants for Solid Oxide Cells, in: M.A. Laguna-Bercero (Ed.), High Temperature Electrolysis, Springer International Publishing, Cham, 2023: pp. 153–205. https://doi.org/10.1007/978-3-031-22508-6_7.
[217] M. Perz, E. Bucher, C. Gspan, J. Waldhäusl, F. Hofer, W. Sitte, Long-term degradation of La0.6Sr0.4Co0.2Fe0.8O3-δ IT-SOFC cathodes due to silicon poisoning, Solid State Ionics 288 (2016) 22–27. https://doi.org/10.1016/j.ssi.2016.01.005.
[218] E. Bucher, C. Gspan, F. Hofer, W. Sitte, Post-test analysis of silicon poisoning and phase decomposition in the SOFC cathode material La0.58Sr0.4Co0.2Fe0.8O3 − δ by transmission electron microscopy, Solid State Ionics 230 (2013) 7–11. https://doi.org/10.1016/j.ssi.2012.08.013.
[219] H. Nami, P.V. Hendriksen, H.L. Frandsen, Green ammonia production using current and emerging electrolysis technologies, Renew. Sust. Energy Rev. 199 (2024) 114517. https://doi.org/10.1016/j.rser.2024.114517.
[220] L.R. Clausen, G. Butera, S.H. Jensen, High efficiency SNG production from biomass and electricity by integrating gasification with pressurized solid oxide electrolysis cells, Energy 172 (2019) 1117–1131. https://doi.org/10.1016/j.energy.2019.02.039.
[221] G. Butera, S.H. Jensen, R.Ø. Gadsbøll, J. Ahrenfeldt, L.R. Clausen, Biomass conversion to methanol integrating solid oxide cells and two-stage gasifier: Effects of carbon dioxide recirculation and pressurized operation, Chemical Engineering Transactions 76 (2019) 1177–1182. https://doi.org/10.3303/CET1976197.
[222] L. Wehrle, D. Schmider, J. Dailly, A. Banerjee, O. Deutschmann, Benchmarking solid oxide electrolysis cell-stacks for industrial Power-to-Methane systems via hierarchical multi-scale modelling, Appl. Energy 317 (2022) 119143. https://doi.org/10.1016/j.apenergy.2022.119143.
[223] M. Gruber, P. Weinbrecht, L. Biffar, S. Harth, D. Trimis, J. Brabandt, O. Posdziech, R. Blumentritt, Power-to-Gas through thermal integration of high-temperature steam electrolysis and carbon dioxide methanation - Experimental results, Fuel Process. Technol. 181 (2018) 61–74. https://doi.org/10.1016/j.fuproc.2018.09.003.
[224] Y. Wang, R. Zhan, Y. Qin, G. Zhang, Q. Du, K. Jiao, Three-dimensional modeling of pressure effect on operating characteristics and performance of solid oxide fuel cell, Int. J. Hydrog. Energy 43 (2018) 20059–20076. https://doi.org/10.1016/j.ijhydene.2018.09.025.
[225] W. Jiang, R. Fang, J.A. Khan, R.A. Dougal, Parameter setting and analysis of a dynamic tubular SOFC model, J. Power Sources 162 (2006) 316–326. https://doi.org/10.1016/j.jpowsour.2006.06.086.
[226] K.P. Recknagle, E.M. Ryan, B.J. Koeppel, L.A. Mahoney, M.A. Khaleel, Modeling of electrochemistry and steam–methane reforming performance for simulating pressurized solid oxide fuel cell stacks, J. Power Sources 195 (2010) 6637–6644. https://doi.org/10.1016/j.jpowsour.2010.04.024.

[227] L. Zhou, M. Cheng, B. Yi, Y. Dong, Y. Cong, W. Yang, Performance of an anode-supported tubular solid oxide fuel cell (SOFC) under pressurized conditions, Electrochim. Acta 53 (2008) 5195–5198. https://doi.org/10.1016/j.electacta.2008.02.032.
[228] A. Momma, K. Takano, Y. Tanaka, T. Kato, A. Yamamoto, Experimental Investigation of the Effect of Operating Pressure on the Performance of SOFC and SOEC, ECS Trans. 57 (2013) 699. https://doi.org/10.1149/05701.0699ecst.
[229] S. Seidler, M. Henke, J. Kallo, W.G. Bessler, U. Maier, K.A. Friedrich, Pressurized solid oxide fuel cells: Experimental studies and modeling, J. Power Sources 196 (2011) 7195–7202. https://doi.org/10.1016/j.jpowsour.2010.09.100.
[230] C. Cadigan, C. Chmura, G. Floerchinger, P. Frankl, S. Hunt, S. Jensen, C. Boushehri, T.L. Vincent, R. Braun, N.P. Sullivan, Performance characterization of metal-supported solid-oxide fuel cell stacks at elevated pressure, J. Power Sources 573 (2023) 233083. https://doi.org/10.1016/j.jpowsour.2023.233083.
[231] A.A. Burke, L.G. Carreiro, J.R. Izzo, Pressurized testing of a planar solid oxide fuel cell stack, Int. J. Hydrog. Energy 38 (2013) 13774–13780. https://doi.org/10.1016/j.ijhydene.2013.08.058.
[232] R. Kikuchi, T. Yano, T. Takeguchi, K. Eguchi, Characteristics of anodic polarization of solid oxide fuel cells under pressurized conditions, Solid State Ionics 174 (2004) 111–117. https://doi.org/10.1016/j.ssi.2004.05.029.
[233] L. Bernadet, G. Gousseau, A. Chatroux, J. Laurencin, F. Mauvy, M. Reytier, Influence of pressure on solid oxide electrolysis cells investigated by experimental and modeling approach, Int. J. Hydrog. Energy 40 (2015) 12918–12928. https://doi.org/10.1016/j.ijhydene.2015.07.099.
[234] S.S. Shy, S.C. Hsieh, H.Y. Chang, A pressurized ammonia-fueled anode-supported solid oxide fuel cell: Power performance and electrochemical impedance measurements, J. Power Sources 396 (2018) 80–87. https://doi.org/10.1016/j.jpowsour.2018.06.006.
[235] S.C. Singhal, Recent Progress in Tubular Solid Oxide Fuel Cell Technology, Proc. Vol. 1997–40 (1997) 37. https://doi.org/10.1149/199740.0037PV.
[236] Y. Luo, Y. Shi, Y. Chen, W. Li, L. Jiang, N. Cai, Pressurized tubular solid oxide H2O/CO2 coelectrolysis cell for direct power-to-methane, AIChE Journal 66 (2020) e16896. https://doi.org/10.1002/aic.16896.
[237] M.T. Mehran, S.-B. Yu, D.-Y. Lee, J.-E. Hong, S.-B. Lee, S.-J. Park, R.-H. Song, T.-H. Lim, Production of syngas from H2O/CO2 by high-pressure coelectrolysis in tubular solid oxide cells, Appl. Energy 212 (2018) 759–770. https://doi.org/10.1016/j.apenergy.2017.12.078.
[238] S.H. Jensen, C. Graves, M. Chen, J.B. Hansen, X. Sun, Characterization of a Planar Solid Oxide Cell Stack Operated at Elevated Pressure, J. Electrochem. Soc. 163 (2016) F1596. https://doi.org/10.1149/2.1171614jes.
[239] M. Henke, C. Willich, C. Westner, F. Leucht, R. Leibinger, J. Kallo, K.A. Friedrich, Effect of pressure variation on power density and efficiency of solid oxide fuel cells, Electrochim. Acta 66 (2012) 158–163. https://doi.org/10.1016/j.electacta.2012.01.075.
[240] Y.T. Hung, S.S. Shy, A pressurized ammonia-fed planar anode-supported solid oxide fuel cell at 1–5 atm and 750–850°C and its loaded short stability test, Int. J. Hydrog. Energy 45 (2020) 27597–27610. https://doi.org/10.1016/j.ijhydene.2020.07.064.
[241] A.M. Martos, S. Márquez, R.S. Pavlov, W. Zambelli, S. Anelli, M. Nuñez, L. Bernadet, J.J. Brey, M. Torrell, A. Tarancón, 3D printing of reversible solid oxide cell stacks for efficient hydrogen production and power generation, J. Power Sources 609 (2024) 234704. https://doi.org/10.1016/j.jpowsour.2024.234704.
[242] M.Á. Morales-Zapata, J. Mora, U. Aydin, A. Orera, M.Á. Laguna-Bercero, Advanced microtubular solid oxide cells for stack integration and operation under pressure, Proceedings of the 16th European SOFC&SOE Forum (2024).

[243] B. Zhang, N.F. Harun, N. Zhou, J.J. Colon-Rodriguez, D. Oryshchyn, L. Shadle, D. Tucker, S. Bayham, A real-time multiphysics model of a pressurized solid oxide electrolysis cell (SOEC) for cyber-physical simulation, Energy Convers. Manag. 298 (2023) 117778. https://doi.org/10.1016/j.enconman.2023.117778.
[244] M. Langerman, E. da R. Silva, D. Nauta, H. van Wees, J. Veldhuis, R. Makkus, F. van Berkel, C. Ferchaud, I. Mirabelli, H. ten Dam, Pressurized SOE stack technology for industrial process integration, in: Proceedings of the EFCF 2024, Lucerne, Switzerland, 2024.
[245] M. Meffert, F. Wankmüller, H. Störmer, A. Weber, P. Lupetin, E. Ivers-Tiffée, D. Gerthsen, Optimization of Material Contrast for Efficient FIB-SEM Tomography of Solid Oxide Fuel Cells, Fuel Cells 20 (2020) 580–591. https://doi.org/10.1002/fuce.202000080.
[246] F. Berkel, C.J. Ferchaud, O. Partenie, M. Linders, Y. van Delft, Solid Oxide Cell Technology Development at TNO, ECS Trans. 103 (2021) 591. https://doi.org/10.1149/10301.0591ecst.
[247] M. Langerman, M. Stodolny, E. da R. Silva, X. Lu, C. Ferchaud, F. van Berkel, Solid Oxide Cell Performance: Spatially Resolved Oxygen Electrode Stability, ECS Trans. 111 (2023) 2277. https://doi.org/10.1149/11106.2277ecst.
[248] S. Korneychuk, C. Grosselindemann, N.H. Menzler, A. Weber, A. Pundt, In-situ TEM reduction of a solid oxide cell with NiO/YSZ fuel electrode, J. Power Sources 625 (2025) 235626. https://doi.org/10.1016/j.jpowsour.2024.235626.
[249] D.G. Goodwin, H.K. Moffat, I. Schoegl, R.L. Speth, B.W. Weber, Cantera: An object-oriented software toolkit for chemical kinetics, thermodynamics, and transport processes, (2022). https://www.cantera.org.
[250] C. Grosselindemann, D. Esau, M. Dorn, F.M. Bauer, L. Wissmeier, A. Weber, From Ideal to Stack-like Contacting of an SOC, ECS Trans. 111 (2023) 533. https://doi.org/10.1149/11106.0533ecst.
[251] M.J. Reddy, J.-E. Svensson, J. Froitzheim, Reevaluating the Cr Evaporation Characteristics of Ce/Co Coatings for Interconnect Applications, ECS Trans. 103 (2021) 1899. https://doi.org/10.1149/10301.1899ecst.
[252] D. Ewald, C. Grosselindemann, D. Esau, F.-M. Fuchs, A. Weber, Stack-like Contacting in Solid Oxide Cells: Electrochemical Characterization and Modeling, J. Electrochem. Soc. 171 (2024) 044506. https://doi.org/10.1149/1945-7111/ad3a16.
[253] A. Gladik, Thermal Design and Validation of a High-Pressure PEMWE Test Bench, Master Thesis (2022).
[254] Kanthal® APMT — Kanthal®, (-). https://www.kanthal.de/produkte-und-dienstleistungen/datasheets/materialdatenbl%C3%A4tter/draht/konstruktionsmaterialien/kanthal-apmt/ (accessed May 14, 2025).
[255] R. Kiebach, K. Agersted, P. Zielke, I. Ritucci, M.B. Brock, P.V. Hendriksen, A Novel SOFC/SOEC Sealing Glass with a Low SiO2 Content and a High Thermal Expansion Coefficient, ECS Trans. 78 (2017) 1739. https://doi.org/10.1149/07801.1739ecst.
[256] C. Endler-Schuck, A. Leonide, A. Weber, S. Uhlenbruck, F. Tietz, E. Ivers-Tiffée, Performance analysis of mixed ionic–electronic conducting cathodes in anode supported cells, J. Power Sources 196 (2011) 7257–7262. https://doi.org/10.1016/j.jpowsour.2010.11.079.
[257] H.I. Geisler, Finite Element Method (FEM) Model and Performance Analysis of Solid Oxide Fuel Cells, (2019). https://doi.org/10.5445/KSP/1000090508.
[258] B.E. Poling, J.M. Prausnitz, J.P. O'connell, The properties of gases and liquids, Mcgraw-hill New York, 2001. https://www.academia.edu/download/62015682/Prausnitz_-_Properties_of_Gases_and_Liquids20200206-55970-35et18.pdf (accessed May 29, 2024).

[259] D. Klotz, J.-C. Njodzefon, A. Weber, E. Ivers-Tiffée, Current-Voltage and Temperature Characteristics of Anode Supported Solid Oxide Electrolyzer Cells (SOEC), ECS Trans. 45 (2012) 523. https://doi.org/10.1149/1.3701344.
[260] H. Geisler, M. Kornely, A. Weber, E. Ivers-Tiffée, Enhancing SOFC-Stack Performance by Model-Based Adaptation of Cathode Gas Transport Conditions, ECS Trans. 57 (2013) 2871. https://doi.org/10.1149/05701.2871ecst.
[261] C. Endler, A. Leonide, A. Weber, F. Tietz, E. Ivers-Tiffée, Time-Dependent Electrode Performance Changes in Intermediate Temperature Solid Oxide Fuel Cells, J. Electrochem. Soc. 157 (2009) B292. https://doi.org/10.1149/1.3270047.
[262] I.D. Unachukwu, V. Vibhu, J. Uecker, I.C. Vinke, R.-A. Eichel, L.G.J. (Bert) de Haart, Electrochemical impedance analysis and degradation behavior of a Ni-GDC fuel electrode containing single cell in direct CO2 electrolysis, Journal of CO2 Utilization 69 (2023) 102423. https://doi.org/10.1016/j.jcou.2023.102423.
[263] D. Klotz, A. Leonide, A. Weber, E. Ivers-Tiffée, Electrochemical model for SOFC and SOEC mode predicting performance and efficiency, Int. J. Hydrog. Energy 39 (2014) 20844–20849. https://doi.org/10.1016/j.ijhydene.2014.08.139.
[264] X. Chen, P.Y. Hou, C.P. Jacobson, S.J. Visco, L.C. De Jonghe, Protective coating on stainless steel interconnect for SOFCs: oxidation kinetics and electrical properties, Solid State Ionics 176 (2005) 425–433. https://doi.org/10.1016/j.ssi.2004.10.004.
[265] C. Xiong, J.A. Taillon, C. Pellegrinelli, Y.-L. Huang, L.G. Salamanca-Riba, B. Chi, L. Jian, J. Pu, E.D. Wachsman, Long-Term Cr Poisoning Effect on LSCF-GDC Composite Cathodes Sintered at Different Temperatures, J. Electrochem. Soc. 163 (2016) F1091. https://doi.org/10.1149/2.0841609jes.
[266] T. Horita, Chromium poisoning for prolonged lifetime of electrodes in solid oxide fuel cells - Review, Ceram. Int. 47 (2021) 7293–7306. https://doi.org/10.1016/j.ceramint.2020.11.082.
[267] S. Wang, M. Katsuki, M. Dokiya, T. Hashimoto, High temperature properties of La0.6Sr0.4Co0.8Fe0.2O3−δ phase structure and electrical conductivity, Solid State Ionics 159 (2003) 71–78. https://doi.org/10.1016/S0167-2738(03)00027-4.
[268] S. Bond, S. Shaw, Introduction of a Low Sealing Stress Vermiculite Based Compression Gasket for SOFCs, ECS Trans. 83 (2018) 159. https://doi.org/10.1149/08301.0159ecst.
[269] M. Bram, L. Niewolak, N. Shah, D. Sebold, H.P. Buchkremer, Interaction of sealing material mica with interconnect steel for solid oxide fuel cells application at 600 °C, J. Power Sources 196 (2011) 5889–5896. https://doi.org/10.1016/j.jpowsour.2011.02.086.
[270] Wasserstoff-Leitprojekte: Wissenswertes, (-). https://www.wasserstoff-leitprojekte.de/wissenswertes (accessed May 14, 2025).